PLASTIC BUCKLING OF CYLINDERS UNDER BIAXIAL LOADING

Thesis by

Jurgen J. Giezen

In Partial Fufillment of the Requirements

for the Degree of

Doctor of Philosophy

California Institute of Technology

Pasadena, California

1988

(Submitted February 25, 1988)

DEDICATION

This work is dedicated to my parents and my wife, whose support and encouragement I could not have done without, and is submitted in memory of my late advisor, Dr. C.D. Babcock.

ACKNOWLEDGEMENTS

I would first like to express my gratitude to the late Dr. Chuck Babcock for his guidance during the course of this investigation. I would also like to express my sincere thanks and appreciation to Dr. Wolfgang G. Knauss and Dr. Josef Singer for their direction and support in the final stages of this work.

Special thanks go to the technicians of GALCIT and to Carol Choy, Carol Mullenax, and all others in Lloyd House who assisted me in preparing this manuscript.

Finally, the financial assistance of the California Institute of Technology and the Bechtel Corporation is gratefully acknowledged.

ABSTRACT

An experimental investigation is carried out to study the effects of nonproportional loading in the plastic range on the buckling load. The discrepancy between experimental and theoretical results points to some principal shortcoming in the analysis. The problem has been simplified by applying axial tensile load and external pressure to a simple cylindrical shell specimen and observing the buckling load for various nonproportional load-paths. Results are compared to numerical predictions (BOSOR5), using classical type plasticity models such as J_2 deformation and J_2 incremental theory. Significant discrepancy was found and attributed to inadequate modeling of the nonlinear material behavior. The effects of geometrical imperfections and large deflections were found to be insignificant, thereby leading to an idea how much of the discrepancy between test and theory is due to the use of an inadequate plastic model. The introduction of the Southwell plot into the plastic shell buckling problem reduced the already minor effects of geometric imperfections.

The Christoffersen-Hutchinson corner theory model was introduced into BOSOR5 in its simplest form as presented by Poh-Sang Lam. Results obtained with this model, which allows corners to form on an initially smooth yield surface, displayed better agreement with experimental data. However, increased computational time and problems related to abrupt changes in load-path at the corner are a major concern at the present time.

TABLE OF CONTENTS

FIGURES AND TABLES

1.0 INTRODUCTION

1.1 GENERAL

The goal of this research is to understand the influence of plasticity on the collapse of engineering structures and, in particular, of shells. Collapse of shells in the plastic range is not a new subject, but it has been treated in a rather *ad hoc* manner for many years. Reference [1] briefly reviews the field and lists references to the many works on the subject. The real stumbling block to a satisfactory resolution of the problem is the definition of the plastic constitutive relation. It is well known that details of the plasticity model can have radical effects on the collapse load calculations. This is particularly true for shell structures. In this research, collapse occurs as a result of bifurcation into a nonsymmetric postbuckling state from a symmetric prebuckling state.

The approach taken in this work is not to develop a full-fledged theory of plasticity constitutive behavior but to study the effects of certain aspects of the plasticity model on the collapse behavior of a simple shell structure. The structure selected for the study is a cylindrical shell, which is subjected to biaxial loading. The loading is combined external pressure and axial tension, which is applied in a rather simple nonproportional manner. As mentioned before, for this problem the prebuckling problem is axisymmetric and buckling is by bifurcation (for the perfect structure) into a mode containing several circumferential waves.

The number of circumferential waves and the stresses at bifurcation are controlled by changing the length of the test specimen. A suitable shell length is chosen, such that the shell is loading in the plastic range during prebuckling, and bifurcation also occurs in the nonlinear range. Four or more waves around the circumference are observed for those shells with buckling stresses well into the plastic range (Table 3.2). These particular shells buckle therefore in modes that are substantially different from the largest initial imperfection modes (2 or 3 circumferential waves), resulting in accurate observation of the buckling phenomenon.

Numerical predictions of the collapse or bifurcation load are carried out using a number of standard plasticity models. Bushnell's "BOSOR5" shell-code is used as a "predictive tool" [Ref. 23]. BOSOR5 incorporates standard J_2 plasticity theory with istropic hardening, using either incremental or deformation theory in the bifurcation analysis. Some references that provide a general background and overview of the subject of plastic buckling are listed in the back of this thesis [Refs. 37,50,66].

Part of this research included the introduction of a corner theory, developed by Christoffersen and Hutchinson (CH)[Ref. 53], into the existing numerical analysis. In this type of analysis, an initially smooth yield surface can develop a corner at the loading point with the associated consequences for the constitutive relations. The idea behind the corner theory is to maintain incremental principles such as a yield surface, convexity and normality of the yield surface, while providing some additional freedom in picking parameters (often based on physical principles) that determine stress-strain constitutive behavior. The formation of a corner results in a region instead of a single normal of possible plastic strains, while the normality condition of incremental theory is still maintained. Proper identification of the plastic strain is dependent upon the correct definition of the corner and the associated parameters.

Tvergaard [Ref. 57,74] has applied the CH corner theory, as described in Reference [53], to axially compressed cylindrical shells. A more suitable form of the theory (for introduction into BOSOR5) can be found in Lam [Ref. 56]. It is in this form that the CH corner theory is introduced in the BOSOR5 shell-code, and is used in the prebuckling and bifurcation analysis. Needleman and Tvergaard [Ref. 73] have also applied this particular theory to elastic-plastic fracture mechanics problems and found agreement with existing theory under certain conditions.

The origins of this research can be found in the treatment of plastically deforming shells subjected to nonproportional loading. In particular papers by Bushnell and Galletly [Ref. 2] and Bushnell [Ref. 3] discuss the problem of internally pressurized torispherical vessel heads that experience nonproportional loading in the knuckle region after the material has yielded. Comparison of test and theory indicates that constitutive modeling is not correct in the plastic domain and needs to be further investigated. This led to the much simplified cylindrical shell problem, which is used to identify the effects of load biaxiality on the buckling problem.

An interesting point in this biaxial loading problem is that the external pressure in this research induces compressive hoop stresses that are structurally destabilizing because of the possibility of buckling (structural instability), while the axial tension is structurally stabilizing through stiffening of the shell against buckling and through the observed reduction of initial imperfections. However, axial tension is also materially destabilizing since it moves the material farther into the plastic region and reduces the stiffness of the structure (material instability). It is therefore possible to observe buckling of the test shell under constant external pressure with increasing axial tension, when the shell is loaded in the plastic region.

1.2 INTERNALLY PRESSURIZED VESSEL HEADS

In the paper by Bushnell and Galletly [Ref. 2], it is mentioned that interest in internally pressurized torispherical vessel heads was stimulated by the failure of a large fluid vessel (coker) undergoing a hydrostatic proof test at Avon, California, in 1956. Galletly [Refs. 4,5] determined from an elastic, small deflection analysis that the stresses exceeded the yield point of the material by considerable margins over substantial portions of the vessel. Various other elastic-plastic analyses of torispherical shells were published and are listed by Bushnell and Galletly [Ref. 2]. Recent work by Galletly on this problem is shown in Reference [69].

In "Plastic Buckling" by Bushnell [Ref. 6], several papers dealing with this type of nonsymmetric buckling of elastic-plastic pressure vessel heads are mentioned. The "Plastic Buckling" paper by Bushnell is the basic reference from which considerable information was extracted to guide the work in this research, and will therefore be referred to quite often in this thesis. Brown and Kraus [Ref. 7] calculated critical pressures for internally pressurized ellipsoidal heads with the use of small deflection theory. Bushnell and Galletly [Ref. 8] found buckling loads for externally pressurized torispherical heads pierced by nozzles and for conical heads using large deflection theory in the prebuckling analysis. Bushnell and Galletly [Ref. 2], Lagae and Bushnell [Ref. 10], and Galletly [Ref. 10, 11] used the BOSOR5 computer program, to compare theoretical predictions with tests by Kirk and Gill [Ref. 12], Patel and Gill [Ref. 13] and Galletly [Ref. 10, 11] for buckling of internally pressurized torispherical and ellipsoidal heads. Figure 1.1 shows the configuration of Kirk and Gill's [Ref. 12] and Patel and Gill's [Ref. 13] torispherical specimens. In Figure 1.2 Galletly's specimen is shown with a deformed meridian at the bifurcation buckling pressure.

Figure 1.3 depicts the torispherical specimens after buckling with the lobes that are due to buckling visible along the upper rim of the shell. This figure is taken from Patel and Gill [Ref. 13]. The actual loading that induces buckling are the circumferential (hoop) compressive stresses, which develop as the internal pressure tries to deform the relatively flat shell end into a hemisphere. Compressive stresses are observed whenever the radius (r) of the torispherical vessel in the knuckle region is diminished from that in the undeformed state, and it is this hoop compression that causes nonsymmetric bifurcation buckling.

For monotonically increasing internal pressure above the yield pressure (pressure that causes initial yield in the material), the circumferential and meridional stresses in the knuckle region do not increase proportionallly. However, during the initial elastic loading these stresses increase proportionally,as is shown in Figure 1.4. The curvature of a path in stress space (after initial yield) followed by a given point in the knuckle region, depends very strongly on the amount of post-yield hardening exhibited by the material from which the vessel head is fabricated. Figure 1.4 shows the stress-path for the membrane stress in the knuckle region for torispherical shells subjected to internal pressure. The less strain hardening in the material behavior, the more this path is curved, as can be observed in Figure 1.4.

The predicted internal buckling pressure obtained with elastic-plastic analysis is less than the pressure obtained with pure elastic analysis. This is due to a slower increase of hoop compression when the material is deforming nonlinearly. When the material is deforming within the plastic range, the shell with the least strain hardening will have the lowest increase in hoop compression and consequently requires a higher internal pressure to cause buckling, unless, the shell fails axially before buckling.

When plasticity is introduced in the analysis, the buckling pressure becomes model-dependent and the use of deformation theory rather than flow theory in the stability analysis leads to lower predicted buckling pressures. How much of the discrepancy between test results and theory is due to initial nonaxisymmetric imperfections in these torispherical specimens, and how much is due to the inability of the analytical model to predict accurately biaxial flow in situations when the material is loaded nonproportionally, remain to be resolved.

The object of this research is to determine whether, through the use of simple shells subjected to non-proportional load-paths, more specific information can be obtained to evaluate classical plasticity models and their performance. The type of loading applied in these experiments reduces the nonaxisymmetric imperfections, such that results will not be dominated by these effects. Simple nonproportional loading is applied beyond the proportional limit of the material, and the buckling behavior is observed either visually or with a probe.

Other issues such as isotropy and buckling detection will also be addressed, since they influence the prediction of the buckling load. However, the main point is to try to determine how much of the discrepancy between test and theory is due to use of an inadequate model for nonlinear material behavior.

2.0 EXPERIMENTAL SET-UP

2.1 GENERAL DESCRIPTION

In order to make some headway in this problem, it was necessary to carry out a large number of experiments. The initial phase of the work concentrated on the development of a low-cost experimental set-up, which could use simple and inexpensive test specimens. A prototype test device was developed, which could subject cylindrical specimens to external pressure while allowing the buckling phenomenon to be viewed through the end plugs. This prototype test device was pressurized with a manually operated pump.

Various modifications of the protoype test device were carried out so that the test set-up could be placed in a displacement-controlled loading machine (INSTRON). As a result of these modifications, the test specimen could now be subjected to biaxial loading (axial tension and external pressure). During these new buckling experiments with large axial loads, the bifurcation point became increasingly difficult to detect and observe. A detection system was developed, which improved repeatability of the experimental work and the accuracy with which the buckling point could be determined.

Because of material creep problems in the displacement-controlled loading machine, the set-up was adapted for use in a load-controlled machine (MTS). Manual operation of the external pressure and axial load was considered inaccurate, and the system was changed to include a function-controlled load-path. The complete system now includes: computer data acquisition, function-controlled loading, displacement sensing of shell wall deformation, and feedback sensing of loads for accurate load control. A system to protect the probe during buckling was also incorporated, when the buckling deformation that was due to constant loads threatened to damage the sensitive system.

Another important aspect of this work was the determination of the test specimen material properties. Past practice in the laboratory had been to mount strain gages on the tensile specimen and manually load and record data. In order to speed up this procedure an existing digital acquisition system (RIMS) was set up to carry out this type of test in a routine manner. To obtain uniaxial test specimens of constant width, a method was devised to machine strips from the original cylindrical tube (from which the specimens were cut). Circumferential stress-strain curves were obtained by internally pressurizing individual tube sections.

2.2 THE TEST CHAMBER (PRESSURE SLEEVE)

The objectives of this research program required the construction of a chamber capable of subjecting a cylindrical test specimen to combined lateral pressure and axial load. It was important that the hydrostatic pressure in the chamber not result in any axial load's being applied to the test specimen. This condition required special attention to the mating of the specimen to its support fixtures. A similar design condition was that specimen displacement be unconstrained in the axial direction, whether or not the specimen was subjected to axial loads.

A feature that had to be incorporated into the design at a later stage was the capability to observe the buckling process. The prebuckling, buckling and postbuckling deformations had to be measured if the buckling point was to be determined accurately. It was decided that a small internal noncontacting probe would best suit the size and accuracy requirements, without making the assembly and disassembly unduly complicated.

Since critical pressures or buckling pressures depend on geometric variables such as length, diameter and thickness, it was necessary to be able to change these variables so that buckling could be obtained under various critical stress states for similar load-paths. Therefore, accommodation of these different geometries into the test chamber had to be rather simple. This resulted in a design where the ends of the pressure chamber could be changed without modification of the pressure containment sleeve.

The final design for the test chamber is shown in Figure 2.1 and is representative of the existing pressure chamber. This design meets all of the above criteria, allowing for efficient testing, and is simple and inexpensive to build. Figure 2.1 illustrates the basic features of the test chamber with the test shell, end plugs and end plates in place. The test specimen or test shell is enclosed within a thick-walled cylinder, which has two round removable end plates. The steel tubes extending from the test chamber are not part of the test specimen, but are end plugs that support the test shell and transmit axial loads to the specimen. Epoxy is used both to provide a watertight seal between the end plugs and the specimen, and also to hold the specimen firmly in place during external pressure testing. Pressurization of the test chamber is accomplished by pumping a hydraulic fluid into the test chamber, and axial tension is achieved through some external loading device in which this experimental set-up is mounted.

2.2.1 END PLUGS AND END PLATES

End plugs are designed to hold the specimen in place and to provide a means of transmitting the axial force to the specimen. An exploded view of the end plug and test specimen section is shown in Figure 2.2. Shoulders are cut into the end plugs so that the rim of the test specimen will not be exposed to the axial component of the hydrostatic pressure. Axial loads that are due to pressurization will be prevented or minimized with this procedure. Axial displacements, which may occur during loading or buckling of the test shell, will not be restrained since the end plugs are free to move axially within the end plates. Observation of the buckling phenomenon is also possible, since the end plugs extend from the test chamber and allow for viewing of the test shell's internal surface.

During the initial phase of the research, this inspection was performed with a flashlight. Observing the surface deformation visually was possible only when no axial loads were applied. However, a more sophisticated displacement sensing device was designed for more accurate observation of the shell-wall deformation. The installation of this device called for changes in the end plug configuration, such that this device could be attached to the end plug without disturbing the axial load transmission. A change in wall thickness of the steel end plugs was also necessary, since the original thinner end plugs tended to deform at the ends when the specimen buckled. A numerical study was undertaken to design for optimum end plug thickness so that test specimen buckling would not cause the end plugs to deform.

Figure 2.3 shows the model and results obtained using the BOSOR5 shell-code. As the end plug thickness is increased, the buckling pressure of the complete structure increases until buckling is no longer affected by a change in wall thickness of the end plug. When the wall thickness of the end plug is very thin, the buckling analysis is not affected by the presence of the end plug and buckling is in the approximate form of an ovalization (n=2). When the thickness of the end plug increases, the problem starts to resemble a shell with ring stiffeners at both ends. Eventually, the problem approaches the condition where the endplugs act as rigid rings, and the resulting buckling mode consists of multiple circumferential waves (n=5) as shown in Figure 2.3. When the buckling pressure becomes independent of end plug thickness, the test shell buckles without affecting the end plug. It is clear from Figure 2.3 that if the end plug is five or more times as thick as the test shell, the end plug will not be affected. The actual end plug is much thicker since the scanning probe turned out not to require much space after assembly.

The end plates that cover both sides of the test section are 1" thick steel plates with 1.5" circular cut-outs through which the end plugs fit to support the test shell. A tight seal is provided by a number of O-rings that have been positioned in several locations in the end plate. A single O-ring is used at the interface between the end plates and the test chamber, and a set of double O-rings is used at the interface between the end plugs and the end plates. These O-rings are also shown in Figure 2.1. The O-rings provide tight seals between moving sections and prevent hydraulic fluid loss under extreme loading conditions, while allowing for virtually unconstrained axial movement of the end plugs. Friction between the end plugs and the end plates is low, since the endplugs can be easily moved by hand when the pressure chamber is in operation.

The length of the test shell will have no effect on the pressure sleeve design, as long as the length of the specimen does not exceed the internal length of the test chamber. However, the end plugs and end plates will have to be changed if a different diameter specimen is to be tested.

2.2.2 HYDROSTATIC AND AXIAL LOADING IN THE TEST CHAMBER

Pressurization of the test chamber and the test specimen is accomplished by pumping a hydraulic fluid into the test chamber, whereas axial loading is provided through an external loading device. A small air vent is also provided to bleed the air from the test chamber during filling operations.

During the initial phase of the research program, a manually operated pump was used in combination with a displacement-controlled loading machine (INSTRON) to control the load-path. Figures 2.4a and b show the rather simple but effective set-up used in the initial phase of the program. A dial-type pressure gauge was used to measure the pressure of the hydraulic fluid in the test chamber and provided therefore a direct measure of the lateral pressure that the test specimen was subjected to. The accuracy of this method depended upon the ability of the observer to read accurately and quickly the maximum pressure before buckling.

Problems that occured when trying to control the axial load with a displacement controlled loading machine (INSTRON) will be discussed in detail in the experimental results section, but displacement-controlled loading of the specimen caused significant relaxation of the tensile load during pressurization. More accurate control of the load-path was achieved when function generators were used to control servovalves and hydraulic actuators, which in turn supplied pressure and tensile loading of the test shell. A pressure transducer was installed in the center of the test chamber to provide a direct feedback signal to the servocontroller. A similar feedback and servocontroller loop is installed in the MTS tensile loading machine for accurate axial load control. After these changes in load control were made, it was possible to prescribe any load path with preset function generator signals in a very precise manner.

2.3 TEST SHELL DESCRIPTION

The test specimen is a drawn 6061-T4 aluminum cylinder, cut to the required length from a standard 12' tube with 1.5" diameter and .028" wall thickness (see Figure 2.5).The tube was ordered from a local manufacturer (TUBESALES) and delivered from existing stock. The specified thickness was .028", but the actual wall thickness varied from tube to tube. It is important to recognize that this tube was not specifically manufactured for this particular use and therefore was not subjected to any special processes or treatments to minimize geometric and material imperfections.

The material properties provided on the "material certificate" by the manufacturer were most likely those of one particular tube, assumed to be an average of a large batch of similar tubes (see Table 2.1 for manufacturer material properties). It was therefore considered necessary to determine accurately the stress-strain properties of each individual tube. Since wall thickness variation influences buckling pressures, accurate measurements of the wall thickness of each specimen were made and recorded prior to testing.

2.3.1 BONDING THE TEST SHELL TO THE END PLUGS

A 1.5" long test shell segment is used in the experiment with a L/D=1. The actual shell is 3.5" in total length, to provide 1" adhesion surfaces at both ends of the shell. The shell-to-end plug bond provides a means of transmitting the axial tensile load from the end plug to the test shell and serves as a seal to prevent the hydraulic fluid from entering the scanning section (see Figure 2.2). Inadequate sealing makes accurate pressurization very difficult, a problem experienced in some tests when leaks developed in the bonding material and pressure could not be maintained by the pump.

To provide clean and grease-free bonding surfaces, the ends of the specimens are cleaned and rinsed with acetone. Prior to bonding, these surfaces are dried and cleaned with an air-jet. After application of the two-component adhesive, the (glued) interface between the specimen and end plug is cured at a temperature of 80°F for one day.During low to medium tension test runs (tensile stress less than 16,000 psi), the EPOXI-PATCH bond material performed satisfactorily. However, during high tension conditions, the bond material failed numerous times, calling for a different bonding material to be used for these high tension tests.

SCOTCH-WELD 2216 B/A epoxy adhesive with extensive pretreatment of the ends of the test section (primer and bathing in a warm sulfuric acid solution) produced the desired strength for these high loading conditions. The length of the bonding surface between the test shell and end plugs was also increased from 1" to 1.5" for these tests. Failure of the bond after these changes was less frequent during high load conditions. The aluminum test shells are now able to substantially yield before the bond material fails.

Removal of the test shell from the end plugs after the test has been completed is accomplished with the help of a soldering torch. This removal process melts the bond material and expands the aluminum shell faster than the steel end plugs, through localized heat application. The procedure allows the shell to be separated from the end plugs and at the same time removes any remaining bonding material, readying the end plugs for use on the next test shell.

2.3.2 WALL THICKNESS AND IMPERFECTIONS

After each test shell is cut from the 12' tube, a series of measurements are made using a micrometer to determine the average wall thickness of each test section. Eight measurements are taken, equally distributed around the circumference of the test shell. Two sets are taken, one for each end of the specimen. Wall thickness varies between .026" and .032" for all test shells, with most shells averaging near a .030" wall thickness for the first series of specimens and .028" for the second series. The end plugs are machined, prior to testing, to fit the various test shells.

Imperfections (n>1) were found to be a maximum of .003", which was relatively small considering that no special care was taken in the manufacturing process to minimize such imperfections. Most initial imperfection scans showed a 3 or 4-wave imperfection pattern, which could have been the result of handling, storage and possibly a worn die. When axial tension without pressure was applied to the test shell, the inital 3 or 4-wave imperfection seemed to diminish during scans at successively higher axial loads. Imperfections increased when external pressure was applied in the absence of axial loading.

2.4 BUCKLING DETECTION SYSTEM

Two difficulties were encountered in the start-up phase of the biaxial tests. First, the use of a displacement-rather than a load-controlled testing machine resulted in some problems. When the axial load was applied and held constant, the load began to relax when external pressure was applied. This problem was overcome in further tests by adapting the test device for use in the hydraulic testing machine, where the load could be controlled instead of the displacement (Section 2.5).

The second difficulty occurred when the specimen was loaded with an axial load that drove the material deep into the plastic range. During most tests buckling was easily detected by a sudden decrease in pressure and a loud "snap" when the buckling waveform appeared. However, once the specimen was loaded deep into the plastic range, the buckling process was much more gradual, and it was necessary to develop appropriate instrumentation to detect the onset of buckling.Improved buckling detection was accomplished through the use of a small circumferentially scanning probe inside the cylindrical test specimen. This scanning device was needed to measure the lateral deflection of the shell during the loading process. A rotating mechanism was designed, since it was important to detect deflection at several points along the shell wall for a complete picture of the buckling wave pattern.

The device uses a noncontacting displacement measuring probe, which is rotated on a shaft, driven by a small electric motor. The circumferential position is given by a photo-optical device, which detects the teeth of a polished gear. The device also triggers an Analog-to-Digital converter, which reads the output voltage of the scanning probe. These voltages are converted to displacement profiles during the actual experiment by the HP calculator. The probe and scanning device are shown in Figure 2.6.

2.4.1 DISPLACEMENT SENSING DEVICE (DSD)

Figure 2.7 depicts a schematic of the dime-shaped Bentley Nevada probe, which is the main component of the Displacement Sensing System. The proximitor-transducer system consists of a Bentley Nevada probe, an extension cable and a proximitor. The transducer uses the eddy currents principle to sense the distance between the probe tip and the observed surface. The 5 mm probe is suitable for use in a confined space and offers approximately 80 mils of linear measuring range.

According to the manufacturer, the proximitor (oscillator and demodulator) generates a signal in the radio frequency range, which is radiated through the probe tip into the observed material, setting up eddy currents. The loss of the return signal is detected by the proximitor, which conditions the signal for linear display or output on a monitor. The interconnecting cable is cut to a precise length to ensure matching of electrical properties in the system.

The DSD transducer, designed for use in this experiment is calibrated with 6061-T4 aluminum as the target at 72°F (22°C) ambient temperature. The 5 mm diameter probe is constructed of fiberglass, which means basically that a 5 mm electrical coil is set in fiberglass for protection. This type of protection turns out to be particularly useful when the buckling process produces such large deformations that the probe and shell wall come into contact and possible damage is prevented by the fiberglass covering.

2.4.2 DSD SCANNING SYSTEM

The noncontacting displacement probe is rotated on a shaft driven by a small electric motor. At the end of the shaft, a spring-loaded fixture holds the DSD probe firmly in place. The spring allows the probe to be moved back during insertion into the testing device. The spring also makes it possible for the probe to be pushed back when the postbuckling deformations become very large and interfere with probe operation. The main task of this spring is to prevent probe-tip damage during any type of contact. Figures 2.8 and 2.9 show a schematic of this fixture with the probe in place, combined with a complete view of the scanning system. It is possible to adjust the position where the probe scans along the shell wall by loosening the nut on top of the probe fixture and turning the fixture to the proper axial position. The scans taken in this research were performed at the mid-length of the specimen since the expected buckling displacement would be largest at this position (half-wave longitudinal buckling). The "probe spacer screw" allows for proper setting of the initial gap between the shell wall and the noncontacting probe. This procedure has to be completed before the actual test with the help of a long screwdriver, and a voltmeter, which is connected to the DSD and indicates the probe to wall spacing. The screwdriver fits in the bottom end plug and reaches into the test section where the specimen and the probe fixture are located.

The shaft leading from the fixture to the electric motor is supported with the help of precision bearings in a steel tube that screws onto the end plugs. Accuracy and precision with respect to support bearings and assembly is crucial, since small errors in the machining and assembly process will lead to large errors in the probe circumferential scanning position. The electric motor is mounted at a 90° angle to the steel support tube and its rotation is transferred with the help of a miter gear set. A polished gear on top of the drive shaft assembly is used for positioning of the probe. The scanning speed is variable and is set for good individual data resolution without significant changes in the continuously increasing applied loads.

A picture of the DSD is shown in Figure 2.10. The DSD, after assembly onto the test chamber and end plugs, can be attached to the axial tension machine. The external structure of the scanning system also serves as the means of transmitting the axial load from the testing machine to the end plugs and specimen. Thus, the DSD is an integral part of the experimental set-up.

2.4.3 CALIBRATION OF THE PROBE

Since the target surface for the Displacement Sensing Device would not be a flat surface but rather the curved wall of a cylindrical shell, the probe was recalibrated on such a surface. A test shell was cut in half, and the probe in its fixture was mounted onto a micrometer test stand above the shell. When the probe tip (5 mm in diameter) was in contact with the shell, calibration was started with the assumption that there was no gap between the probe-tip and shell (however, a flat probe tip and a curved shell won't perfectly mate). The probe was withdrawn from the surface at .010" increments and readings were taken, which led to the calibration curve as shown in Figure 2.11 . Probe voltage varies from 0 to -20 Volts. In order to make these signals compatible with the Analog to Digital converter input limits (-10 V to 10 V), a 10 V off-set signal was added to the probe output.

The predicted .080" linear range can be observed from the calibration data, but to make full use of the Analog to Digital converter input range, a third-order polynomial is fitted to the calibration data in the .080" to .140" nonlinear range. The computer, in addition to taking data, also provides warning messages to the operator when the probe gets dangerously close to the shell wall (less than .010" spacing as determined from calibration data). When this occurs, the probe should be readjusted or the experiment stopped.

2.4.4 POSITION SENSING CIRCUITRY

The circumferential position is given by a photo-optical device that detects the teeth of a polished gear. The gear is located on top of the drive shaft. The noncontacting displacement measuring probe and gear are attached to this drive shaft(Figures 2.8 and 2.9). The electrical circuitry designed for position sensing detects a voltage change from the photo-optical device and triggers the external clock of the data acquisition system. The data acquisition system then records the voltage of the Bentley Nevada proximity transducer system (a measure of the probe and wall separation). The change in voltage in the photo-optical signal is due to reflection of the emitted signal from the polished gear tooth surface onto the detector [Figure 2.12]. It is crucial to keep all gear teeth in a polished and clean condition so that no data points are missed during successive scans. The initial idea of using a photo-optical device for positioning of the probe was obtained from Singer, Arbocz and Babcock [Ref. 14], Arbocz and Babcock [Ref.15]. In their work, a metallic strip with alternating blackened sections was used to obtain axial position along a shell. Since resolution of a similar strip on a small wheel is not high enough for this experiment, an existing small gear was adopted for this purpose.

Since the gear used in the DSD has sixty-four teeth, a full circumferential scan consists of sixty-four data points covering 360 degrees. Buckling of the 1.5" test shells is expected to produce 4 or 5 waves around the circumference (under this type of loading), which averages to approximately 14 data points per wave. This is considered a high enough resolution to observe the buckling process in detail.

The circuitry determines the same starting point for each succesive scan. A small "starting" hole was drilled in the face of the gear, and a second detection system was installed above and below the gear. Each time the"starting" hole passes through this system, a signal is sent to the controlling electronics, which then opens the Beta channel on the data acquisiton system depending (Beta channel controls data acquisition). When the Beta channel is closed, the external clock feature is disabled and no data are taken. However, when the Beta channel opens, data can be taken and data acquisition starts at the same location on the shell wall for each scan. It is therefore possible to superimpose all scans on one graph during the experiment and to view the progression of the buckling process as the loads are increased.

2.5 AXIAL AND CIRCUMFERENTIAL LOAD APPLICATION

Initial tests were done with the aid of a displacement-controlled loading machine (INSTRON) and a manually operated hydraulic pump. Problems such as axial load relaxation of the specimen during pressurization and inaccurate pressure control in the test chamber led to a change in load-control systems and configuration. More sophisticated systems using servo-controllers and hydraulic actuators were incorporated into the experimental set-up to provide more accurate control of the loadpath.

Presently, the axial-loading machine (MTS) is able to maintain a prescribed load level and prevents undesired relaxation of the axial load. Figures 2.13a and b depict some of the electronic and mechanical hardware systems associated with the modified and improved loading capability. The hydraulic source for both circumferential and axial loading systems is the same in the present configuration. A schematic of the improved loading configuration is shown in Figure 2.14.

2.5.1 DESCRIPTION OF THE SERVO-HYDRAULIC AXIAL LOADING DEVICE (SLD)

A simplified hydraulic and electrical schematic of the servohydraulic loading device (SLD) is presented in Figure 2.15. The mechanical portions of the SLD are contained in four basic modules: 1) the hydraulic power supply, 2) a flow control module containing valving and filters, 3) accumulators and 4) the load frame (MTS), to which the servovalve, actuator, load cell and LVDT (Linear Variable Differential Transformer) are attached. In addition to the mechanical components, a console contains associated eletronics components and is shown in Figure 2.13a.

The hydraulic power supply (a) incorporates a 20 HP electric motor, a positive displacement pump rated at 11.6 GPM at 2670 psi and a 60 gallon reservoir. This power unit is modified to include a four pass heat exchanger (b). Cooling water flow is controlled by a thermally activated water control valve. The power supply has been further modified by the addition of a thermal switch that will cause shut-down if the hydraulic fluid level falls below switch level.

The flow control module contains all the hydraulic circuit elements necessary for both the pressure line to, and return line from, the servo-valve. A solenoid-operated, directional control valve (c) permits either direct flow at rated power supply output to the servovalve or at pressures as low as 75 psi via a pressure-reducing valve (d). The latter option provides a "smooth start-up" feature for the SLD. System high and low pressure filters are also located on this module (e).

The high pressure hydraulic fluid as well as the return flow to reservoir is conducted in 3/4-inch diameter steel tubing lines that run from the power supply and flow control module to the load frame, a distance of approximately 100 feet (f). The main accumulators (g) are located at the load frame end of the hydraulic line. A 3-quart unit in the pressure line acts both as a shock absorber to provide isolation from hydraulic shocks originating at the load-frame-mounted servovalve and as a source of intermittent reserve volume flow. A 1-quart unit in the return line also provides vibration isolation and protects the low pressure filter from transient overpressures.

The load frame, which is rated at 22,000 lbs (h)., is fitted with a double rod end hydraulic cylinder (i) (Miller Fluid Power Corp., Model 53R), which was modified to attach an LVDT probe and accommodate the LVDT case in a 6-inch deep hole provided in the lower end of the rod. The LVDT case is supported by housing that is rigidly attached to the actuator body. A servo-valve (j) which is rated for 10 GPM at 3000 psi is mounted on the loading frame. An assortment of commercially available load cells (k) may be attached to the cross-head of the loading frame.

A servocontroller and signal conditioning electronics for both the actuator rod LVDT and the load cell are located on a console along with two digital volt meters (DVM) and assorted switches (1). This panel permits either LVDT or load cell signal to be switched into the servocontroller as the feedback signal. A D.C. command signal ranging from approximately -10V to +10V is controlled by a 10-turn potentiometer. Each DVM may be switched to exhibit any one of the following: command signal, LVDT output or load cell output. The load cell output is used as the feedback signal for axial load control during the experiments, and the LVDT signal is used to monitor axial elongation of the test specimen. A 5000 lb "STRAINSERT" universal load cell is mounted on the cross-head of the MTS loading frame for these experimental purposes.

As shown in Figure 2.16, a loading bolt connects the load cell to a universal joint, which is attached to the DSD section of the test chamber. Near the bottom of this figure the attachment of the lower end plug to the MTS hydraulic actuator is also visible. An accurate axial load and feedback system is now available. The feedback system operational instruction is basically a comparison of control signals with appropriate action taken depending upon the difference between the signals. The error signal is the difference between the input (function) control signal and the loadcell (feedback) return signal. The feedback system tells the servo-controller to take action so that the error signal remains within preset limits. The error input parameter determines how closely the system loading follows the command signal.

The feedback gain is another parameter that controls the response quickness of the loading system. Low gain means that convergence to the required load setting is slow, while high gain causes the servo-controller to react instantly. Though the latter seems, ideal it causes problems when sudden vibrations occur in the system or nonstandard control signals are introduced. Sometimes the high gain and resulting immediate feedback response cause small vibrations to result in large destructive behavior of the entire system, which can be stopped only by reducing the gain setting. Other parameters for control of the feedback system are also available but not as important as those mentioned above.

2.5.2 DESCRIPTION OF SERVO-HYDRAULIC PRESSURE DEVICE (SPD)

A second system of accumulators, servo-controller and actuator, feeding from the same hydraulic supply as the SLD, can be attached at point A and B in Figure 2.15. This system is designed to provide hydrostatic pressure control within the test chamber, as shown in Figure 2.14. During initial experimentation with the servo-hydraulic pressure device (SPD), hydraulic fluid from the main supply was used as the pressurization fluid. The system in this configuration was unstable during high load conditions and often started to oscillate with very little damping. The problem was magnified when a high feedback gain was used. Subsequent destruction of the specimen was often the final result. As a result of this problem it was necessary to use a separate fluid to pressurize the test chamber.The schematic shown in Figure 2.14 depicts the double actuator system, which uses the second actuator to force a hydraulic fluid into the test chamber for pressurization.

The feedback signal for the SPD is provided by a "SCHAEVITZ" pressure transducer, which is mounted in the center of the test chamber and is located directly over the specimen. The transducer is a type P270 with a 0-2000 psi pressure range. The hydraulic supply is identical to the one discussed for the SLD except for the electronics, which are seperate and provide the pressure control inputs. Each hydraulic system has accumulators to "smooth" any unsuspected pressure perturbations.

2.5.3 FUNCTION GENERATOR CONTROL

Control of the servo-valves and therefore the load-path is now entirely possible through the input of the appropriate electronic signals to the controllers of the axial and circumferential loading systems. A function generator (EXACT Co.) with the ability to slowly vary an input signal is used for this purpose. It is now possible to increase a signal from 0 Volts to any desired magnitude over any desired time without manual interference. The function generator therefore controls loading with an electronic signal input to the servo-controllers. Determination of the correct voltage levels and timing can be accomplished with the appropriate calibration data and amplification factors of the load cell and pressure transducer feedback components. The desired tension and pressure load-path can then be preset on the function generator and no further load-path adjustments are necessary. The first experiments in each set call for slow increase of the axial load signal to a specific level while holding the pressure at zero. After the required axial load is achieved, the pressure signal is increased until buckling occurs. A second type of experiment consists of reversed loading in which the pressure is held at a constant level, while the axial tension is steadily increasing.

The data acquisition system is set to record periodic pressure and tension values during the experiment. In particular, when circumferential scans are made of the shell wall, the load data have to be recorded concurrently. After each test the load and DSD scan data are stored on a floppy disk for future reference and evaluation.

Immediate verification of correct progression of the load-path is provided on a Hewlett-Packard plotter, which is directly connected to the servo-controller feedback signals. This feature allows excellent control and manipulation of the experiment in progress. An actual plot of one such load-path is shown in Figure 2.17, and the diagram provides some measure of the accuracy of the load-control system. The apparent blot and subsequent return to a no-load condition on the load diagram is due to the Signal Interruption System (SIS), which will be explained next.

2.5.4 SIGNAL INTERRUPTION SYSTEM (SIS)

Prevention of damage to the sensitive scanning probe during buckling turned out to be a necessary consideration in the experimental design. During the experimental phase when a manually operated pump was used, it was found that maintaining the critical pressure after buckling (either continued pumping or air was trapped in the system) caused large postbuckling deformations to occur. The probe within the specimen would often contact the shell wall and only escape damage due to the spring feature, which allowed it to move back with the wall. However when loading with the servo systems, loads are maintained even after buckling, and the possibility of extensive damage to the probe is greatly increased.

A signal interruption system (SIS) is available for this purpose, which compares the feedback signal from the pressure transducer and the control signal, from the pressure servo-controller. Normal operation dictates that these signals are equal or very close to each other in magnitude. The difference between both signals is the error signal and it is this difference which is the crucial input to the Signal Interruption System (SIS). If this error suddenly exceeds a certain preset level, indicating a momentary rapid drop in pressure in the chamber associated with buckling, the SIS immediately ramps the load control signals to zero and prevents any further deformation. Deformations remain moderate and cannot affect the DSD probe. It is not possible to continue loading until the SIS has been manually reset. There is therefore no record of a postbuckling path for these experiments where the buckling is violent and damage to the probe is possible. When the axial load is very large, the postbuckling path becomes stable and the SIS does not interrupt the loading, since the shell can carry additional load after bifurcation. The bucklingwave forms without a general collapse of the shell, and subsequent load increase is possible without harming the probe. Additional displacement scans can be made during the postbifurcation phase, since the wall displacements remain relatively small.

2.6 MATERIAL PROPERTIES

Knowledge of the elastic and plastic behavior of the material is of importance for analysis and interpretation of test results. A rapid material test was therefore devised, subjecting strips of the shell wall material to uniaxial tension in a laboratory loading machine. Stress and strain data are recorded during the experiment with help of the data-acquisition system and plotted for immediate observation of the material behavior.

After the test is completed, stress and strain data are also recorded on a floppy disk for future manipulation. A similar test was designed to evaluate circumferential material behavior from internal pressure loading in comparison with axial stress-strain data. Although the hoop stress in the shell is compression, it is felt that properties from a uniaxial tension test will provide some insight into the question of isotropy.

After all tests have been completed on the same tube, all stress-strain data are plotted on one graph and an average material behavior is determined by fitting a (Ramberg-Osgood) power law to the entire set of data. This (power law) material curve is then used for the analysis phase of the research. It is known that the material behavior or stress-strain curve has a significant influence on the plastic buckling calculation and therefore needs to be determined accurately and implemented in the analysis during the preprocessor phase (BOSOR5).

2.6.1 UNIAXIAL TEST SPECIMEN

The test specimens for the uniaxial material tests are cut from the aluminum tube with little loss of material. Accuracy of stress-strain data can be increased if many such tests are performed on each tube. A method was therefore devised, which allows uniform axial strips to be cut from a single tube section. Since tube collapse and plastic deformation have to be prevented when cutting the uniaxial test strips from the tube wall, a mandrel that snugly fits into the tube was also manufactured. Generous application of lubrication oil prevents plastic deformation of the test section, which would otherwise occur when excessive force is used while positioning the tube over a nonlubricated mandrel. The mandrel and tube are then placed in a milling machine, which is used to cut equidistant slots in the shell as shown in Figure 2.18. After the milling process, the tube is removed from the mandrel and each test specimen is cut from the machined tube by severing the ends with a metal cutter. Each machined section yields an average of 10 specimens for uniaxial testing.

2.6.2 END FIXTURES AND TESTING EQUIPMENT

A displacement-controlled testing machine (INSTRON) is used for the uniaxial tests of the aluminum specimens. The aluminum strip (or specimen) is held tightly in place by two grips, which attach to the loading machine as shown in Figure 2.19. An extensometer is then placed on the specimen where the cross-sectional area is most accurately known. This extensometer is also shown in Figure 2.19. The extensometer provides strain data to the data acquisition system, which also obtains load data from the load cell in the INSTRON. Figures 2.20 a and b depict the experimental set-up required to obtain axial stress-strain curves. Included in the laboratory set-up are a loading machine, data acquisition system, storage and a plotting device.

The loading machine is set to increase the displacement at a predetermined rate until failure of the specimen occurs. This rate is slow enough to provide for adequate resolution of the stress-strain data points and simultaneous plotting of the material stress-strain curve on the Hewlett-Packard plotting system. Some of these uniaxial stress-strain curves will be shown in the next chapter.

Approximately 10 material tests and resulting stress-strain curves were obtained for each tube, with scatter sufficiently low among the individual curves so that a representative stress-strain curve could be easily identified.

2.6.3 CIRCUMFERENTIAL PROPERTIES

Since the test specimens are cut from a drawn tube, variation in axial versus circumferential properties is possible. A separate test was designed to investigate this possibility and to produce similar stress versus strain curves, for circumferential material behavior, as were obtained for the axial specimens. Comparison of axial versus circumferential stress-strain behavior will help evaluate the validity of the assumption of initial material isotropy in the analysis.

Specimens are cut directly from stock tubes and are approximately 6" long cylindrical sections. Radius and thickness of the shell walls are measured for use during the material tests. After a strain gauge has been attached in the center of the shell to measure circumferential strain, the shell is ready for testing. Load application in this test occurs through internal pressurization of the shell.

2.6.4 INTERNAL PRESSURE TESTING EQUIPMENT

A separate test had to be devised to subject cylindrical specimens to internal pressure. Shown in Figure 2.21 and Figure 2.22 is the final design of the internal pressure device.

The cylindrical test specimen is glued, using a two-component epoxy, to an aluminum fixture at one end. An external steel hose clamp helps prevent expansion of the glued end and subsequent leakage of the hydraulic fluid. The internal pressure set-up is designed to induce circumferential stresses without introducing axial loads within the specimen. Therefore, the other end of the shell is not glued to the end fixture, which includes the hydraulic fluid supply, pressure measurement and bleed valve. A tight fit is obtained with the help of rubber O-rings as shown in Figure 2.21. Again, steel hose clamps are used to prevent expansion of the tube and the escape of hydraulic fluid. Axial shell motion is now possible and virtually unconstrained since the hose clamps have not been tightened. Some oil leakage is expected and observed during the start-up of the experiment.

When the tube is pressurized, the shell is free to move axially without constraint. To prevent the end piece from being forced out of the tube, the whole set-up is constrained within the INSTRON axial displacement machine during loading. A solid steel filler section is placed within the specimen to decrease the volume of hydraulic fluid needed. This also prevents large oil spills when a leak is sprung during testing.

Stress and strain data are again obtained by the data acquisition system. Pressure is measured by the pressure transducer and converted to stress in the shell wall with radius and thickness data. Strain is measured with a small strain gauge (CEA-06-0620W-120, Measurements Group) and provided to the data acquisition system with the help of a laboratory wheatstone bridge. Before each test run, pressure and strain readings are zeroed with the help of bridge balances. Figure 2.23 depicts the laboratory set-up for this experiment, which is similar to the set-up for the axial tests. However, this time the INSTRON testing machine is used to restrain the endplugs in the axial direction.

2.6.5 RAMBERG-OSGOOD APPROXIMATION

Since a smooth material curve is desired for better convergence properties in the numerical code, an average power law approximation is determined of all available material curves. The stress-strain curve for the analysis can be fitted with the well-known Ramberg-Osgood three-parameter fit.

Determination of the proper parameters is done by trial and error. First, all available stress-strain curves of the same tube are plotted on a single graph. The Young's modulus is then easily determined from the linear portion of all graphs. The next step includes making adequate estimations of the yield stress and hardening parameter. A specially designed program will then plot on the same graph the Ramberg-Osgood curve. Varying the hardening parameter will then produce the desired curve, which will be an average of all the stress strain curves plotted.

During some of the experiments the displacement increase is arrested to determine whether significant relaxation of the material will take place. It is not immediately obvious whether the relaxation recorded is due to actual material relaxation or due to settling of the loading machine. However, during internal pressure tests of the specimens, the load can be held constant and the strain behavior observed.

Since material input parameters of the numerical code are not the same as those of the Ramberg-Osgood model, some minor manipulation of these parameters is necessary before they can be used as input for the buckling calculation. The Ramberg-Osgood model form is different from the power-law model in BOSOR5 in the hardening parameter definition only (i.e., n=N-1).

It is important to recognize that BOSOR5 uses the power-law approximation only to input the stress-strain data smoothly. The data are discretized in small linear line segments, depending upon the number of points specified in the pre-processor.

2.7 RIMS PORTABLE DATA ACQUISITION SYSTEM AND PROGRAMS

The data acquisition system used throughout the various experiments consists of a Hewlett-Packard computer, plotter and disk drive, interfaced with a "Preston" analog to digital converter for conversion of the experimental analog signals. The A/D converter is an 11-bit system giving ± 5mV accuracy for an input signal of 10 Volts or less. Several programs have been written using the acquisition system for uniaxial tests, buckling experiments and data manipulation. The complete system is incorporated in a movable unit and can be easily transported from one experiment to the other (e.g., buckling testing to uniaxial testing). The Analog-to-Digital converter has four operational input channels with preselected and programmable gains all of which are used during actual experimentation. The digitized signals are stored in the calculator using direct memory access in a 2-byte word. The memory can accommodate approximately 7000 such pieces of information. The data are converted to the standard calculator format (8-byte word) and stored on the cassette tape or floppy disk. The external clock and Beta channel of the A/D converter is an essential part of the scanning system. It allows for external control of data acquisiton at the proper time.The opening and closing of the Beta channel determines when the data acquisition system is ready to accept data.

2.7.1 UNIAXIAL TEST PROGRAM (STRESS-STRAIN)

The basic features of this program include the continuous acquisition of stress-strain data and subsequent plotting of these data. An existing program by Tipton [Ref. 16] was modified for these purposes. Calibration of the load cell and extensometer is the first objective of the program. This requires, under the control and directives of the program, that calibration weights be added to the load cell calibration fixture. The program tells the user to add the correct weight at the proper time. Then, the program asks for calibration data for the extensometer. The central idea in supplying these strain data is the same as for the load data.

Load cell or extensometer data can be entered manually, recalled from memory or obtained directly from a calibration while the program is in operation. After these calibration data have been entered into the program, a least squares fit will be performed on both sets of data. The slope of the linear calibration curve, intercepts and standard deviations are calculated and printed for interpretation of accuracy. These variables now form the basis of the uniaxial test and if these calibration data are inaccurate, the test data will be inaccurate.

At this point the program asks for the total length of the test and for the required data resolution The program will then compute the number of data points to be taken by the RIMS system.

When the actual test is started, the stress-strain behavior of the material can be directly observed on the plotting system. The program will obtain data on a continuous basis from the load-cell and extensometer for a preset time. After the test is finished, these data are transferred from local memory to a more permanent medium.

An extension of this program helps in the determination of the average stress-strain curves by generation of generic Ramberg-Osgood stress-strain curves. The user can vary hardening and yield parameters to obtain the best fit with the actual experimental data. After the user selects the most suitable stress-strain curve, the relevant parameters such as yield and hardening are printed for input into the numerical analysis.

2.7.2 BUCKLING TEST PROGRAM (TUBE)

The main features of this program (TUBE) are control of circumferential scanning and recording of load and displacement data. This program has been written to record all pertinent data obtained during tests with the DSD and load-control systems.

After the DSD has been properly positioned in the test chamber, a scan is initiated with no loads imposed on the structure. The Analog-to-Digital converter will not provide the program with scan data until the Beta channel on the converter has been activated (or opened). Data acquisition starts at the same location on the shell because of a second sensing system, which is located over the position sensing gear in the DSD. Once the Beta channel is opened, the program waits for the external clock pulse before data are taken from the displacement sensing circuitry. The external clock will trigger each time a polished gear tooth passes the detection system until the complete shell has been scanned. Resolution of the data points is picked high enough for buckling detection. Immediately after the scan the program obtains load-data from the load cell and pressure transducer and stores these data along with the DSD scan data. Tube axial displacements are read directly from the LVDT in the axial loading machine and are recorded for a number of experiments.

Besides plotted output of the scan or displacement profile, the program also prints load-path data on the system printer. This output is kept with the plotted output and provides a means of identifying where and how the data are stored. The program will then return to its starting point and wait for a new signal to proceed with another scan. After the complete test has been finished and the specimen has buckled, the data set for the whole experiment is transferred from local memory to permanent memory in the form of a floppy disk. Figure 2.24 depicts some of the experimental scans together with results obtained after manipulation of experimental data. Load-path and a buckled specimen are also shown in this figure.

Extensions of this program include several plotting options of the scan and load data. Data can be recalled from memory and replotted after the initial imperfection has been subtracted. This type of manipulation shows more clearly the formation of the buckling waveform and the number of buckling waves. Another option allows the user to plot load versus displacement of any particular location on the shell wall. Good results are obtained if the user specifies these points to be those locations on the shell wall where maxima and minima occur in the buckling waveform. Included in this section of the program is the capability of generating Southwell plots from the load versus displacement data. These Southwell plots turn out to be very helpful in the determination of critical loads, as will be explained later.

2.8 RUN CONDITIONS

A short description of a complete experimental test run will follow in the conclusion of this chapter. Test preparation starts with accurate wall thickness measurements of the specimen to be tested. The specimen is then glued to the end plugs and cured for the required time. When the bond is completely cured, the test specimen and end plugs are placed in the test chamber, after which the end plates are put into place. The Displacement Sensing Devise (DSD) is then inserted into the proper end plug and turned until it is locked into place. Care is taken that the probe, which has been fully retracted with the positioning bolt, does not contact the wall and thus subsequently sustain damage to its sensitive tip.

Figure 2.25 shows the three components: test chamber, DSD and test shell section unassembled but in proper vertical relation to each other. The test shell shown has already buckled, but large postbuckling deformations have been prevented by the Signal Interruption System (SIS). The coaxial cable, which carries the probe signal, runs down and out of a side slot on the lower endplug, as shown in Figure 2.16. A slipping coaxial joint just outside this slot allows the probe to turn continuously without winding the coaxial cable and possibly disturbing the probe position. The coaxial cable provides a means of transmitting the probe signal undisturbed to the proximitor, located near the data acquisition system. From this point, the conditioned signal is picked up by the data acquisition system (and a digital voltmeter) for experimental and recording purposes.

Probe positioning is the next concern, since the probe is still fully retracted after insertion. A long screwdriver is inserted into the lower end plug and with the help of a flashlight, the positioning bolt is turned until the probe to wall distance is within the linear range of the DSD calibration. A digital Voltmeter connected to the proximitor provides the necessary information for proper positioning. Next, a scan is completed and on the basis of this scan the probe is repositioned. This procedure is repeated until a satisfactory position has been found. This location will be such that all circumferential points are within the linear range, but skewed towards the higher part of the calibration curve. As the load increases, the deformations will tend to be more radially inward than outward and the probe reading will therefore remain within the linear region during the experiment.

Position data are picked up by the DSD and sent to the data acquisition system. Green blinking lights on the control circuitry indicate data acquisition of each individual point. An external platform supports the pressure sleeve since the end plugs are free to move within the pressure chamber and do not provide support. Hydraulic fluid enters near the bottom of the pressure chamber through an external valve. The bleed valve on top of the dial indicator helps air escape during filling operations. Figure 2.26 a and b shows the support equipment and the test set-up. The initial scan is made with no load applied to the system.

To initiate the scan, the DSD electronic circuitry is reset and one of the two green indicators on the system lights up, indicating that the system is waiting for the correct starting position. The data acquisition program must now be advanced to the point where it waits for the external clock to trigger before data can be taken and stored. When the green light goes out and the neighboring light starts to blink at a constant rate, the beta channel has been activated and data are being acquired until a full circumferential scan has been completed. Pressure and tension data are also recorded by the program and printed together with displacement data by the system printer. The option of rejecting the scan allows the user to redo the scan before plotting and storing the scan at that load level.

After the pressure chamber has been filled with hydraulic fluid and properly bled of all remaining air, the actual loading of the specimen can start when the Signal Interruption System (SIS) has been activated. Function generator control is now running the experiment and the operator only specifies when the scanning system should perform a scan. Regular intervals during low loading conditions with increased scanning near the buckling point are advised for accurate buckling load determination. This way more points are obtained near the buckling load producing better Southwell plots as shown in Chapter 3.

Buckling often occurs quite suddenly accompanied by a noticable "pop" and is immediately followed by a load decrease due to rapid decrease of control signals by the SIS. Often the probe gets stuck between large buckling waves and unwinds itself from the DSD drive shaft. This "unwinding" prevents probe damage since the scanning motor continues turning the probe-shaft after buckling The thread on the shaft is such that continued turning of the shaft causes the probe to unwind from its support and drop down into the lower endplug, a highly desired feature that saved the probe many times. Data acquisition continues but because of a constant probe signal, the last plot, after Fourier analysis, is often quite different and out of bounds when compared to previous scans during the same experiment.

Sometimes during high tension operations the shell is able to carry load after buckling and shell buckling deformations are of the order of prebuckling deformations. The Signal Interruption System does not shut off the load control signals during these loading conditions. The next scan after buckling will then produce the postbuckling shape, since the probe is still able to scan the shell wall. Besides the changed shape of the shell wall, a temporary vibration in the loading system also indicates buckling. The vibration is stopped by reducing the amplifier gain of the load feedback loop. The load-path is traced on a plotter that is connected directly to the load signals during the experiment, and this plot provides another means of determining approximate buckling load and any other operational problems of the system.

Removal of the buckled specimen is possible by reversing the assembly process. Figures 2.27 a and b depict some of the specimens after they have been removed from the end plugs through the application of localized heat. It is important to note that often the specimen shows little indication of buckling when the SIS is in operation. Large postbuckling deformation is prevented when the load is removed from the system. However, the specimens shown in Figures 2.27 a and b have been exposed to continued loading after bifurcation, to bring out the buckling wave form for visual inspection. Normally, one would not be able to see the buckling waveform with the naked eye because of the load interruption by the SIS. Finally, all pertinent data are transferred to permanent storage and the system is ready for the next test.

3.0 EXPERIMENTAL RESULTS

3.1 MATERIAL PROPERTIES

Material properties are available for two sets of experiments, each representing the material behavior of the specific tube from which the buckling specimens are cut. The manufacturer delivers 12' stock tubes with a material certificate listing the various material properties. These properties are presented in Table 3.1.

Since a more accurate description of the nonlinear and linear behavior of the material is required, tests designed to obtain stress-strain curves representing the average uniaxial behavior of the individual tubes are performed. After the properties for each tube have been obtained, a numerical analysis of the experiment is carried out using these material properties. A Ramberg-Osgood fit is also performed to facilitate the input of these material characteristics into the BOSOR5 analysis.

3.1.1 STRESS-STRAIN EXPERIMENTS

Two similar 6061-T4 tubes with different wall thickness are used for both the buckling experiments and the uniaxial stress-strain tests. Material properties are available for both tubes, and specimens cut from these tubes will be referred to as "set A" (average wall thickness = .030") and "set B" (average wall thickness = .028"). Each tube has an outer diameter of 1.5 inches and produces approximately fifteen to twenty usable specimens for the actual buckling experiments. Uniaxial specimens are obtained from eight-to ten-inch long tube sections, which are cut from the end of each 12' tube.

3.1.2 AXIAL MATERIAL BEHAVIOR "SET A"

Axial material specimens, cut from a ten-inch tube section, are the only type of uniaxial specimens tested for "set A" (Figure 3.1). Various uniaxial tests were performed for this tube, but to avoid repetition, results of only a few are shown in Figure 3.1. Some specimens were unloaded while others were held at prescribed displacement levels to ascertain the effects of load relaxation and material creep.

It is not clear from these tests whether the load relaxation observed is due to material behavior or due to settling of the loading machine. The loading system for these uniaxial tests is a displacement-controlled machine with variable speeds. The displacement-controlled nature of system makes it impossible to maintain a given load level very precisely. The average length of a uniaxial test is approximately ten minutes, and loading is accomplished at the lowest axial straining rate (.01 inch/min).

Some of the differences between the various stress-strain curves shown in Figure 3.1are most likely due to an inaccurate determination of the cross-sectional areas of these specimens. Curves that tend to be farthest away from the average stress-strain curve also tend to have the largest cross-sectional areas. Specimens with large cross-sectional areas (widths) have significant transverse curvature, and rectangular approximation underestimates the actual area by approximately 2-8%. This results in higher stress calculations by the data processing system for a given load input. Uniaxial specimens with very large widths and therefore large cross-sectional areas are loaded to only a few percent strain such that the load does not exceed the maximum capacity of the load cell.

After all the material curves have been plotted, an average stress-strain curve is determined and a Ramberg-Osgood fit of this curve is carried out. This power law approximation facilitates the input of material data into the numerical analysis. Figure 3.2 depicts the average material curve with the power law superimposed on it . A yield point of 19,000 psi is determined, assuming the standard .002 % permanent set at yield. Significant deviation of the Ramberg-Osgood fit from the average material curve occurs beyond 1.5% strain as is observed in Figure 3.2. Since the effective prebuckling strain in the buckling experiments is expected to be less than 1.5%, the Ramberg-Osgood fit will be sufficiently accurate to describe the material behavior in the analysis.

3.1.3 AXIAL AND CIRCUMFERENTIAL MATERIAL BEHAVIOR "SET B"

Specimen "set B" includes axial as well as circumferential material properties, which should be approximately the same for an initially isotropic material. Figures 3.3 and 3.4 show the results of the axial stress-strain tests and the Ramberg-Osgood fit to the average material curve, respectively. Again, some of the specimens were unloaded or held at constant displacement levels to determine creep and unloading behavior. However, most constant displacement tests were performed at load levels far exceeding the maximum expected bifurcation load and are therefore not very representative of behavior of actual experimental conditions. When displacement is arrested during the experiment, it takes approximately one to three minutes for the load level to stabilize. The yield point for these axial stress-strain curves is 18,000 psi. This yield point is determined in the same manner as in specimen set A.

For specimen "set B," circumferential stress-strain behavior is also obtained by internally pressurizing a section of the tube. Strain measurements are recorded with the help of a strain gauge, which is attached to the shell wall at midlength. Results of this experiment are shown in Figures 3.5 and 3.6. Again, Ramberg-Osgood curve fitting is applied to the average material curve. The yield point is observed to be approximately 17,000 psi. Fewer experiments were done for this material test because of the amount of material required for each experiment

The load level in this load-controlled experiment can now be held constant while creep of the material is observed. For a plastically deformed uniaxial specimen, creep stabilizes after approximately two minutes. The specimen creep behavior is not considered in the actual buckling calculation but was recorded only experimentally for complete material characterization. The creep tests were performed at large strain levels (1-3%), which were never obtained in the buckling experiments.

Various axial and circumferential stress-strain curves are plotted in Figure 3.7. Figure 3.8 shows a comparison between the axial and circumferential (Ramberg-Osgood) stress-strain curves. It is apparent from these figures that circumferential stress-strain results show a more gradual transition (or knee region) than the axial results. The yield stress is slightly lower, while the hardening behavior of these specimens seems to be somewhat higher. Differences seem small enough to warrant the use of isotropic assumptions that were made for "set A" after only axial behavior was determined. Both material curves, although only slightly different, are used in the analysis for "set B." This way the effects of material behavior on the overall results can be studied. Computational results are obtained using both material curves and are presented in Chapter 4.

3.2 PRELIMINARY RESULTS

During the development phase of the experimental set-up, a 6061-T4 aluminum tube with an average wall thickness of .028" served as a prototype testing medium. Some results were obtained using specimens cut from this tube. Stress-strain data were not available for this particular tube since no uniaxial tests were done. The method of cutting uniaxial specimens from the tube with the help of a mandrel was developed much later in the research. Figure 3.9 shows a typical stress-strain curve for 6061-T4 aluminum, which is similar to those presented in the Aerospace Structural Handbook.

3.2.1 VARIABLE LENGTH SPECIMENS

Results for these buckling tests were obtained by reading the pressure on the appropriate gauge at the instant of buckling. This method of determining buckling is neither accurate nor repeatable. Results obtained from these preliminary tests help introduce a physical understanding of the buckling experiments.

Table 3.2 shows the influence of test shell length on the buckling pressure [Ref. 17] and wavenumber. Both decrease as the test shell length is increased. Variation in buckling pressure between the first and second set of specimens (using this primitive method of bifurcation detection) is 5-10% at maximum, which is indicative of the low imperfection sensitivity of the experiment.

Shells with length (L) / diameter (D) ratios equal to 1 are used for the actual experiments since these specimens have buckling pressures, which will take the material into the plastic region prior to bifurcation. In addition, the bifurcation wavenumber is large enough (4 or 5 waves) so that the bifurcation mode does not coincide with the largest imperfection modes. The shell with this geometry now forms the focus of the investigation. It is important to realize that the main purpose of the investigation is to study the effects of plasticity, not geometry, on bifurcation.

3.2.2 AXIAL LOAD RELAXATION AND BIAXIAL RESULTS

Some preliminary biaxial tests were carried out using the displacement-controlled loading machine and pressure chamber to study buckling of specimens cut from the above mentioned tube. These specimens have L/D ratios equal to one, and bifurcation is detected by observing the pressure gauge during the buckling process. Specimens are loaded up to a predetermined axial load, after which the pressure in the pressure sleeve is increased until bifurcation occurs. Since the axial loading machine is a displacement-controlled machine, relaxation of the axial load during high loading conditions will occur when the material creeps. Figure 3.10 shows the results for these tests, and the load relaxation problem is apparent in specimens nine and ten. The biaxial tests were carried out in the second quadrant of the σ_1, σ_2 plane. A number of tests on nominally identical shells also showed that buckling pressures were repeatable to $\pm 2\%$. Load-paths with constant external pressure and variable axial load also resulted in buckling of the test-shell. In this case, the axial load is not primarily responsible for buckling, but changes shell stiffness in such a way that the constant external pressure is able to buckle the shell . These aspects will be addressed in greater detail later in this chapter.

In Figure 3.10, pressures have been converted to (circumferential) hoop stress values. The initial "Von Mises" yield surface is also shown to provide a sense of the prebuckling plastic deformation. Repeatability observed in these early experiments together with results from the more carefully controlled buckling experiments (to be discussed next) forms the basis for the argument that under this type of loading imperfections seem to have little effect on the bifurcation point of a 6061-T4 aluminum shell (imperfections sensitivity is minimal).

Problems such as inaccurate bifurcation detection and load relaxation led to the development of the Displacement Sensing Device (DSD) for buckling detection and adaption of the axial loading system (to load-controlled operation) for more precise control of the actual load-path. The actual experimental results presented in the next section have all been obtained with the modified loading system. Buckling loads are now determined with the help of load-transducer and DSD data from the experiment. This manner of determining the buckling load is very repeatable and is not very sensitive to the proximity of the last recorded load to the actual bifurcation point (as shown in the next section).

3.3 EXPERIMENTAL RESULTS "SET A"

The first set of experiments and results of "set A" represent those specimens that have an average wall thickness of .030". Measurements of the shell wall are made with a micrometer prior to the experiments and are averaged over the circumference. Eight measurements are taken, equally distributed around the circumference of each end of the shell. Thickness variations of the shell wall have been found to be within .002" on either side of the average. The first buckles form appear at those locations where the shell wall is the thinnest. This is verified in experiments in which the buckling system is shut down at the first signs of buckling. The SIS limits are set so that even the smallest drop in pressure will induce an immediate unloading response of the system.

In these experiments, the test shell has buckled according to the displacement data and the buckling waveform is present. The displacements are so small that a visual inspection does not show signs of buckling. The specimens in which a definite buckling waveform can be observed have been subjected to continued loading to bring out the bifurcation deformation. The axial wave in the buckled shell is always a half-wave, while the number of circumferential waves is dependent upon loading path, geometry and end conditions. The probe scans at the midlength of the shell, since the axial half-wave has the largest displacement at this point, and data obtained with this probe are used to generate a circumferential profile of radial displacements.

Graphical output generated by the data acquisition system consists of load path plots, imperfection scans and displacement profiles, which are obtained with the help of the DSD system. In addition to the graphical output, the system printer also prints pressure, tension and displacement profile data. Additional displacement data are given in the form of Fourier coefficients corresponding to the $n = 1$ and $n = 0$ modes. These modes are lower than the expected bifurcation modes and are substantially affected by probe-eccentricity. Probe-eccentricity may be a result of nonalignment of the shaft supports in the DSD scanning drive during assembly.

After the experiments have been completed, data reduction is available in the form of load versus displacement plots and Southwell plots. Mechanics of the Southwell plots will be explained in Section 3.3.1. The Southwell plots of load-displacement data are used to obtain the bifurcation loads of the corresponding "perfect" shells. The Southwell plot seems to work well for most experiments under low axial tension, but does not work as well in those regions where the postbifurcation behavior is less unstable because of the high axial load. In these regions, bifurcation loads are determined to be between the last prebuckled load point and the next postbuckling reading taken after the shell has buckled. In Patel and Gill [Ref. 13], the authors refer to the load at which the rotating probe first detected buckling as the "Incipient" load (i.e., $P_{incipient}$ is the load at which buckling is first detected). The load at which the first buckle could be felt by touching the surface is called P_{clear} and the load at which the buckle was fully developed is $P_{incipient}$. In the Patel and Gill paper, there is a discussion about the lack of an exact method to determine the buckling pressure. It is hoped that the use of the Southwell plot will relieve some of these problems. The last recorded load will also be reported, but the Southwell method is used to "smooth" the results in that it predicts the corresponding buckling load of the "perfect" shell. This is an empirical observation from the experiments and has not yet been analytically justified. The last recorded load in this research will be denoted by the "Incipient" buckling load ($P_{incipient}$).

During the first set of experiments the axial load is held constant, while for the reversed loading case the pressure is held constant and the tensile stress is increased. For the constant pressure loading, the Southwell method does seem to have some additional problems in predicting the buckling load of the "perfect" buckling load. The increasing axial tensile stress "softens" the material until the external pressure is able to buckle the test specimen. It appears that those experiments in which many datapoints were obtained near the buckling point did produce better results than those in which fewer points were recorded. The discrepancy observed in this case may be partly due to insufficient data, but that was never a problem in the constant tension tests, and this observation should therefore be treated with caution.

3.3.1 CONSTANT TENSION EXPERIMENTS

During this set of experiments the axial tensile stress was increased at approximately 2000 psi increments between experiments. Axial load was increased in each experiment until the desired load level had been obtained. After this constant level was attained, increasing external pressure was applied. Thus, while circumferential stress was increasing, axial stress was held constant with the MTS load controller. The test continued until buckling occurred.

An average test takes approximately 40-60 minutes, which is sufficient time for 20-30 displacement scans without significant load variation during the scan. Axial tensile stress is increased in increments between individual experiments up to a maximum axial tensile stress of 24,000 psi, which is well past the axial yield point of the 6061-T4 aluminum. Four representative experiments of this complete set will be presented here, Figures 3.11, 3.12, 3.13, and 3-14. Figures 3.11 (a-f) show the results of an experiment in which no axial load is applied. Figure 3.11a depicts the load-path. The tensile stress imposed on the test shell is plotted along the vertical axis, while the horizontal axis represents the external pressure. The hoop stress in the shell is directly related to the external pressure through the thickness and the radius of the specimen. In Figure 3.11b circumferential scans (radial displacements), which are recorded during the experiment at regular intervals, are shown. A Fourier analysis has been performed and amplitudes of modes $n = 1$ and $n=0$ have been calculated. The $n = 1$ and $n = 0$ modes are now subtracted from the scan data since these modes are not components of the buckling mode and may be results of factors other than shell imperfection. Again, possible probe eccentricity significantly effects these coefficients. Full scans can be reconstructed by adding the Fourier components back into the plotted circumferential scans. The horizontal axis in Figure 3.11b represents the tooth number or circumferential position (i.e. #32 = 180°, #64 =360°, etc.). The discrete circumferential numbering is due to the positioning gear as explained in the previous chapter.

After buckling occurs, the next circumferential profile of radial displacements is often quite different when compared to all previous scans. Since the probe contacts the wall or gets stuck between large buckling waves, it no longer rotates but unwinds from the drive shaft while recording constant displacement values. After this last erroneous scan is completed and a Fourier analysis is performed, a completely different scan is plotted, indicating that the shell has buckled and has trapped the scanning probe. Figure 3.11b shows scan number 22, which is the scan just after the shell has buckled.

The first scan is shown again in Figure 3.11c and shows the initial imperfection of the shell wall after removal of modes $n = 0$ and $n = 1$. When this scan is subtracted from the scans shown in Figure 3.11b, the actual buckling waveform can be clearly distinguished

(Figure 3.11d). In this case five full waves form the buckling pattern. The shell is not perfect and the buckling mode grows as the load approaches the bifurcation load, similar to the imperfect elastic shell behavior. The growth of the bifurcation mode is a well-known result for elastic imperfect shells [Refs. 14, 15] and is also observed for plastic buckling of shells in these experiments.

To obtain the buckling load from the load and displacement data, the Southwell method [Ref. 18] is employed for moderate axial loads. Justification for the use of this method for plastic shell buckling will be addressed later, but for now it suffices to state that the characteristic linear region is observed for most of the experiments, and the use of this method is therefore empirically justified. The Southwell process is started with load displacement plots of the maxima and minima in the buckling wave form. The gear tooth number (i.e., location of maxima and minima) is specified and the data reduction system plots load versus displacement for these particular locations. Figure 3.11e shows a few load-displacement plots of some of the maxima and minima observed in Figure 3.11d. The displacements have been normalized (subtracted from) with respect to the initial imperfection. Southwell plots shown in Figure 3.11f are now easily generated from the normalized load-displacement plots. The curves become linear as the shell moves farther into the plastic region and closer to the buckling point. This linear behavior is observed and not derived from theory for plastic shell buckling.

The Southwell method for elastic column buckling problems implies that the inverse slope of this linear region corresponds to the bifurcation load of the "perfect" column [Ref. 18]. This theory was extended to plastic columns by Wang [Ref. 19]. Both Southwell and Wang applied their theories to Von Kármán's columns [Ref. 20] and found good agreement over the respective ranges of applicability. The paper by Wang has been forgotten for many years but was recently brought back to the foreground by Singer [Ref. 21]. A similar interpretation is applied here and the critical load is the inverse slope of the Southwell plot and is shown in this figure. Obtaining the buckling load from the slope of the linear portion of the Southwell plot would be justifiable according to Sobel [Ref. 22]. Sobel states that the Southwell method is applicable to any rectangular hyperbola which displays this characteristic shape. He shows that a function of this nature can be mapped to a straight line and need not be associated with a particular physical phenomenon. This would explain why, as long as the characteristic load-displacement curve is observed, the Southwell method may also be applicable to plastic buckling of cylinders. In this case, where the axial tensile stress is zero, the buckling load obtained with help of the Southwell method is 978 psi. The maximum observed load is 932 psi. Often this maximum observed pressure is referred to as the incipient buckling pressure or $P_{incipient}$. Table 3.3 contains some of the data recorded during this experiment to provide the reader with some insight in the "wealth" of data available for each experiment.

Figures 3.12 (a-f) represent the (5th) experiment in which the axial tensile stress was held at 8,300 psi. Load control interruption (SIS) is observed during buckling and the last profile scan is again quite different from previous scans due to a stuck probe. This buckling wave form consists of five full waves, with some waves better developed than others. All waves are observed after the initial scan is removed and subtracted from these profiles. Once again Southwell plots of these data become linear as the buckling point is approached. For this case the Southwell method yields a critical pressure of 889 psi. The maximum observed pressure is 865 psi.

Figures 3.13 (a-f) represent the (11th) experiment in which the axial tensile stress is 16,300 psi. All figures are basically the same; however, prebuckling deformations seem to be larger in this case. The buckling wave form has also changed from a 5-wave to a 4-wave pattern. Remember, the geometry of the specimen is still the same, while only the load path traversed has changed. This means that a higher axial tensile stress is applied before external pressure is applied. The "perfect" shell buckling pressure using the Southwell method is 750 psi. The maximum recorded pressure is 730 psi. In this experiment displacement scans are obtained quite close to the buckling load.

Figures 3.14 (a-f) represent the (14th) last experiment of this kind on the .030" thick test shells. Problems occurred at higher loads due to endplug-testshell bonding failure. Four circumferential waves form the buckling pattern with a constant axial tensile stress of 23,300 psi. Displacements are much larger when compared to previous experiments. However, a noteworthy point is that bifurcation is stable, and the tube does not collapse as observed in previous experiments. In addition, the SIS device does not interrupt the load control signals because of negligible pressure change during buckling. This indicates that the drop in pressure is within the preset limits of the SIS and the load system is able to maintain the load on the test shell without interruption.

The manner in which bifurcation is detected in this case is through a sudden vibration of the MTS load system when the shell buckles. The vibration is due to a sudden small load perturbation, which the loading system has trouble controlling because of high feedback gain in the load control loop. This vibration can be stopped by momentarily reducing the gain of the feedback loop in the servo-controller. After the vibration is stopped and while the load is still increasing, it is possible to scan the shell and obtain a buckled pattern. Bifurcation determined with the help of the Southwell method is found to occur at 612 psi. The incipent buckling load ($P_{incipient}$) load is 589 psi. In the next experiment set ("set B"), the load is increased after stable buckling until a limit point is reached. Buckling is then determined to occur between the last prebuckling and the next postbuckling load reading.

A stable bifurcation as described above occurs under high axial loads and in this set of tests is not accurately documented since the system is shut down every time vibration starts. Sudden vibration of the loading system is now recognized as a stable bifurcation and has been more deeply investigated in experiment "set B." The initial imperfection is the first scan to which all other scans are "normalized" (subtracted from). However, in this case the last profile before external pressure is applied is the new base scan. This scan is subtracted form the DSD profiles to obtain a better picture of the buckling waveform as shown in Figure 13.14 d. This change of "normalizing" profile is required since high axial loading changes the initial imperfection scan significantly. Figure 3.14c shows the two imperfection scans; #1 is the scan before any load is applied to the shell and #4 represents the scan at maximum axial stress before external pressure is applied. As expected, #4 has a reduced imperfection that is due to the (geometric) stabilizing axial loading.

3.3.2 CONSTANT PRESSURE EXPERIMENTS

These experiments are similar to the constant tension experiments, but this time loading is reversed. Pressure is applied until the desired load is achieved; subsequently, tension is slowly increased until buckling occurs (Figure 3.15 a). Only three different test results are available for "set A," since this type of loading was not considered to be the main focus of this investigation (analysis also proved not to be successful with BOSOR5 and incremental theory). However, for comparison purposes these three tests are available and one such test is shown in Figures 3.15 (a-f).

In this case the intial imperfection scan is different from the profile that is observed after the pressure has reached its constant value. The base scan is the last scan taken before the axial tensile stress is increased and is used to normalize all other scans. Profiles in Figure 3.15 b are normalized as shown in Figure 3.15d. Figure 3.15c shows the initial imperfection (#1) before and after (#9) external pressure is applied. The scan before the tensile loading is begun will now serve as the base scan (scan #9). It is interesting to note that the external pressure has increased the imperfection. Again, Southwell is applied to the results in Figure 3-15 c; however, the load variable in this case is not pressure but axial tensile stress. Thus, when external pressure is held at 750 psi, the shell buckles when an axial tensile stress of 12,300 psi is achieved according to the Southwell method. The maximum recorded axial load is 11,630 psi. The Southwell method seems to be less effective in these cases where buckling occurred under increasing axial stress. It is clear that buckling is always due to the external pressure loading condition; however, in this case increasing axial tensile stress reduces material stiffness (i.e., reduces the elastic modulus properties to "tangent" modulus properties that are lower for a "softening" material curve) until the shell buckles under the constant external pressure. This may explain why Southwell's method is not as effective when tensile stress instead of external pressure is used as the load parameter in the plot.

3.3.3 COMBINED RESULTS "SET A"

All results for "set A" have been summarized in Figures 3.16a, b, and c. Figure 3.16b is basically identical to Figure 3.16a, except that the pressure variable has been converted to circumferential stress or hoop stress using the thin shell formulation. The initial "Von Mises" yield surface (based on a yield stress of 18,000 psi) for the 6061-T4 material is also plotted to obtain an overall reference on how deep into the plastic region buckling occurs. Most results are available for constant tension tests with a few test results using reversed loading (i.e., constant pressure). Smooth curves (hand-drawn) have been fitted to the experimental data to bring out the "sense" of the experimental results, and should not be confused with theory. Figure 3.16c is used to show the smoothing effect of the Southwell plot on the buckling pressure data. Because of the load type control in this experiment the exact load path is now known, which was not the case in Figure 3.10. In tests with constant axial loading, the bifurcation wave form changes from five to four waves at about 12,000 psi axial tensile stress. Buckling results obtained with the Southwell method appear to fit well along a smooth curve with little error. Earlier investigations showing less than 5% variation in buckling pressures are reaffirmed here. Test shells have varying initial imperfections, but according to these results the imperfections have negligible effect under the type of loading experienced in this experiment.

Constant pressure experiments have also been plotted on Figure 3.16a. Although not many experiments were done in this category, it appears that the results are close to the results obtained for the reversed loading path. More experiments of this type were performed for experiment "set B," and they will be discussed in more detail. It suffices to state that the test shells did buckle under this type of loading and that the curve representing these bifurcation points appears to be below (closer to the elastic region) the curve for constant tension experiments, but not by much. It is important to recognize that Southwell results are not plotted for the constant pressure experiments. The buckling points shown in 3.16a are the maximum recorded axial stresses during the experiment. Again, this is due to the earlier arguments that axial stress really is not the loading condition that causes the specimen to buckle and therefore may create some problems in the Southwell plot.

3.4 EXPERIMENTAL RESULTS "SET B"

In this set of experiments the geometry and load-path are basically the same as in "set A." However, the average wall thickness in this set is only .028" leading to bifurcation loads which tend to be lower then those recorded for "set A". Again, thickness variations of the shell wall are within .002" of the average wall thickness (.028") as measured with a micrometer. When studying the buckled test shells, it appears that the initial buckle forms in the thinnest section of the shell wall. Data acquisition and reduction are the same for "set A" and "set B" and will not be discussed again. In this test set, higher axial loads are obtained because of improved bonding of the test shell to the end plugs. Bonding surfaces are treated with an etching solution before they are glued and this improves the resulting bond significantly.

3.4.1 CONSTANT TENSION EXPERIMENTS

In this experimental set the axial load is increased at approximately 4000 psi increments between each experiment. Test time of each shell varies from experiment to experiment but is approximately 40-60 minutes. In these experiments the axial displacements of the shells is recorded by the MTS load-frame LVDT and the data acquisition system. Only three representative experiments will be presented since fewer experiments are performed, and results do not show significant physical changes from the results in "set A".

Figures 3.17 (a-f) represent the results from an experiment where the axial tensile stress is maintained at 4000 psi. Since at low axial tensile stress the material is barely plastically deforming, prebuckling deformations tend to be rather small. The fact that there is not as much plastic deformation in the prebuckling state is due to the thinner shell wall and the associated lower buckling loads. This also manifests itself in the Southwell plots in that the linear regions tend to be more restricted than those seen in "set A."

A "perfect" shell buckling load can still be easily identified using the Southwell method. In this case, using Southwell, the buckling load would be 756 psi under a tensile stress of 4,200 psi. The maximum recorded load during the experiment is 707 psi. Again, this load is often referred to as $P_{incipient}$ or the incipient buckling load. Another noteworthy point is that the shell buckles into four waves, whereas the .030" shells under these loading conditions buckle into five circumferential waves.

During these experiments some scans were made before applying the Fourier analysis, and these scans are shown in Figure 3.18. The scans can be easily retrieved for all other experiments by adding the $n = 0$ and $n = 1$ modes back into the stored scan data. However, in this case the profiles have been plotted directly during the experiment to show the actual data before manipulation.

Figures 3.19 (a-f) are the results of a test in which the axial load is held at 12,100 psi. Four circumferential buckling waves are visible in Figure 3-19 c, and a critical load of 651 psi is determined with the help of Figure 3.19 f which is the associated Southwell plot. Some of the additional scan data are shown in table 3.4. In this case the axial displacement data, which are obtained with the LVDT, are also included. Since a load-displacement plot for these axial displacements is not required to determine the bifurcation load but may be of interest for other purposes, a plot is included (for T.S. = 12100 psi) at the end of this chapter (Figure 3.25). External pressure is plotted versus "normalized" (subtracted from initial scan) axial displacement data. Axial displacement in this case means displacement of the entire experimental set-up (column), since the LVDT is mounted below the hydraulic actuator.

As the axial load is increased, the postbifurcation behavior becomes stable as shown schematically in Figure 3-20. The effectiveness of the Southwell plot diminishes to the point where it is almost impossible to distinguish a linear region in the plot and to determine the associated buckling pressure for the "perfect" shell. Bifurcation is determined to occur between the last recorded load prior to buckling and postbuckling load when the full buckled waveform has developed. Since the bifurcation is stable, a load reading and a displacement scan can be obtained after buckling, showing the buckled wave form. Loading can even continue until a limit point is reached and the shell collapses completely.

Most often the buckling process is accompanied by a sudden vibration in the loading system. This is due to the sudden formation of the buckling waveform and the inability of the load-control loop to dampen the simultaneously occurring load perturbations. Axial and circumferential feedback loops seem to interact and result in the described vibration during stable bifurcation. An example of the behavior as described above is shown in Figures 3.21 (a-f). Axial loading is 20,100 psi, and the shell has already plastically deformed because of this large initial axial load. It is difficult to determine whether the circumferential displacements grow in the buckling mode when external pressure is applied, since the displacements are very small during prebuckling loading. However, when buckling occurs, there is a sudden increase in displacement and a shift (or an additional wave) in the waveform. In Figure 3.21e a load versus displacement plot is shown for various maxima and minima. The maximum load recorded before buckling is approximately 335 psi. This is also the location on the load-path where the vibration in the loading system is detected. The bifurcation is stable and loading can be continued after buckling until a limit point is reached. A Southwell plot of the prebuckling loads and displacements is disappointing, with the actual buckling load being significantly overpredicted. The buckling load corresponds to that load when vibrations in the loading system occurred. The postbuckling deformations are included to help establish the location of the actual buckling point.

Plotting Southwell data leading up to the limit point appears to result in a linear region, which would predict a limit load of 575 psi in accordance with Southwell's method. The investigation does not focus on this limit point behavior, but a Southwell plot is included for reference purposes.

3.4.2 CONSTANT PRESSURE EXPERIMENTS

For these constant pressure experiments, loading has been reversed and buckling is again observed when the tensile stress is increased under constant pressure. Figures 3.22 (a-f) depict the results when the external pressure is held at 620 psi. Again, the initial imperfection must be differentiated from the base scan, which is the scan taken when the pressure first reaches 620 psi and no tensile stress has yet been applied. Using the Southwell plot, the critical load is equal to 11,237 psi, while the maximum axial stress recorded is 10,293 psi.

Since more reversed loading experiments were performed for "set B," an additional constant pressure test is presented here. This time the constant pressure is much lower (500 psi) and the associated displacements before buckling (during axial loading) are larger than those recorded during the test shown in Figure 3.22. Figures 3.23 (a-f) depict the results of this experiment. In these constant external pressure experiments the last load readings, not the Southwell derived loads, are plotted in the buckling diagrams, since the calculated axial stresses using Southwell's method deviated significantly from observed experimental stresses in some cases. This is probably due to the external pressure's being the condition that induces buckling, while the axial stress only serves to reduce the material stiffness such that bifurcation can take place. It is noted, however, that for those few experiments in which the Southwell plot seemed to perform well, more datapoints were obtained in the immediate vicinity of the buckling load.

The maximum recorded axial tensile stress is 18,200 psi for a constant external pressure of 500 psi. In spite of the seemingly incompatibility between the Southwell plot and the constant pressure results, some empirical justification for the use of this method may be found for this type of loading. Table 3.5 shows the other scan data available and also displays the axial displacement data. A load displacement plot for the axial data can be found in Figure 3.26 at the end of this chapter. In this case tensile stress is plotted versus "normalized" axial displacement as shown in Figure 3.25.

3.4.3 COMBINED RESULTS "SET B"

Results for this experimental set have been summarized in Figures 3.24 a, b, and c. Again solid curves have been "hand-fitted" through the experimental data to bring out the "sense" of the results. Figure 3.24 b represents the results after the pressure variable has been converted to a hoop stress. The "Von Mises" yield surface has been plotted in this figure to show the amount of plasticity occuring before buckling. It is clear from this figure that buckling occurs closer to the elastic region. Figure 3.24 c shows the "smoothing" effect of the Southwell manipulation on the constant tensile stress buckling data.

Bifurcation wave numbers in this case are not affected by load-path and are determined to be four full circumferential waves for all experiments. Although material behavior of this set is slightly different from that observed in "set A", comparison of experimental results is extremely helpful in establishing the effects of wall thickness and therefore plasticity on buckling. Since a thinner wall lowers the buckling pressure under constant axial tensile stress, less plastic deformation takes place in the prebuckling phase. Table

3.6 also shows the experimental results for this set of experiments.

3.4.4 AXIAL DISPLACEMENT AND LOAD DATA "SET B"

The LVDT in the MTS load controller, which is normally used for displacement controlled experiments, is an excellent means of obtaining axial shell deformation data during the experiment. In Figures 3.25a and b these data are plotted for experiments in which the axial tensile stress is maintained at 12,100 psi (a), and the external pressure is maintained at 500 psi (b). These results are available for each experiment in "Set B", but have not been used or manipulated in this research beyond the stage shown in Figures 3.25a and b (Tables 3.4 and 3.5). The results have been "normalized" (subtracted from) with respect to the first displacement reading and are plotted for reference purposes.

4.0 BOSOR5 ANALYSIS

4.1 BOSOR5 AND SHELL PARAMETERS

Analysis of the experiment is carried out with an axisymmetric shell code developed and updated by Dr. David Bushnell at the Lockheed Palo Alto Research Laboratory [Ref. 23]. The main thrust of the numerical investigation is to study the effects of plasticity (plastic models) on the calculated buckling loads. These numerically calculated buckling points are then compared with the experimental results. The next step will be to evaluate the performance of each individual plastic model.

Better understanding of the plastic buckling process is gained by comparing test and theory. In this way the significance of imperfections, post-yield strain hardening and nonproportional material loading can be evaluated. In this research the emphasis was on experiment and the study of various plastic models as compared to experimental results. A more extensive discussion of the BOSOR5 analysis can be found in References [23-29].

BOSOR5 is an extension of BOSOR4 in that it allows for plastic deformation of the material and for bifurcation within the plastic range. In order to solve a plastic bifurcation problem, BOSOR5 requires the input of material parameters such as Poisson's ratio, Young's modulus and a complete uniaxial stress-strain curve to describe the plastic behavior of the material.

BOSOR5 includes options for plastic buckling analysis using either J_2 deformation or J_2 incremental theory as implemented by Bushnell [Refs. 24,25]. Results using these theories will be presented for both sets of experiments (A and B). Specimens in "set A" and "set B" have different wall thickness parameters, which are derived by averaging the wall thickness over the entire circumference of each individual specimen ("set A "= .030", "set B" = .028").

In addition to existing plastic models, a plasticity model allowing for corners to develop on an initially smooth yield surface (Christoffersen and Hutchinson [Ref. 53]) has been introduced into the BOSOR5 shell code. Performance of this corner theory is compared to experimental and analytical results, using existing models. Corner theory results will be presented in this chapter, while discussion of the theory and other details will be covered in Chapter 7.

Various assumptions regarding the type of end conditions applied to the shell will also be discussed, the most important condition being the in-plane warping of the shell during buckling. Suppression or complete freedom of in-plane warping significantly affects the calculated buckling load. Two types of analysis are performed for "set A." First a complete restriction is imposed on the in-plane warping during the initial calculation. Then the buckling calculations are performed again and this time the in-plane warping is unrestrained during buckling. This means that the axial displacements in the buckling calculation are free, and the ends of the shell are allowed to assume any in-plane shape. Axial displacements during prebuckling calculations are again restrained, since this most likely models the actual experimental condition.

Besides the various existing buckling analyses and the newly implemented analysis, there is an additional modification in the BOSOR5 shell code. Theoretically, if no shear is present in the prebuckling phase, shear response during bifurcation should be initially elastic. Bushnell implemented a modified shearing response $\bar{G}$ (G bar) in BOSOR5, based on work done with cruciform columns which buckle in shear when subjected to axial compression by Gerard and Becker [Ref. 42]. Prebuckling loading in this analysis involves no shearing terms since these shells are axisymmetric structures under axial load and circumferential external pressure only. Buckling into a nonaxisymmetric mode does involve shearing and the type of shear response can significantly influence the calculated bifurcation point. The motivation behind $\bar{G}$ (G bar) will be discussed in detail in the next chapter; however, at this point it suffices to state that $\bar{G}$ (G bar) has been changed to G(elastic) to obtain results representing pure J_2 incremental theory.

Figures 4.1 and 4.2 represent a typical input file of local and global data, which is submitted to the BOSOR5 shell code. In addition to the usual geometric and material properties there are control parameters in the input file which specify the type of operations to be carried out (buckling, plasticity model, end conditions, etc.). Symmetry is used in this problem along the mid-length of the shell to facilitate the input of the geometry and end conditions. The glued end of the shell has constraints placed on axial displacement (u=0)and moment (M=0), while the center of the shell has constraints applied to the slope of the surface (dw/dx=0) and circumferential displacement (v=0).

There are six rigid body modes, three translational and three rotational. These modes are shown in Figure 4.3 and need to be constrained to obtain a unique solution. All of these body motions can be prevented by a meridional station at which to restrain the axial displacement u^* and the circumferential displacement v^* or v. Figure 4.3 shows why this is the case and also shows the type of end conditions that have been applied to the numerical test shell. Note that the numerical analysis makes use of the symmetry of the specimen about the mid-plane.

4.2 NUMERICAL ANALYSIS "SET A"

The first numerical analysis involves those specimens having a .030" wall thickness. Uniaxial properties for "set A" are obtained as discussed in Chapter 2. Loading for this set consists of applying a prescribed tensile stress to the specimen before the pressure is numerically increased in incremental steps. After the test shell buckles in the numerical analysis (i.e., stiffness determinant changes sign), the buckling calculations can be restarted at a lower load with smaller load increments to obtain a more accurate bifurcation point. Bifurcation points are obtained with a numerical accuracy of five pounds per square inch.

For example, if a shell was determined to buckle between 900 and 950 psi, the analysis was restarted with 5 psi increments from 900 psi. The final buckling load was determined to be halfway between the last numerically calculated loads.

4.2.1 CONSTANT TENSION "SET A"

Figure 4.4 shows the results obtained from both numerical (BOSOR5) and experimental work. The analysis allows for both plastic models to be used to calculate the bifurcation point. Either incremental theory $\overline{G}$ (G bar) or deformation theory can be specified for the plastic analysis. In-plane warping at the ends is restrained for the results presented in Figure 4.4. Numerical results using the physically less acceptable deformation theory correspond better to the experimental results than those obtained with the more physically sound incremental theory. Deformation theory seems to perform better although it overpredicts or underpredicts depending upon the level of axial tension to which the shell is subjected. Underprediction of actual experimental values is not common in buckling theory and is one of the reasons why caution should be exercised when seeking justification for deformation theory results. Especially, when a numerically perfect shell analysis yields a lower buckling load than the observed experimental buckling load of a physically imperfect specimen, there is reason to question the analysis and plasticity model. For proportional loading (external pressure only), both theories predict approximately the same result and within 5% of the observed buckling pressure. As long as load-paths do not diverge too much from this proportional path, both theories do relatively well. This does not contradict theory, since deformation and incremental theory are the same for proportional loading. However, as paths tend towards more nonproportional loading, significant differences between the two theories start to emerge.

Some empirical justification for the inclusion of the "less respected" deformation theory in a numerical analysis such as the BOSOR5 code can be found here. Deformation theory, although path-independent, captures the weakening behavior of the material with increasing axial load as observed in the experiment. Incremental theory, in contrast, still displays the stiffening character as observed for axially stiffened elastic shells (axial tension on elastic shells increases resistance to buckling because of external pressure). Deformation theory predicts buckling to occur in five circumferential waves, whereas experimentally, a change in buckling waveform (five to four waves) is observed as the axial load increases. This change of circumferential buckling wave number is predicted by the J_2 incremental theory. In the case of analysis with incremental theory, the buckling curve consists of two curved segments, each representing a fixed number of circumferential waves. Above approximately 12,000 psi tensile stress, incremental theory shows a significant stiffening trend, which is not observed experimentally. Overall the "sense" of the incremental data is incorrect as can be observed from Fig 4.4. The apparent discrepancies between incremental and deformation theory buckling loads for proportional loading are due to end effects. When the ends of the short shell are unrestrained (i.e., endplugs are neglected), both theories predict identical buckling pressures and adhere to the generally known result that deformation theory and incremental theory are the same for proportional loading.

A closer investigation of incremental theory as implemented by Bushnell produces the result that the shear response during buckling has been modified to correspond to the shearing response predicted by a deformation theory model. There is no shear present in the prebuckling analysis because of the nature of the problem, but when the shell deforms nonaxisymmetrically during buckling, shearing is introduced and needs to be accounted for in the numerical analysis. The shear modification will be addressed in Chapter 5, but to understand the actual response of pure J_2 incremental model, the shear term was changed to an elastic response as predicted by J_2 incremental theory when no shear was present in the prebuckling analysis. Results using this shear response are also shown in Figure 4.4 and are indicated by "incremental theory (G)," whereas results using the modified BOSOR5 shear response are denoted by "incremental theory (G) (G bar)," It is clear that pure incremental theory results in even larger disagreement with experimental results. Bushnell's use of a modified shearing response is justified from a standpoint that predictive capability is slightly improved, but results are still unsatisfactory. Modification of the shear response reduces the error but does not physically improve the "sense" of the results.

Resistance to buckling and the number of circumferential waves that form during buckling is also influenced by the amount of in-plane warping allowed at the ends [Ref. 34]. In Figures 4.5a and b the effects of end warping on the buckling load are presented. When in-plane warping is unrestrained instead of restrained (in-plane axial displacements at the ends of the shell are free to assume any shape necessary to compensate for the formation of the out-of-plane buckling wave-form) during the buckling analysis, buckling resistance of the test shell is considerably reduced. The actual boundary condition during buckling is most likely between these two extremes and within the shaded areas as shown in Figures 4.5 a and b. The shaded regions in Figure 4.5b become more narrow as the axial stress component increases. This indicates that sensitivity to the type of end condition reduces with increasing axial stress, which seems physically correct. Including these effects in the analysis does not explain the discrepancy between the experimental results and the numerical analysis.

Wall thickness of the model-shell in the BOSOR5 analysis has been taken to be the average thickness measured in the actual experiments. However, it seems that taking the lower bound of the shell thickness data may be more appropriate, since buckling of the shell starts at the thinnest section in the shell wall. This will reduce the predicted buckling pressure by approximately 5-8% according to some sample runs when no axial load was applied. Although a thinner wall thickness reduces the gap between the numerical data and the experimental data, the "sense" of BOSOR5 data is not expected to change with this parameter.

4.2.2 CONSTANT PRESSURE "SET A"

Analysis of the reversed loading problem is unsuccessful, using incremental theory. BOSOR5 predicts failure in tension because of the accumulation of excessively large axial strains, and bifurcation as observed in the experiments is not predicted in the analysis.

Buckling was definitely observed in the experiments and should be predicted by the bifurcation analysis. The path independent deformation theory predicts buckling at the same locations in stress space (as in the constant tension numerical analysis), except that these points are approached along another stress path.

From an engineering standpoint this seems not to be too much of a problem, since experimentally the shell under reversed loading buckled very close to the bifurcation points for the constant tension experiments. Analysis with deformation theory is the only analysis that predicts bifurcation for both loading conditions and therefore adds to the paradox that the seemingly (physically) incorrect deformation theory performs (again) better than the more physically sound incremental theory. It is important to realize that underprediction as observed for part of the loading problem remains a definite indication that deformation theory is also incorrect. Corner theory as discussed in the last section of this chapter experiences the same problem as the J_2 incremental theory for this reversed load-path. Corner theory does not predict bifurcation for this reversed load-path and eventually predicts failure that is due to excessive accumulation of axial strains.

4.3 NUMERICAL ANALYSIS "SET B"

A similar analysis as in "set A" is carried out for the second set of specimens. However, this time the calculations for unrestrained end conditions (and modified shear response in the BOSOR5 incremental analysis) are not performed under the assumption that results will be similar to those shown for "set A." It is expected that use of elastic shearing response will again produce a much stiffer behavior, while unrestrained axial displacements at the end of the shell will "soften" the buckling behavior. The only calculated results involve shells that have fully restrained axial displacements in the prebuckling and buckling analysis corresponding to a rigid boundary condition.

4.3.1 CONSTANT TENSION "SET B"

In Figures 4.6 and 4.7 results are shown using the original deformation and incremental theories G (G bar) as they are available in the BOSOR5 analysis. Figure 4.6 shows the result using the axial material curve in the BOSOR5 analysis. For this set circumferential properties were obtained in addition to the axial properties, and the analysis is repeated using an average circumferential stress-strain curve. These results will show the effect of material definition on the numerical analysis. Results are shown in Figure 4.7.

Since more waves form around the circumference of the shell, it is likely that circumferential material behavior may be of greater significance in the buckling analysis than the axial behavior. Variation between axial and circumferential material behavior seems to be small enough to warrant the use of isotropic assumptions in the case of "set A." Circumferential properties do show an earlier and more gradual transition from linear to nonlinear material behavior although the difference is small. Results are shown in Figure 4.7. It is important to realize that circumferential properties are obtained under uniaxial "hoop" tension that is due to internal pressurization of the test shell. In actuality, the hoop stress in the experiment is compressive and material properties may vary slightly using a compressive test. It is much more difficult to obtain compressive properties of the specimen, since the shell will buckle before much of the plastic behavior can be observed, but ideally one should use an external pressure test.

Results using either material curve and J_2 incremental theory display a stiffening behavior with increasing axial stress, which is not observed experimentally. For low axial loads, bifurcation prediction using either material curve is approximately the same. This may be a result of the thin (0.028") shell wall, resulting in a buckling stress, which is very near the elastic region and therefore is not very much affected by the nonlinear part of the material curve. However when axial loads become large, the effective stress state is much deeper into the plastic range, where the difference between the axial and circumferential material behavior is more pronounced. Comparing both figures and assuming that compressive behavior is identical to tensile behavior, it can be said that the proper definition of the uniaxial stress-strain curve affects the analysis, but not to such a degree that the "sense" of the results is changed.

It is interesting to note that results obtained with circumferential properties and deformation theory are located entirely outside of the experimental results when circumferential properties are used. The underprediction that was distressing in the previous analysis does not occur here. Deformation theory captures the reduction in buckling resistance with increasing axial load and is also able to predict bifurcation for the reversed load-path.

4.3.2 CONSTANT PRESSURE "SET B"

Numerical analysis using BOSOR5 is unsuccessful since failure is predicted to occur because of large strains at load values well beyond the observed buckling loads. Deformation theory does predict buckling independent of the load path as in "set A." A complete analysis using this reversed load-path was not performed, since path independence of the deformation theory is expected to produce similar results as those shown in Figures 4.6 and 4.7. Using incremental theory (G) (G bar), the numerical shells do not bifurcate but buckling is again observed in the experiments using this reversed load-path. An improved model that obtains better results for the constant tension tests will, it is hoped also increase the predictive capability for bifurcation under increasing axial tension and constant pressure. It seems logical that improvement should first be sought in the constant tension experiment with varying external pressure, since it is the external pressure that causes bifurcation and collapse of the shell. Reversed loading changes material stiffness until the shell can no longer resist buckling (due to the external pressure), and bifurcation in this case is an entirely different phenomenon. Correct modeling of this behavior seems to be even more difficult since axial tension indirectly induces buckling (external pressure is primarily responsible). It appears that the analysis using incremental properties is unable to recognize the "softening" influence of the axial load on the stiffness of the shell. The shell still fails because of accumulation of excessive axial strains, as if the presence of external pressure is not recognized.

4.4 CHRISTOFFERSEN-HUTCHINSON CORNER THEORY

In addition to the J_2 incremental and deformation theory models, a plasticity model [Ref. 53] allowing for corners to develop on an initially smooth yield surface was introduced into the BOSOR5 shell code. This Christoffersen-Hutchinson (CH) model is discussed in depth in Chapter 7, and only results from the numerical analysis will be presented in this chapter. When corners form on an initially smooth yield surface, the definition of plastic strain changes significantly. While retaining concepts such as normality and convexity, there are now multiple possibilities for the definition of hardening parameters and direction of the new plastic strain increment. These parameters are most often picked such that physical behavior is duplicated. The formation of a corner on an initially smooth yield surface may be possible [Ref. 52] but has not yet experienced acceptance as a valid physical occurrence. It is important to point out that introduction of the CH corner theory in BOSOR5 does not consitute a firm belief in such phenomena, but rather an attempt to investigate the effects of such a theory on the present buckling analysis. Numerical results that show poor agreement with test results may improve with the corner theory and possibly direct the research effort in trying to solve the plasticity problem.

4.4.1 CH/BOSOR5 RESULTS "SET A"

Figures 4.8 and 4.9 show results from the BOSOR5 analysis using this corner theory. It is evident that the corner theory predicts the wave change as observed in the experiment. However, of greater interest is the"sense " of the results using the CH corner theory, which seems to better correspond with experimental results. As can be seen from Figures 4.8 and 4.9, further steps need to be taken to improve the predictions using this theory. The parameters chosen in the implementation of the CH theory were not chosen to optimize results but to facilitate operation of the model. Computational time, even with these simplifications, increases significantly when the corner theory is used in the BOSOR5 buckling analysis. An average run using the J_2 incremental theory takes approximately 20 minutes of computational time, while a corner theory run takes approximately 1 hour of computational time(4-5 times). Figure 4.9 shows a range of possible results that are due to changes in the type of end conditions applied to the test shell.In-plane warping during buckling is either restrained or freed completely as shown in Figure 4.5a. Results are similar to those obtained with other theories and seem to indicate that the type of end condition does not affect the "nature" of the buckling analysis.

Another interesting point is the problem that occurs when the initial application of the axial load takes the material into the plastic range. For these numerical studies the corner theory does not predict buckling but axial failure that is due to excessively large strains. In the CH paper [Ref. 53] a reference is made to abrupt changes in the load-path within the plastic region . Certain strain components become very large when such abrupt changes in the loading path take place according to CH. This may explain why bifurcation is not predicted when initial axial stresses yield the material before external pressurization is applied. Application of external pressure at this point causes a shape change in the load-path at the corner, resulting in abnormally large strain components and subsequent yield failure prediction. This is a definite problem of the corner theory that was also experienced by Tvergaard [Ref. 57].

A final point can be made about the CH corner theory in "set A." When axial stresses are low, results obtained with the CH theory tend to be close to those predicted using true J_2 incremental theory (i.e., elastic shearing response). This supports the fact that for nearly proportional loading these theories predict the same bifurcation point.

4.4.2 CH/BOSOR5 RESULTS "SET B"

In Figure 4.10 the CH corner theory results are depicted for the second set ("set B"). In this figure the most conservative results are those obtained with the circumferential material properties. The circumferential stress-strain curve has a slightly higher hardening exponent, which may explain why the predicted buckling loads are larger when extensive plastic deformations have occurred in the prebuckling phase. Only when the material has just yielded and buckling occurs, as is the case when the axial load is negligible, is the buckling load using axial properties slightly higher (yield point of axial material is somewhat higher).

For nearly proportional loading both results are approximately the same bifurcation points. The shell wall in this set is much thinner (.028"), and bifurcaton occurs close to the elastic region. This may explain why, in the case when axial loads are small, there is little dependence on material behavior. When axial loads are very large, the abrupt change in the load-path causes certain strain components to be overpredicted as was observed for "set A" and the buckling analysis fails.

According to BOSOR5/CH the shell fails because of a large accumulation of axial strains, not as a result of bifurcation. This is contrary to what is observed in the experiments and only helps to undermine the possible acceptance of such a theory. The corner theory seems to have a few positive aspects that cannot be found in the J_2 incremental theory. These advantages are reduced by other factors such as increased computation time and sensitivity to abrupt changes in the load-path.

5.0 BOSOR5 OPERATION

5.1 NUMERICAL CONVERGENCE AND SHEAR RESPONSE USING BOSOR5

In this chapter some of the issues regarding numerical convergence during prebuckling calculations and shear response in the buckling analysis will be addressed. This discussion should be preceded by a closer look at the mechanics of the BOSOR5 numerical code. Such a discussion can be found in References [23-29], in which Bushnell and Lagae address the various aspects related to the development and operation of the BOSOR5 code.

In overview, BOSOR5 is based on a finite difference energy method and incorporates a strategy for solving problems with both large deflections and nonlinear material properties. Because of its axisymmetric nature, integration over the entire shell is very much simplified, significantly reducing computational time. BOSOR5 [Refs. 23,29] can handle segmented and branched shells with discrete ring stiffeners, meridional discontinuities and multilayer construction. However, the analysis in this research involved only a single shell segment, with no ring stiffeners or meridional discontinuities, constructed out of a single layer of nonlinear material.

Bushnell refers to the code as a special-purpose program, a middle ground between an asymptotic analysis and a general purpose nonlinear analysis. The analysis is similar to the general nonlinear approach in that the continuum is discretized and the nonlinear prebuckling equilibrium is solved "by brute force." Figures 5.1a and 5.1b are used to clarify the operation of the code and have been taken from Bushnell. These figures do not represent the post-buckling path in this experiment due to an external presure loading condition instead of axial compression. A more accurate description of the post-buckling path in the experiment is shown in Figure 3.20 in which the postbuckling has a more neutral character. In BOSOR5 the emphasis is on the calculation of the prebuckling fundamental path, OB or OA in Fig 5.1a, and the determination of the bifurcation point B and its associated buckling mode. Thus, because of the nature of the analysis, calculation of the post-bifurcation path BD or of the load-deflection path OEF of the imperfect structure is not possible. Circumferential imperfections cannot be modeled in BOSOR5 and nonaxisymmetric deformations in the pre-buckling analysis are not allowed. The nonlinear prebuckling behavior is easily modeled through the inclusion of moderately large deflections and nonlinear material behavior in the analysis.

Maxima on load-deflection equilibrium curves such as point A in Fig 5.1a and bifurcation points such as point B in Fig 5.1b can be calculated with relatively small amounts of computer time because discretization in the axisymmetric BOSOR5 is one-dimensional. Only the meridian needs to be discretized because displacements are axisymmetric in the prebuckling analysis and vary harmonically in the circumferential direction in the bifurcation analysis. One-dimensional discretization leads to stiffness matrices with very small average bandwidths that can be efficiently stored and calculated (i.e., inexpensively). A rigorous strategy is used to solve the nonlinear axisymmetric prebuckling problem, including at each load level nested iteration loops: an inner loop for nonlinear behavior that is due to moderately large displacements and an outer loop for elastic-plastic-creep material property updating. The strongly convergent and therefore very reliable Newton-Raphson method is used in the inner loop and a subincremental strategy is used in the outer loop. The relative efficiency and economy with which such one-dimensional numerical problems can be solved on the computer permits parameter studies that are not feasible with more general multidimensionally discretized configurations.

The plastic prebuckling analysis in BOSOR5 is always performed with the J_2 incremental theory, whereas in the bifurcation analysis the user has the option of selecting the J_2 deformation or the J_2 incremental theory. A simple graphical illustration of the difference between both theories, as can be found in any introductory plasticity course, is shown in Figure 5.2 for clarification and for simple explanation of some concepts in this chapter. Plastic strain in the case of deformation theory is nonlinearly related to stresses and is independent of the increment of stress (i.e., similar to linear theory, where only the state of stress is required). This deformation theory is unable to model elastic unloading from an elastic-plastic boundary. In the J_2 incremental theory, plastic strain is given in terms of a vector having size ($\lambda(d\underline{\sigma}, \underline{\sigma}, \underline{\varepsilon}^p)$ = hardening parameter), and direction ($dF/d\underline{\sigma}(\underline{\sigma}, \underline{\varepsilon}^p)$ is the normal of the convex yield surface at loading point) of the increment of strain. Thus, if the bar in Fig 5.2 has just yielded because of an axial stress σ_{11} and a subsequent small twist (shear stress) is applied to the bar, the plastic strain increment will occur along the x_1-direction (i.e., normal to the yield surface). Because of the dependence of the plastic strain on the size and shape of the instantaneous yield surface, this theory is highly path-dependent, and the history of material deformation has to be accurately known. This makes closed-form solutions for other than the simplest problems impossible and makes incremental analysis a prime candidate for the application of a numerical code, where history and other path parameters can be stored and updated as the load increases. However, in the numerical analysis, problems such as convergence and load-step become a major issue. Load-step size is directly related to this problem and although BOSOR5 turned out to have a feature that prevents the load-step from becoming too large, an initial study was undertaken to examine these effects.

Another important issue with respect to BOSOR5 operation is the shear response in the bifurcation analysis. Because of the axisymmetric nature of the problem, shear does not occur in the prebuckling phase. When the specimen buckles and nonaxisymmetric deformations are introduced, shearing does occur and is required in the bifurcation analysis. An additional term (shear) is therefore introduced in the material response matrix. More details can be found in Bushnell [Ref. 24], where the components of the stiffness matrix and the introduction of shear during nonaxisymmetric buckling are discussed.

True J_2 incremental theory would dictate that the initial shear response is elastic since the yield-function (F) is not a function of shear stress in the prebuckling problem, but in BOSOR5 this response is modified by Bushnell . This modification is included such that the shear term corresponds more closely to experimentally observed behavior of axially compressed cruciform columns that fail in shear [Ref. 36].

5.2 LOAD STEP INVESTIGATION

It is possible to compare numerical results obtained with the BOSOR5 numerical code to analytically derived results for certain special cases.A simplified (bilinear) form of the stress-strain curve is required for this analysis. A test shell with unconstrained ends is subjected to an external pressure and axial tension load-path. This can be easily modeled with the BOSOR5 shell-code. For the analysis, external pressure and axial load can be converted using the thin-shell formulations to axial and circumferential stresses. A plane-stress problem can be formulated and the resulting strains of this plane stress problem can be compared to those obtained in the numerical analysis. The input parameters to the plane-stress problem are σ_{11}, σ_{22} the hoop and axial stress as mentioned above and the outputs are the resulting strains. Note the exact definition of the hoop stress and axial stress. The effects of various load-step sizes on the "closeness" of analytical and numerical results can now be investigated. It is expected that large load-steps will cause the numerical solution to diverge from the analytic solution. It should then be possible to determine an optimum load-step that will best suit convergence and time efficiency considerations.

5.2.1 ANALYTIC PLANE STRESS SOLUTION

Figure 5.3 shows the bilinear uniaxial material curve, while Figure 5.4 shows a diagram of the unconstrained shell. The material is bilinear and α determines the hardening character of the material, while σ_y is the uniaxial yield stress of the material. A J_2 incremental theory will be used in the analysis since this is also used in the prebuckling analysis in BOSOR5 (buckling is not allowed). Thus, the plane-stress formulation is as follows:

$$\begin{aligned}
&\sigma_{33} = \sigma_{31} = \sigma_{32} = 0 \\
&\varepsilon^e_{11} = \frac{1}{E}(\sigma_{11} - \nu\sigma_{22}) \\
&\varepsilon^e_{11} = \frac{1}{E}(\sigma_{22} - \nu\sigma_{11}) \qquad\qquad (5.1.1) \\
&\varepsilon^e_{33} = -\frac{\nu}{E}(\sigma_{11} + \sigma_{22}) \\
&\varepsilon^e_{12} = \frac{1}{2G}\sigma_{12} = 0 \text{ (no shearing)},
\end{aligned}$$

where

ν = Poisson's ratio
E = Young's modulus
G = Shear modulus

ε^e_{ij} = Elastic Strain Component

In this case,

$$\sigma_{11} = \frac{PR}{t} \qquad\qquad \sigma_{22} = \frac{T}{2\pi Rt} \qquad\qquad (5.1.2)$$

P = external pressure

T = axial load

R = radius of shell

t = wall thickness.

Since plasticity is going to occur in this problem, a "Von Mises" yield condition is assumed;

$$\sigma_e^2 = 3J_2 = \frac{1}{2}[(\sigma_{11} - \sigma_{22})^2 + \sigma_{22}^2 + \sigma_{11}^2] \quad , \qquad (5.1.3)$$

$$\sigma_e = \sigma_y$$

where σ_e is the equivalent stress and can be written as

$$\sigma_e^2 = \sigma_{11}^2 - \sigma_{11}\sigma_{22} + \sigma_{22}^2 \ .$$

Taking differentials of Equation 5.1.3,

$$2\sigma_e d\sigma_e = (2\sigma_{11} - \sigma_{22})\, d\sigma_{11} + (2\sigma_{22} - \sigma_{11})\, d\sigma_{22}$$

$$\frac{d\sigma_e}{\sigma_e} = \frac{1}{2}\frac{(2\sigma_{11} - \sigma_{22})\, d\sigma_{11} + (2\sigma_{22} - \sigma_{11})\, d\sigma_{22}}{\sigma_{11}^2 - \sigma_{11}\sigma_{22} + \sigma_{22}^2} \ . \tag{5.1.4}$$

This form will now be useful when describing J_2 incremental plasticity. Incremental theory can be described as follows:

$$d\underline{\varepsilon}^p = \frac{1}{H} \langle n, d\sigma \rangle\, \underline{n}$$

$$\langle n, d\sigma \rangle = \begin{cases} (n, d\sigma) & \text{if } (n, d\sigma) > 0 \\ 0 & \text{if } (n, d\sigma) < 0 \end{cases} \tag{5.1.5}$$

H = plastic modulus

$\underline{n}$ = direction unit vector.

A particular application of the above incremental theory, which is based on a smooth "Von Mises" yield surface, is also known as the J_2 incremental theory of plasticity. For the J_2 incremental theory, the above equations reduce to

$$<\underline{n}, d\underline{\sigma}> = <n_{ij}\, d\sigma_{ij}>$$

$$n_{ij} = \frac{S_{ij}}{\sqrt{2J_2}}$$

$$<n, d\underline{\sigma}> = \frac{1}{\sqrt{2J_2}} \frac{<d(S_{ij}\, S_{ij})>}{2}$$

$$<n, d\underline{\sigma}> = \frac{<dJ_2>}{\sqrt{2J_2}}$$

$$d\underline{\varepsilon}^p = \frac{1}{H(J_2)} \frac{<dJ_2>}{2J_2} \underline{S} \qquad (5.1.6)$$

$\underline{S}$ = deviatoric stress tensor,

where $$S_{ij} = \sigma_{ij} - \frac{1}{3}\sigma_{kk}\delta_{ij} .$$

$H(J_2)$ can be determined from a uniaxial test and is shown to be

$$\frac{1}{H(J_2)} = \frac{3}{2}\left(\frac{1}{E_t(J_2)} - \frac{1}{E}\right) \qquad (5.1.7)$$

E_t = tangent modulus.

Then,

$$d\underline{\varepsilon}^p = \frac{3}{4}\left[\frac{1}{E_t(J_2)} - \frac{1}{E}\right] \frac{<dJ_2>}{J_2} \underline{S} \quad . \qquad (5.1.8)$$

However, using 5.1.3 and 5.1.6, the above equation can be rewritten in component form;

$$d\varepsilon^p_{ij} = \frac{3}{2}\left[\frac{1}{E_t} - \frac{1}{E}\right] \frac{d\sigma_e}{\sigma_e} S_{ij} \qquad (5.1.9)$$

The preceding discussion with regard to the plastic behavior of the material can be found in any basic plasticity text and will not be further detailed here.

Total strains are composed of elastic and plastic strains and the ε_{11} component of the total strain can be written as follows:

$$d\varepsilon_{11} = d\varepsilon^{e}_{11} + d\varepsilon^{p}_{11}$$

$$d\varepsilon_{11} = \frac{1}{E}(d\sigma_{11} - \nu d\sigma_{22}) + \frac{3}{2}\left[\frac{1}{E_t} - \frac{1}{E}\right]\frac{d\sigma_e}{\sigma_e}S_{11}\ , \qquad (5.1.10)$$

where $$S_{11} = \sigma_{11} - \frac{1}{3}\sigma_{kk} = \frac{2}{3}\sigma_{11} - \frac{1}{3}\sigma_{22}.$$

Combining Equations (5.1.4) and (5.1.10), the following equation describing the increment of plastic strain (5.1.11) can be obtained;

where $$S_{11} = \sigma_{11} - \frac{1}{3}\sigma_{kk} = \frac{2}{3}\sigma_{11} - \frac{1}{3}\sigma_{22}.$$

Combining Equations (5.1.4) and (5.1.10), the following equation describing the increment of plastic strain (5.1.11) can be obtained;

$$d\varepsilon_{11} = \frac{1}{E}(d\sigma_{11} - \nu d\sigma_{22}) + \frac{1}{2}\left[\frac{1}{E_t} - \frac{1}{E}\right](\sigma_{11} - \frac{1}{2}\sigma_{22})\left\{\frac{(2\sigma_{11} - \sigma_{22})\, d\sigma_{11} + (2\sigma_{22} - \sigma_{11})\, d\sigma_{22}}{\sigma^2_{11} - \sigma_{11}\sigma_{22} + \sigma^2_{22}}\right\}. \qquad (5.1.11)$$

The derivation can be repeated to obtain the other incremental strain component;

$$d\varepsilon_{22} = \frac{1}{E}(d\sigma_{22} - \nu d\sigma_{11}) + \frac{1}{2}\left[\frac{1}{E_t} - \frac{1}{E}\right](\sigma_{22} - \frac{1}{2}\sigma_{11})\left\{\frac{(2\sigma_{22} - \sigma_{11})\, d\sigma_{22} + (2\sigma_{11} - \sigma_{22})\, d\sigma_{11}}{\sigma^2_{22} - \sigma_{22}\sigma_{11} + \sigma^2_{11}}\right\}. \qquad (5.1.12)$$

Both equations for strain increments have now been derived and a load-path needs to be specified to obtain the total strains for the particular load-path. The load-path is shown in Fig 5.5, and this path is calculated numerically in BOSOR5 and analytically in this section. The load-path consists of an initial σ_{11} stress, which takes the material to the yield surface. This stress is negative to coincide with the hoop stress generated because of external pressure on the numerical simulation. Next, σ_{11} is held at a constant level and σ_{22} is increased incrementally to account for incremental plasticity. This is the important part of the load-path and will be derived here with the help of a "dummy" time variable (t). Conditions for a constant σ_{11} path are:

$$\begin{array}{ll} \sigma_{11} = -\sigma_o & d\sigma_{11} = 0 \\ \sigma_{22} = \dfrac{\sigma_o t}{T} & d\sigma_{22} = \dfrac{\sigma_o dt}{T} \end{array} \quad , \qquad (5.1.13)$$

T = total time to travel load-path as shown in Fig. 5.5.

Representation of the load-path with the help of a time variable facilitates the derivation but has no physical significance since this is time-independent plasticity. Combining results from Equations 5.1.12 and 5.1.13 and assuming a bilinear form of material behavior (with $E_t = E/\alpha$), the following is obtained:

$$d\varepsilon_{11} = \frac{1}{E}\left(-\nu\sigma_o\frac{dt}{T}\right) + \frac{1}{2}\left[\frac{\alpha - 1}{E}\right]\left(-\sigma_o - \frac{1}{2}\sigma_o\frac{t}{T}\right)\left\{\frac{\left(\dfrac{2\sigma_o t}{T} + \sigma_o\right)\sigma_o\dfrac{dt}{T}}{\sigma_o^2 - \sigma_o^2\dfrac{t}{T} + \sigma_o^2\dfrac{t^2}{T^2}}\right\}\frac{dt}{T} \quad . \qquad (5.1.14)$$

Reducing this equation leads to

$$d\varepsilon_{11} = \frac{-\nu\sigma_o}{E}\frac{dt}{T} + \frac{\sigma_o}{2}\left[\frac{1 - \alpha}{E}\right]\left\{\frac{1 + \dfrac{5}{2}\dfrac{t}{T} + \dfrac{t^2}{T^2}}{1 + \dfrac{t}{T} + \dfrac{t^2}{T^2}}\right\}\frac{dt}{T} \quad . \qquad (5.1.15)$$

A change of variable and some additional manipulation yields

$$\frac{dt}{T} = dS \qquad \frac{t}{T} = S \qquad 0 < S < 1$$

$$d\varepsilon_{11} = \frac{-\nu\sigma_o}{E}dS + \frac{\sigma_o}{2}\left[\frac{1 - \alpha}{E}\right]\left\{1 + \frac{\frac{3}{2}S}{1 + S + S^2}\right\}dS \quad . \qquad (5.1.16)$$

Integrating, we find

$$\varepsilon_{11} = \left\{ \frac{-\nu\sigma_o}{E} + \frac{\sigma_o}{2}\left[\frac{1-\alpha}{E}\right] \right\} S + \frac{3}{8}\sigma_o\left[\frac{1-\alpha}{E}\right]\left\{ \ln(1+S+S^2) - \frac{2}{\sqrt{3}}\arctan\frac{1+2S}{\sqrt{3}} \right\} + C\,. \quad (5.1.17)$$

C = constant to be determined.

Initial conditions are required to obtain the closed form solution. Conditions at S = 0 are those that occur when the material has just reached the elastic- plastic boundary. Thus, ε_{11} is just the elastic strain and according to Equation 5.1.1,

$$\text{when } S = 0 \quad , \qquad \varepsilon_{11} = -\frac{\sigma_o}{E}\,.$$

Substituting the initial condition in Equation 5.1.17 determines C:

$$C = \frac{\sigma_o}{E} + \sigma_o\left[\frac{1-\alpha}{E}\right]\frac{\pi}{8\sqrt{3}} \quad . \qquad (5.1.18)$$

The complete solution can now be written as

$$\varepsilon_{11} = \frac{\sigma_o}{E}\left[\left(-\nu + \frac{1-\alpha}{2} \right) S + \frac{3}{8}(1-\alpha)\left\{ \ln(1+S+S^2) - \frac{2}{\sqrt{3}}\arctan\frac{1+2S}{\sqrt{3}} \right\} - 1 + \frac{(1-\alpha)\pi}{8\sqrt{3}} \right] . \quad (5.1.19)$$

The derivation can be repeated for the ε_{22} component with the following result:

$$\varepsilon_{22} = \frac{\sigma_o}{E}\left[\alpha S - \frac{\sqrt{3}}{2}(\alpha - 1)\arctan\frac{1+2S}{\sqrt{3}} + \nu + \frac{\pi(\alpha-1)}{4\sqrt{3}} \right] \quad . \qquad (5.1.20)$$

A plot can be generated showing ε_{11} and ε_{22} as a parametric curve with S as the running variable (0<S<1). This curve is shown in Figure 5.6, and it forms the base curve to which the numerical results can be compared. The reversed load-path ($\sigma_{22} = \sigma_o$, $\sigma_{11} = -\sigma_o t/T$) yields similar results (strains have opposite sign) both numerically and analytically for prebuckling strains and will not be repeated here.

5.2.2 BOSOR5 RESULTS

Results of the numerical analysis with various load-steps are also shown in Fig 5.6. It is apparent from Figure 5.6 that convergence of numerical solutions is not very sensitive to the load-step size. This at first seemed rather unusual, but closer investigation of the BOSOR5 analysis and supporting documentation produced the answer. Included in the analysis is a "subincremental" method, which is very useful for problems involving large deflections, plasticity and possible creep. This method permits the use of large load or time increments. The internal time increment is subdivided into equal subincrements, such that each effective strain subincrement is less than .0002. Therefore, the total effective strain $d\varepsilon$ is subdivided into $d\varepsilon/.0002$ equal subincrements. The time increment in BOSOR5 has no physical meaning if the problem does not involve creep behavior. For each subincrement the direction of plastic flow is considered to be constant, given by the normal to the yield surface at a location in stress space determined by the result at a previous subincrement. The direction of plastic flow is permitted to change continuously within a single load interval. The subincremental strategy involves determination of the subincrement (dt), such that the maximum change in effective stress during each interval (dt), is less than a certain fixed percentage of the total effective stress. A load-step size of 50 lb/in for axial load/length and 50 lb/in^2 for external pressure is determined to be optimal for prebuckling and buckling calculations presented in this research as shown in Figure 5.6. These load-step increments correspond to approximately 1500 psi stress increments after conversion with radius and thickness parameters. Table 5.1 shows some of the analytically calculated strain values, while Table 5.2 shows the numerically calculated strain values given a specific "time" increment. Figure 5.7 shows the load functions with the fictitious time increment, which are specified in the BOSOR5 preprocessor.

All subsequent numerical operations with BOSOR5 and associated plastic models (incremental, deformation and corner) are now performed with load-step sizes which are relatively close to those mentioned above. In buckling calculations, once buckling is detected, a restart of the numerical code at a lower load with smaller load increments will help determine the critical load more accurately. It is also important to note that in the load-step study, buckling is suppressed to obtain prebuckling results at large strains. The shell will bifurcate, under the assumed loading and end conditions, at much lower loads than those achieved in the load-step study. This indicates that if the analysis is not specifically directed to search for a change in sign of the stiffness determinant, computation continues on the primary equilibrium path. The same analysis is performed for the load-path as described at the end of Section 5.2.1, in which the path is reversed. The difference is that in this numerical analysis, the roles of external pressure and axial tension are reversed. The final result is a strain path similar to the path described above, but the sign of the strain components has been reversed. A third path included proportional increases in hoop and axial stress, which resulted in no new information regarding the desired load-step or time increment. Strains along this path increased proportionally in both analytic and numeric analyses. Overall, it can be said that the inclusion of the subincremental method in the BOSOR5 analysis reduces significantly the problem of load-step control for convergence.

5.3 BIFURCATION BUCKLING IN THE PLASTIC RANGE

Bifurcation analysis using BOSOR5 is explained in Reference[24] while the concepts and the basic principles in the analysis can be found in "Plastic Buckling" [Ref. 6]. In overview, the BOSOR5 bifurcation analysis checks for a change in sign of the determinant of the stiffness matrix, given a preselected number of circumferential waves. The change in sign is the criterion for the existence of a nontrivial solution which represents another branch on the equilibrium diagram. Once it has been determined that bifurcation has occurred for the preselected number of circumferential waves, the analysis checks for a lower buckling load, given a range of circumferential wave numbers. This range is specified by the user in the preprocessor of BOSOR5.

When plastic flow occurs, the transition from the prebifurcation state to the buckled state is path-dependent and therefore nonconservative. However, Hill [Refs. 30,31] shows that as long as the path is reasonably direct, the variation in energy dissipation from one path to another consists of higher-order terms only. Another issue which Bushnell addresses has to do with the effects of loading rate during buckling. In 1889 Engesser [Ref. 32] presented his tangent modulus theory for columns and Considère [Ref. 33] introduced the concept of strain reversal. In 1895 Engesser then derived the "double" modulus theory in which the column unloads elastically on the concave side during buckling. In 1910 von Kármán [Ref. 20] presented the theory and included experimental results (Engesser-Kármán theory).

Shanley in 1947 [Ref. 35] explained why the tangent modulus theory agreed better with tests than the reduced modulus theory. The explanation hinged on the concept that the column is free to bend at any time, allowing for nonuniform strain distribution without strain reversal. This means that elastic unloading does not occur during buckling if the material point is nonlinearly loading in the prebuckling phase. Duberg and Wilder in 1950 [Ref. 36] show that for practical engineering materials the maximum load-carrying capability of the column is just above the tangent modulus bifurcation point. This concept is extended to two dimensional problems in the "total loading" condition, which basically states that the material properties or "tangent properties" in the prebifurcation analysis are maintained in the eigenvalue analysis. Thus, in BOSOR5 a material point that is plastically loading just before bifurcation is assumed to continue plastic loading during buckling. Sewell [Ref. 37] gives an extensive bibliography in which experiments and analysis using the tangent modulus theory are being compared. Another review of the above issues can be found in Reference [6].

5.3.1 FLOW THEORY AND DEFORMATION THEORY

Incremental or flow theory seems to better predict the plastic behavior of a structure that is plastically deforming. Simple experiments such as the one presented in Figure 5.2 provide evidence that general flow theory is physically based and deformation theory is not. A paradox arises in the buckling analysis when deformation theory seems to better predict experimental results. The discrepancy may have to do with whether or not the instantaneous yield surface has corners. Experiments by Smith and Almroth [Ref. 38] have shown that a region of very high curvature on the yield surface may develop, which smooths out with time.

Closer investigation of the BOSOR5 analysis leads to the observation that the shear response in the incremental bifurcation analysis is not the usual elastic response. In the prebuckling analysis, shear is absent because of the nature of the problem and the axisymmric analysis. Stress and strain components, which are important in the prebuckling analysis, are σ_1, σ_2, ε_1, ε_2 , but when shear is introduced in the buckling analysis, because of the formation of nonaxisymmetric bifurcation modes, additional terms such as σ_{12}, ε_{12} need to be considered. The inclusion of the extra shearing term in the material response matrix, leads to a stiffness matrix which accounts for shearing during transition from the prebuckled to the postbuckled state [Ref. 24].

According to the J_2 incremental theory the definition of the plastic strain is as follows:

$$d\varepsilon^p = \underline{\lambda}\frac{dF}{d\underline{\sigma}}$$

where F is chosen to be the smooth "Von Mises" yield surface. At the instant of bifurcation, shearing stress and strain are added to the simple prebuckling loading condition. According to Onat and Drucker, no matter what smooth symmetric loading function is assumed, the normal to the loading surface does not have a component in the shear strain direction. This means that all incremental theories of plasticity that do not have a corner at the loading point predict a purely elastic shear response ($d\underline{\varepsilon}^p = 0$) between shear stress and strain. Experimental evidence seems to suggest that a modified shear response may actually produce better results. In particular, the discrepancy in the prediction of bifurcation buckling loads is most pronounced in the case of an axially compressed cruciform column (Stowell [39];l Drucker [40]; Cicala [41]; Bijlaard [42]; Gerard and Becker [42]; and Onat and Drucker [43]).

A short cruciform column buckles in a torsional mode, when subjected to axial compression. The prebifurcation stress state is pure compression, while bifurcation introduces shear. As discussed before, if no shear is present in the prebuckling analysis, the shearing response during buckling should be initially elastic (G) when incremental theory is used, as argued again by Bushnell [Ref.6].

In contrast, if deformation theory is used in the bifurcation analysis, the instantaneous shear modulus is [Ref. 6]:

$$\bar{G} = \frac{G}{1 + 3G\left(\frac{1}{E_s} - \frac{1}{E}\right)}$$

E = Young's modulus

E_s = secant modulus

G = elastic shear modulus.

Figure 5.7 taken from Gerard and Becker [Ref. 42] shows that experiment indicates that $\bar{G}$ (G bar) instead of G should be used in the bifurcation analysis. In Figure 5.7, (a) represents the incremental result and (b) the deformation theory result, which agrees with experimental data. There has been some argument that this discrepancy may be due to small initial imperfections that introduce a small amount of shearing strain in the prebifurcation state, which reduces the shear response. A second argument contributes the effect of incorrect shear response to the plastic model used in the analysis.

In this research for shells under a particular loading, it is shown that the discrepancy is most likely due to incorrect plastic modeling, and imperfection sensitivity plays a secondary role. This statement is supported by results in Figure 4.4, which otherwise would indicate that imperfection sensitivity increases with increasing axial tensile load. Increased imperfection sensitivity is unlikely to occur with increasing axial load, since the axial load tends to "smooth out" imperfections. A corner theory might possibly alleviate some of the above problems and is included in the analysis of experimental data obtained in this research.

The discrepancy observed in the cruciform column forms the basis for Bushnell's modification of the shearing term in the bifurcation analysis [Refs. 24,25]. Bushnell modified the predicted initial elastic shear response from the J_2 incremental theory such that it coincided instead with the shear response observed in the deformation theory. This modified response $\bar{G}$ (G bar) reduces the buckling resistance of the shell significantly as can be seen in Figures 4.4 and 4.5b. These figures show the results for the various cases mentioned above. In order to ascertain the effects of the shear modification, BOSOR5 was temporarily changed to respond elastically in shear as would have been predicted by a pure J_2 incremental theory.

In addition to incremental analysis, BOSOR5 also has the option to conduct the entire bifurcation analysis with the deformation theory. This means that the prebuckling analysis is still performed with the J_2 incremental theory but that the stiffness matrix used in the bifurcation analysis is assembled using J_2 deformation properties. Besides deformation shear response, all other stress-strain properties are related using a deformation theory approach when this theory is selected for the bifurcation analysis.

This option exists in BOSOR5 because evidence seems to indicate that the J_2 deformation theory often agrees better with experimental results in the bifurcation analysis. BOSOR5 leaves it up to the user and his experience to determine the proper buckling load from the two results. Modifying the shear response has helped reduce some of the discrepancy but really is not more than a convenient "fix" until more rigorous methods can be developed.

6.0 SOUTHWELL PLOT

6.1 SOUTHWELL METHOD AND PLASTIC BUCKLING

Determining the exact bifurcation load during the experiment proved to be a difficult task. Especially during initial tests (Fig. 3.10), the buckling point was determined rather arbitrarily. In fact, the buckling load was assumed to be the very last prebuckling load reading on the dial-type pressure gauge. This pressure gauge was attached to the hydraulic supply line, which provides the pressure in the test chamber.

A pressure transducer, which is presently located in the pressure chamber directly over the test specimen, has improved the accuracy since more readings can be taken by the data-acquisition system than can be taken manually by observing a pressure gauge.

Accuracy is strongly dependent on "how close" the last load reading is to the actual bifurcation load. It seems logical to describe the last recorded reading as the "incipient" buckling load, indicating that buckling is about to occur. It is expected that scatter in these "incipient" buckling results could be further reduced if the actual buckling load could be approached even closer, using higher accuracy in the load control system. After improving the load reading capability by more precise control of the load measurement, it is likely that any scatter left in the data is due to shell and load imperfections. This scatter cannot be further reduced using more careful experimental methods, since these are inherent errors in the test-shell and loading system.

As a result of the above considerations, a method was sought which would accurately determine the buckling loadfor the "perfect" shell. This is the ultimate load that can be achieved, if the shell is physically perfect with no geometric or material imperfections that reduce the stiffness of the specimen. Since a proven method for plastic buckling of cylinders was not available and data from the experiments consist of displacement profiles and load readings, a method was sought that would determine the buckling load from the existing load-displacement profiles. The Southwell plot [Ref. 18] determines the "perfect" column buckling load for elastic imperfect column problems under axial compression.

Effectiveness of this method in the case of plastic buckling of cylinders under a particular type of loading would have to be evaluated after implementation, since at the present time no rigorous justification exists that would allow an extension of the theory to these types of problems.

6.2 THE SOUTHWELL PLOT

The Southwell plot was orginally proposed in 1932 by Southwell [Ref. 18] for determination of the theoretical buckling load of a perfect column P_E (Euler load) from experiments on real imperfect columns. Figures 6.1a, b and c show the application of the Southwell plot to an imperfect column problem [Ref. 47]. Figures 6.1a, b and c are representative of the discussion that can be found in any text that employs the Southwell plot to determine the "perfect" column buckling load from an imperfect column experiment. Basically, by plotting the buckling displacement over the applied load versus the buckling displacement, the Southwell method is able to arrive at the "perfect" column buckling load. When load-displacement data from a buckling experiment of an imperfect column are plotted according to Southwell, the Southwell plot displays a linear character near the buckling load ($P=P_E$). The inverse slope of this Southwell plot is the "perfect" Euler load. The attractive feature of the Southwell method is that it "smooths" data in parametric studies by removing the effects of imperfection (geometric, load, etc.). This method is based on small deflections and elastic material behavior, and therefore it seems unlikely at first that this theory can be extended to plastic buckling of cylinders as in this research.

Wang [Ref. 19] showed that the Southwell method can be extended to the inelastic region for columns under certain conditions. Wang applied the Southwell plot to von Kármán's 1910 [Ref. 20] short columns and to Gerard's 1947 Republic Aviation Corporation short columns detailed in Reference [11]. Test data showed that the characteristic linear behavior, as is observed in elastic Southwell plots, is also observed for plastic buckling of beams. Predicted buckling loads are close to the (Engessor-von

Kármán) double-modulus theory buckling load (P_r), which is derived analytically.

The above mentioned work by Wang in which justification for Southwell's method in the inelastic region is obtained was basically forgotten until Singer [Ref. 21] revived the work in 1988. Singer rederives the work done by Wang with additional argumentation and has compared his work with experimental results of von Kármán [Ref. 20] with good agreement. In Singer's paper, references are made to recent reviews of the Southwell method and to papers by Sobel [Ref. 22], Massey [Ref. 44] and Newman [Ref. 45], in which the Southwell method has been applied empirically to plastic buckling problems and which suprisingly do not mention the existence of Wang's work.

The 1983 Sobel paper [Ref. 22] in which the Southwell method is applied to plastic buckling of elbows is of particular interest since in the appendix, Sobel argues logically that the characteristic load-deflection curve near the buckling point will yield the Southwell buckling load through simple mathematical manipulation. This would imply that any rectangular hyperbolic curve of the proper form will yield the bifurcation load if plotted as a Southwell plot. If this is the case, this would indicate that the physical interpretation as presented by Southwell is only a special case of a standard mathematical manipulation of such a curve and that the plot could be applied to any load-displacement curve of similar form. The relevance of elastic or inelastic behavior would also no longer exist. The main stumbling block remains, that one has no assurance that the plot, as discussed by Sobel, will converge to the actual buckling load for the "perfect" physical structure.

6.2.1 SOUTHWELL FOR PLASTICALLY LOADED SHELLS

In previous sections the discussion centered on the application of the Southwell method to inelastic column problems. Theoretical justification by Wang and Singer [Refs. 19,21]was found for those problems in which the column material is strain-hardening.

Extending the theory to problems in which the structure is not a column (shells, plates) is not based on sound theoretical foundations at the present time and should therefore be approached with caution. The nonexistence of a rigorous theoretical justification does not preclude the use of the Southwell theory in these problems but requires careful evaluation and explanation of the results obtained with the Southwell plot. The elastic Southwell theory and its plastic extension for inelastic beams may serve as a basis for extending it to other problems such as plates and shells.

In this research the Southwell plot was used for plastic buckling of cylindrical shells, which seems far removed from the initial elastic buckling of elastic beams. However, limited theoretical justification for the use of the Southwell plot is in the analysis of elastic cylinders under axial compression was presented by Donnell [Ref. 46] and by Galletly and Reynolds (1956) [Ref. 76]. The application of the Southwell method in this research basically assumes an extension of the theory to plastic buckling of shells under the prescribed loading. Results indicate that its use in particular loading cases and under certain conditions may be justified from an experimental standpoint.

Observed "incipient" buckling loads from experiment and Southwell derived "perfect" buckling loads agree within 5-10%, indicating that the imperfection sensitivity of this problem is not severe. Imperfection sensitivity is always considerably less for elastic cylindrical shells under external pressure than under axial compression. The Southwell plot has a pronounced "smoothing" effect on the assembly of buckling results in this research. The "smoothing" effect derived from the Southwell plot is a highly desirable feature when comparing experimental data to analysis in a parametric study. This effect is shown in Figures 3.16c and 3.24c.

6.3 RELIABILITY AND PATH DEPENDENCE

For those experiments where the axial tensile load was held at a constant level and buckling occured under increasing external pressure, the Southwell method performed quite satisfactorily. Repeated testing produced almost identical loads, leading the author to assume that the Southwell method is a reliable method of determining the buckling point of the "perfect" shell under these loading conditions.

However, load-deflection curves for the reversed loading path are not as smooth or even of the same nature as those for the constant tension experiments. These Southwell plots often do not exhibit the load-displacement behavior as seen in Figures 6.1a, b and c. The resulting Southwell plots produce inconsistent results when compared to the maximum recorded loads. Only when many loadpoints near the buckling load are obtained has the Southwell method a tendency to result in reasonable bifurcation loads as is shown in Chapter 3. Because of the inconsistent behavior of the Southwell plot, the Southwell-derived buckling loads for these types of load-paths are included for reference only. This means that the plotted values in the figures in Chapter 3 are the last recorded load readings (incipient buckling loads) before buckling, not the "Southwell loads".

As mentioned in an earlier chapter, the problems for the constant external pressure load-paths may be due to the nature of the buckling process. The external pressure load parameter in the Southwell plot is the load that induces buckling, since it introduces compressive hoop stresses in the test shell. However, in the reversed loading case, the load that induces buckling is constant (external pressure is held at a constant value), while the axial load modifies the material behavior (softens) until the external pressure in the form of a hoop stress buckles the specimen. If this axial load or axial tensile stress is used in the Southwell plot, it seems plausible that results can be inconsistent.

Another case presenting additional problems is the high axial tensile load experiment. When the axial load becomes larger than a particular value, the postbifurcation path becomes stable and the Southwell plot overpredicts the buckling load significantly. Figure 3.26e shows that the load displacement curves are not rectangular hyperbolas. This occurs in both types of experiments and is dependent upon the magnitude of the axial load imposed on the shell structure. Buckling is then determined to occur between the last prebuckling load reading and the next postbuckling reading as shown in Figure 3.21c.

7.0 CHRISTOFFERSEN-HUTCHINSON J_2 CORNER THEORY

7.1 CORNER THEORY

The experimental and numerical results obtained in this research have been presented in Figures 4.4 , 4.5 ,4.6 and 4.7. These results help substantiate the observation, that bifurcation analysis using a classical flow theory of plasticity with a smooth yield surface is inadequate. Results from highly nonproportional loading tests show substantial overestimation of the actual buckling point by the numerical analysis. In addition, for these load-paths the results obtained with incremental and deformation theory differ the most. Results of this research contribute to the paradox mentioned in "Plastic Buckling" [Ref. 6] that the "less respectable" deformation theory predicts buckling points better than the more physically sound incremental theory.

Deformation theory under certain circumstances underestimates the observed buckling pressure, a fact that is disturbing since a numerically "perfect" shell is used to analyze an "imperfect " physical test specimen. In similar situations for elastic shells, the "perfect" analysis results in nonconservative buckling loads that are multiplied by a "knock-down" factor to obtain better agreement with experiment. In contrast, the J_2 incremental or flow theory is observed to underestimate certain critical plastic strain components during nonproportional loading, resulting in significant overprediction of the buckling load during the bifurcation analysis.

The work carried out by Bijlaard[Refs. 48, 49] and more recently by Hutchinson [Ref. 50] and Tvergaard [Ref. 51] on plastic buckling and tensile instability in biaxial sheet problems [ref.53], indicates that smooth yield surface incremental plasticity usually predicts response in elastic-plastic deformation that is too stiff when the path is nonproportional. In addition, it is suggested that the deformation theory of plasticity should be applied to a wider range of deformations than simply to proportional loading. Geometric imperfections are implicated as a possible source of poor performance of the numerical analysis. However, if this is the case, results in this research would imply that these imperfections influence the buckling calculations to such a large degree that the numerical results derived with a J_2 incremental theory are of no physical significance (assuming incremental theory to be correct). This is questionable and supports the notion that the discrepancy is largely due to incorrect material modeling.

Experimental results in this research showed very little sensitivity to various initial geometric imperfections when the test shell is subjected to the same load-path repeatedly. In addition, results shown in Figure 4.4 would imply that large axial tensile preloads increase imperfection sensitivity. However, these axial loads have a tendency to "smooth out" imperfections and therefore reduce the effects of imperfections. It is therefore doubtful that imperfections are the root of the current problem.

Better understanding of the plastic behavior is expected to improve plastic modeling and eventually to improve predictive capability of the buckling analysis. At the present time various other models exist that use multiple yield systems [Ref. 76], kinematic hardening, corners,etc.. A theory that allows corners to develop on an initially smooth yield surface is the focus of the investigation in this chapter. Experimental evidence of the existence and formation of these alleged corners [Refs. 52, 61] is inconclusive and is not the topic of investigation in this research. The manner in which corner theory influences the bifurcation analysis is of greater interest in the present analysis. Figure 7.1 shows the growth of a yield surface, which is able to form a corner at the loading point, and was taken from Reference[6].

A particular corner theory model is suggested by Christoffersen and Hutchinson (CH) [Ref. 53]. A particular version of the CH corner theory plastic model was introduced into the BOSOR5 code and compared to experimental results. Before discussing the actual implementation of this model, some general statements regarding the CH model need to be made.

In the above reference[Ref. 53], imperfection sensitivity is discounted with the help of an example numerical analysis of a sheet necking problem in which the inclusion of imperfections does not improve results. The authors then show that deformation theory predictions often agree better with experiments in bifurcation problems. This leads to the next step in which a flow theory model with deformation theory "moduli" is developed and introduced.

Justification for the use of deformation theory "response moduli" is discussed by Batdorf [Ref. 54] and Sanders [Ref. 55] in which they use flow theories that have a corner at the loading point on the yield surface. This type of flow theory can be cast in a form that for nearly proportional loading the response is identical to the response using a deformation theory. The CH corner theory is a special case of these theories based on physical principles and has been introduced in various solid mechanics fields such as fracture mechanics [Ref. 56], finite deformations [Ref. 53] and more recently in bifurcation problems for shells under axial compression [Ref. 57].

Corner theories such as the physically based slip theory of Batdorf and Budiansky [Ref. 58], and the theory of multiple yield systems are quite complicated and difficult to implement numerically. Sewell [Ref. 59] used the theory of multiple yield systems, introduced by Hill [Ref. 62], as a basis for constructing a corner on the yield surface. This theory was rather limited since it could be applied only to a particular problem and was not easily extended to a more general stress problem. A phenomenological corner theory (CH) of plasticity suitable for numerical calculations of more general stress problems was therefore developed. The particular problems and issues of the process of implementing the CH theory in the BOSOR5 analysis will be addressed in the following sections.

7.2 CH CORNER THEORY IN BOSOR5

The development of this particular corner theory is discussed in detail by Christoffersen -Hutchinson [Ref. 53], but some general aspects of this theory are needed to develop some understanding for the particular choice of parameters in the implementation of this model. A general overview of the principles and ideas presented in the CH paper is presented in the Appendix (A). A specific corner theory (J_2 corner theory) based on an initially smooth yield surface as discussed in the CH paper has been introduced in BOSOR5. This is one of the simplest versions of the theory and has the additional attraction that Poh -Sang Lam [Ref. 56] has derived stress-strain relations for this theory in a suitable form, which facilitates implementation . The closed-form equations derived by Poh-Sang Lam for fracture mechanics problems are shown at the end of the Appendix (A).

7.2.1 BOSOR5 MODIFICATION

Introduction of the selected corner theory into the axisymmetric shell code proved to be a demanding but straightforward task. First, details of the operational parameters in the plasticity subroutine had to be precisely understood. This often involved tracing the parameter development through the many other subroutines that make up the BOSOR5 shell-code. Several contacts with the designer of the program (D. Bushnell, Lockheed) were helpful in determining the nature and importance of specific numerical parameters and furthered the understanding of the code. Once all parameters in the plasticity subroutine were fully understood, the mechanics of the equations in the routine were subjected to intensive scrutiny and traced back to the equations presented in Reference [28]. The last step consisted of removing the J_2 incremental model and substituting the J_2 corner theory model. Implementation was performed in such a fashion that individual segments could be tested for proper operation. This was followed by complete testing of the model for a particular load-path.

Documentation provided sufficient information for comprehension of code mechanics, but some difficulty was experienced in resolving the nature of some of the control parameters. This is possibly a result of joining BOSOR4 (an elastic buckling code) and a subroutine that provides plasticity modeling, together with the enhanced capability of predicting bifurcation in the plastic range.

7.3 J_2 CORNER THEORY

Christoffersen and Hutchinson (CH) [Ref. 53] constructed a J_2 corner theory based on the J_2 deformation theory as a special case of their general corner theory (Appendix A). In this specialization, λ is taken to be proportional to the stress deviator while C is the instantaneous plastic compliance as calculated from J_2 deformation theory. The J_2 corner model as described in the CH paper is designed to model the growth of a yield surface vertex and the consequent softened response for those load-paths that deviate from the proportional load-path. When the load-path is nearly proportional and falls within the total "loading range" (forward cone) at the yield surface corner, the CH corner theory would be identical to the J_2 deformation theory. The function providing coupling between the "total loading range" and the elastic unloading range is chosen such that the transition is smooth and the rate potential is strictly convex as defined in the CH paper. Figure 7.2 is taken from CH [Ref. 53] and shows the corner and associated angles that are discussed in the Appendix (A).

When the J_2 corner theory was introduced in the BOSOR5 shell-code, assumptions regarding certain operational parameters, as mentioned below, were made. These parameters were chosen such that implementation of the corner model was facilitated. It is expected that more careful manipulation of these parameters will improve predictive capability; especially a larger "total loading range" will most likely result in closer agreement with present deformation theory predictions.

Important parameters besides the size of "total" loading region (θ_o) are the corner description, and loading and unloading behavior. Fully nonlinear response was chosen to represent the behavior at the vertex. The existence of this "thoroughly" nonlinear behavior ($\theta_o = 0$) with no linear range is considered to be a limiting case of all possible total loading ranges (i.e., $\theta_o > 0$). Obviously, θ_o cannot exceed an angle of ($\theta_c - \pi/2$), since otherwise normality conditions would be violated.

Another aspect is the issue of the sharpness of the corner and its definition. In Tvergaard [Ref. 57], the maximum attainable angle of the corner is limited to a prescribed value. This poses a restriction on the plastic strain increment during extended plastic loading, which may better simulate actual conditions. Restricting the corner limits the departure of the yield-surface from a smooth J_2 incremental yield-surface. However, in the CH model in BOSOR5, the corner angle is not restricted, and the corner can become quite sharp during extended plastic loading. This again made the implementation of the corner theory much simpler and is not considered to be a major problem.

In BOSOR5, when unloading occurs, the corner is not preserved but instead a smooth yield-surface is formed again based on the maximum effective stress encountered. This type of behavior is physically not very likely but is easy to implement, since only one parameter needs to be stored when unloading occurs (uniaxial yield stress). This does correspond in some way to observations by Smith and Almroth [Ref.38]: that a region of very high curvature may develop on the yield surface, which "smooths out" with time. It is not expected that large regions of unloading will occur during prebuckling in the analysis of the cylindrical test shell, under the prescribed loading conditions. The exact description of the unloading behavior is therefore not expected to be very critical in the analysis. Some unloading that is due to bending may occur near the ends of the shell, when external pressure is applied on an already axially (tension) preloaded shell.

When the material first yields, using a "Von Mises" criterion, there is obviously no corner on the yield surface. For this first increment of plastic strain, the constitutive relation derived from the J_2 deformation theory is used to start the plastic strain calculation. Then, as soon as the corner has formed, the constitutive relations given in Lam [Ref. 56] are activated and continue plastic modeling. Finally, the definition of the corner conforms to the description in the example in the CH paper and may be restrictive because of its simplicity.

In spite of all the above simplifications and assumptions, it is expected that results will provide a physical "feeling" of the performance and possibilities of this corner theory. Improved predictive capability should result from more careful specifications and evaluations of the above mentioned parameters. The manipulation and parametric study of these parameters are not the subject of the investigation. In addition, significant increases in computational time using the presently implemented version of the corner theory model make extensive parameter studies of the individual variables inefficient. As previously mentioned, computation time increases fourfold or more, depending on the amount of plastic deformation in the shell.

7.3.1 IMPLEMENTATION OF THE J_2 CORNER THEORY

In BOSOR5 the subroutine responsible for constitutive modeling and updating of material properties is called PRE33. Figure 7.3 shows an overview of the main-processor routines of BOSOR5 in which PRE33 can be found. PRE33 updates material properties, given the new total strains derived in PRE22 after solving the nonlinear prebuckling problem. However, the routine most interesting to this research is called "FLOW" and can be found in PRE33. This subroutine uses either the J_2 deformation or the J_2 incremental theory to calculate plastic strain components for a given point along the meridian and within the thickness of the shell wall.

The J_2 corner theory model is introduced into "FLOW" and the code immediately following the calculations of the incremental time interval. The time interval as discussed before is chosen such that the effective strain increment is less than .0002. After obtaining the time step (dt), the total strain increase (ε_{11}, ε_{22}) is subdivided into incremental strain steps (c_1, c_2). These incremental strains (c_1, c_2) now constitute the input parameters for the corner theory model for which the corresponding changes in stress are calculated. A schematic of the J_2 corner theory model, which is implemented in the BOSOR5 shell-code, is shown in Figures 7.4a and b. Figures 7.4a and b outline the major steps of the corner model, which were programmed into BOSOR5. The model consists of approximately 250 lines of code including the subroutine "TROOT," which solves the equation for the angle β as given in Lam [Ref. 56].

The main inputs are the incremental strains (c_1, c_2) as is demonstrated at the top of the schematic. The next step in the program is the calculation of the various required moduli such as the tangent and the secant modulus at the current effective stress level. The effective stress and the uniaxial material curve are used for this purpose as in the case of the J_2 incremental theory. Following these calculations, the program checks to see whether the material is yielding, unloading or is still loading within the elastic region. In the last case, the corner theory calculations are bypassed and elastic behavior is assumed.

However, if the material has yielded, the program initiates the corner theory calculations. It is important to recognize that if the material yields for the first time, the initial "Von Mises" yield surface is smooth and the corner theory cannot be applied. If this is the case, the pure J_2 deformation theory is used for the very first increment when no corner exists on the smooth yield surface, but control is reverted to the newly implemented model as soon as a corner forms.

Next, the parameters describing the corner itself are calculated and the equation to determine β, which is taken from CH, is solved prior to implementing the constitutive relations. Solving the above mentioned equation is accomplished by subroutine "TROOT," which is activated each time a new set of strain increments is available. This subroutine is basically a modified and existing equation solver.

An important issue at this point is the strain increment normal to the shell surface ($d\varepsilon_{33}$). In the elastic calculations for shell theory, this component is disregarded because of plane-strain assumptions, but in the corner theory as presented by Lam [Ref. 56], this component is required. As is well known in elastic shell theory, plane-strain assumptions are combined with the assumption that the transverse stress is much smaller than the in-plane stresses in the shell. The plane-stress assumption is carried over in the plastic behavior of shells in this research. In the Lam [Ref. 56] formulation, the transverse strain component is required and the additional equation is obtained with the bulk modulus, which relates the strain invariant $d\varepsilon_{kk}$ to the stress invariant $d\sigma_{kk}$.

The final step of the corner theory model consists of the calculation of new stress increments, using the constitutive relations as presented in Lam [Ref. 56]. These relations define the incremental stresses ($d\sigma_{11}$, $d\sigma_{22}$), and they are in turn used to determine the elastic and the plastic components of the original strain increments c_1 and c_2 (BOSOR5).

7.3.2 OBSERVATIONS OF THE J_2 CORNER THEORY

Prior to the actually performing a bifurcation analysis using the J_2 corner theory, it was desirable to verify the operations of BOSOR5 and the J_2 corner theory model. Each individual element had been carefully checked for proper operation during implementation of the model, but whether the complete model would function properly was difficult to verify since there are no known solutions for this model and problem. Proper operation of the J_2 corner theory, in that it predicts identical results as J_2 incremental theory, was verified for the proportional load-path in which axial tensile stress and circumferential hoop stress are increased proportionally and are of equal magnitude ($\sigma_{11} = -\sigma_{22}$).

When the tensile axial preload is applied before external pressure, bifurcation prediction is not possible using J_2 corner theory, since the analysis fails because of large axial strains. This is most likely due to a phenomenon peculiar to the corner theory, which was observed by Christoffersen and Hutchinson [Ref. 53]. In the CH paper it is mentioned that if an abrupt change in load-path takes place, certain crucial strain components are overpredicted using the corner theory. This is exactly what happens when large axial tensile loads are present in the test-shell problem. The initial application of the axial load is sufficient to yield the material and form a corner. When external pressure is subsequently applied, a sharp change in load-path takes place at the corner. The sharp change in load-path and the resulting large axial strains cause BOSOR5 to predict failure that is due to extensive axial yield. This failure occurs each time the initial tensile load yields the material before external pressure is applied. This may be a significant shortcoming of the theory, if behavior at the corner cannot be smoothed to prevent such large axial strain predictions and buckling cannot be predicted.

As mentioned before, both J_2 incremental and corner theories are unable to predict buckling for the reversed load-paths. Both analyses fail because of a significant accumulation of axial strains and resulting yield-failure prediction. Deformation theory does not have this problem and predicts bifurcation at the same location as on the original load-path when the axial tension was held at a constant value.

8.0 DISCUSSION AND CONCLUSIONS

This final chapter will discuss significant experimental and numerical analysis observations. Possible improvements will also be discussed. The subsections deal with conclusions for specific parts of the research and are categorized as follows:

1/ experimental set up

2/ experimental results

3/ analysis results.

The last section summarizes the overall conclusions of the experimental results and currently available analysis.

8.1 EXPERIMENTAL SET-UP

The experimental set-up as built and operated in these experiments performed as expected. Some minor problems that did not influence results still exist and can be solved during future experimentation to increase experimental efficiency.

The actual end condition existing at the end of the shell (during buckling) is not known precisely and is expected to be "bond"-dependent. During the analysis phase, the calculated buckling loads proved to be sensitive to the type of end condition, and as a result of this observation the experimental buckling load is also expected to be sensitive to this end condition. The bonding of the test shell to the end plug is an important factor in determining the amount of in-plane warping possible during buckling. Increasing the bond surface area and pretreating the surfaces allows for larger loads to be applied to the test shell but seems not to affect the end condition itself, since experimental results did not change as a result of this modification.

The DSD scanning system is an accurate and inexpensive system with sufficient resolution to determine buckling patterns of four or five circumferential waves (12-16 points/wave). A more continuous scan can be obtained by increasing the number of data points around the circumference and increasing the number of stored data points in the data acquisition system. An issue that may also be addressed in future experimentation is the question of better probe protection. An ideal set-up would stop the scanning process the instant buckling is detected and therefore would help preserve the sensitive probe. Currently, the probe continues rotating and often unwinds from the support shaft when a large "buckling lobe" is encountered.

Probe positioning is a rather cumbersome process and could possibly be facilitated by an internal screw mechanism. This would prevent the difficult maneuvering with a long screwdriver and flashlight, to turn the probe spacer screw at the bottom of the probe drive shaft to position the probe.

Probe sensitivity may be better understood by studying the effects of shell (material) imperfection and curvature of the scanned surface. Preliminary investigation of the effects of shell curvature resulted in calibration of the probe on an actual curved-shell segment. Some of the irregular spikes occasionally observed in the displacement plots may be due to wall thickness variation or material imperfection, not to a result of wall deformation. Subtracting the initial imperfection from the scan profiles eliminates the effects of these spikes. Using the probe with the smallest probe-tip (5mm) reduces the error that is due to wall curvature and conserves space in an already confined environment.

Biaxial load control with the help of feedback-controlled loading systems improves accuracy significantly. The actual operation of the experiment is much simpler by specifying a control signal on the function generator, than by manually adjusting load parameters. A secondary fluid for pressurizing the test chamber circumvents all previous internal feedback problems between the two loading systems. Plotting the load-path in real time provides accurate control and understanding of the loading process, while having an SIS system to prevent probe damage is crucial in a load-controlled environment with unstable postbuckling.

Uniaxial material properties are obtained in a fast and simple manner, and no real changes seem necessary, except that during internal pressure tests, more strain gages should be applied to the outside of the shell. This will average the strain around the surface and reduce the effects of load and local imperfections.

The importance of having real-time displacement and load-path plots cannot be emphasized enough. Having these inputs provides the investigator with accurate information of the experimental progress. Increased scan density can be determined using these data and drift in load signals can be minimized by manipulating "gains" of the feedback system, depending on the real-time displays. The experiment turns out to be quite sensitive to outside "noise," which introduces large load fluctuations and is therefore best performed at a time when little other activity is being conducted in the laboratory.

Finally, experiments are interrupted before a visible buckling wave has formed; therefore, a buckled test shell cannot be distinguished form an original specimen if the SIS is in operation. Continued loading beyond the bifurcation point (after removal of the scanning system) provides a good buckling wave for visual inspection, as is shown in Figures 2.27a and b.

8.2 EXPERIMENTAL RESULTS

Experimental accuracy was significantly increased with the introduction of the circumferential profile scans for radial displacements and function-controlled loading. Although initial experiments experienced load relaxation problems, the results turned out to be quite representative, and more advanced tests did not change the general structure of these results. The most distinctive feature of these initial experimental results is that as the axial tensile load increases, the resistance to buckling that is due to the external pressure decreases when the shell is plastically deforming. It is known that for biaxial elastic buckling of cylinders, axial tension has a stabilizing effect and resistance to buckling actually increases. In contrast, for plastic buckling the axial tensile load alters ("softens") the material behavior such that less external pressure is required to buckle the cylinder loaded in tension (constant axial tension and increasing external pressure experiments).

This change of material response also causes buckling under constant external pressure and increasing tension. The increasing axial tensile load is able to "soften" the material response to the point that the buckling resistance to the constant external pressure has diminished to such a degree that the shell buckles into a nonaxisymmetric shape.

The circumferential profile plots contribute significantly to the understanding of the formation of the buckling waveform. This waveform develops independent of the initial imperfection as is the case in elastic buckling, except when the imperfection has the same shape as the buckling mode. The profiles are excellent tools in controlling the experiment and determining the buckling loads by observing the displacement of individual points on the shell wall. Load-displacement curves for these individual points can be obtained from the scan profiles. The ultimate buckling load can often be estimated from the individual load-displacement curves for maximum and minimum points on the shell wall as can be seen from experimental results. The shape of these curves suggests possible applicability of the Southwell plots. Experimentation with Southwell plots worked surprisingly well for the constant axial tensile stress experiments, but not so well for the reversed load-paths. Still, there is sufficient empirical evidence that the Southwell plot can be applied to the constant tension experimental data to obtain the buckling load for the "perfect" shell.

One should remember that for the constant external pressure experiments, the increasing axial stress induces buckling in an indirect manner by changing the material behavior. It is therefore likely that the Southwell method (which is primarily based on the load parameter which induces buckling) does not perform as well in this type of loading environment as it did for the constant tension experiments.

Figures 3.16 and 3.24 definitely show the "smoothing" characteristic of the Southwell plot and the apparent little path dependence of the buckling experimental results. The reversed load-path seems to result in slightly lower buckling points, but as explained these results have not been derived from Southwell plots. These points represent the last observed loads before buckling. The number of buckling waves that form around the circumference is dependent upon the load-path (load magnitude) as observed from experimental data. Higher axial tensile loads result in fewer waves around the circumference. Buckling for the .030" ("set A") thick shells occurs deeper in the plastic region than for the thinner .028" ("set B") shells. Path dependence of the buckling loads of the test shells appears to be less in the thinner shells. This could be a result of the bifurcation points' being nearer to the elastic region in which path independence prevails. Overall, both sets of results look basically similar, although it seems that the thinner (.028") shell results exhibit a little more curvature when viewing the entire data set. The thinner (.028") shell results fall much closer to the elastic region, and in the case of small axial tensile load, the analysis is almost completely elastic.

8.3 ANALYSIS RESULTS

BOSOR5 analysis, using either of the available plasticity models, proved to be unsuccessful in predicting the buckling behavior over the entire range. Deformation theory results did model the "softening" behavior as the axial loads increased but for some load-paths significantly underpredicted the experimental results.

Underprediction of the observed experimental buckling load is physically disturbing and uncommon for shell-buckling problems. In contrast, the more physically sound incremental theory displays a "stiffening" behavior with increasing tensile load as is observed for elastic-buckling problems. Thus, as axial tension increases, the discrepancy between experimental data and numerical analysis increases. The overall "sense" of the incremental data is incorrect as can be seen from Figure 4.4.

Introduction of elastic shearing response, as is predicted by pure incremental theory, does not improve the results. It clarifies why Bushnell has included a "modified" shear response, since predictions are somewhat lower and therefore closer to experimental results, but the general "sense" of the data is not changed.

Incremental theory predicts an approximately correct change in circumferential wave-number as is observed in the experiment. Besides having the standard dependence on shell geometry and load-path, the circumferential wave number is also dependent on the shell end condition as is shown in the analysis.

The effect of the end conditions is such that unrestrained in-plane displacements cause the buckling load to diminish and reduce the circumferential buckling wave-number in some cases. This behavior is expected but apparently does not alter the analysis enough to predict the "sense" of the experimental results. It is clear from analysis that at higher axial loads the influence of the type of in-plane end condition decreases. This seems logical since an increase in plastic behavior of the shell (reduced stiffness) will reduce the effects of edge influences on total shell behavior.

With the above argument in mind, it is possible to address the issue of imperfection sensitivity, which is often blamed for the discrepancy between experiment and analysis. The point was already made in an earlier chapter that it seems difficult to comprehend that the influence of imperfections is so large that the analysis results have no physical meaning whatsoever. In addition, the experimental results seem to indicate that the various initial imperfections had little influence by virtue of the apparent "smoothness" of experimental results. From results shown in Figure 4.5b, one would conclude that the effects of imperfections increase when axial loads become very large. This is contradictory to the general understanding that the initial axial tensile load reduces the existing imperfections and therefore should reduce imperfection sensitivity.

Using the above arguments, it is felt that the root of the problem lies in the plastic model, not in the imperfection sensitivity for this problem. Admittedly, circumferential imperfections cannot be modeled by BOSOR5 because of the axisymmetric nature of the numerical analysis. Therefore, a possible next step should be to apply a less restricted analysis to this problem, to verify the effects of nonaxisymmetric imperfections. Inclusion of small axial (along the meridian) imperfections, which are the only kind possible, did not affect the buckling loads significantly during initial trials with BOSOR5.

Reversed load-paths in which the load, which is primarily responsible for buckling (external pressure), is held constant while the axial tensile load (which reduces material stiffness) is increased, cannot be successfully modeled using incremental theories in BOSOR5. On the other hand, the path-independent deformation theory does predict the same buckling locations on the load diagram for the reversed load-path. From an engineering standpoint this would at least result in a bench mark, since experiment shows that for the reversed load-path, buckling does occur and is very close to previous results.

A point should be made that in the analysis an "average" wall thickness of the physical specimen was used and that often the minimum shell thickness was up to .002" less. Since buckling is observed to start in the thinnest section of the shell wall, it would seem prudent to use the minimum shell thickness in the analysis instead of the average thickness. This results in a shift of the entire numerical data, closer to the experimental data (by 5-8% as reported in Chapter 4), but is not expected to change the "sense" of the data.

For the thinner shells ("set B"), the results are basically the same except that for this analysis two sets of material curves are available. Circumferential properties seem to have a slightly lower yield point but a slightly higher hardening parameter. Differences appear to be small enough to maintain conditions of isotropy (if the compressive response of the material is the same as the tensile response) in the analysis.

Results using the deformation theory differ only slightly using either material curve. The higher hardening curve exhibits much stiffer behavior and also does not underpredict the experimental data. Numerically calculated buckling wave-numbers depend on the load-path, whereas the experimental shells buckled in four circumferential waves for the entire range. It is expected that further study with variable end conditions may alter the numerical analysis to fit the experimental behavior more precisely.

More distinctive differences are obvious for the J_2 incremental analysis. For low axial loads, numerical data using either material curve are basically the same, but for large axial loads some significant physical differences start to emerge. As expected, this implies that the more plastic the material is deforming, the more critical is the exact definition of the material behavior. Neither material curve is able to eliminate the discrepancy between experiment and analysis, and therefore only strengthens the belief that improvement should be sought through better material modeling.

The introduction of the corner theory shows some definite improvement in that it predicts the "sense" of the experimental data, while the bifurcation wave number is also predicted correctly. However, the problems associated with the corner theory may outweigh the advantages at the present time. As the model is currently implemented in BOSOR5, extensive calculations are required, and computation time has increased four to five times. Careful parametric studies may result in better agreement between corner theory results and experiment. A search for optimum parameters with current computational time seems prohibitive, and there is no guarantee that parameters that produce good results in this type of experiment will also give better results under other loading conditions.

Computation time could possibly be reduced by "streamlining" various calculations within the model. Currently, a large part of the computational time is allocated for solving the (CH) equation, which determines the angle β, and for the calculation of the third out-of-plane component of the strain. Improvement in either computation will decrease computational time significantly and may make extensive parameter studies feasible.

Christoffersen and Hutchinson [Ref. 53] bring up the point that the CH corner theory tends to overestimate crucial strain components, when abrupt changes in load-path occur near the corner. This may explain why BOSOR5 analysis fails for large initial axial tensile loads on the shell. The application of the tensile load causes a corner to form because of axial yielding of the material. When subsequent external pressure is applied the load-path changes abruptly, and as stated by CH, large axial strains are computed. The accumulation of these strains is enough to trigger the code to predict an axial failure. Improvement of predictive capability for these load-paths will most likely occur when the functions and variables that define the corner are more closely studied and changed to obtain a smoother transition. As can be observed from earlier data, a smooth yield surface does not exhibit this behavior for abrupt changes in load-path.

When the corner theory is applied to the thinner shell ("set B"), results exhibit much "stiffer" behavior, which is reminiscent of incremental type response. However, the "sense" of the data is still similar to experimental results. The "stiffer" behavior may be due to the location of the bifurcation points, which are now much closer to the elastic region. When this is the case, a corner has had little time to develop, and the appearance of an approximately "smooth" yield surface causes a material response similar to the (smooth yield surface) J_2 incremental theory. As the shell wall thickness increases, a sharper corner will develop before buckling, because of more extensive plastic loading, and corner theory properties will start to play a more significant role.

8.4 GENERAL CONCLUSIONS

Experimental results are representative for simple nonproportional loading on cylindrical shell specimens. The most general result can be concluded from Figure 4.4 and basically implies that the presently used plastic models (J_2 incremental and deformation theories), which are the most common plastic models available, do not model correctly the type of biaxial loading studied. Widely used material models such as J_2 incremental and deformation theory do not perform satisfactorily when trying to obtain buckling loads of simple shells under multiple loading of the type studied. Results do show that for proportional loading problems (pure external pressure), the models predict failure much better, but that the introduction of biaxial load components significantly reduces the accuracy of the analysis. The error is attributed to the plastic model and therefore is expected to influence other problems besides the simple shell discussed here. The approach in this research is to use careful experimentation to examine the effects of plastic constitutive modeling on buckling.

Currently, pure J_2 incremental theory does not predict material behavior correctly for those types of shell problems where a biaxial loading condition, like external pressure and axial tension, exists. Bushnell's modification of the shear behavior has shown that using a deformation type shear response, reduces the error between experiment and analysis but does not fully explain plasticity modeling problems. Although the present analysis seems to indicate that shearing alone will not solve the problem, proper identification of the shear influence may yield better results and understanding of the material behavior.

Deformation theory although "less respected" does capture the observed softening behavior for problems under constant axial loads. In addition, this theory can also predict buckling for the reversed load-path, which none of the incremental theories is able to do. Path independence is not observed in nonproportional plastic loading and deformation theory is therefore included primarily as an "engineering" design tool to help estimate the experiment buckling load.

Corner theory maintains the desirable features of an incremental theory (normality, convexity, yield surface), but definition of the corner is an unresolved problem. At the present time, corner theory has improved predictive capability, but the various parameters that need to be specified "a priori" have to be optimized. Numerical efficiency is not optimal and it seems unlikely that the model in its present form (BOSOR5) is a viable option for a practical predictive analysis.

A final point should be made regarding the isotropy assumptions, since the experimental work as performed in this research, though showing little effects which would indicate anisotropy, does not conclusively rule out the possibility of nonisotropic plastic deformation. A smooth yield surface theory with nonisotropic behavior has not been studied and therefore cannot be ruled out as a possible solution.

A.0 APPENDIX (A)

The following discussion is a brief overview of the main principles and ideas of the Christoffersen-Hutchinson corner theory [Ref. 53] and the treatment of these equations in Poh-Sang Lam's thesis [Ref. 56].

The CH paper starts the derivation with Hill's [Refs. 30,31] observation that there exists a convex plastic (rate) potential W^P, such that

$$\overset{\circ}{\varepsilon}^{P} = \frac{\partial W^{P}}{\partial \overset{\circ}{\sigma}} \qquad \text{(A .1)}$$

In addition, a detailed specification of the corner is presented and shown in Figure 7.2. The parameter λ in Figure 7.2 is picked to be the symmetric deviator tensor and is directed along the axis of the cone, while θ is the "angle" between the stress increment and the cone axis. The conical surface separating the unloading and plastic flow region is taken as $\theta = \theta_c$. Stress increments falling within the range $\theta \leq \theta_0$ are linearly related to the corresponding plastic strain increments; i.e.,

$$\overset{\circ}{\varepsilon}^{P} = C\,\overset{\circ}{\sigma} \qquad \text{(A.2)}$$

This region is often called the total loading region. In the region $\theta_0 < \theta < \theta_c$, the relation between the plastic strain-increment and stress-increment is nonlinear and provides a continuous transition from the total loading range to the region where the plastic strain-rate is zero $(\theta \leq \theta_c)$.

When $\theta_0 = 0$ the plastic response is often referred to as "throughly nonlinear behavior" and represents the limiting case of this theory.

Normality requires that the plastic strain increment always falls within the forward cone of normals. The current state of stress and its history determine the compliance tensor C and the "direction" of λ. In the specialization as implemented in BOSOR5, λ is taken to be proportional to the stress deviator and C are the instantaneous "plastic" compliances from J_2

deformation theory. In the total loading range,

$$W^p = \frac{1}{2} C \, \mathring{\sigma} \mathring{\sigma} \qquad \text{(A .3)}$$

In order to bridge the gap between the total loading and elastic unloading regions, a function $f(\theta)$ is introduced in the CH paper,

$$W^p(\mathring{\sigma}) = \frac{1}{2} f(\theta) \, C \mathring{\sigma} \mathring{\sigma} \qquad \text{(A .4)}$$

where

$$f(\theta) = \begin{cases} 1, & \theta \le \theta_o \\ 0, & \theta \ge \theta_c \end{cases}$$

In the transition range $\theta_o \le \theta \le \theta_c$, f is chosen such that the convexity condition is satisfied and also that the plastic strain rate or incremental strain varies continuously with the stress rate (or increment) at $\theta = \theta_o$ and $\theta = \theta_c$. The intricacies of the derivation can be found in the CH paper, but choosing C to play the role of a metric while specifying the geometry of the corner in the stress space ($\theta = \theta_c$) in conjunction with equation A.1 leads to the following form of the plastic strain rate (or strain increment) according to Christoffersen and Hutchinson.

$$\mathring{\varepsilon}^p = f(\theta) \left[(1 - k(\theta) \cot \theta) \, C + k(\theta) \, (\sin\theta \cos\theta)^{-1} \mu \otimes \mu \right] \mathring{\sigma} \qquad \text{(A .5)}$$

where

$$k(\theta) = -\frac{1}{2} \frac{f'}{f}$$

In strain space, μ is directed along the corresponding cone axis in plastic strain space according to Christoffersen and Hutchinson. The complete discussion can be found in Reference [53].

A.1 J_2 CORNER THEORY

The following discussion can be found in more detail in Lam [Ref. 56].

The small strain version of the rate potential as given by Christoffersen and Hutchinson is

$$W(\overset{\circ}{\underline{\sigma}}) = \frac{1}{4G} Q(\beta)\, \overset{\circ}{S}_{ij} \overset{\circ}{S}_{ij} + \frac{1-2\nu}{6E} \overset{\circ}{\sigma}{}^{2}_{kk} \qquad (A.6)$$

where

$$\overset{\circ}{\varepsilon}_{ij} = \frac{\partial W}{\partial \overset{\circ}{\sigma}_{ij}}$$

$$Q(\beta) = 1 + 3G\left[\left(\frac{1}{E_t} - \frac{1}{E_s}\right)\cos^2\beta + \left(\frac{1}{E_s} - \frac{1}{E_t}\right)\sin^2\beta\right] f(\theta)$$

$$\tan\theta = a^{1/2}\tan\beta, \qquad a = \left(\frac{E}{E_s} - 1\right)\left(\frac{E}{E_t} - 1\right)^{-1}$$

β = angle between stress rate and the yield cone axis and stress space

$f(\theta)$ = transition function given in CH

$\overset{\circ}{S}$ = deviatoric stress rate

$\overset{\circ}{\underline{e}}$ = deviatoric strain rate

$\underline{n} = \frac{\underline{S}}{(\underline{S} \bullet \underline{S})^{1/2}}$

E_t = tangent modulus

E_s = secant modulus.

According to Lam [Ref. 56], since $W(\overset{\circ}{\underline{\sigma}})$ is strictly convex, the inversion of stress rate and strain rate is permissible, yielding the folowing constitutive law:

$$\overset{\circ}{S}_{ij} = \frac{2G}{Q + \left(1 + \frac{1}{2}\frac{Q'}{Q}\cot\beta\right)} \left\{ \overset{\circ}{e}_{ij} + \frac{n_{ij}}{2\sin\beta}\frac{Q'}{Q}\left[\frac{\overset{\circ}{e}_{kl}\,\overset{\circ}{e}_{kl}}{1 + \frac{1}{4}\left(\frac{Q'}{Q}\right)^2}\right]^{1/2} \right\} \qquad \text{(A .7)}$$

$$\text{where } Q' = \frac{\partial Q(\beta)}{\partial\beta} \quad \text{and} \quad n_{ij} = \frac{S_{ij}}{\sqrt{S_{kl}\,S_{kl}}}$$

The right-hand side of Equation A.7 is given in CH and contains an unknown angle β, which can be solved through

$$\tan(\beta - \alpha) = -\frac{1}{2}\frac{Q'(\beta)}{Q(\beta)}$$

where α is the angle between the deviatoric strain rate and the current deviatoric stress. A more detailed description can be found in Lam [Ref. 56].

References

[1] Babcock, C.D., "Shell Stability," *Journal of Applied Mechanics*, Vol. 50, 935-940 (Dec. 1983).

[2] Bushnell, D., and Galletly, G.D., "Stress and Buckling of Internally Pressurized Elastic-Plastic Torispherical Vessel Heads Comparisons of Test and Theory," *Journal of Pressure Vessel Technology*, 39-53 (Feb. 1977).

[3] Bushnell, D., "Nonsymmetric Buckling of Internally Pressurized Ellipsoidal and Torispherical Elastic-Plastic Pressure Vessel Heads," ASME *J. of Pressure Vessel Technology*, Vol. 99, 54-63 (1977).

[4] Galletly, G.D., "Stress Failure of Large Pressure Vessels - Recommendations Resulting from Studies of the Collapse of a 68 ft. High x 45 ft. Diameter Pressure Vessel," Tech Report No. 45-57, Shell Development Corp., Emeryville, California (March 1957).

[5] Galletly, G.D., "Torispherical Shells - A Caution to Designers, Published in Pressure Vessel and Piping Design - Collected Papers," ASME, N.Y. (1960).

[6] Bushnell, D., "Plastic Buckling,"in *Pressure Vessels and Piping: Design Technology 1982, a Decade of Progress*, edited by S.Y. Zamrik and D. Dietrich, ASME, N.Y. Book No.G00213 , pp.47-117 (1982).

[7] Brown, K.W. and Kraus, H., "Stability of Internally Pressurized 2:1 Ellipsoidal Shells," *J. Pressure Vessel Technology*, Vol. 100, 335-343 (1978).

[8] Bushnell, D. and Galletly, G.D., "Comparison of Test and Theory for Nonsymmetric Elastic-Plastic Buckling of Shells of Revolution, "*Int. J. Solids Structure*, Vol. 10, 1271-1286 (1974).

[9] Lagae, G. and Bushnell, D., "Elastic-Plastic Buckling of Internally Pressurized Torispherical Vessel Heads," *Nuclear Engineering and Design*, Vol. 48, 405-414 (1978).

[10] Galletly, G.D., "Internal Pressure Buckling of Very Thin Torispherical Shells - A Comparison of Experiment and Theory," 3rd SHiRt Conf., London, paper G2/3 (1975).

[11] Galletly, G.D., "Elastic and Elastic-Plastic Buckling of Internally Pressurized 2:1 Ellipsoidal Shells," *J. Pressure Vessel Technology*, Vol. 100, 335-343 (1978).

[12] Kirk, A. and Gill, S.S., "The Failure of Torispherical Ends of Pressure Vessels Due to Instability and Plastic Deformation - An Experimental Investigation," *Int. J. Mech. Science*, Vol. 17, 525-544 (1975).

[13] Patel, P.R. and Gill, S.S., "Experiments on the Buckling Under Internal Pressure of Thin Torispherical Ends of Cylindrical Pressure Vessels," *Int. J. Mech. Science*, Vol. 20, 159-175 (1978).

[14] Singer, J., Arbocz, J., and Babcock, C.D., "Buckling of Imperfect Stiffened Cylindrical Shells Under Axial Compression," AIAA *Journal*, Vol. 9, pp. 68-75 (Jan. 1971).

[15] Arbocz, J., and Babcock, C.D., "The Effect of General Imperfections on the Buckling of Cylindrical Shells," *Transactions of the* ASME, Ser. 36, E, *Journal of Applied Mechanics*, 28-38 (March 1969).

[16] Tipton, B., "PASSD - Program for the Acquisition of Stress-Strain Data," California Institute of Technology (April 1984).

[17] Davidson, B. and Tsuha, W., "Buckling of Thin-Walled Cylindrical Shells Subjected to a Uniform Lateral Pressure," Ae 104c Report, California Institute of Technology (May 1983).

[18] Southwell, R.V., "On the Analysis of Experimental Observations in Problems of Elastic Stability," *Proceedings of the Royal Society of London*, Vol. 135, pp. 601-616 (April 1931).

[19] Wang, C. "Inelastic Column Theories and an Analysis of Experimental Observations," *Journal of the Aeronautical Sciences* ,Vol. 15, 283-29 (May 1948).

[20] von Kármán, Th., "Untersuchungen über Knickfestigkeit," *Mitteilungen über Forschungsarbeiten*, Verein deutscher Ing., Berlin (1910).

[21] Singer, J.,"On the Applicability of the Southwell Plot to Plastic Buckling," SM 88-2, California Institute of Technology (1988).

[22] Sobel, L.H., "The Southwell Method for Predicting Plastic Buckling Loads for Elbows," *Journal of Pressure Vessel Technology*, Vol. 105, 2-8 (Feb. 1983).

[23] Bushnell, D., "BOSOR5 - A Computer Program for Buckling of Elastic-Plastic Complex Shells of Revolution Including Large Deflections and Creep," Vol. I: User's Manual, Input Data, LMSC D407166; Vol. II; User's Manual, Test cases, LMSC D407167; Vol. III; Theory and Comparisons with Tests, LMSC D407168, Lockheed Missles Space Co., Sunnyvale, California (Dec. 1974).

[24] Bushnell, D., "Bifurcation Buckling of Shells of Revolution Including Large Deflections, Plasticity and Creep," *International Journal of Solids Structures*, Vol. 10, 1287-1305 (1974).

[25] Bushnell, D., "A Strategy for the Solution of Problems Involving Large Deflections , Plasticity and Creep," *International Journal of Numerical Meth. Engineering*, Vol. 11, 683-708 (1977).

[26] Bushnell, D., "Buckling of Elastic-Plastic Shells of Revolution With Discrete Elastic-Plastic Ring Stiffeners," *International Journal of Solids Structures*, Vol. 12, 51-66 (1976).

[27] Lagae, G. and Bushnell, D., "Elastic-Plastic Buckling of Internally Pressurized Torispherical Vessel Heads," *Nuclear Engineering and Design*, Vol. 48, 405-414 (1978).

[28] Bushnell, D., "Large Deflection Elastic-Plastic Creep Analysis of Axisymmetric Shells," in *Numerical Solution of Non Linear Structural Problems*, edited by R.F. Harturg, AMD Vol. 6, ASME, pp. 103-138 (1973).

[29] Bushnell, D., "BOSOR5 - Program for Buckling of Elastic-Plastic Complex Shells of Revolution Including Large Deflections and Creep," *Computers and Structures*, Vol. 6, 221-239 (1976).

[30] Hill, R., "On the Problem of Uniqueness in the Theory of a Rigid/Plastic Solid," *J. Mech. Phys. Solids*, Vol. 4, 247-255 (1956).

[31] Hill, R., "A General Theory of Uniqueness and Stability in Elastic/Plastic Solids," *J. Mech. Phys. Solids*, Vol. 7, 207-225 (1959).

[32] Engesser, F. "Ueber die Knickfestigkeit gerade Stäbe," *Z. Architek Ing.*, Vol. 35, 455 (1889).

[33] Considère, A., "Résistance des Pièces Comprimées," *Congress Inst. Procédés de Construction*, Annexe, Librairie Polytechnique, Paris, p. 371 (1981).

[34] Singer, J.,"The Effect of Axial Constraint on the Instability of Thin Circular Cylindrical Shells under Uniform Axial Compression," *Int. J. Mech. Sci.*, Pergamon Press Ltd, Vol. 4, 253-258, (1962)

[35] Shanley, F.R., "Inelastic Column Theory," *J. Aeronautical Sci.*, Vol. 14, 261-267 (1947).

[36] Duberg, J.E. and Wilder, T. W III, "Column Behavior in the Plastic Stress Range," *J. Aero. Sci.*, Vol. 17, 323 (1950).

[37] Sewell, M.M., "Survey of Plastic Buckling," *Stability* , edited by H. Leipholz, University of Waterloo Press, Ontario, Chapter 5 (1972), pp. 85-197.

[38] Smith, S. and Almroth, B.O., "An Experimental Investigation of Plastic Flow Under Biaxial Stress," *Experimental Mechanics* (June 1970).

[39] Stowell, E.Z., "A Unified Theory of Plastic Buckling of Columns and Plates," NACA TN1556 (April 1948).

[40] Drucker, D.C.,"A Discussion of Theories of Plasticity," *J. Aero. Sci.*, Vol. 16, 567-568 (1949).

[41] Cicala, P., "On the Plastic Buckling of a Compressed Strip," *J. Aero. Sci.*, Vol. 17, 378-379 (1950).

[42] Gerard, G. and Becker, H., "Handbook of Structural Stability: Part I - Buckling of Flat Plates," *NACA Tech. Note*, (1957), p. 3781.

[43] Onat, E.T. and Drucker, E.T., "Inelastic Instabitity and Incremental Theories of Plasticity," *J. Aero. Sci.*, Vol. 20, 181-186 (1953).

[44] Massey, C., "Southwell Plot Applied to Lateral Instability of Beams," *Engineer*, Vol. 218, No. 5666, 320 (Aug. 1964).

[45] Newman, J.B., "Inelastic Column Buckling of Internally Pressurized Tubes," *Experimental Mechanics*, Vol. 13, 265-272 (1973).

[46] Donnell, L.H., "On the Application of Southwell's Method for the Analysis of Buckling Tests," *Stephan Timoshenko 60th Anniversary Volume*, McGraw-Hill, New York (1938), pp. 27-38.

[47] Simitses, G.J.,"An Introduction to the Elastic Stability of Structures," Prentice-Hall Civil Engineering and Engineering Mechanics Series (1976), pp. 66-68.

[48] Bijlaard, P.P., "A Theory of Plastic Buckling with its Application to Geophysics," Koninklijke Nederlandsche Akademie van Wetenschappen, Amsterdam, *Proceedings of the Section of Sciences*, Ser. A, 41, No. 5 (1938), pp. 468-480.

[49] Bijlaard, P.P., "A Theory of Plastic Stability and its Application to Think Plates of Structural Steel," Koninklijke Nederlandsche Akademie van Wetenschappen, Amsterdam, *Proceedings of the Section of Sciences*, Ser. A, 41, No. 7 (1938), pp. 731-743.

[50] Hutchinson, J.W., "Plastic Buckling," *Advances in Applied Mechanics*, Vol. 14, 67-144 (1974).

[51] Tvergaard, V., "Effect of Kinematic Hardening on Localized Necking in Biaxially Stretched Sheets," *Int. J. Mechanical Sciences*, Vol. 20, 651-658 (1978).

[52] Budiansky, B., Dow, N.F., Peters, R.W., and Shepherd, R.P., "Experimental Studies of Polyaxial Stress-Strain Laws of Plasticity," Structures Research Division, NACA (1951).

[53] Christoffersen, J. and Hutchinson, J.W., "A Class of Phenomenological Corner Theories of Plasticity," *J. Mech. Phys. Solids*, Vol. 27, 465-487 (1979).

[54] Batdorf, S.B., "Theories of Plastic Buckling," *J. Aero. Sci.*, Vol. 16, 405-408 (1949).

[55] Sanders, Fr., J.L., "Plastic Stress-Strain Relations Based on Linear Loading Functions," *Proceedings of the Second U.S. National Congress of Applied Mechanics*, ASME, N.Y. (1954), p. 455.

[56] Lam, P., "Numerical Analysis of Stable Crack Growth in Elastic-Plastic Materials in Small Scale and General Yielding," Thesis - T&A.M. Report No. 455, University of Illinois at Urbana - Champaign (Dec. 1982).

[57] Tvergaard, V., "Plastic Buckling of Axially compressed Circular Cylindrical Shells, " *Thin-Walled Structures*, Vol. 1, 139-163 (1983).

[58] Batdorf, S.B. and Budiansky, B., "A Mathematics Theory of Plasticity Based on the Concept of Slip," NACA TN No. 1871 (1949).

[59] Sewell, M.J., "A Plastic Rule at a Yield Vertex," *J. Mech. Phys. Solids*, Vol. 22, 469-490 (1974).

[60] Bertsch, P. K., Findley, W.N.,"An Experimental Study of Subsequent Yield Surfaces-Corners, Normality, Bauschinger and Allied Effects," in *Proceedings 4th U.S. Nat. Congr. Appl. Mech.,* ASME (1962), pp. 893-907

[61] Giezen, J., Babcock, C. D.,"Elastic-Plastic Collapse Problems," SM 86-17, GALCIT, California Institute of Technology, (september 1986)

[62] Hill, R., "Generalized Constitutive Relations for Incremental Deformation of Metal Crystals by Multislip,"*J. Mech. Phys. Solids*, Vol. 14, 95-102 (1966).

[63] DYM, C.L.," The Construction of a Shell Theory," in *Introduction to the Theory of Shells*, Pergamon Press, Glasgow (1982),pp. 21-50

[64] Singer, J.,"The Effect of Axial Constraint on the Instability of Thin Circular Cylindrical Shells Under Uniform Axial Compression," *Int. J. Mech. Sci.*, Pergamon Press Ltd., Vol. 14, 253-258 (1962).

[65] Bushnell, D.,"Plastic Buckling of Various Shells,"*ASME J. Pressure Vessel Technology,* Vol. 104, 51-72, (1984).

[66] Budiansky, B., and Hutchinson, J.W., "Buckling: Progress and Challenge," in *Proceedings of Symposium Trends in Solid Mechanics*, Delft University Press (1979), pp. 93-116.

[67] Hutchinson, J.W., Tennyson, R.C., and Muggeridge, D.B., "Effect of a Local Axisymmetric Imperfection on the Buckling Behavior of a Circular Cylindrical Shell Under Axial Compression," *AIAA Journal*, Vol. 9, No. 1, 48-52 (Jan. 1971).

[68] Afiak, W., Jullien, J.F., and Waeckel, N., "Plastic Buckling of Imperfect Cylindrical Shells Under Axial Load," *ECCS International Colloquium on Stability of Plate and Shell Structures*, Ghent University, Ghent (April 1987).

[69] Galletly, G.D., and Aylward, R.W., "Plastic Collapse and the Controlling Failure Pressures of Thin 2:1 Ellipsoidal Shells Subjected to Internal Pressure," *Journal of Pressure Vessel Technology*, Vol. 101 (Feb. 1979).

[70] Schmidt, J., and Stracke, M., "Buckling Strength and Post Buckling Behavior of Short Cylindrical Shells Under External Pressure in the Elastic-Plastic Region," *ECCS International Colloquium on Stability of Plate and Shell Structures*, Ghent University (April 1987).

[71] Unal, Z., and Esin, A., "Plastic Torsional Buckling of Thin-Walled Circular Cylinders," *Materialprüfung*, Vol. 28 (1986).

[72] Horton, W.H., Bailey, S.C., and Edwards, A.M., "Nonsymmetric Buckle Patterns in Progressive Plastic Buckling," *Experimental Mechanics*, 433-444 (Sept. 1966).

[73] Needleman, A. and Tvergaard, V., "Crack-Tip Stress and Deformation Fields in a Solid with a Vertex on its Yield Surface," in *Elastic-Plastic Fracture: Second Symposium*, Vol. I - Inelastic Crack Analysis, ASTM STP 803, edited by C.F. Shih and J.P. Gudas, American Society for Testing and Materials (1983), pp. I-80 - I-115.

[74] Tvergaard, V., "On the Transition from a Diamond Mode to an Axisymmetric Mode of Collapse in Cylindrical Shells," *Int. J. Solids Structures*, Vol. 19, 845-856 (1983).

[75] Phillips,A., Eisenberg, M.A. ,"A Theory of Plasticity with Non-Coincident Yield and Loading Surfaces," *Acta Mechanica*, Vol. 11, 247-260, (1971).

[76] Galletly, G. D.,Reynolds, T.E.,"A Simple Extension of Southwell's Method for Determining the Elastic General Instability Pressure for Ring-Stiffened Cylinders Subject to External Hydrostatic Pressure,"*Proceedings Society of Experimental Stress Analysis,* Vol. 13 (1956), pp. 141-152.

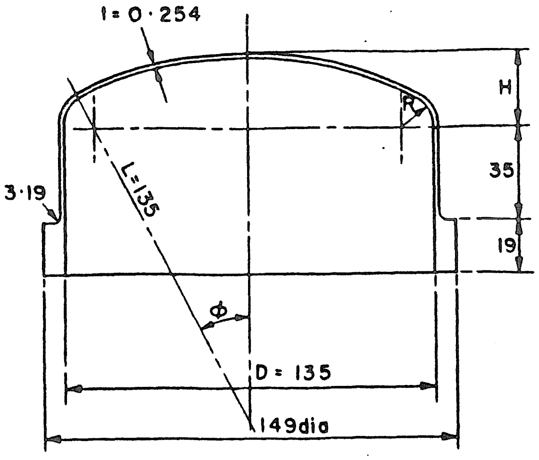

(Dimensions in mm)

FIG. 1.1 TEST SPECIMEN NOMINAL GEOMETRY (FROM PATEL AND GILL [3]).

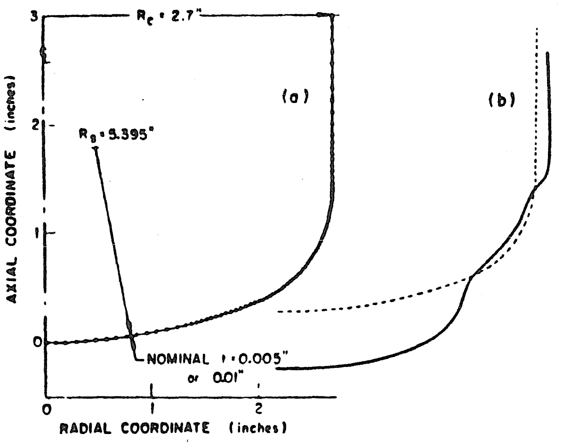

FIG. 1.2 ALUMINUM OR MILD STEEL TORISPHERICAL HEAD TESTED UNDER INTERNAL PRESSURE BY GALLETLY AT THE UNIVERSITY OF LIVERPOOL: (A) BOSOR5 DISCRETE MODEL; (B) EXAGGERATED VIEW OF PREBUCKLING DEFLECTED SHAPE AT THE BIFURCATION BUCKLING PRESSURE (FROM BUSHNELL AND GALLETLY [2]).

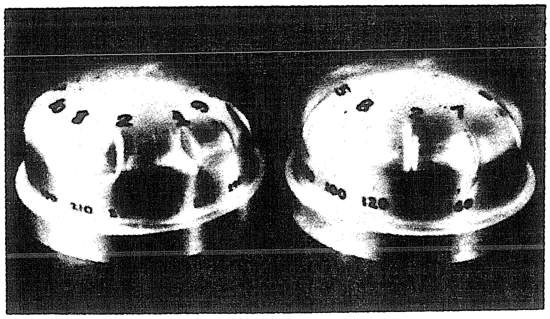

FIG. 1.3 TWO OF PATEL AND GILL'S SPECIMENS AFTER TESTING (FROM PATEL AND GILL [3]).

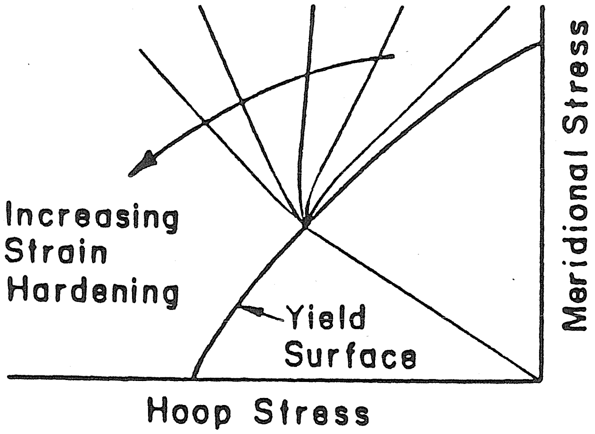

FIG. 1.4 STRESS PATH FOR MEMBRANE STRESS IN KNUCKLE REGION FOR TORISPHERICAL SHELL UNDER INTERNAL PRESSURE.

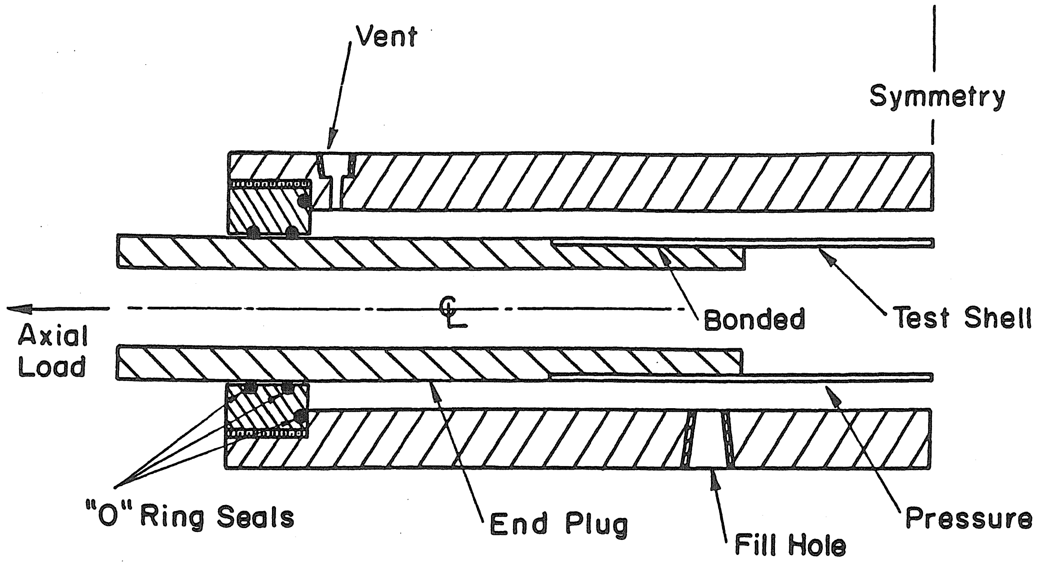

FIG. 2.1 BIAXIAL LOAD TEST FIXTURE.

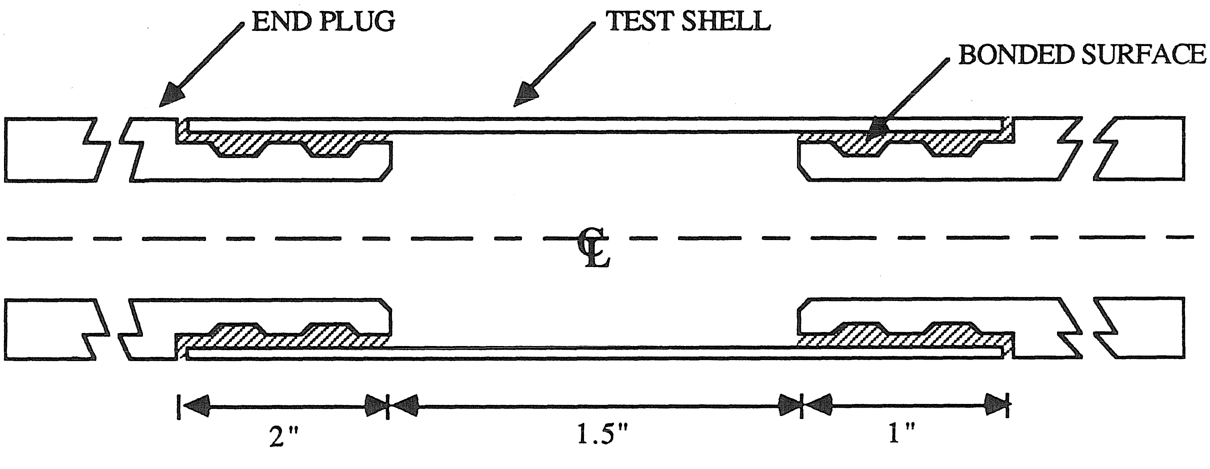

FIG. 2.2 TEST SHELL AND ENDPLUGS.

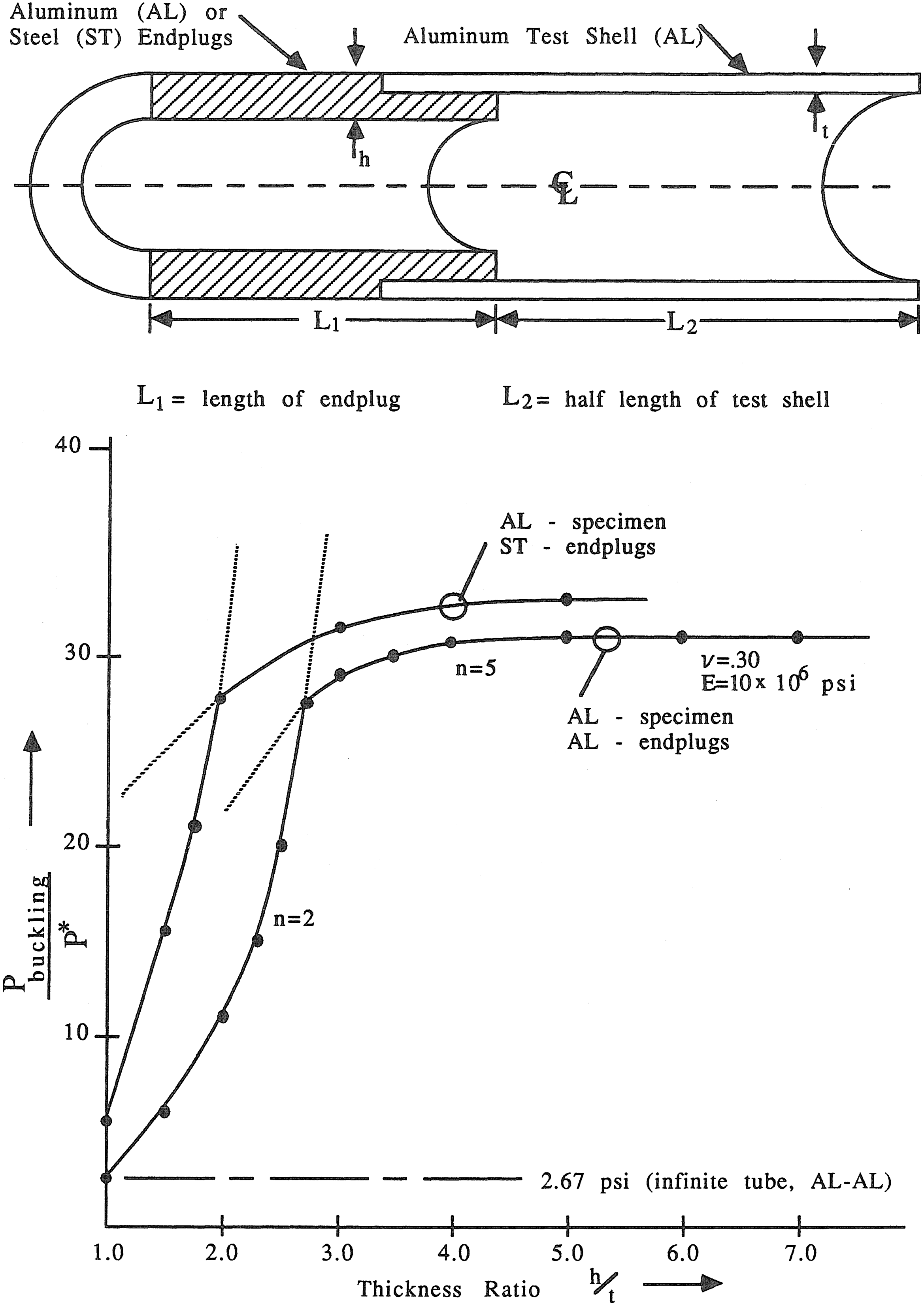

FIG. 2.3 ENDPLUG THICKNESS STUDY.

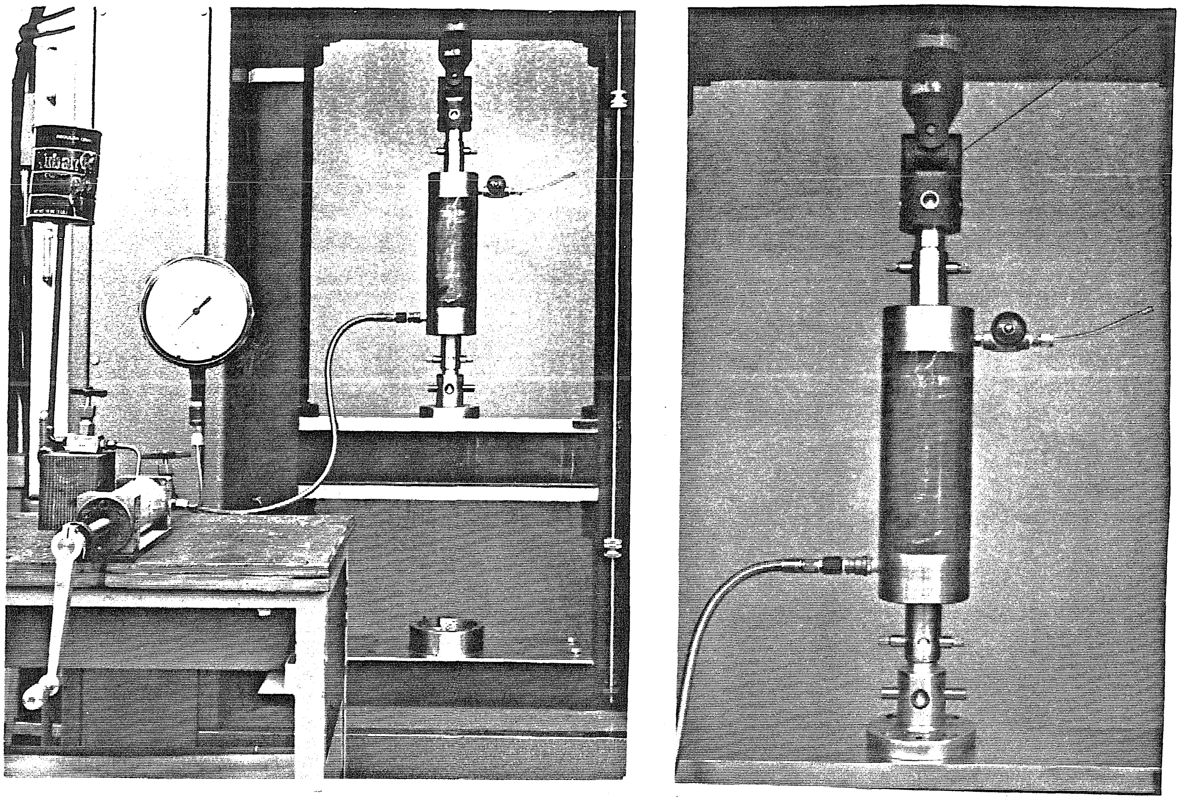

FIG. 2.4a & b BIAXIAL LOAD TEST-FIXTURE IN INSTRON TEST MACHINE.

R = 0.736 in (OD = 1.500 in)
t = 0.028 in
L = 1.50 in

Material Al 6061-T4

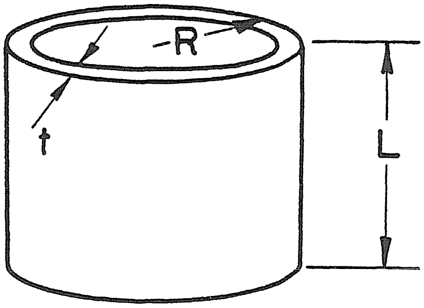

FIG. 2.5 TEST SPECIMEN.

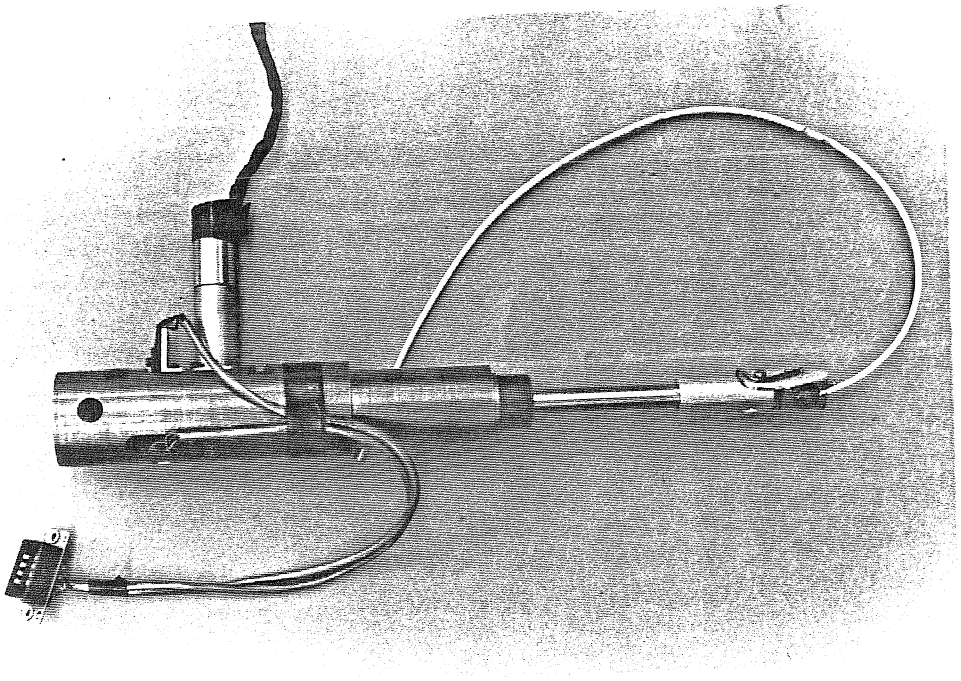

FIG. 2.6 PROBE AND SCANNING DEVICE (DSD).

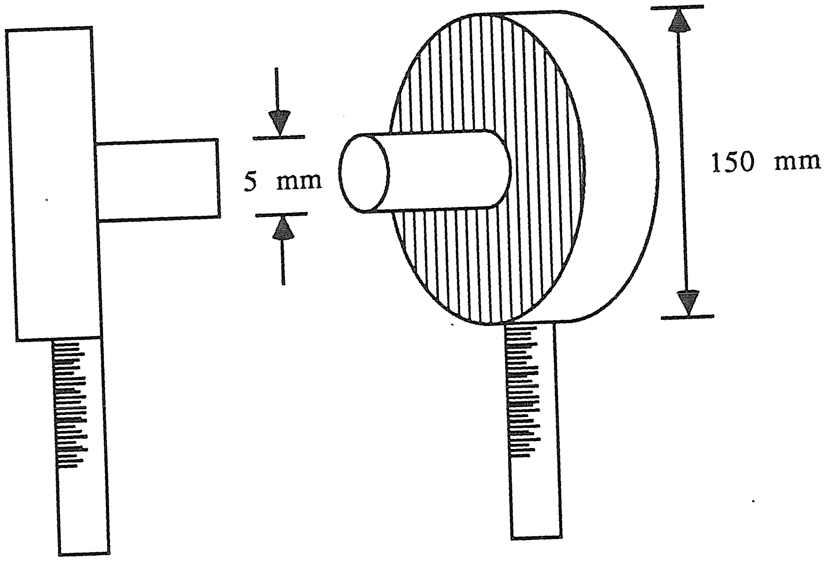

FIG. 2.7 BENTLEY NEVADA (DSD) PROBE.

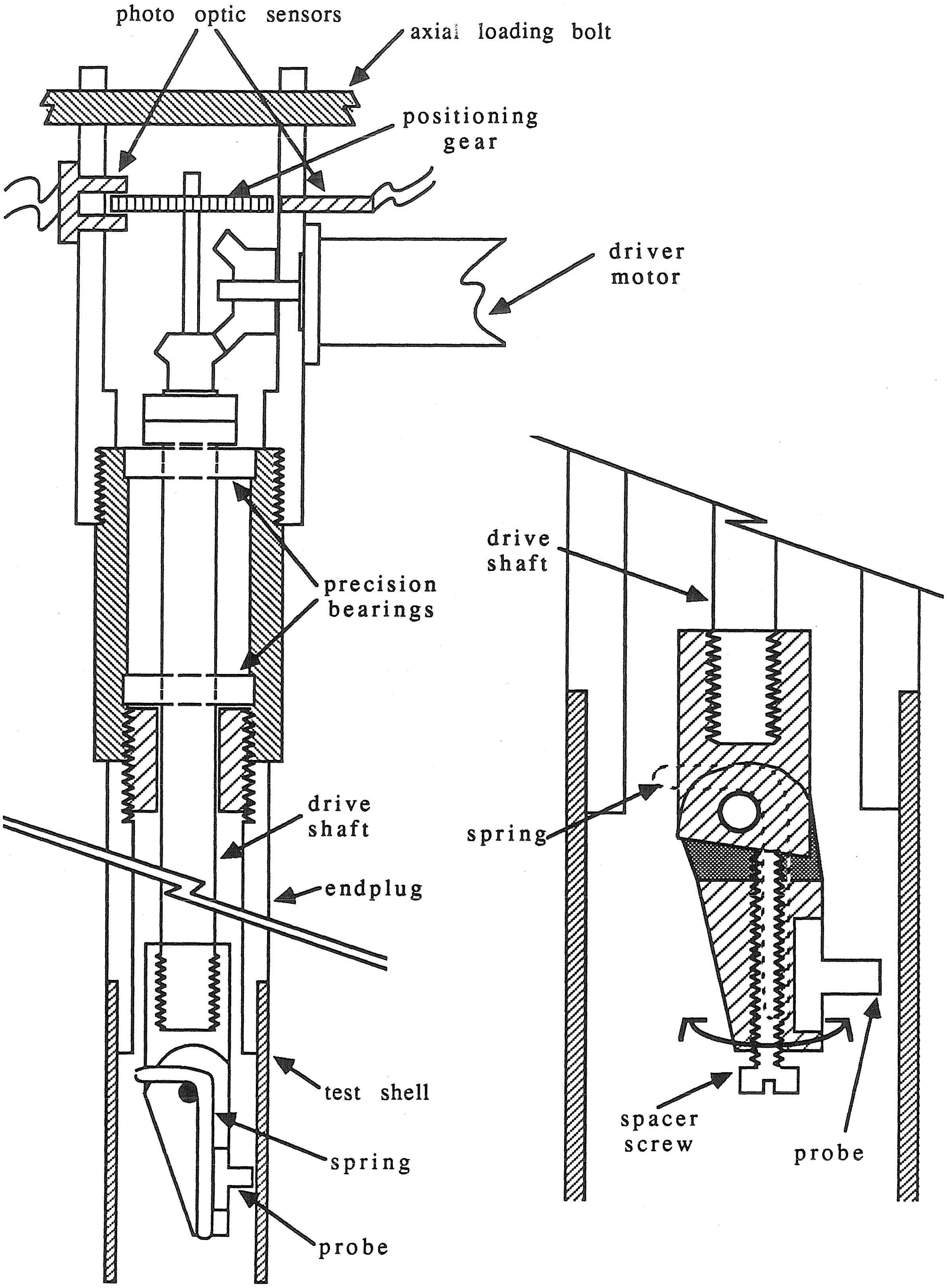

FIG. 2.8 & 2.9 SCHEMATIC OF DISPLACEMENT SCANNING DEVICE (DSD).

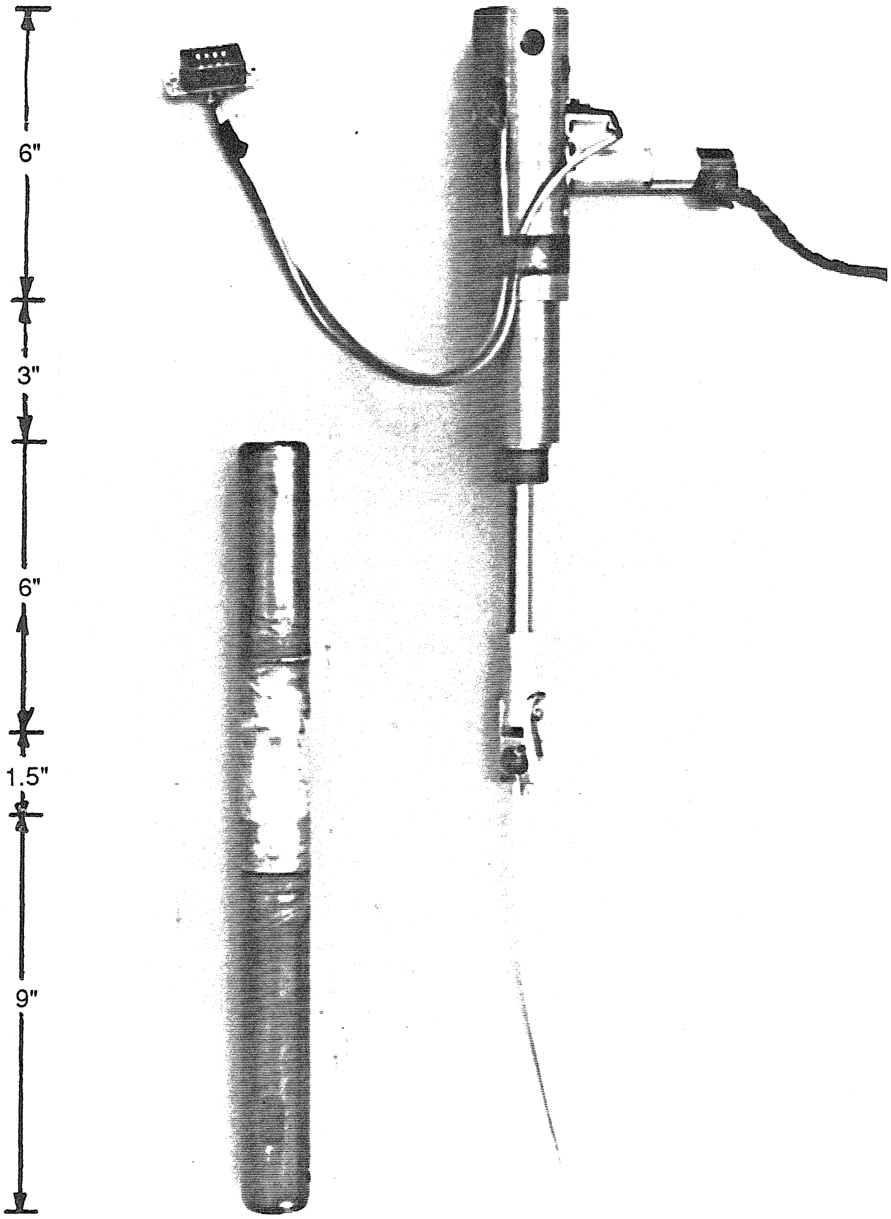

FIG. 2.10 DSD AND TEST SHELL NON ASSEMBLED.

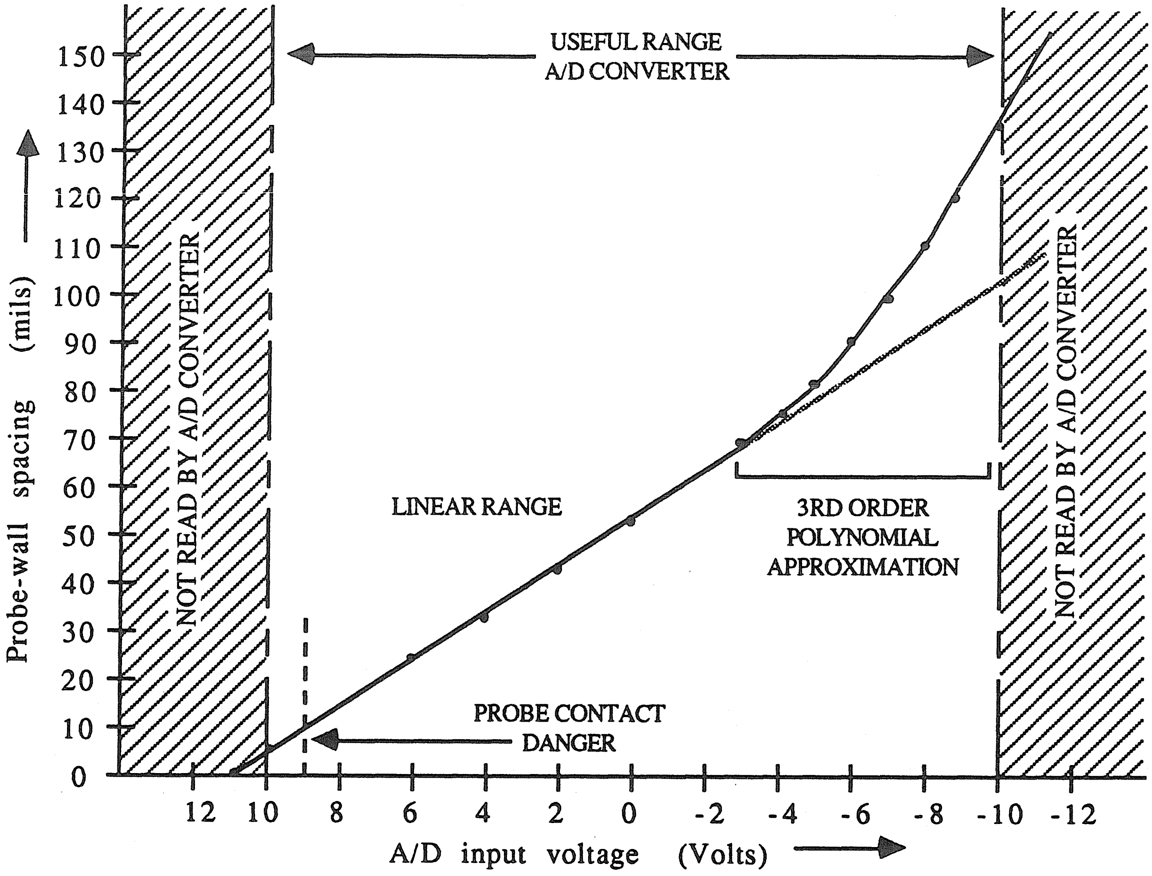

FIG. 2.11 DSD CALIBRATION CURVE.

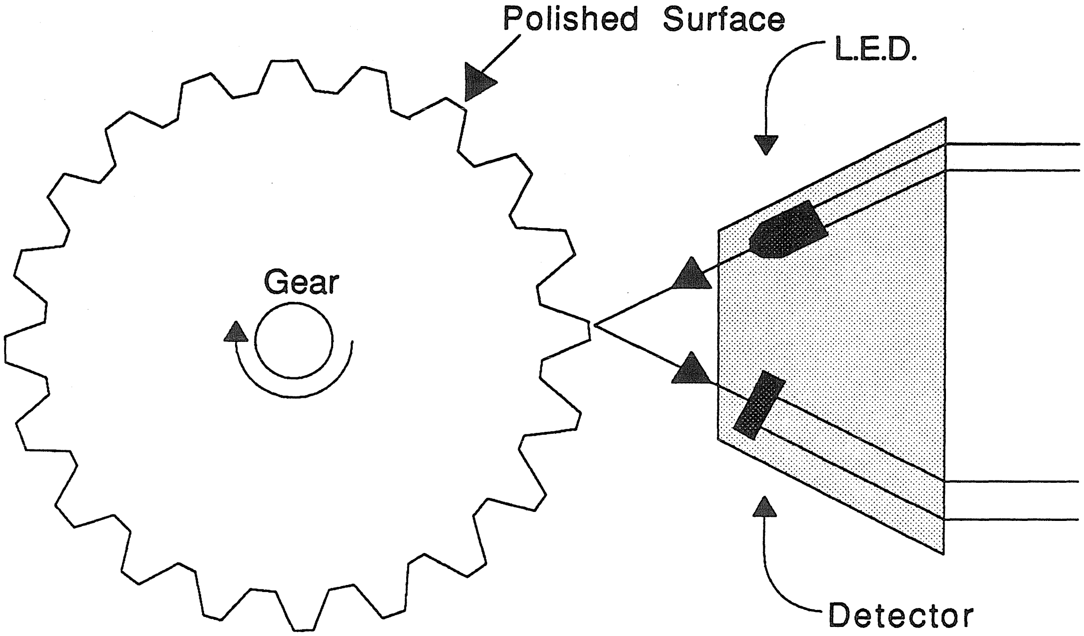

FIG. 2.12 PHOTO-OPTICAL POSITION SENSOR.

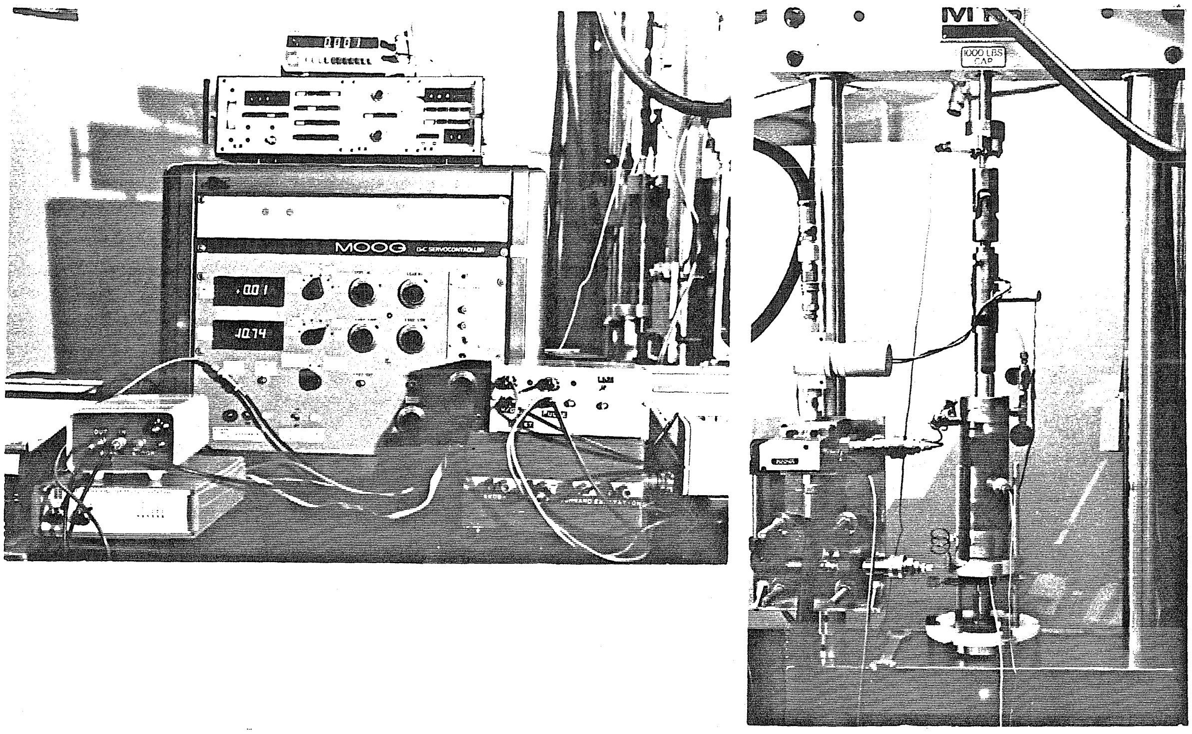

FIG. 2.13 a &b LOAD CONTROL EQUIPMENT.

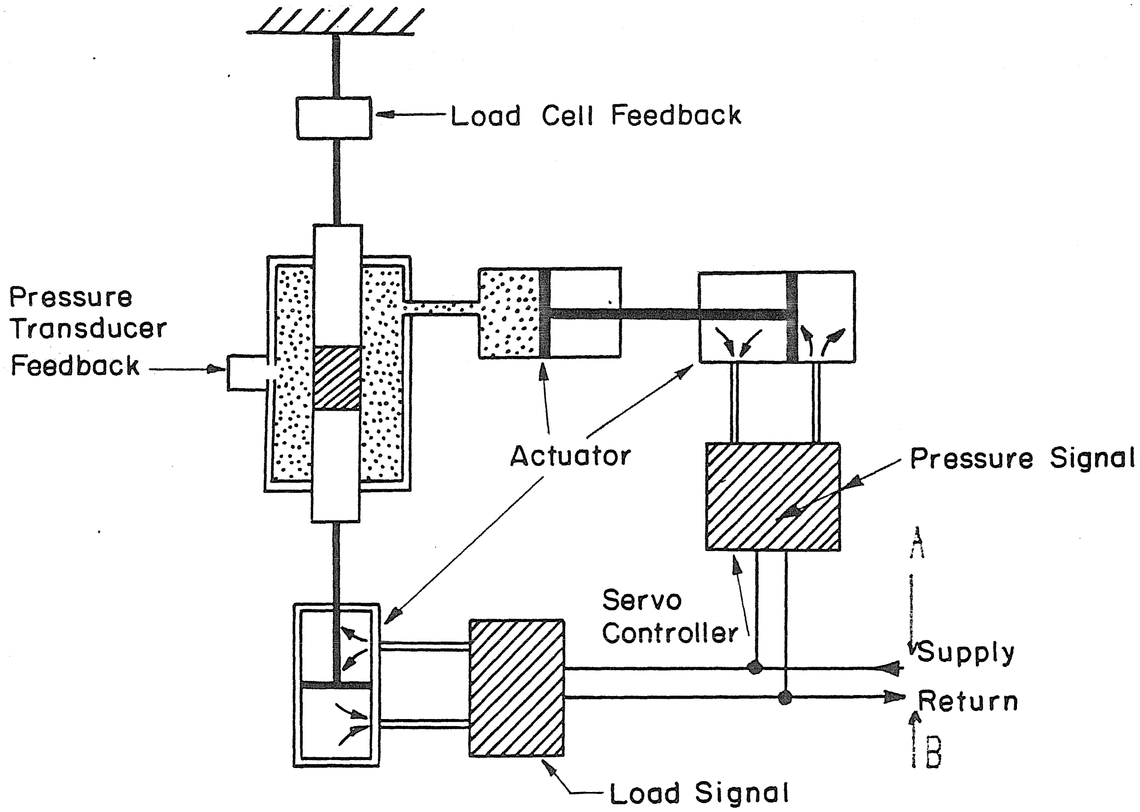

FIG. 2.14 HYDRAULIC CONFIGURATION (EXTERNAL PRESSURE).

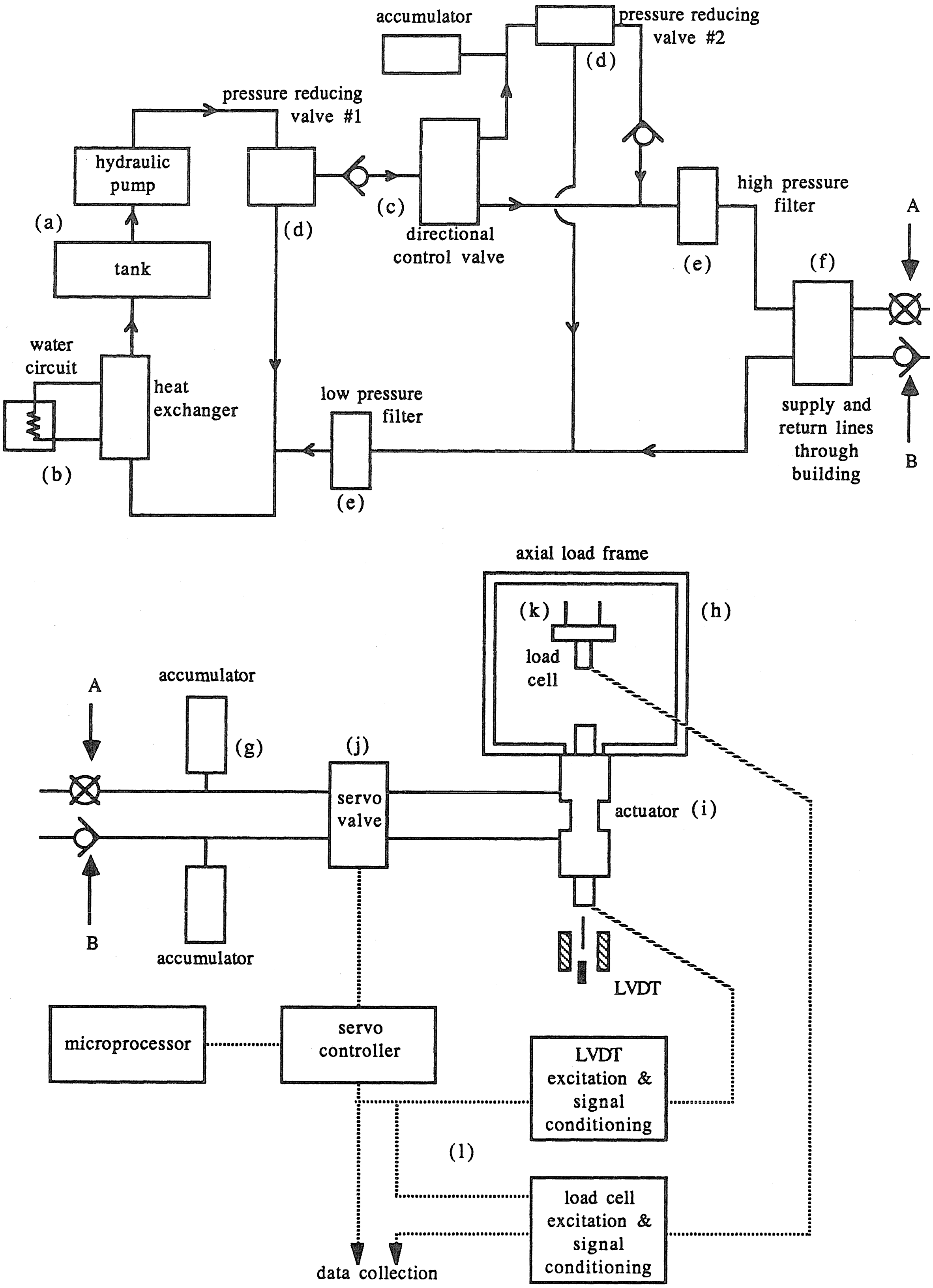

FIG. 2.15 HYDRAULIC SYSTEM SCHEMATIC .

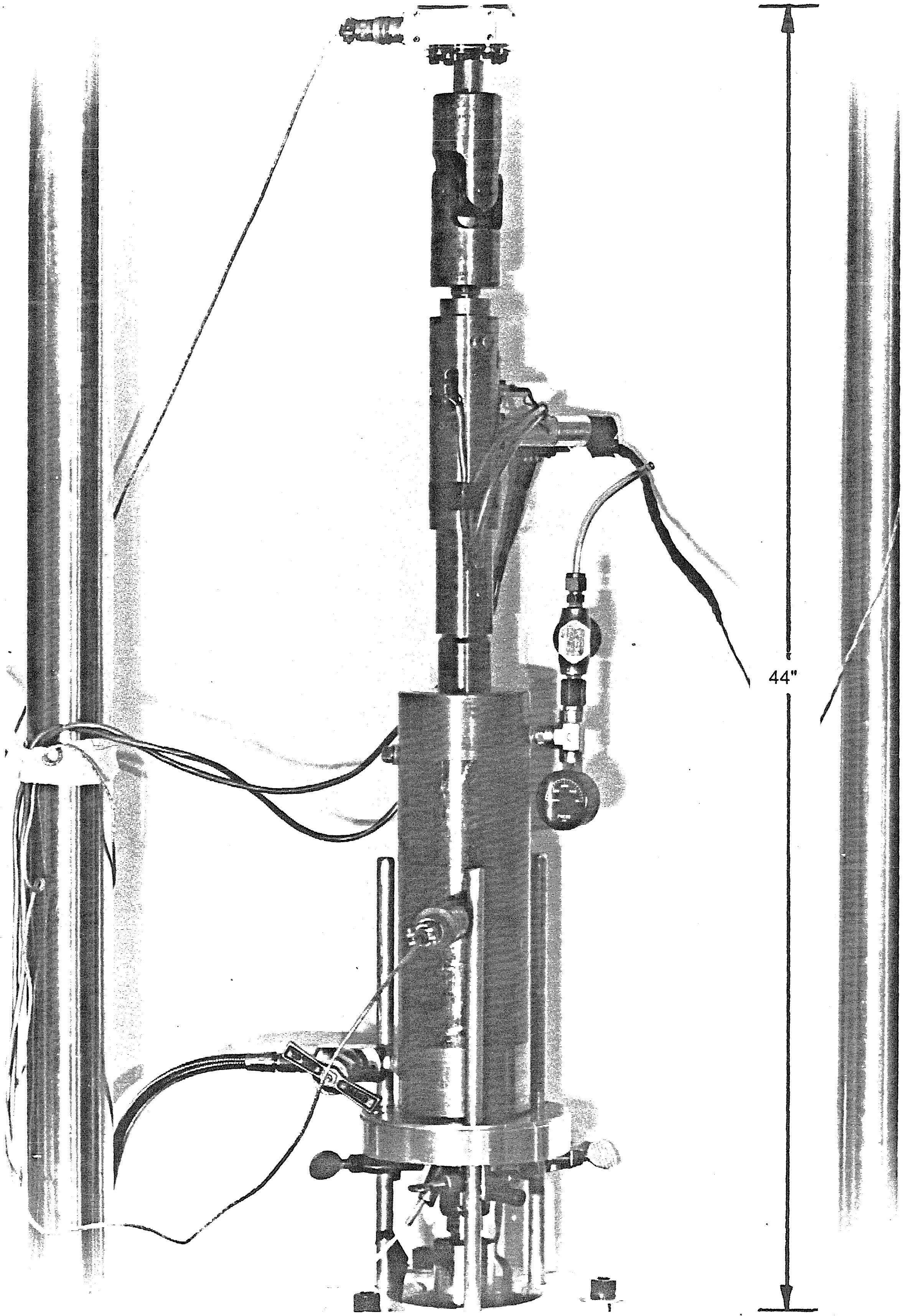

FIG. 2.16 EXPERIMENT IN MTS AXIAL LOAD CONTROLLER.

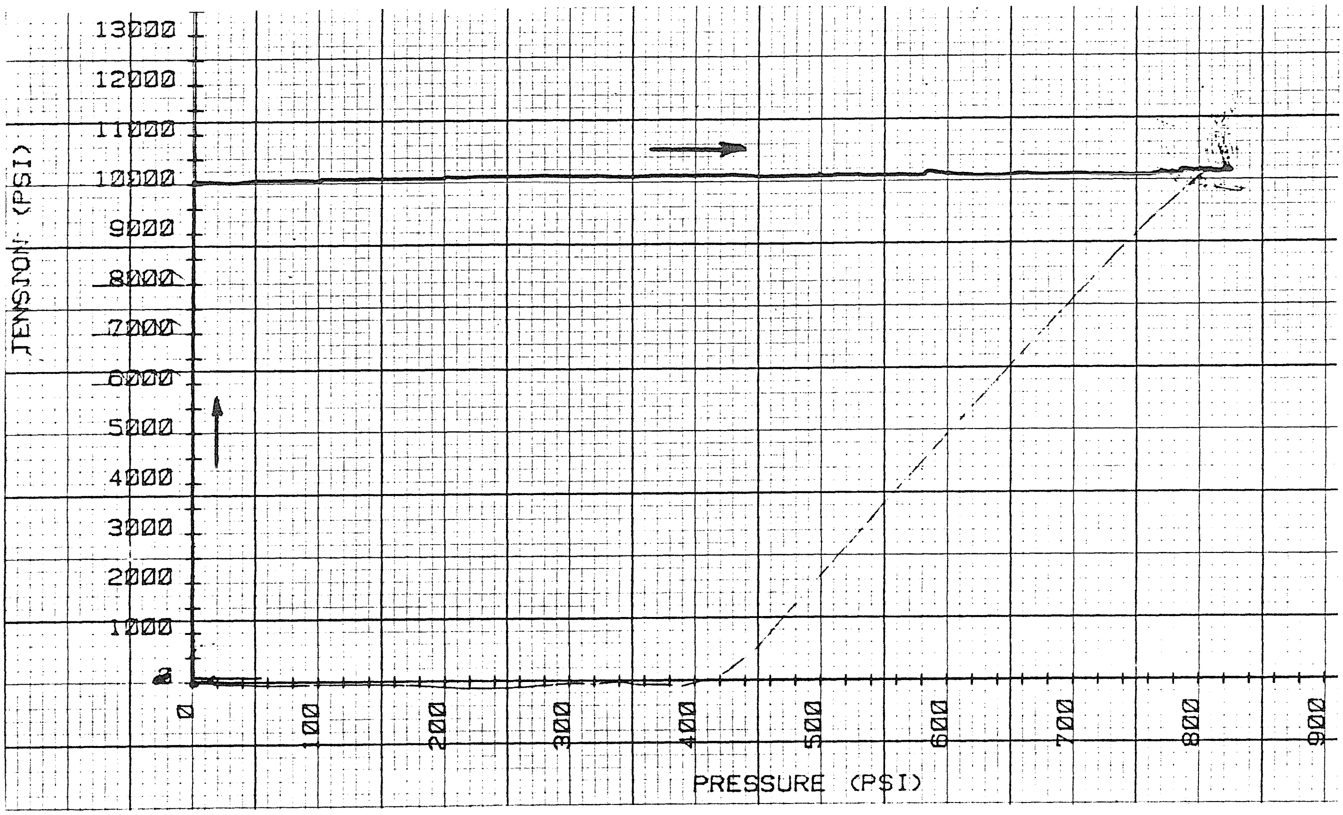

FIG. 2.17 LOAD-PATH TRACE AND S.I.S. OPERATION.

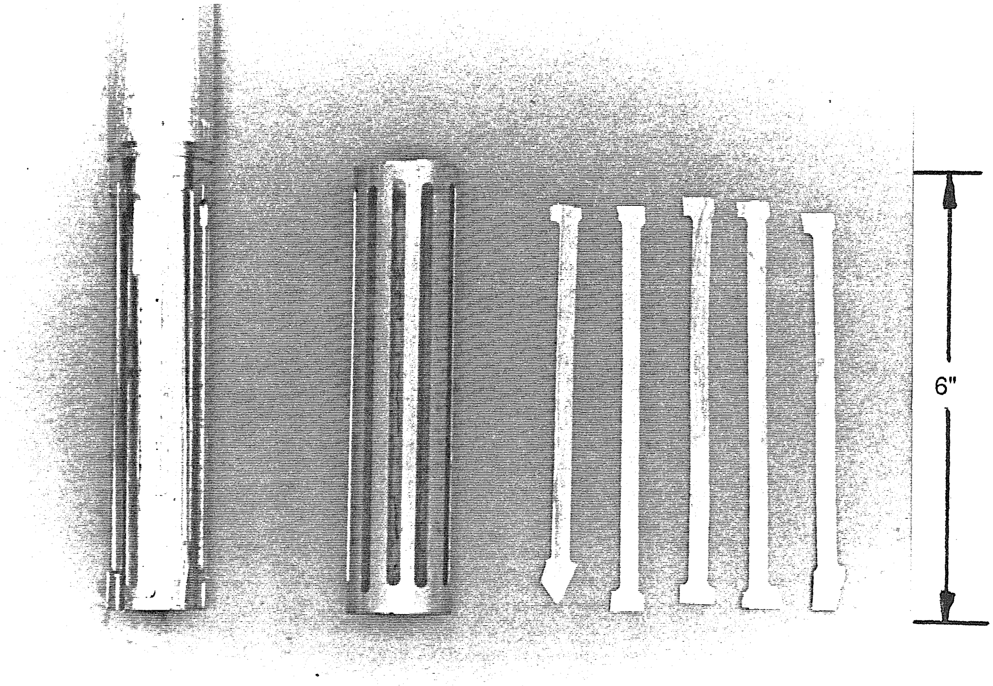

FIG. 2.18 UNIAXIAL TEST SPECIMEN.

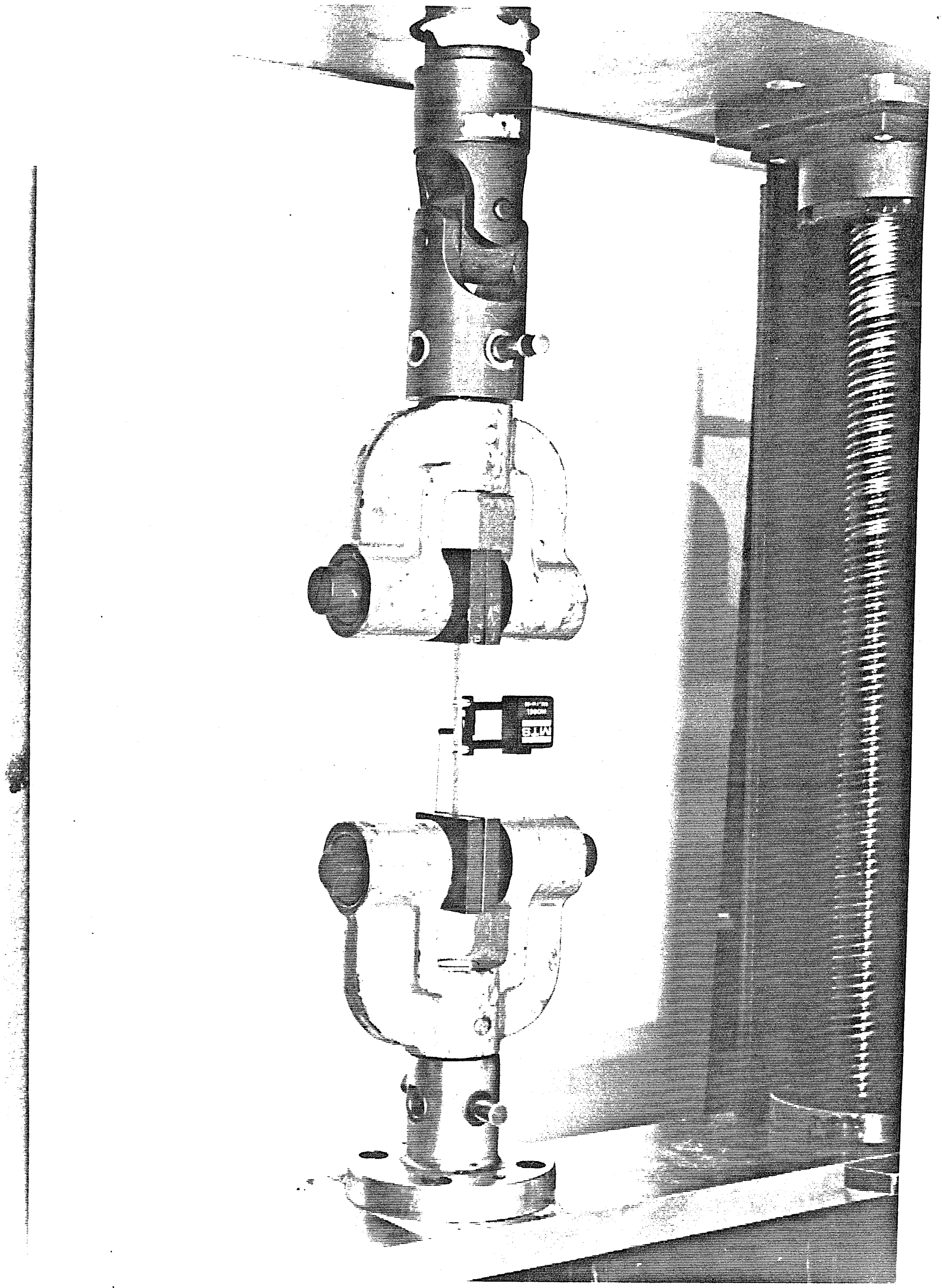

FIG. 2.19 SPECIMEN AND EXTENSOMETER IN INSTRON LOADING MACHINE.

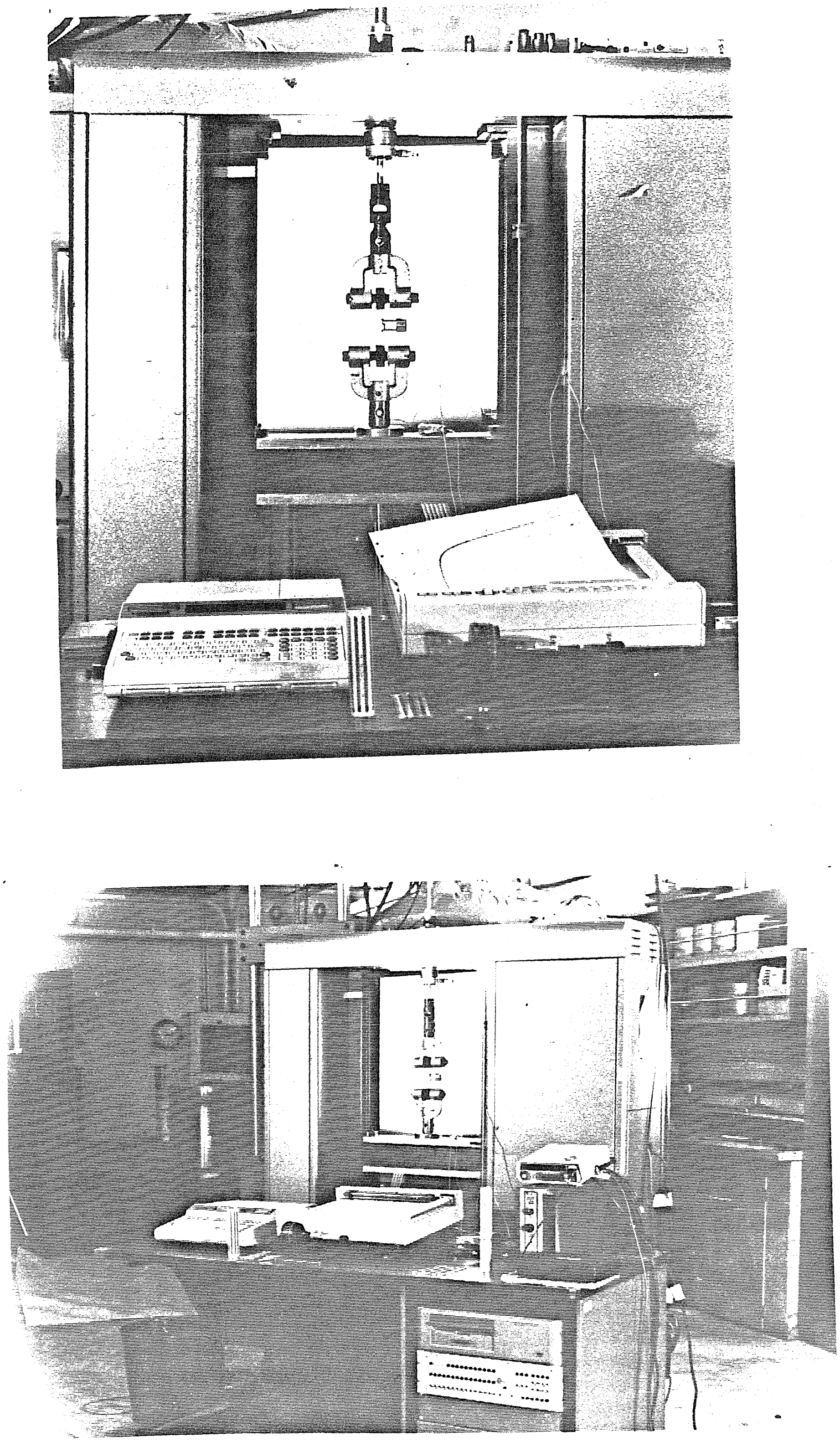

FIG. 2.20 a&b LOAD SYSTEM AND DATA-ACQUISITION.

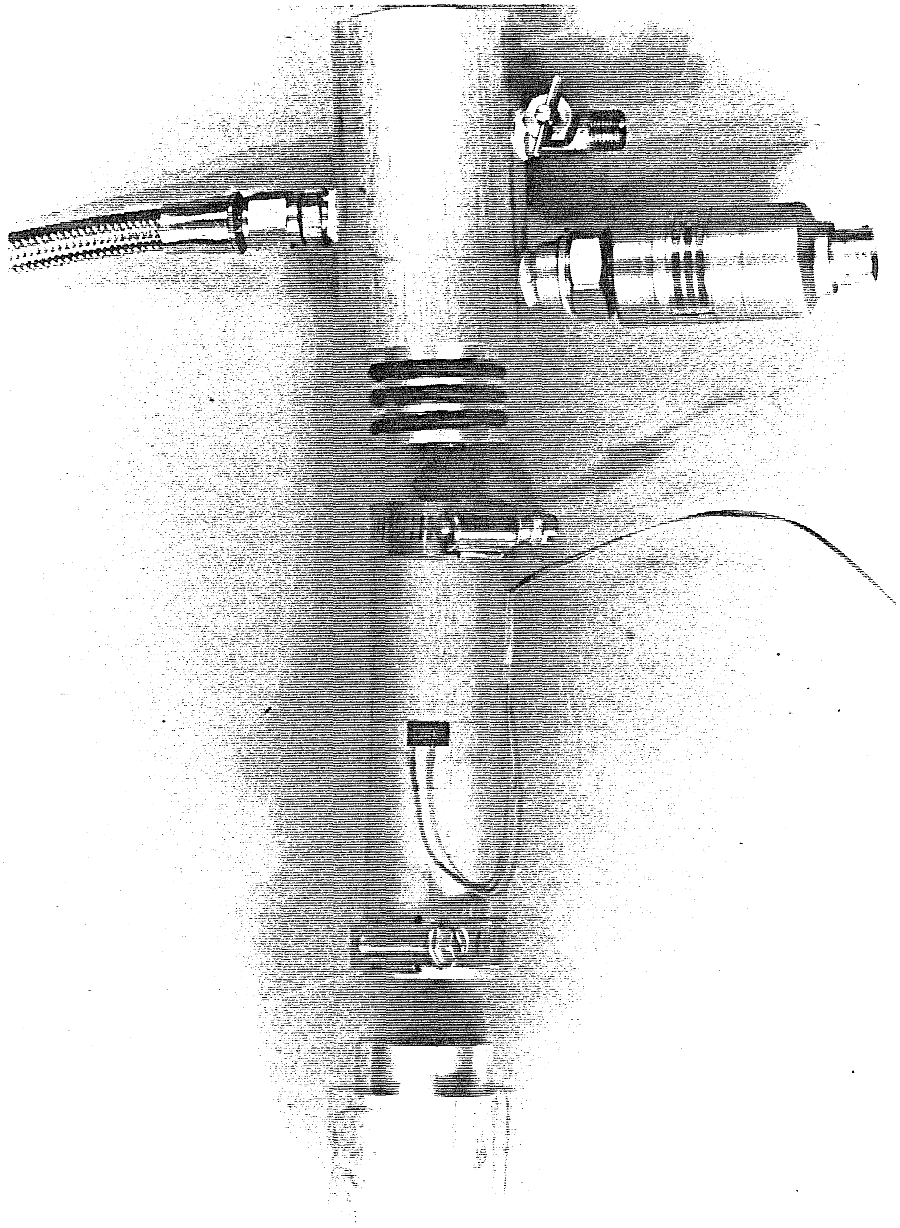

FIG. 2.21 INTERNAL PRESSURE TEST EQUIPMENT.

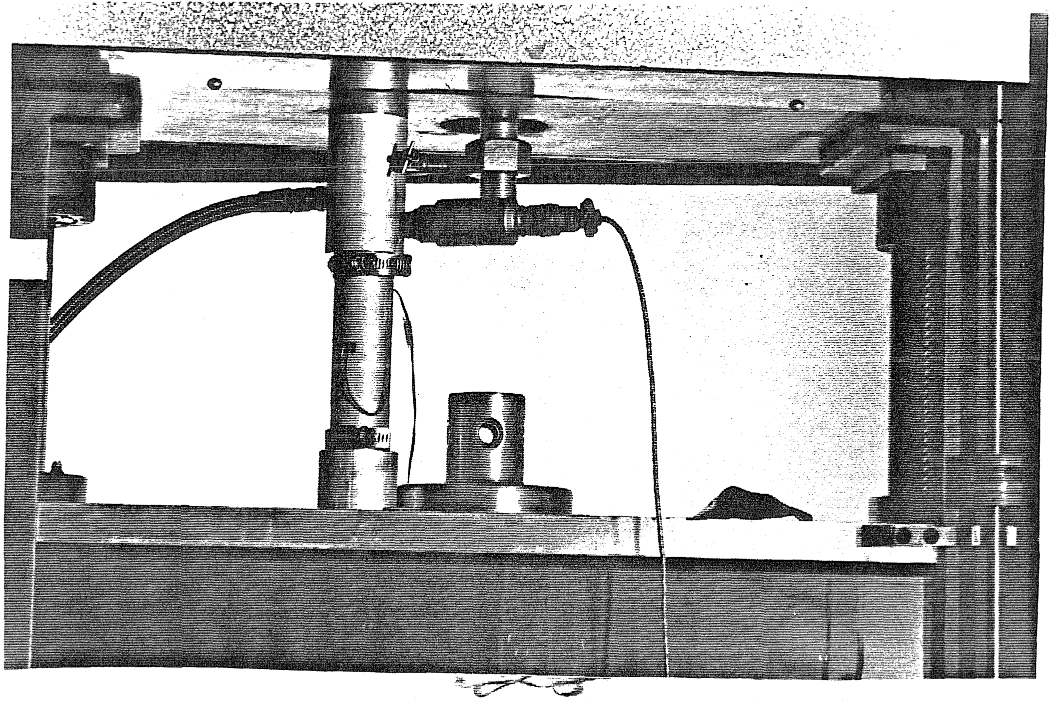

FIG. 2.22 TEST SPECIMEN AND SUPPORT EQUIPMENT.

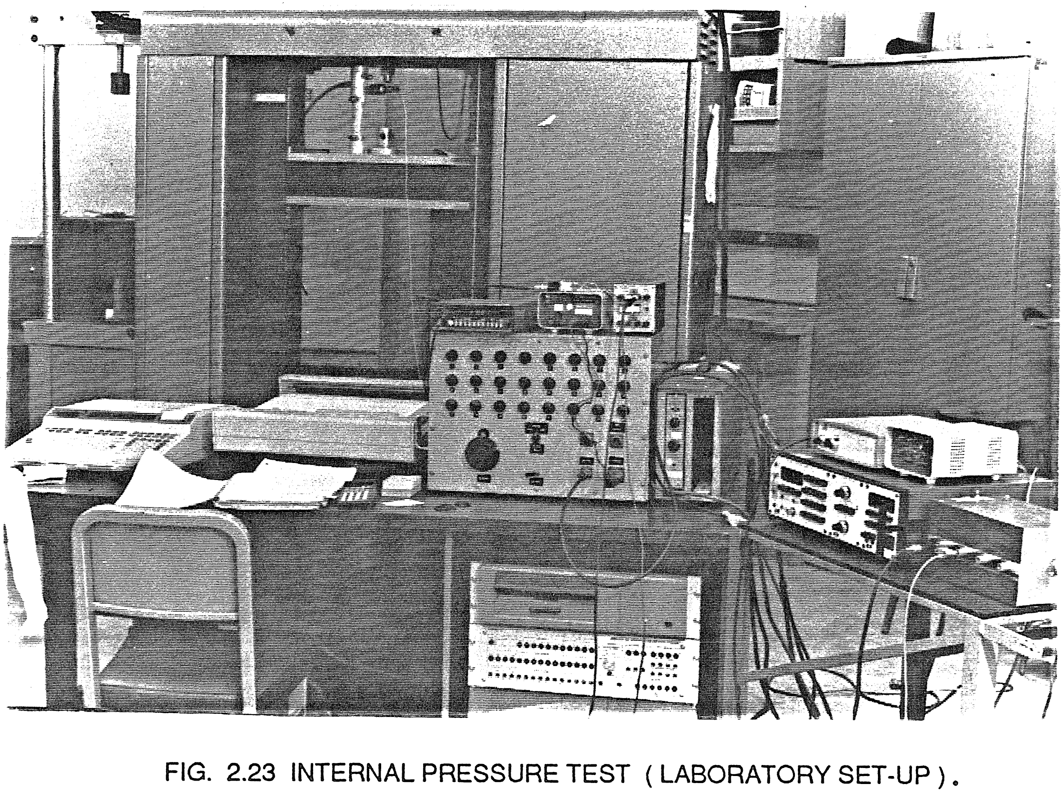

FIG. 2.23 INTERNAL PRESSURE TEST (LABORATORY SET-UP).

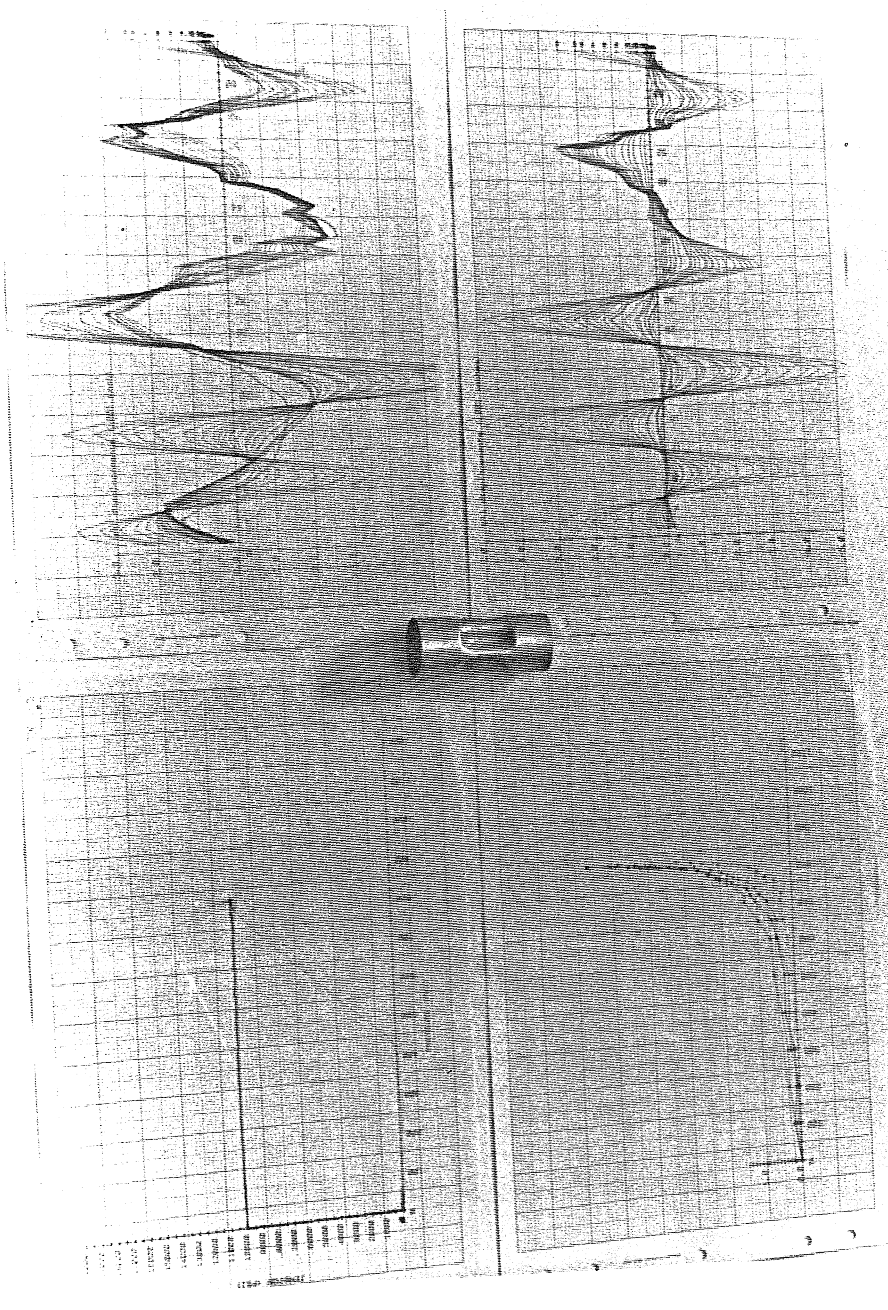

FIG. 2.24 DISPLACEMENT SCANS AND LOAD PATH PLOTS (FROM EXPERIMENT) .

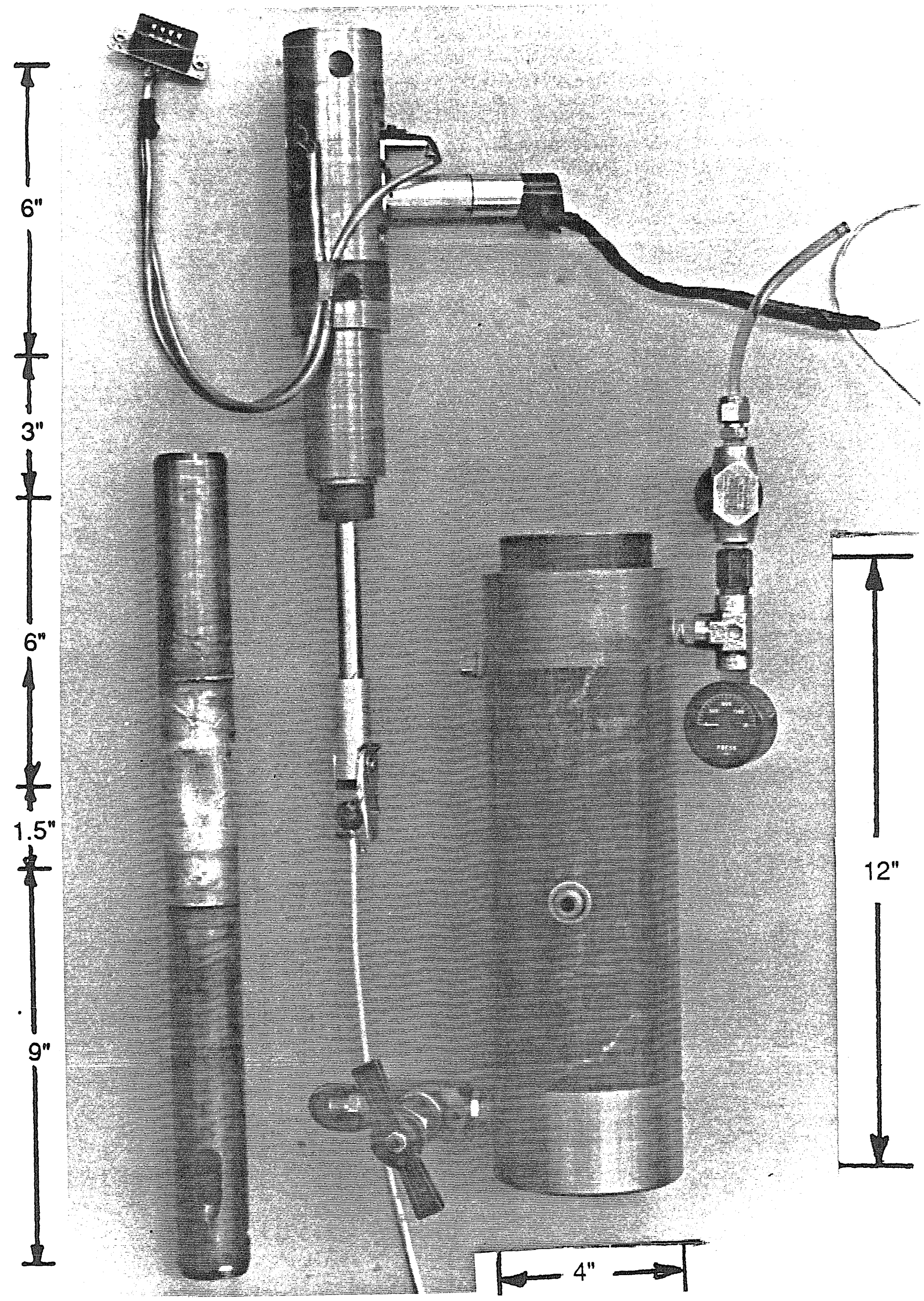

FIG. 2.25 TEST CHAMBER, DSD AND TEST SHELL (NONASSEMBLED).

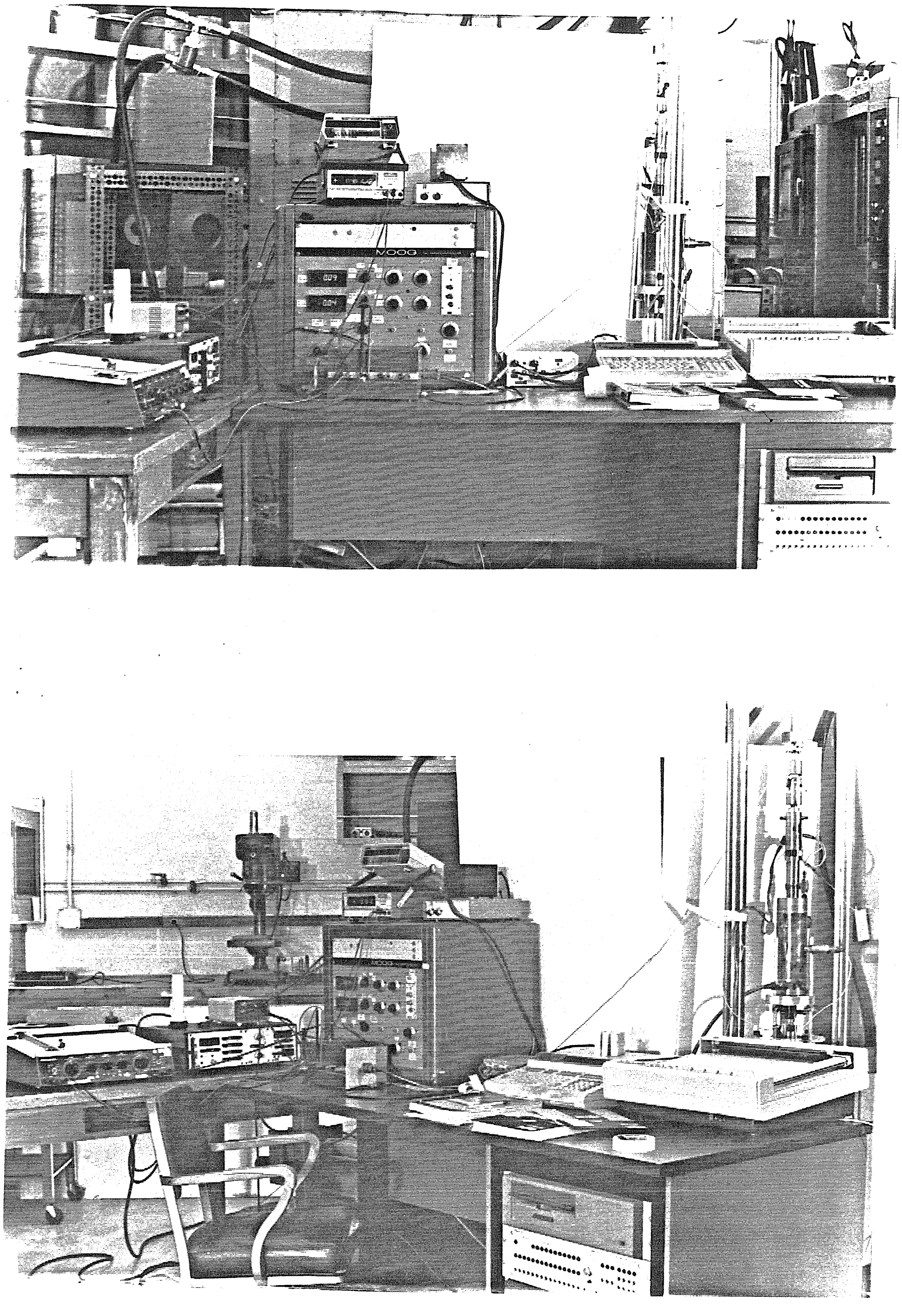

FIG. 2.26 a&b SUPPORT EQUIPMENT AND TEST SET-UP.

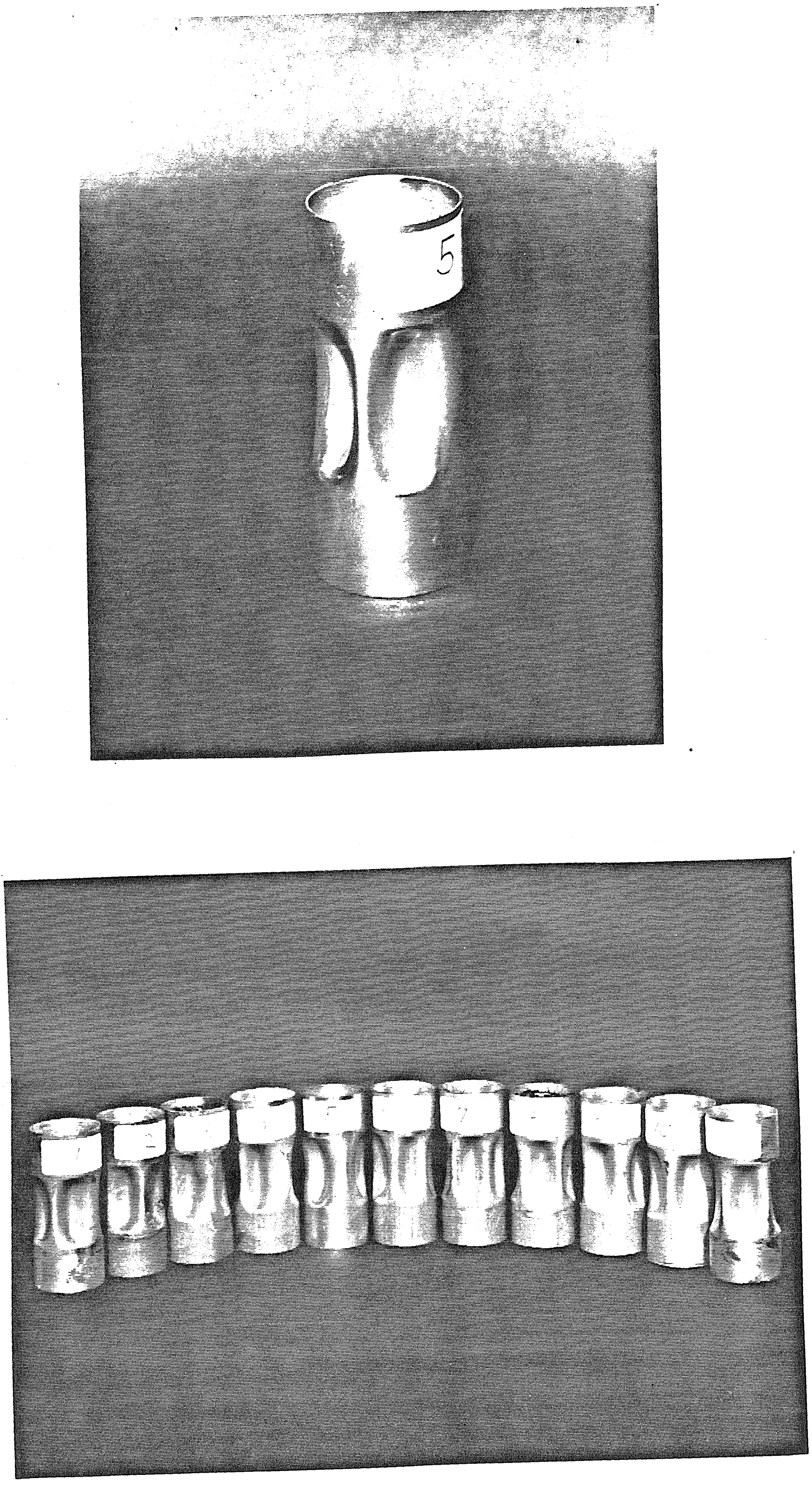

FIG. 2.27 a&b TEST SPECIMENS.

TUBESALES
MATERIAL CERTIFICATE

Specification	WWT-700/6
Size	1-1/2 X .028
Quantity	12' - 0" X 3
Grade	DRAWN 6061-T4
Manufacturer	ALCOA
Lot Number	270347

CHEMICAL ANALYSIS

	MIN	MAX
Si	.40	.80
Fe	---	.70
Cu	.15	.40
Mn	---	.15
Mg	.80	1.2
Cr	.04	.35
Zn	---	.25
Ti	---	.15
Other		.15 (.05 each)
Al Remainder		

MECHANICAL PROPERTIES

	MIN
Ultimate Strength	30,000 psi
Yield Point	16,000 psi
Elongation	16%

TABLE 3.1 MATERIAL PROPERTIES.

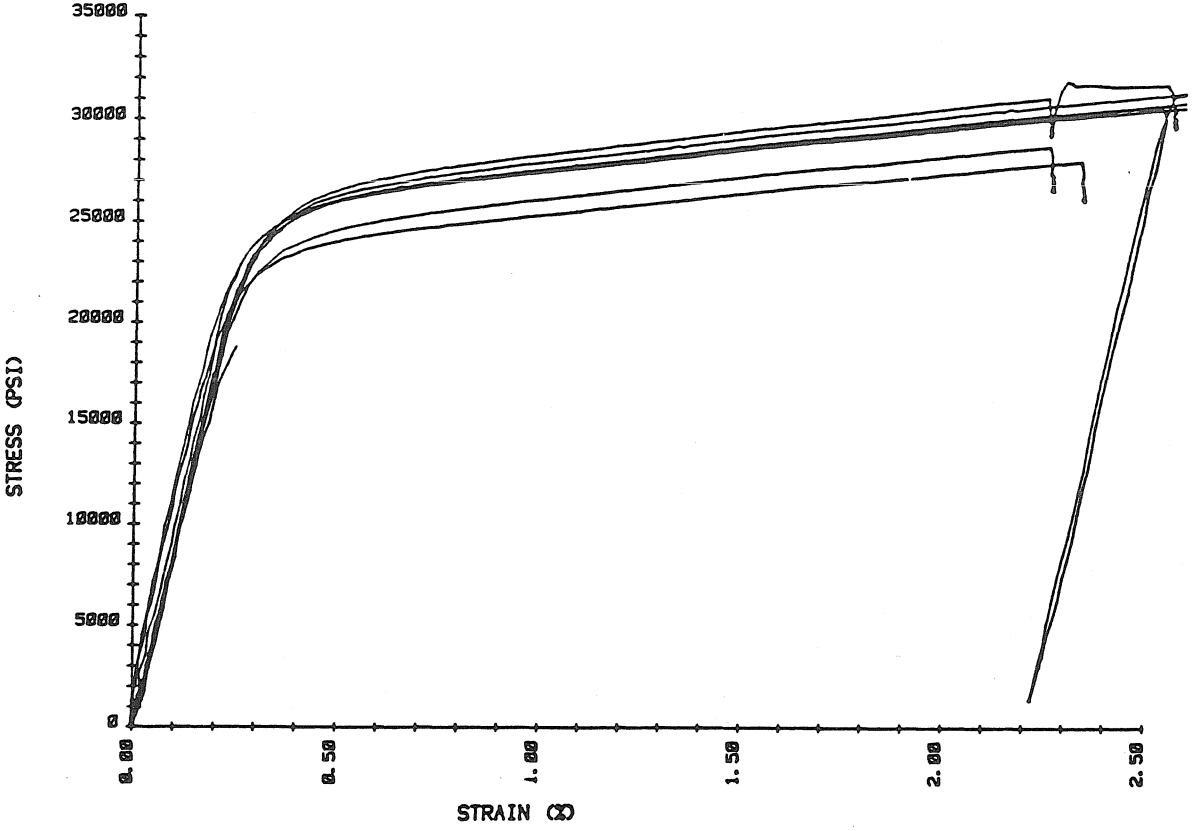

FIG. 3.1 AXIAL STRESS-STRAIN CURVES (SET A).

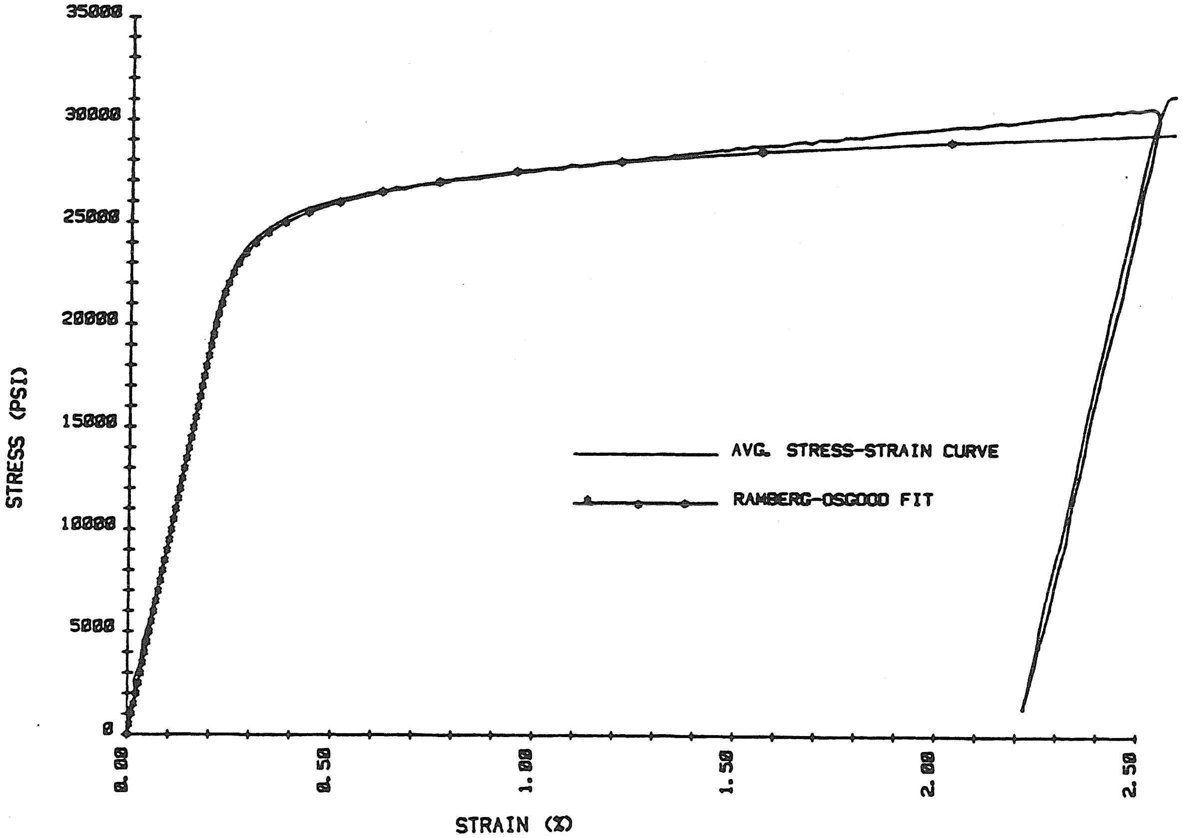

FIG. 3.2 RAMBERG-OSGOOD FIT (SET A, AXIAL).

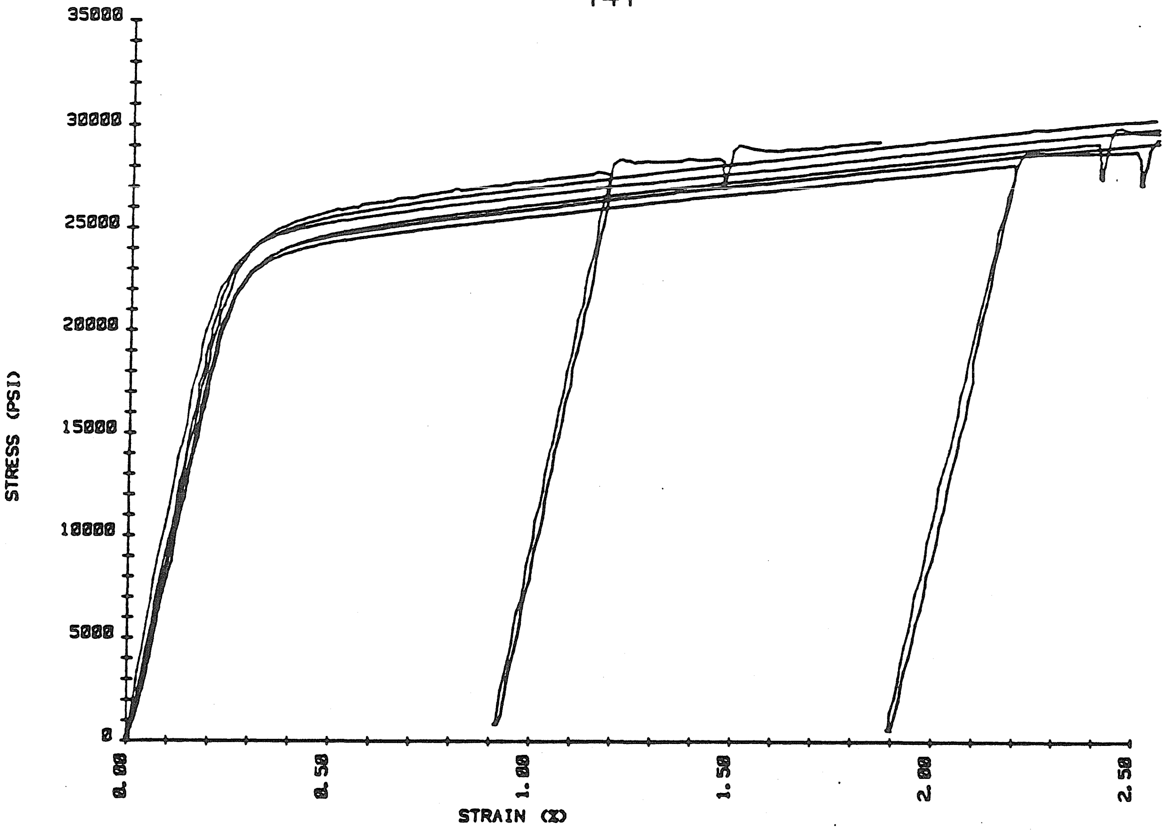

FIG. 3.3 AXIAL STRESS-STRAIN CURVES (SET B) .

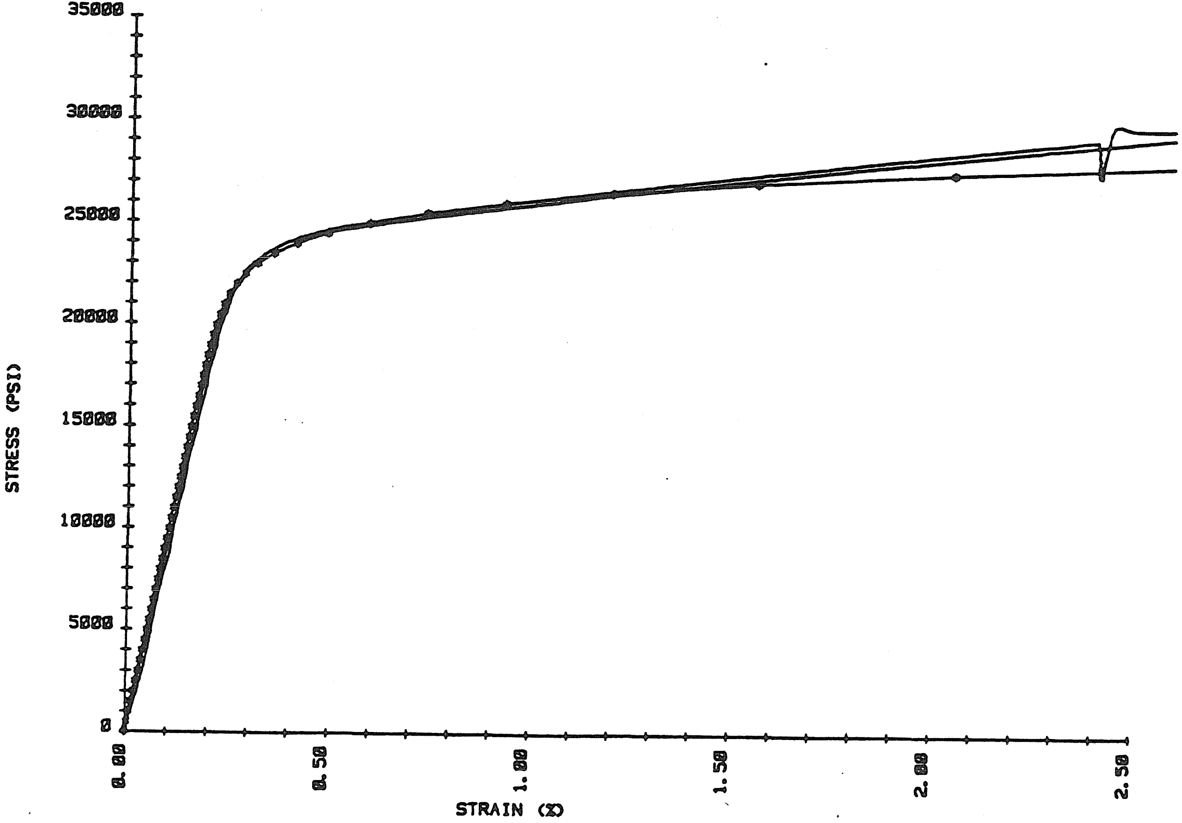

FIG. 3.4 RAMBERG-OSGOOD FIT (SET B, AXIAL) .

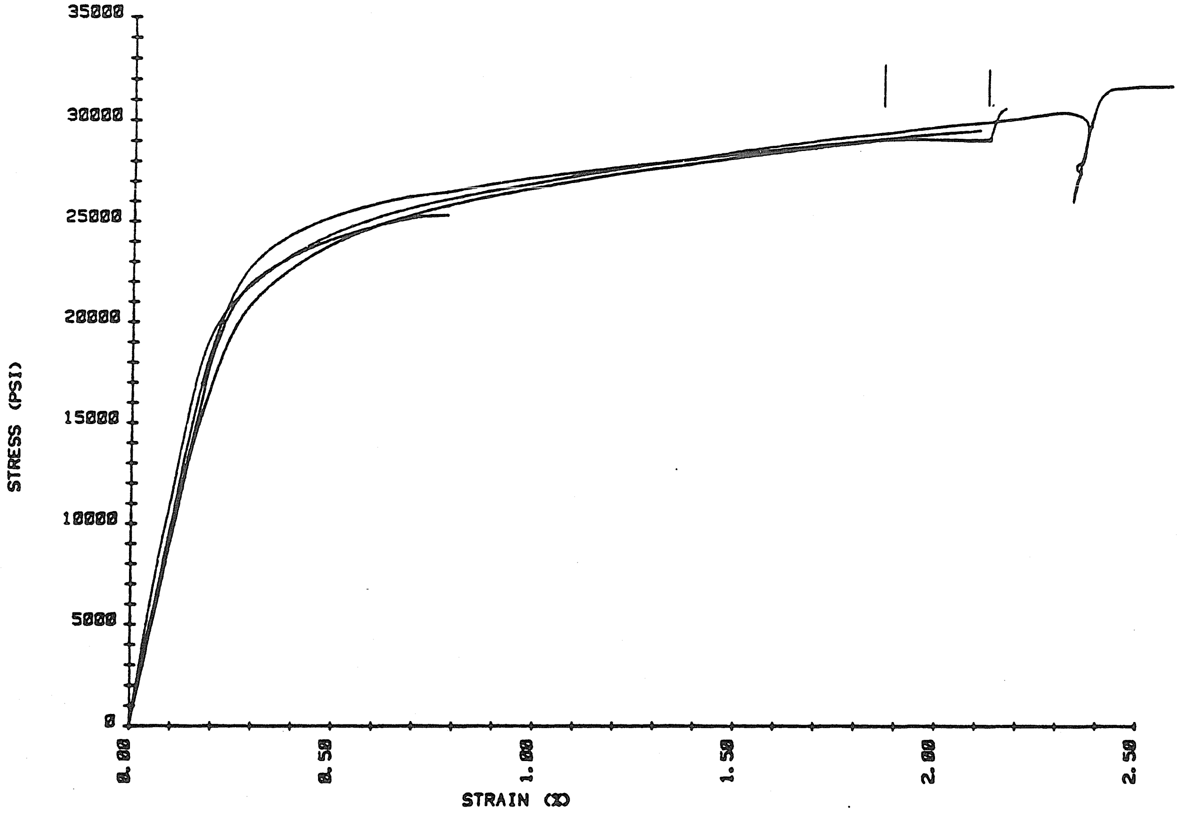

FIG. 3.5 CIRCUMFERENTIAL STRESS-STRAIN PLOT (SET B).

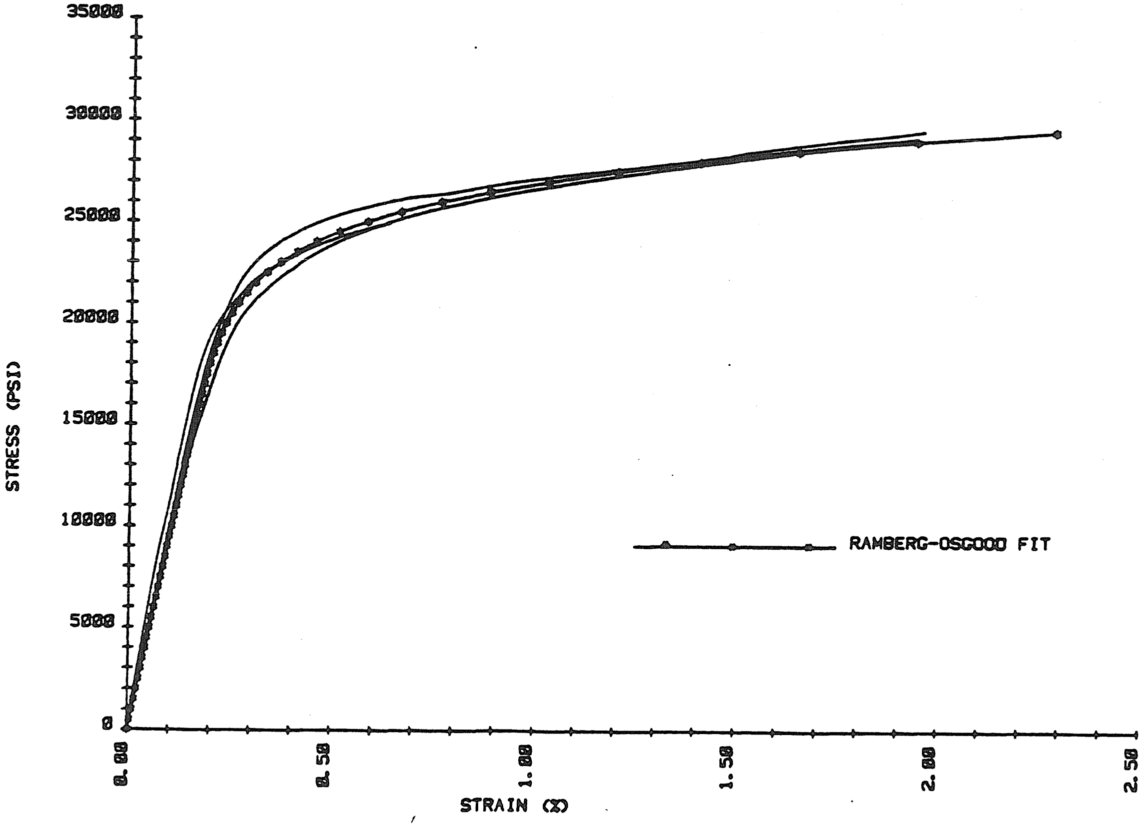

FIG. 3.6 RAMBERG-OSGOOD FIT (SET B, CIRCUMFERENTIAL).

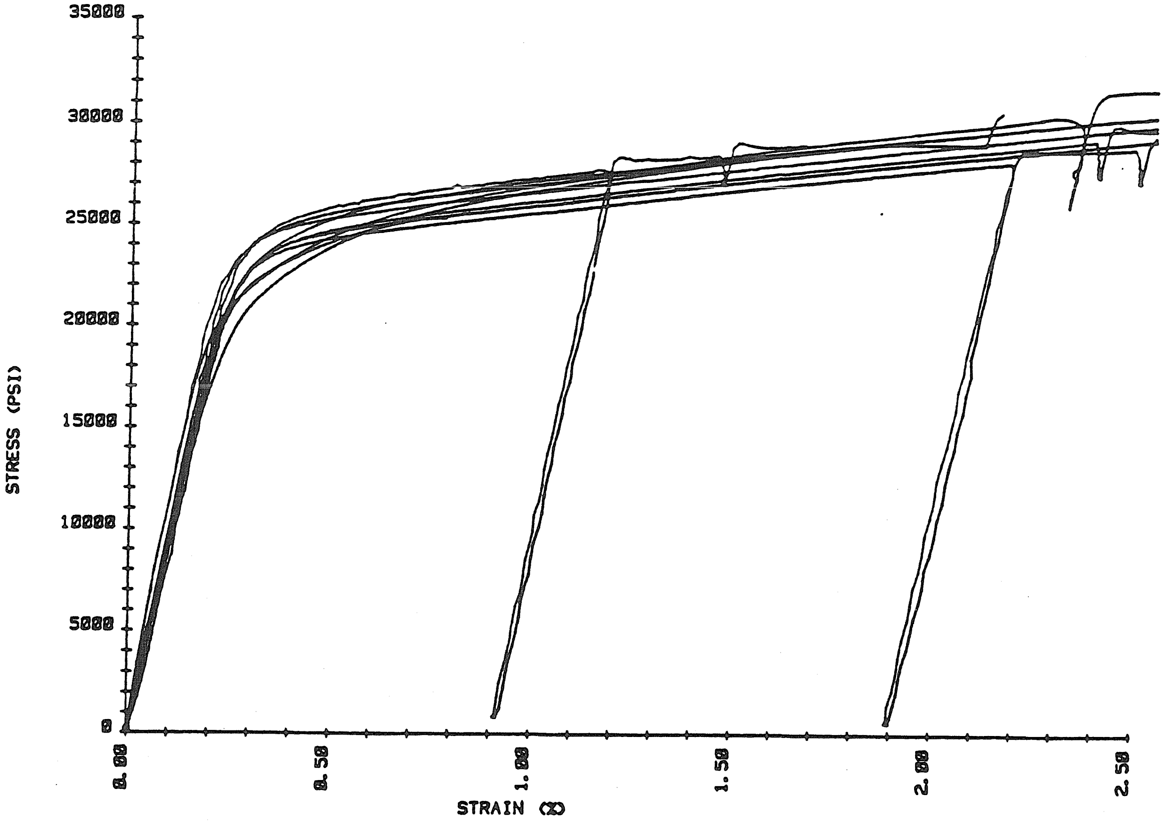

FIG. 3.7 AXIAL AND CIRCUMFERENTIAL MATERIAL BEHAVIOR (SET B).

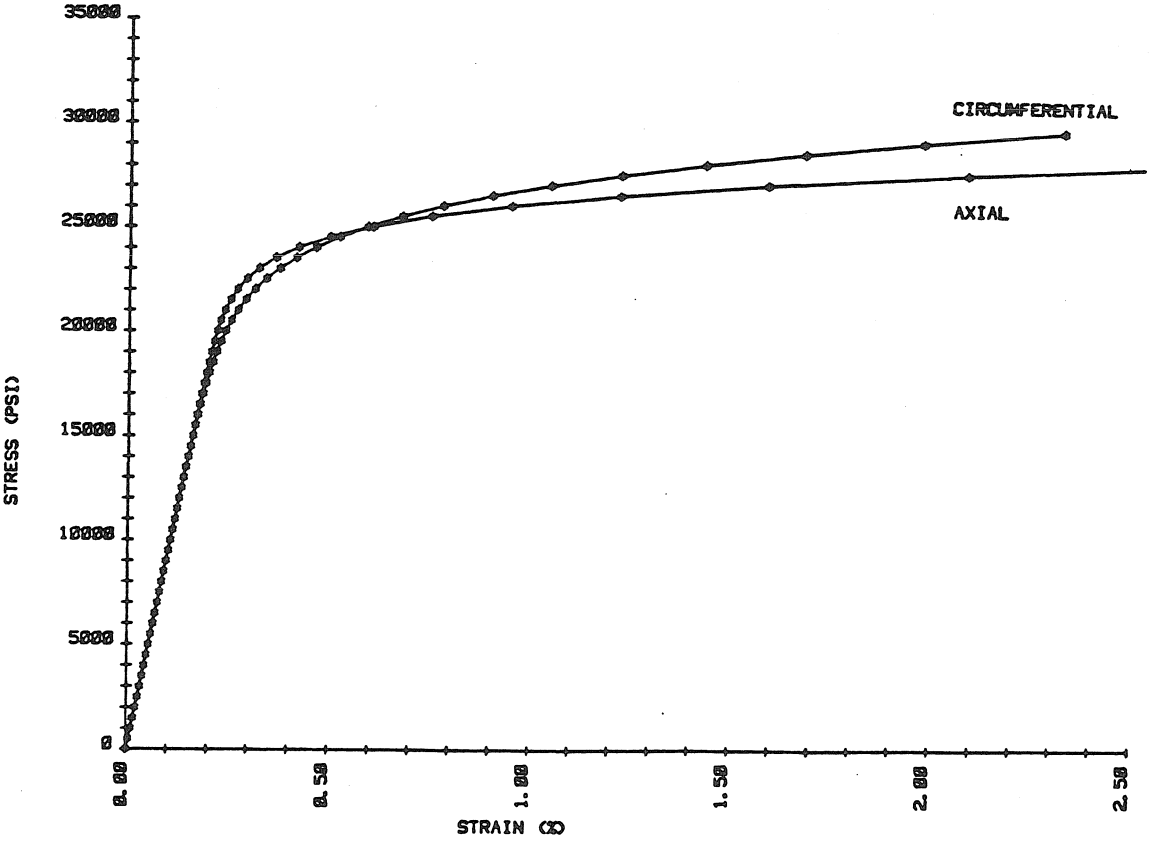

FIG. 3.8 AXIAL AND CIRCUMFERENTIAL RAMBERG-OSGOOD PLOTS.

	Specimen 1		Specimen 2	
L(in)	P_{cr} (Psi)	n	P_{cr} (Psi)	n
1.0	940	5	960	5
1.5	820	4	800	4
2.0	670	4	720	4
2.5	660	4	630	3
3.0	530	3	590	3
4.0	360	3	520	3
4.5	300	3	400	3
5.0	370	2	380	2
5.5	300	2	330	2
6.0	330	2	270	2

L = LENGTH OF TEST SHELL
n= NUMBER OF CIRCUMFERENTIAL WAVES
* ALL PRESSURES IN LBS/INCH^2
SHELL THICKNESS = 0.028"

TABLE 3.2 EARLY EXTERNAL PRESSURE TEST.

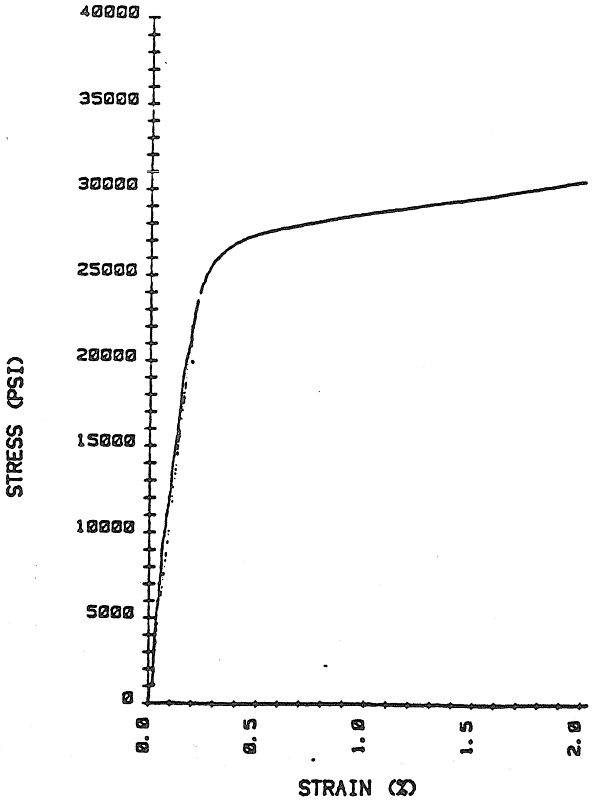

FIG. 3.9 TYPICAL STRESS-STRAIN CURVE, AL 6061-T4.

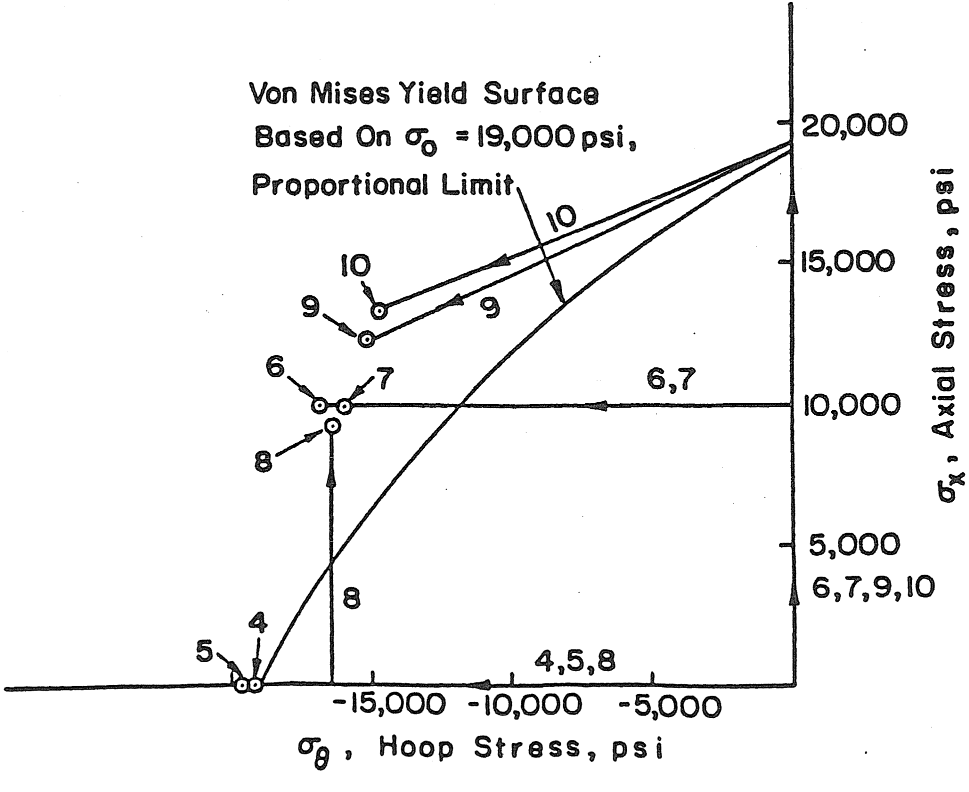

FIG. 3.10 LOAD-PATHS FOR INITIAL BIAXIAL TESTS.

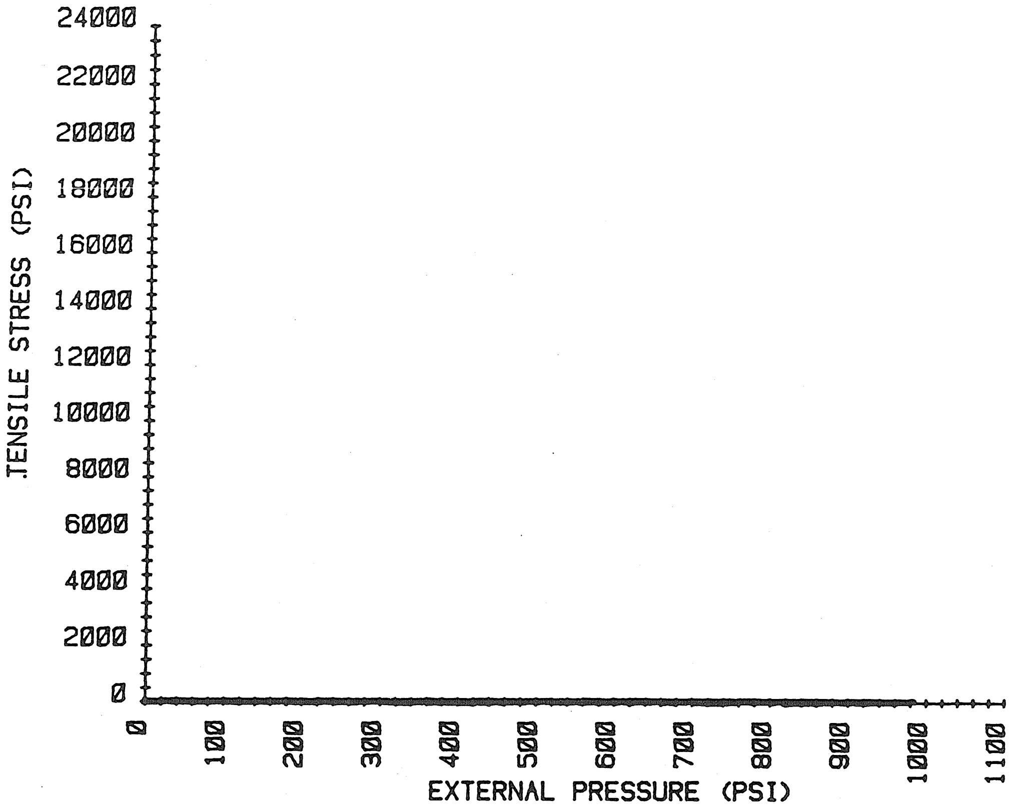

FIG. 3.11a LOAD-PATH DIAGRAM.

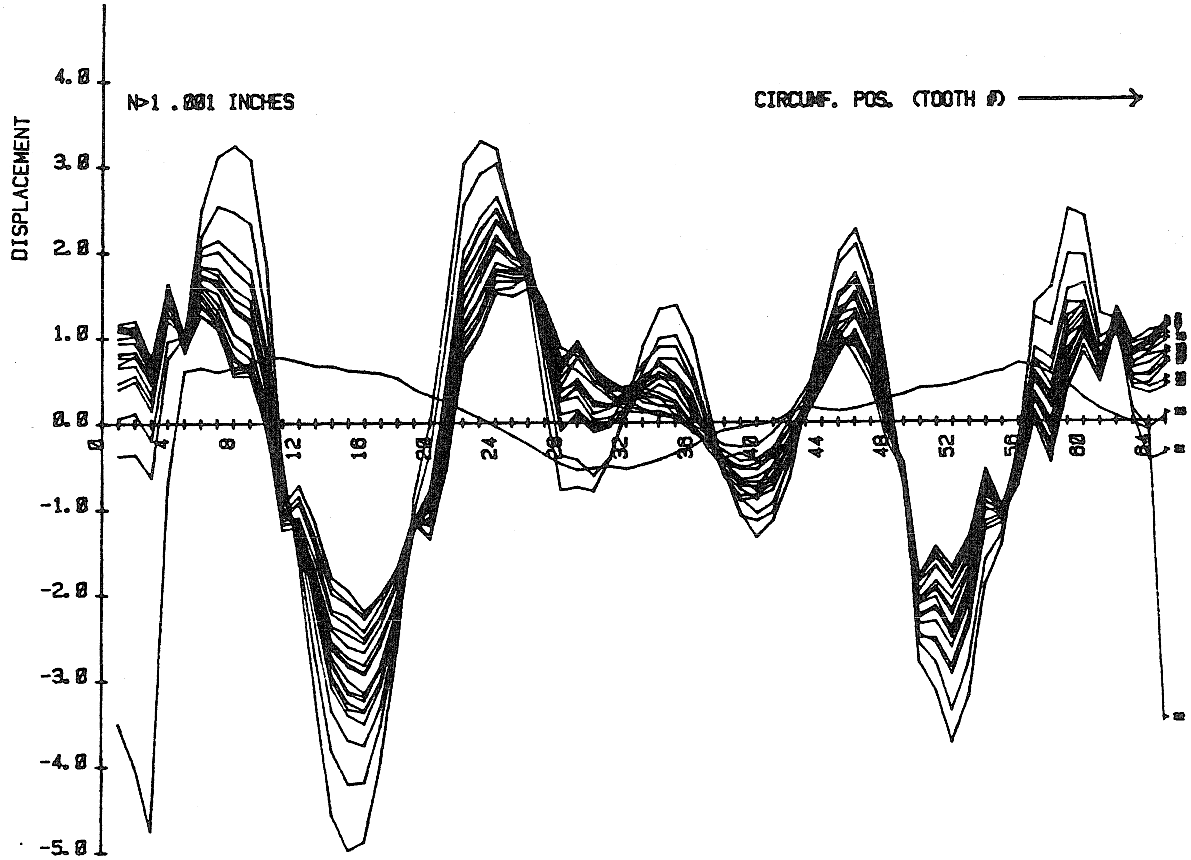

FIG. 3.11b RADIAL DISPLACEMENT SCANS (TENSILE STRESS= 0 PSI).

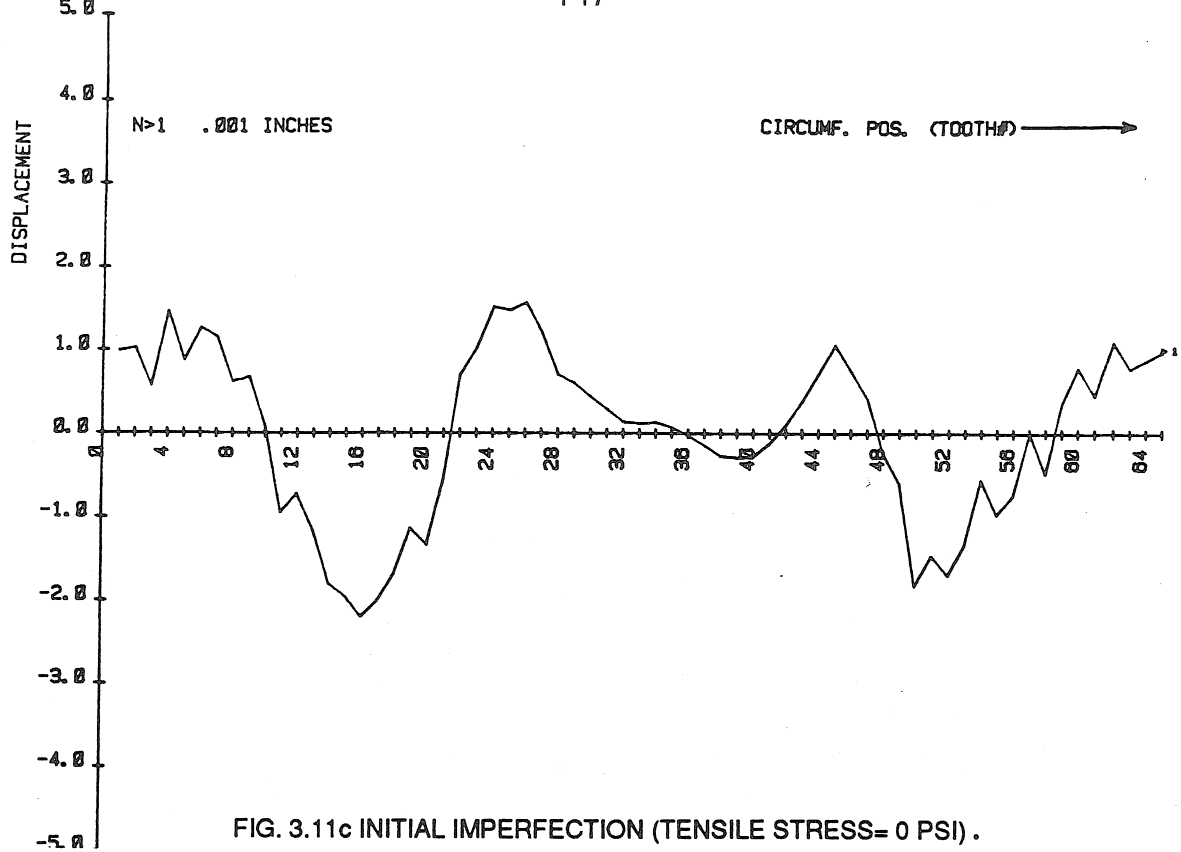

FIG. 3.11c INITIAL IMPERFECTION (TENSILE STRESS= 0 PSI) .

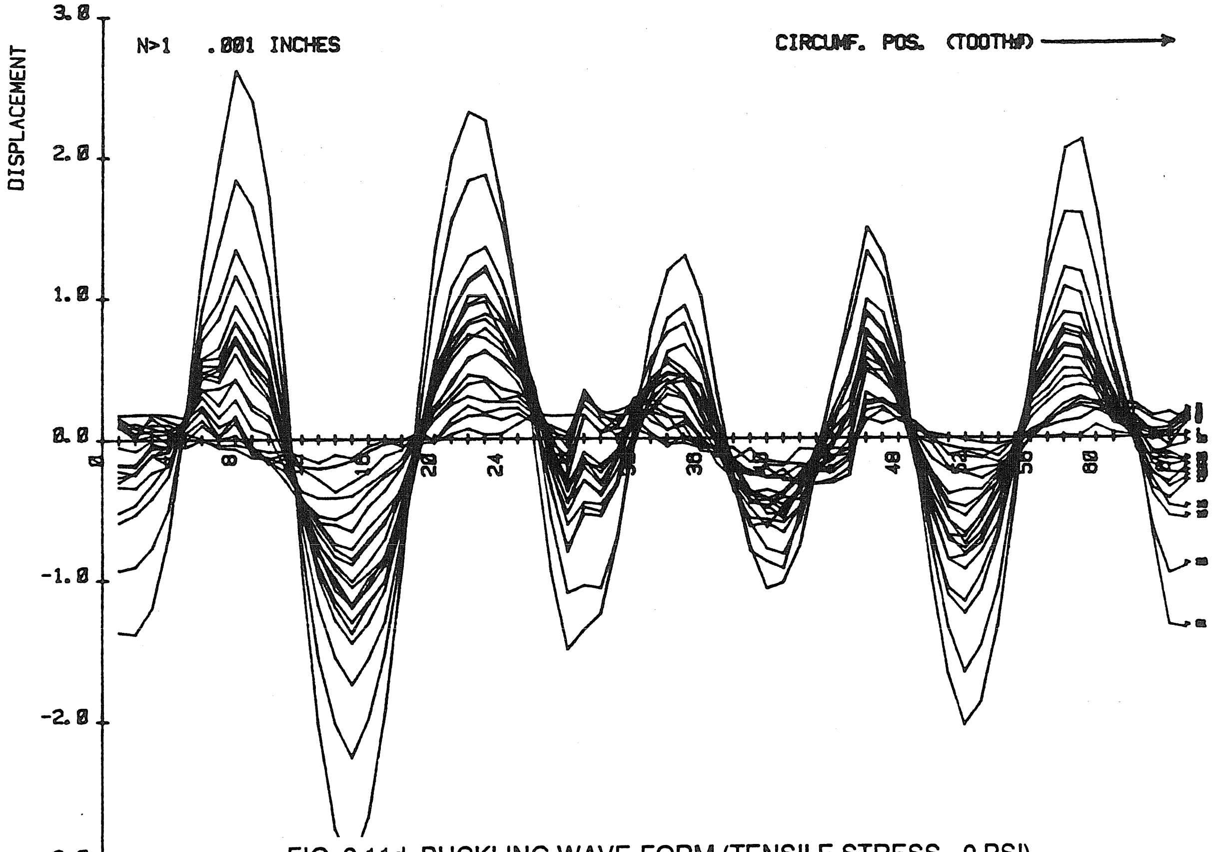

FIG. 3.11d BUCKLING WAVE FORM (TENSILE STRESS= 0 PSI) .

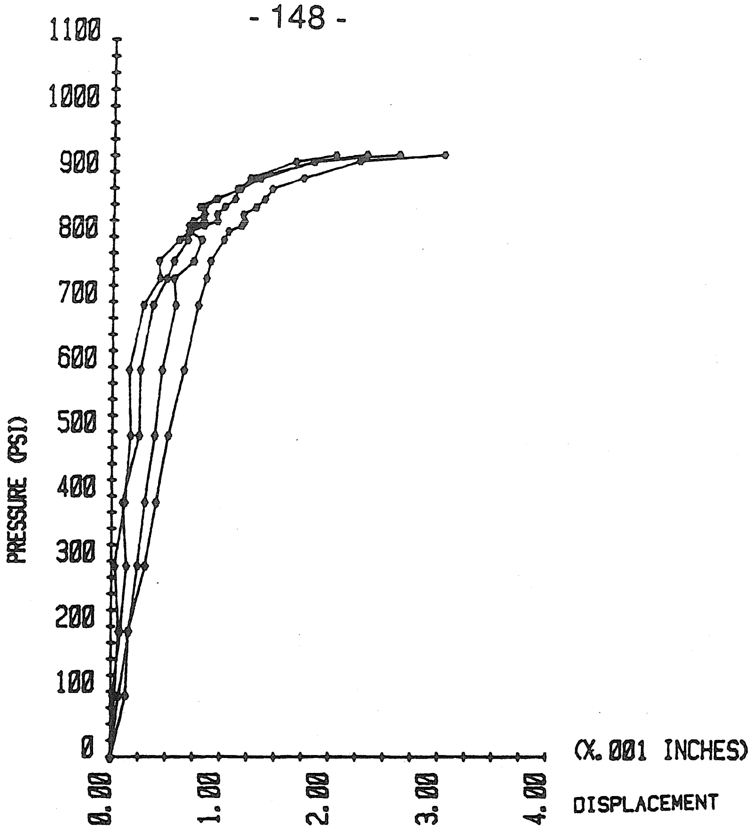

FIG. 3.11e LOAD-DISPLACEMENT (NORMALIZED) PLOT (T.S.= 0 PSI).

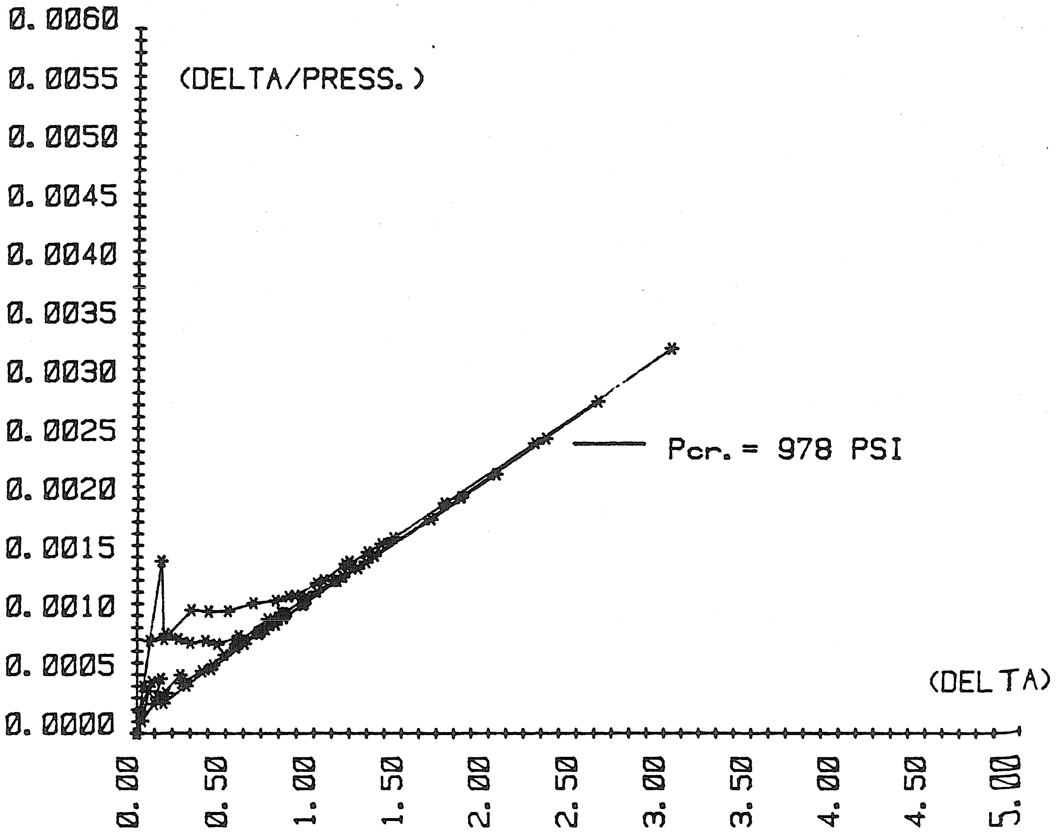

FIG. 3.11f SOUTHWELL PLOT (T.S.= 0 PSI).

	FOURIER COEFFICIENTS (n=0 & n=1)			EXT.	TENSILE
SCAN #	A_0	A_1	B_1	PRESS.(Psi)	STRESS(Psi)
1	25.6	2.4	-11.4	0	0
2	25.3	2.4	-11.5	100	0
3	25.1	2.3	-11.3	200	0
4	25.0	2.3	-11.1	300	0
5	24.8	2.3	-11.1	397	0
6	24.7	2.3	-11.0	500	0
7	24.5	2.3	-10.9	601	0
8	24.3	2.3	-10.8	701	0
9	24.2	2.3	-10.8	742	0
10	24.1	2.3	-10.8	769	0
11	24.0	2.3	-10.8	802	0
12	24.0	2.3	-10.8	815	0
13	23.9	2.3	-10.8	823	0
14	23.9	2.3	-10.8	830	0
15	23.9	2.3	-10.7	841	0
16	23.9	2.3	-10.8	852	0
17	23.8	2.3	-10.8	857	0
18	23.8	2.3	-10.7	880	0
19	23.7	2.3	-10.8	897	0
20	23.5	2.4	-10.7	922	0
21	23.4	2.4	-10.6	931	0
22	23.4	2.4	-10.6	932	0

IMPERFECTION SCAN = $D(\theta)$ (0.001")

$$D(\theta) = A_0 + A_n \cos(n\theta) + B_n \sin(n\theta)$$

TABLE 3.3 SCAN DATA FOR CONSTANT TENSILE STRESS = 0 PSI ("SET A").

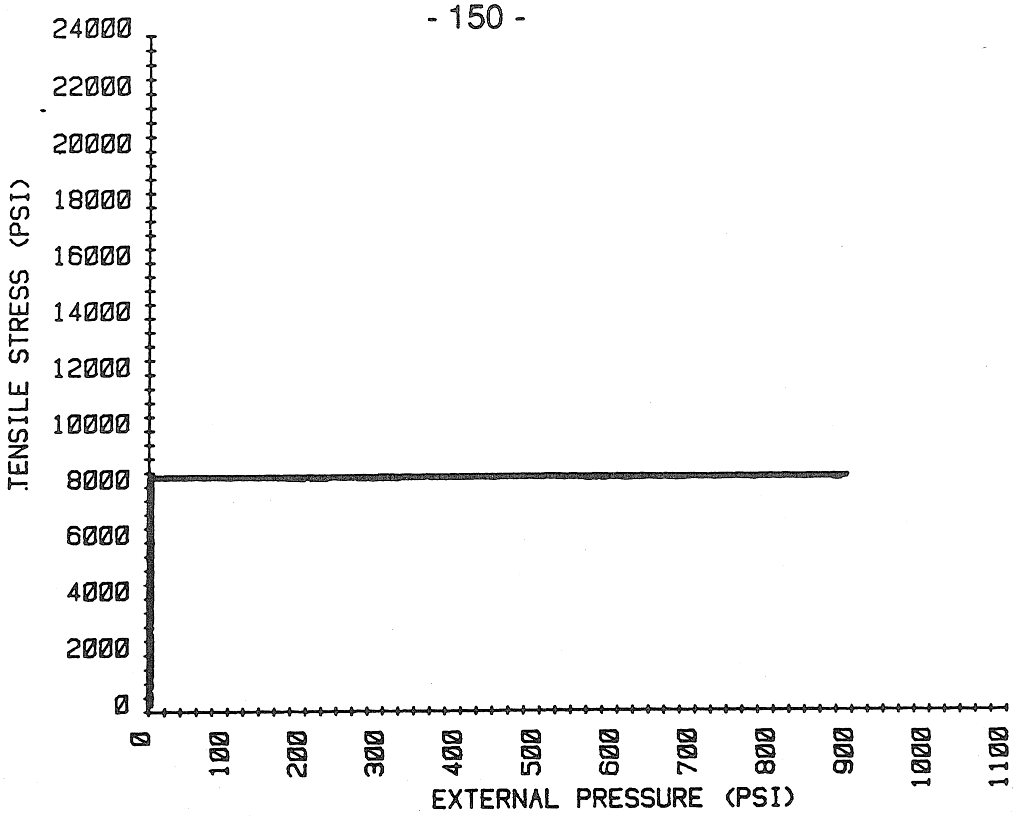

FIG. 3.12a LOAD-PATH DIAGRAM.

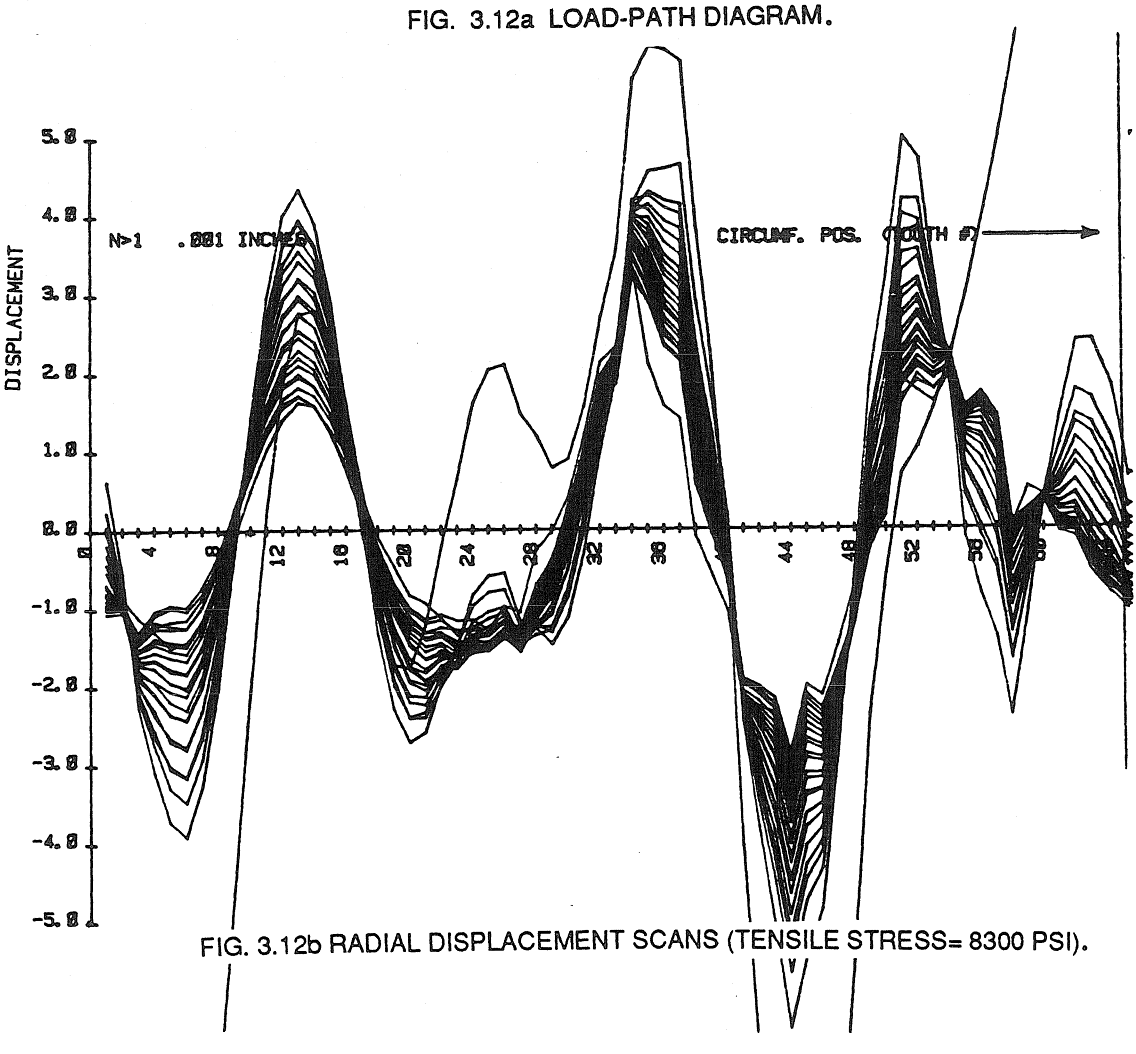

FIG. 3.12b RADIAL DISPLACEMENT SCANS (TENSILE STRESS= 8300 PSI).

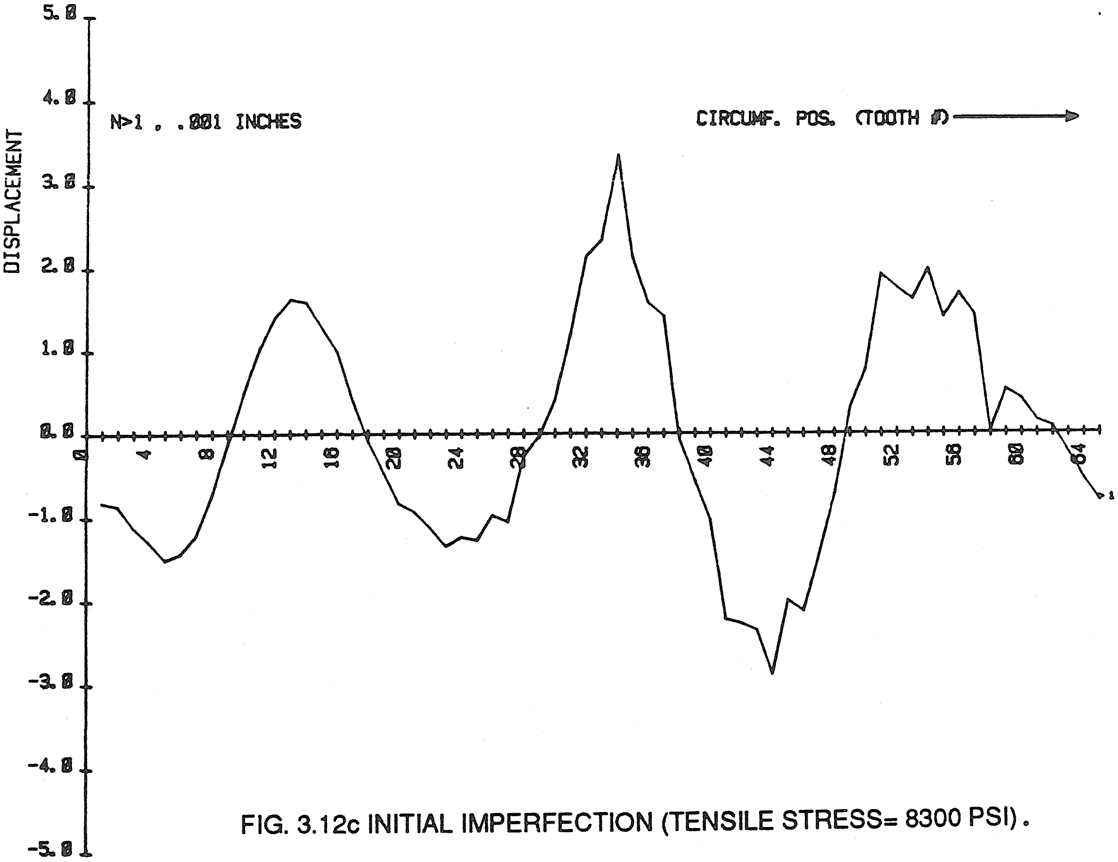

FIG. 3.12c INITIAL IMPERFECTION (TENSILE STRESS= 8300 PSI).

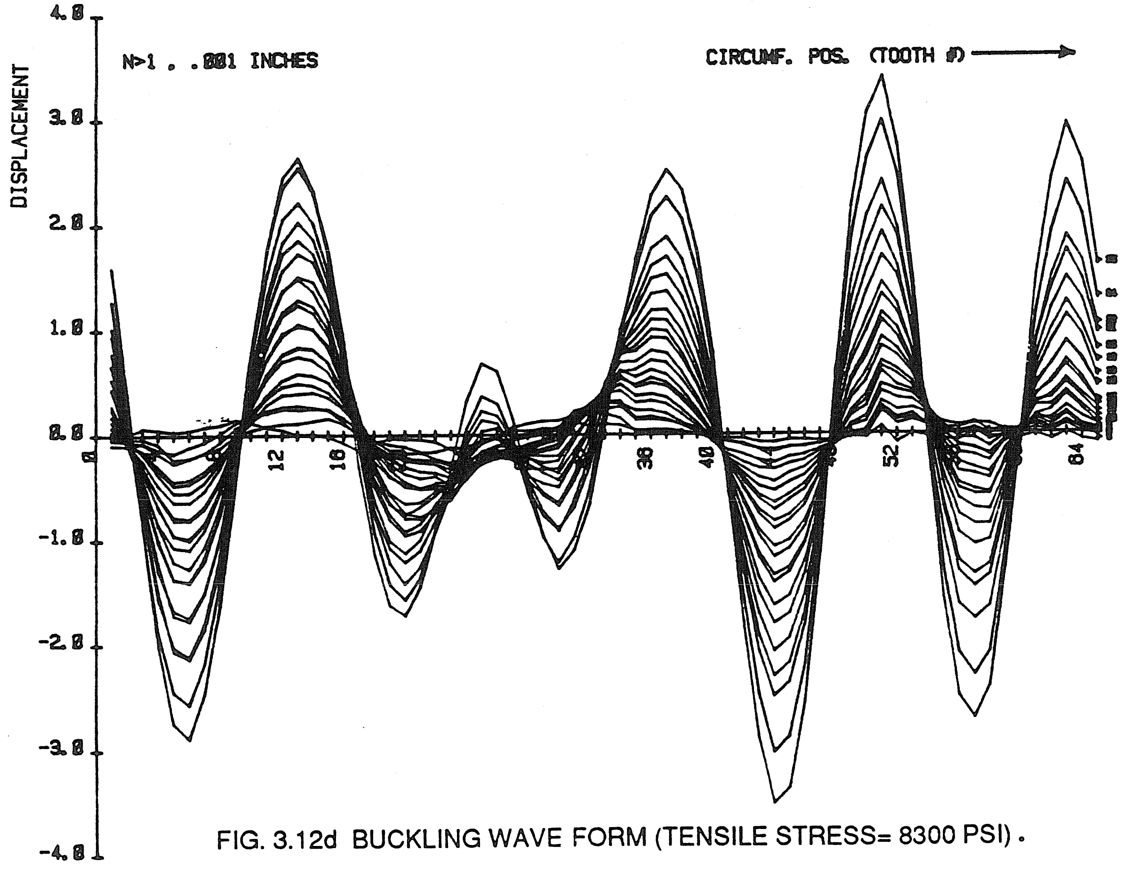

FIG. 3.12d BUCKLING WAVE FORM (TENSILE STRESS= 8300 PSI).

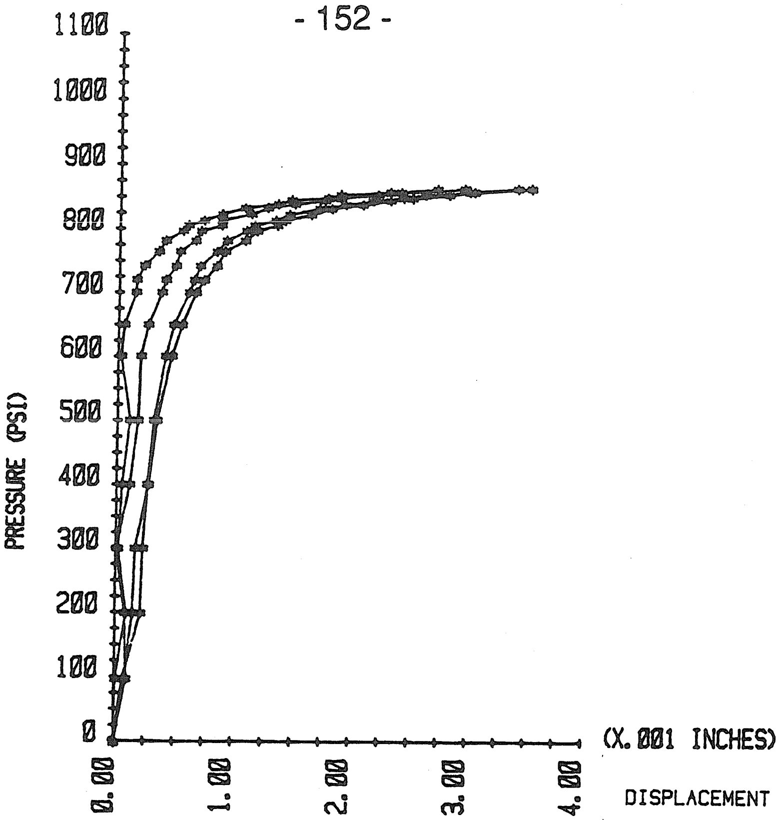

FIG. 3.12e LOAD-DISPLACEMENT (NORMALIZED) PLOT (T.S.= 8300 PSI).

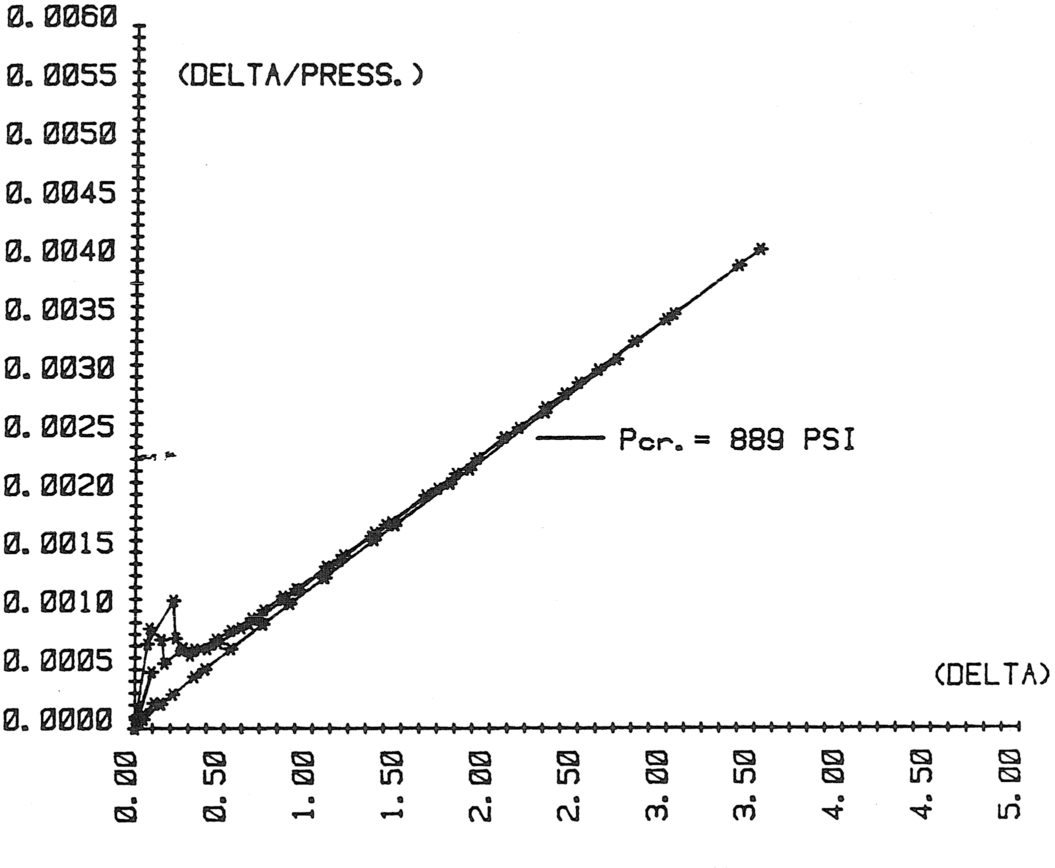

FIG. 3.12f SOUTHWELL PLOT (T.S.= 8300 PSI).

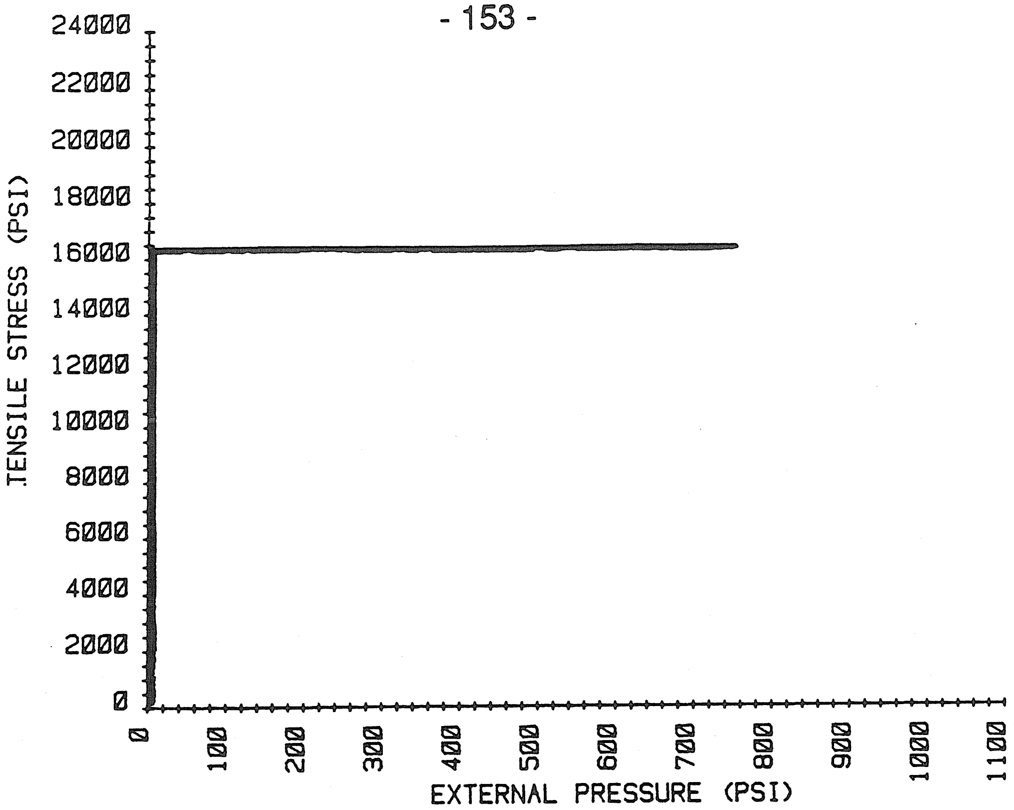

FIG. 3.13a LOAD-PATH DIAGRAM.

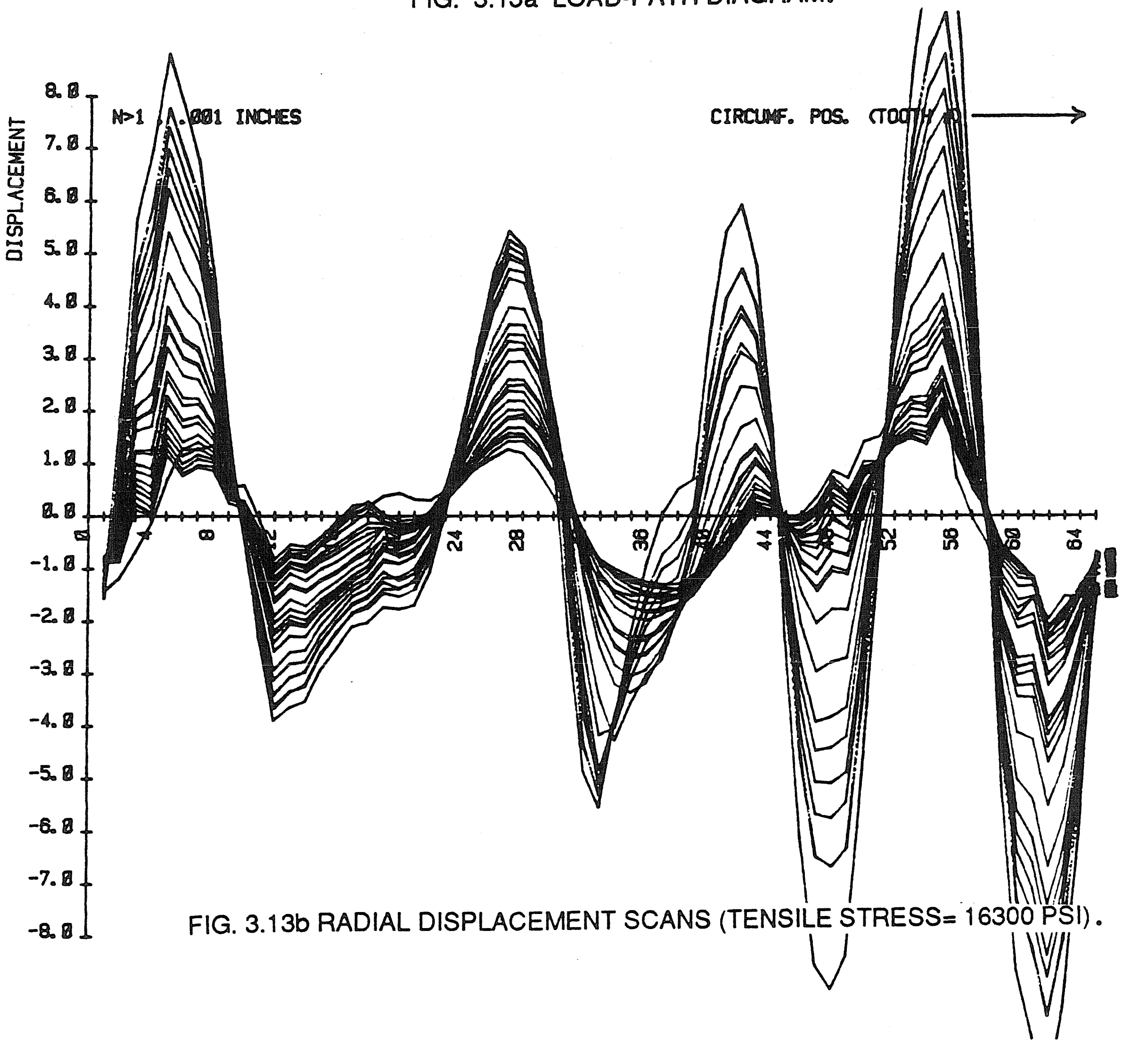

FIG. 3.13b RADIAL DISPLACEMENT SCANS (TENSILE STRESS= 16300 PSI).

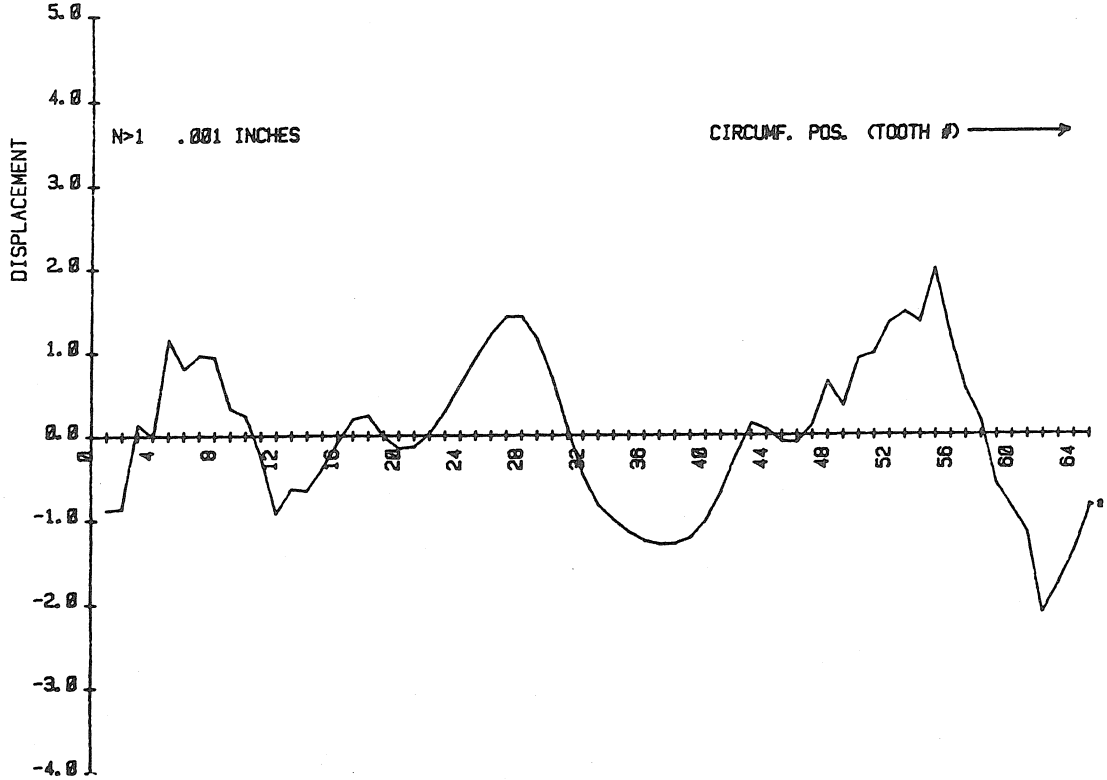

FIG. 3.13c INITIAL IMPERFECTION (TENSILE STRESS= 16300 PSI).

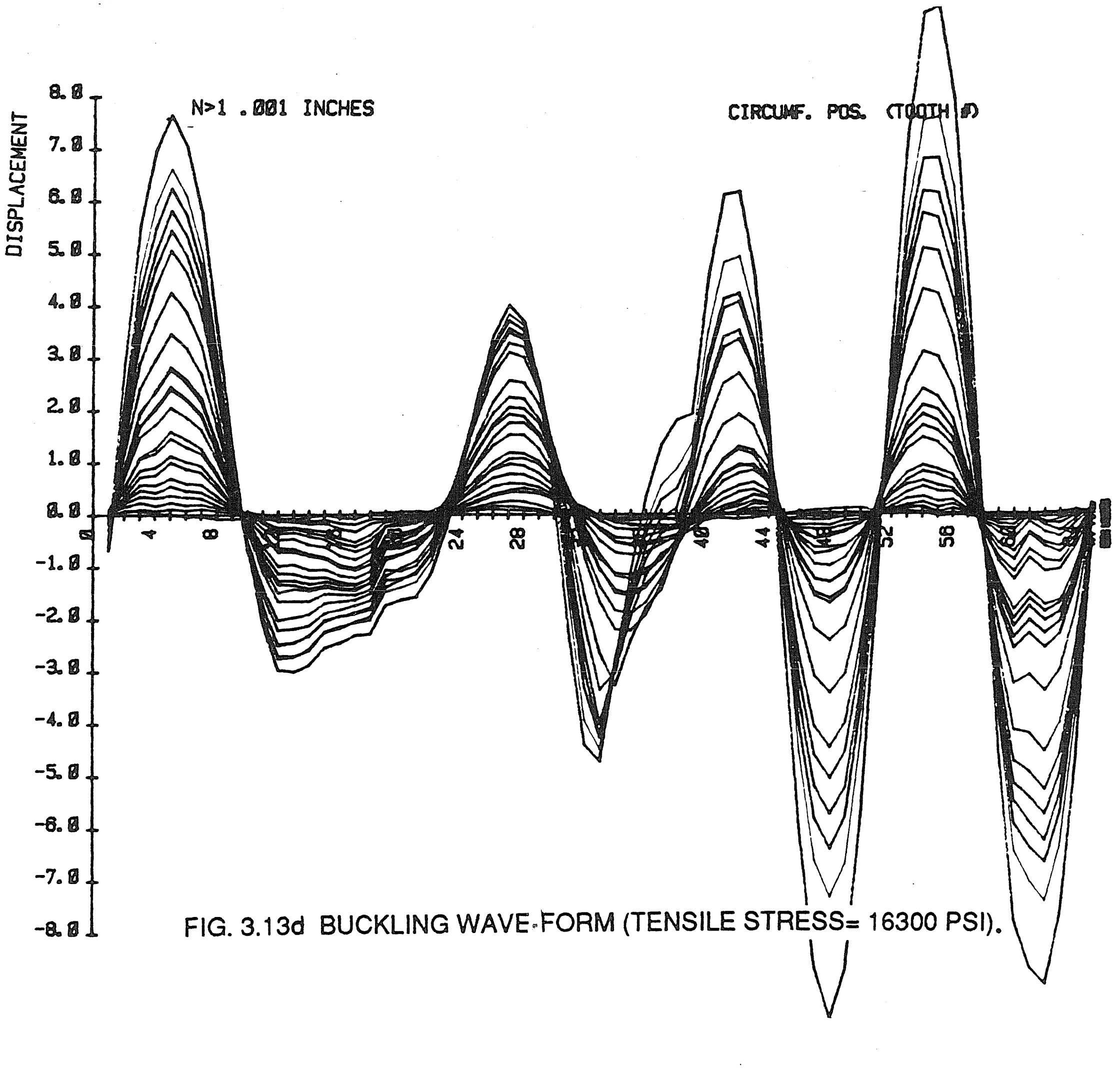

FIG. 3.13d BUCKLING WAVE-FORM (TENSILE STRESS= 16300 PSI).

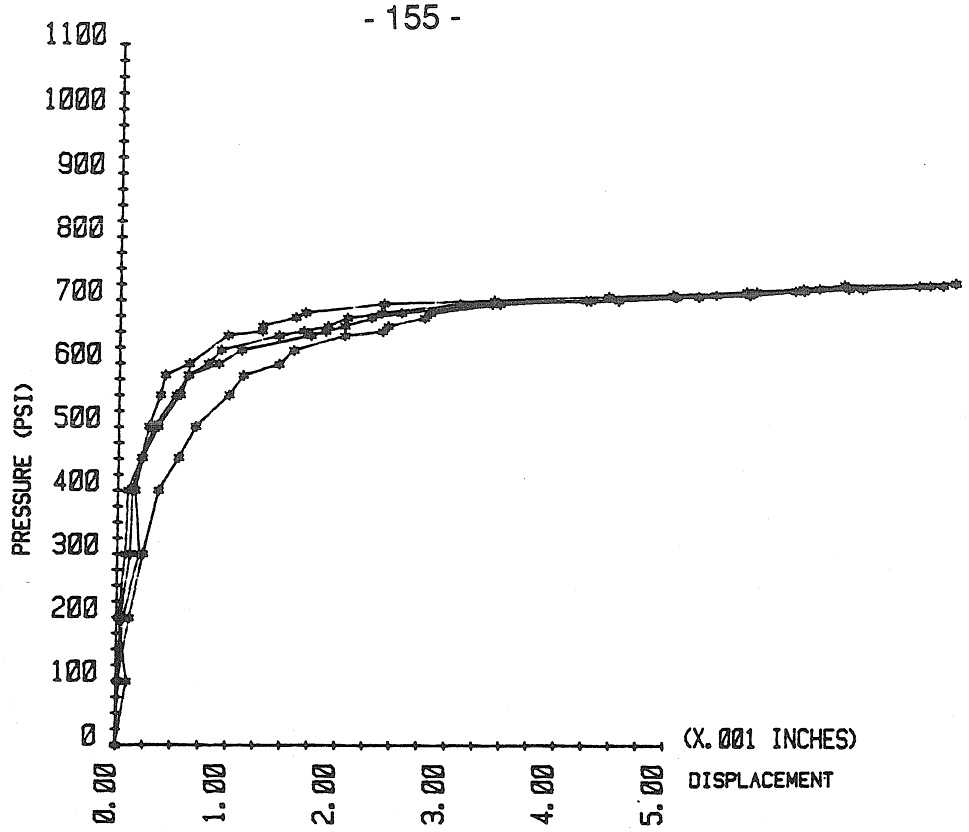

FIG. 3.13e LOAD-DISPLACEMENT (NORMALIZED) PLOT (T.S.= 16300 PSI).

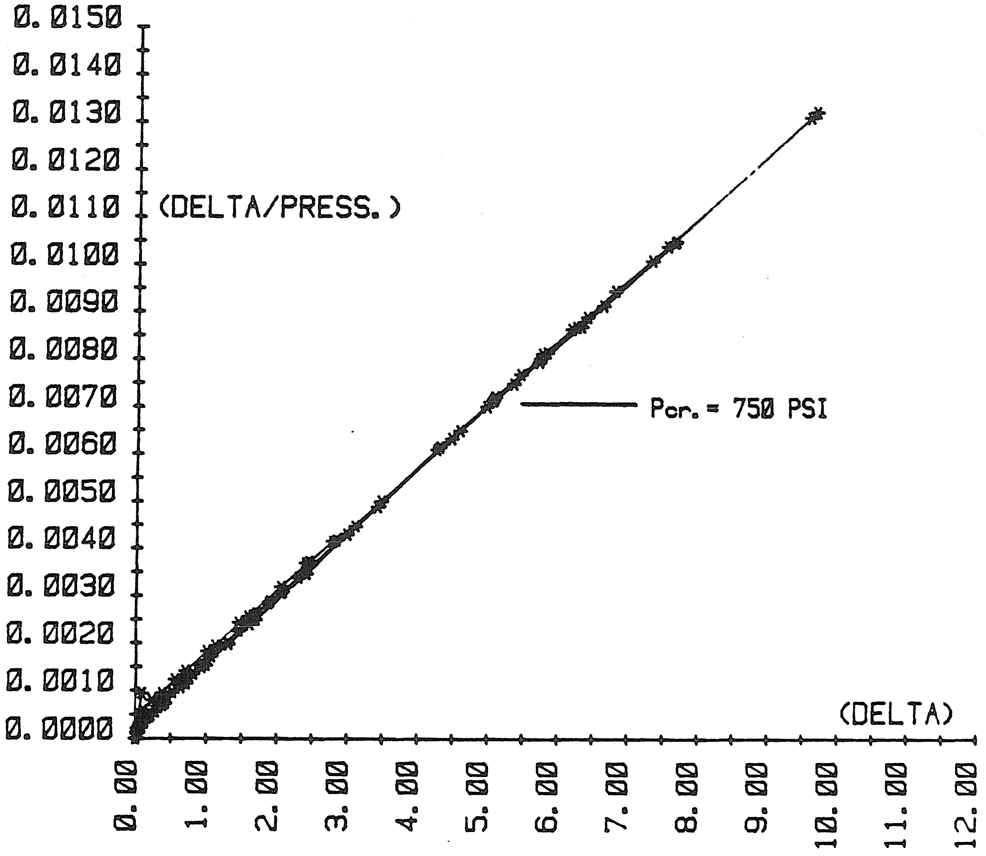

FIG. 3.13f SOUTHWELL PLOT (T.S.= 16300 PSI).

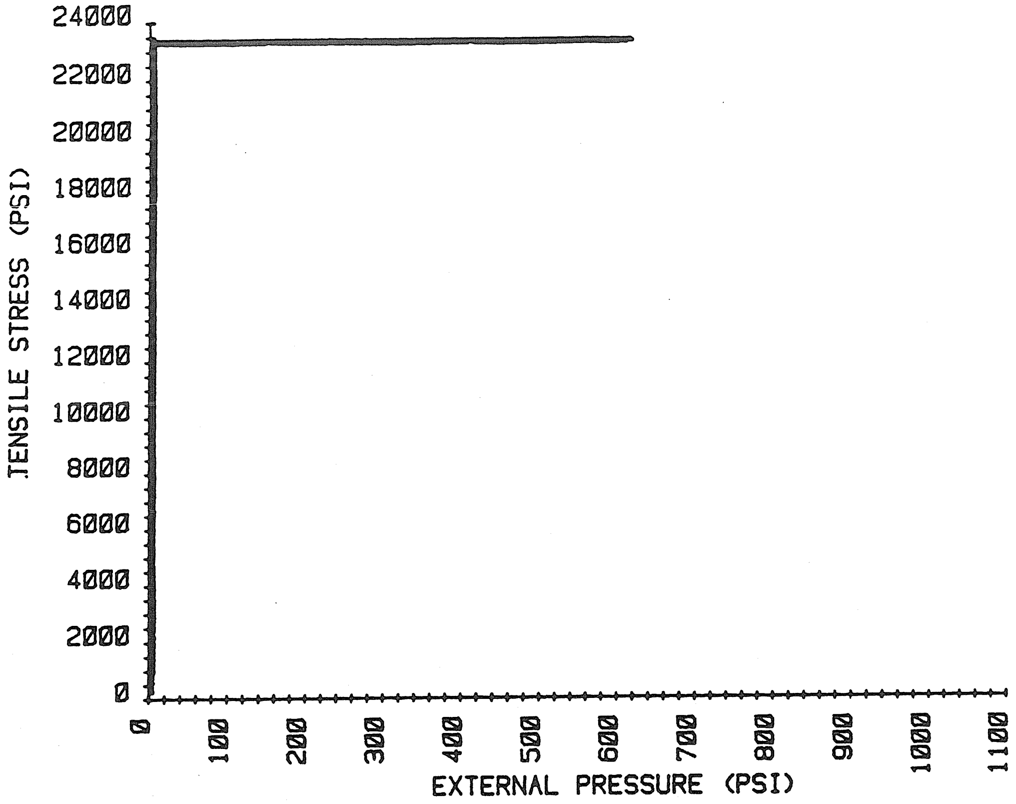

FIG. 3.14a LOAD-PATH DIAGRAM.

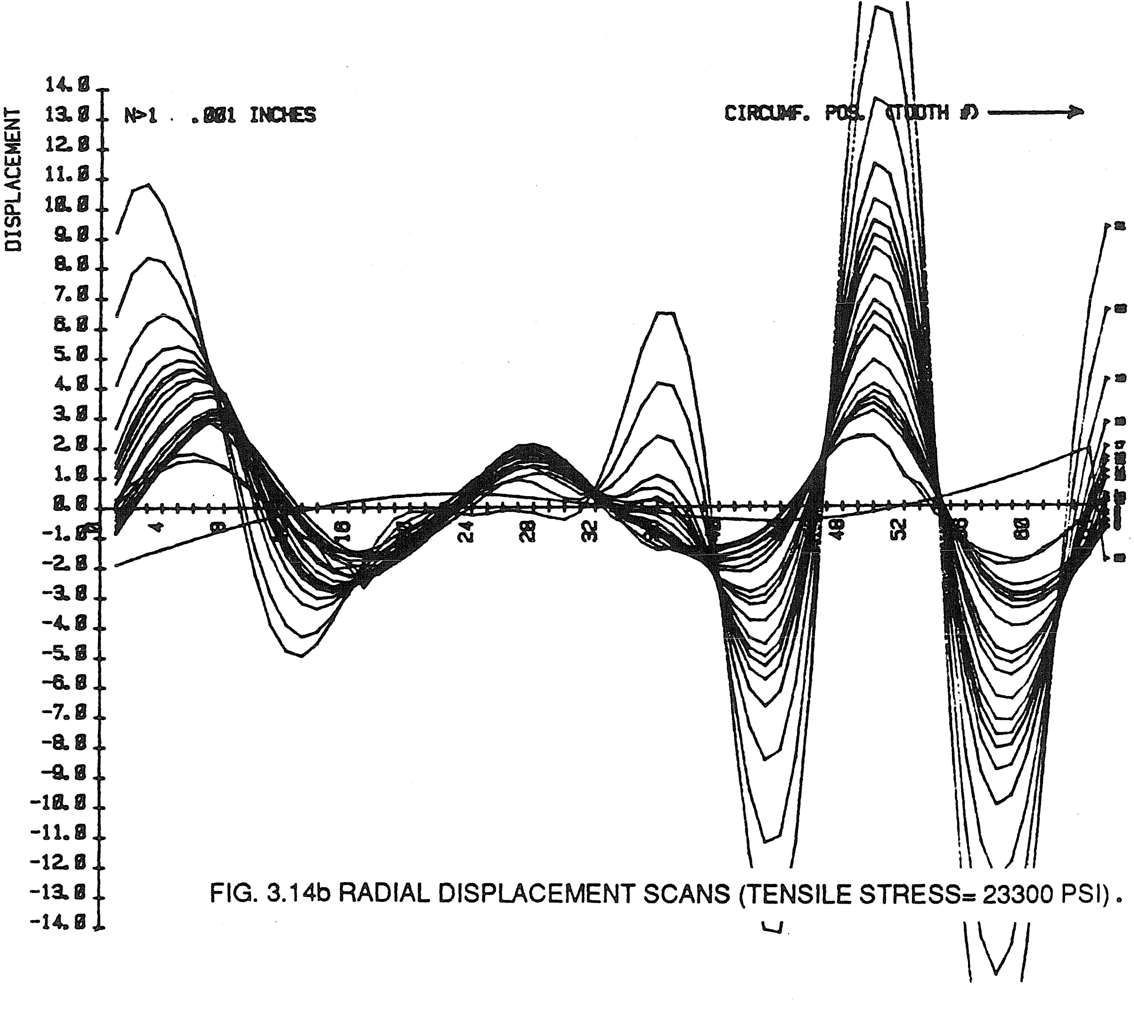

FIG. 3.14b RADIAL DISPLACEMENT SCANS (TENSILE STRESS= 23300 PSI).

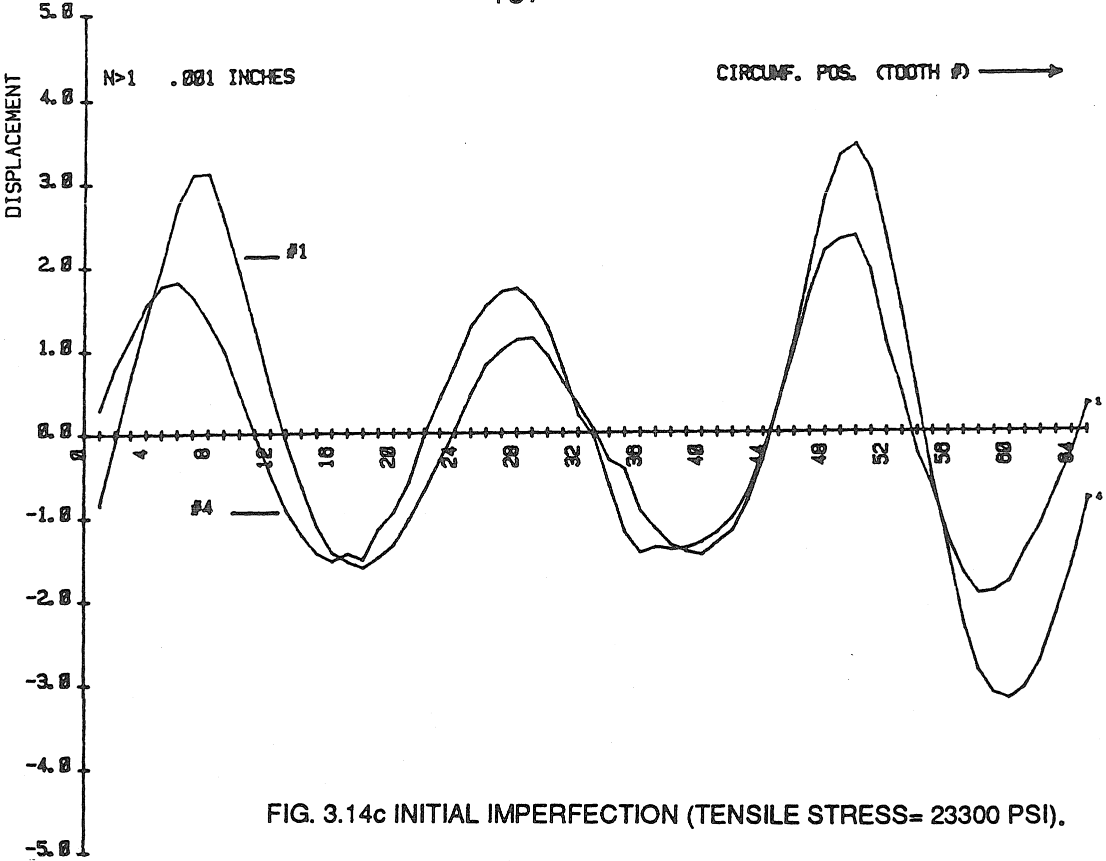

FIG. 3.14c INITIAL IMPERFECTION (TENSILE STRESS= 23300 PSI).

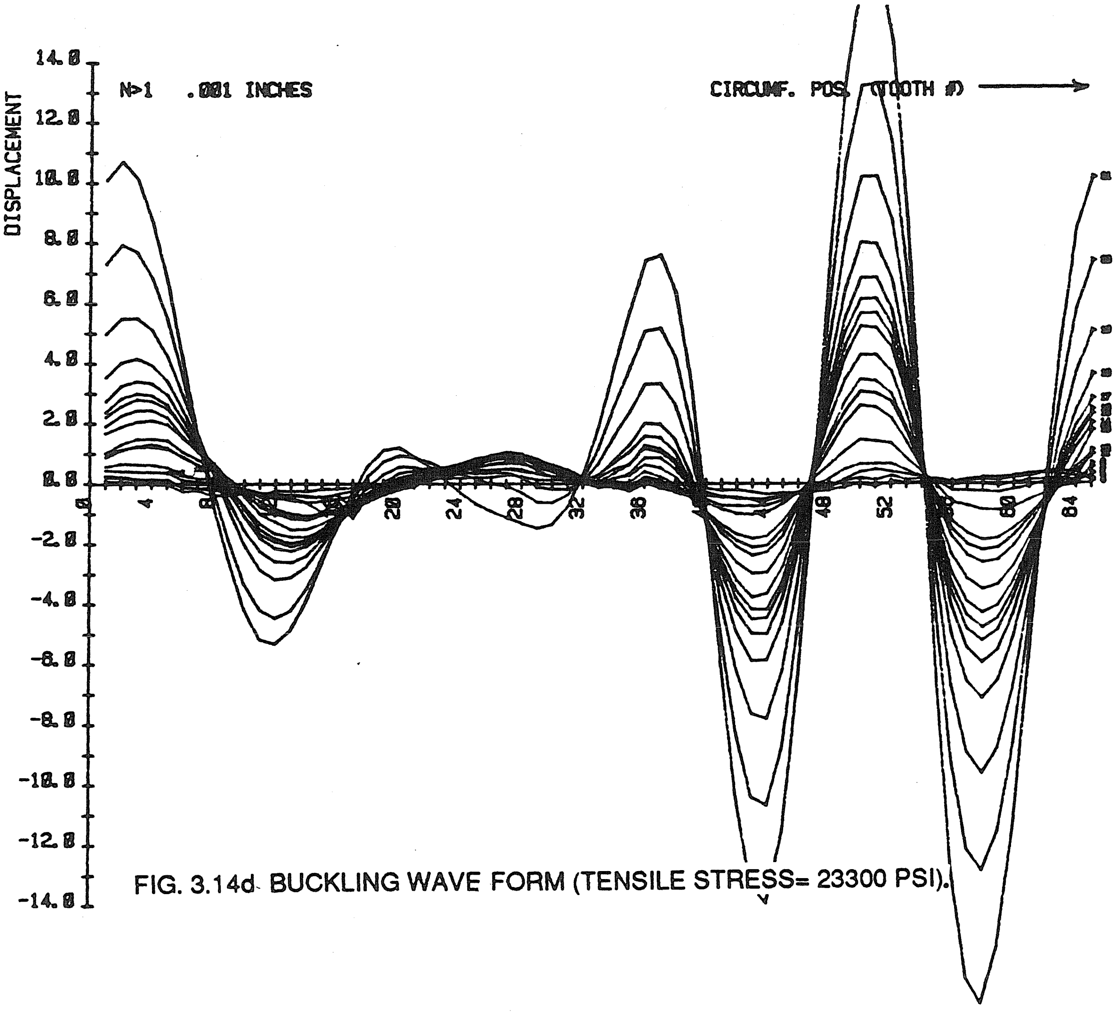

FIG. 3.14d BUCKLING WAVE FORM (TENSILE STRESS= 23300 PSI).

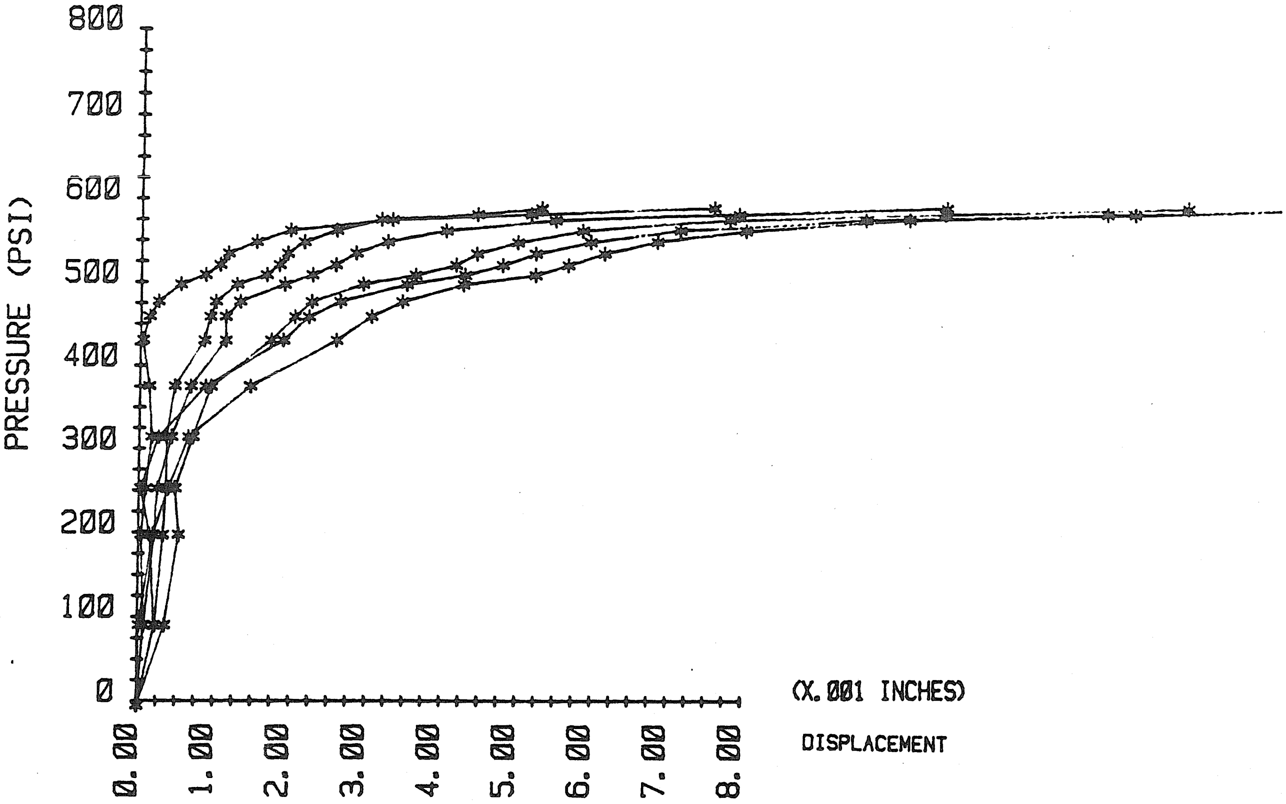

FIG. 3.14e LOAD-DISPLACEMENT (NORMALIZED) PLOT (T.S.= 23300 PSI).

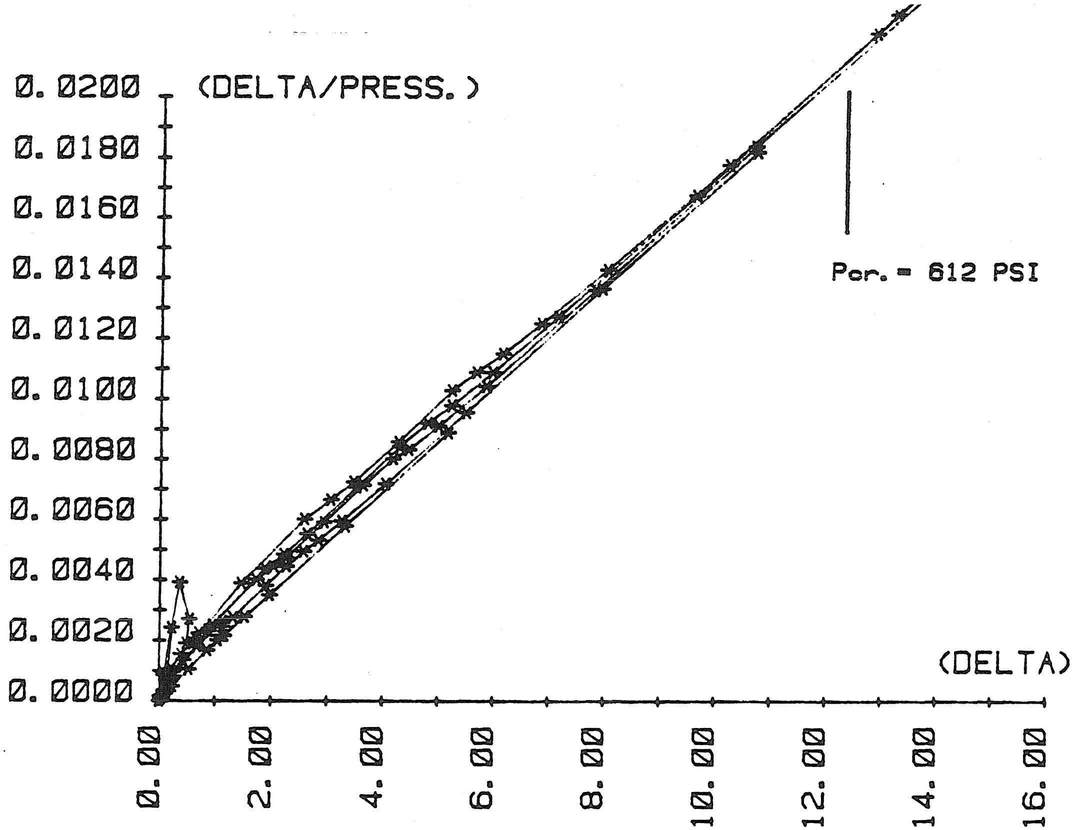

FIG. 3.14f SOUTHWELL PLOT (T.S.= 23300 PSI).

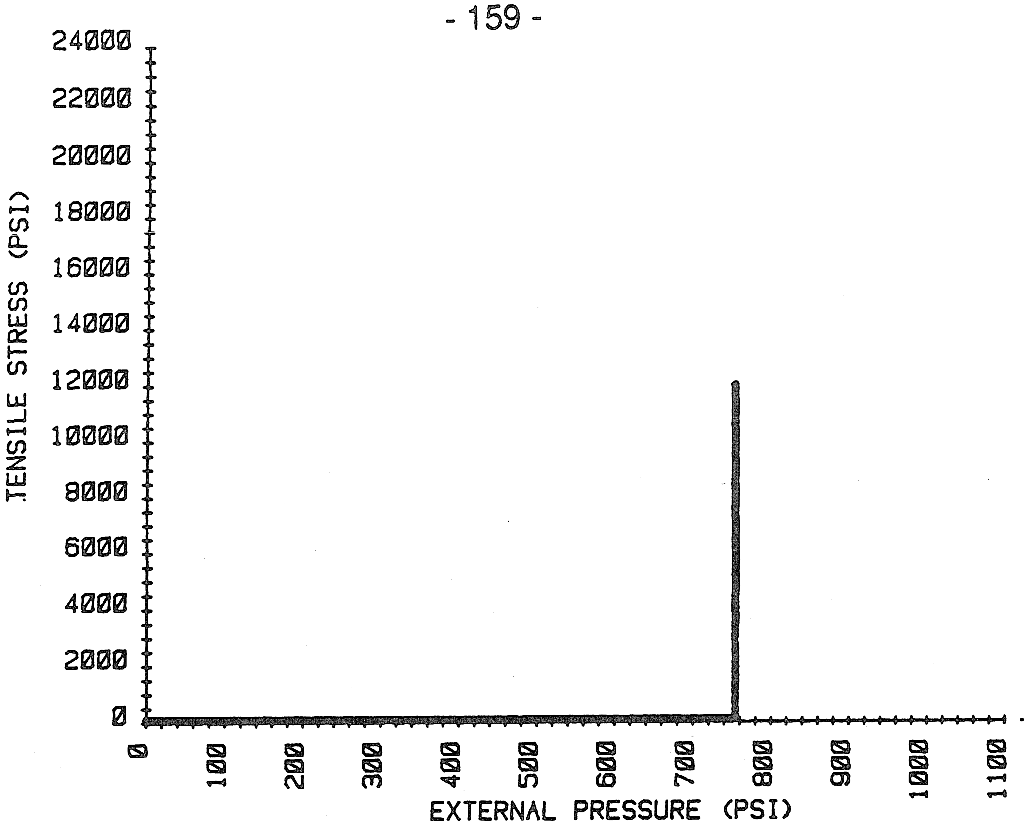

FIG. 3.15a LOAD-PATH DIAGRAM.

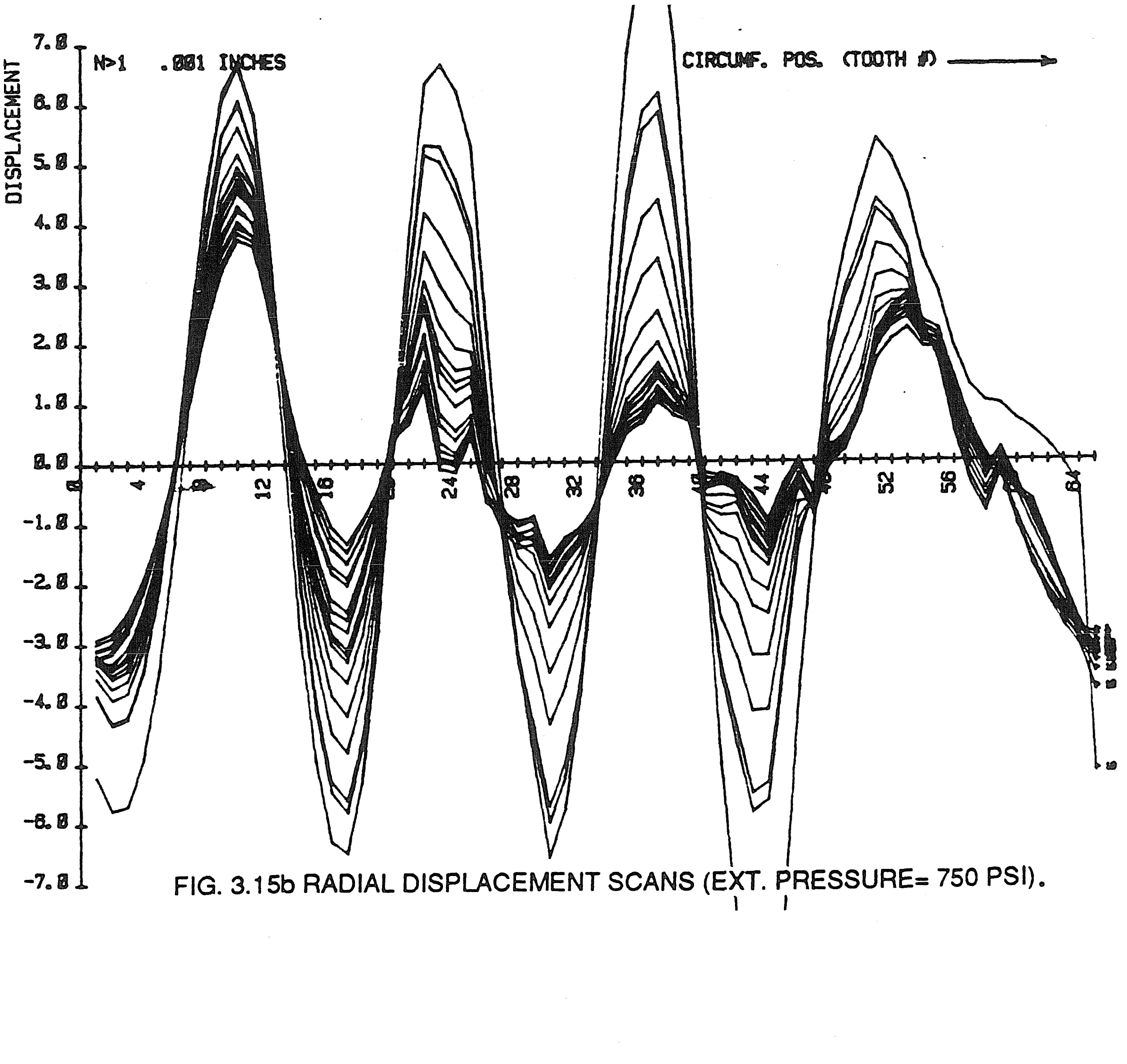

FIG. 3.15b RADIAL DISPLACEMENT SCANS (EXT. PRESSURE= 750 PSI).

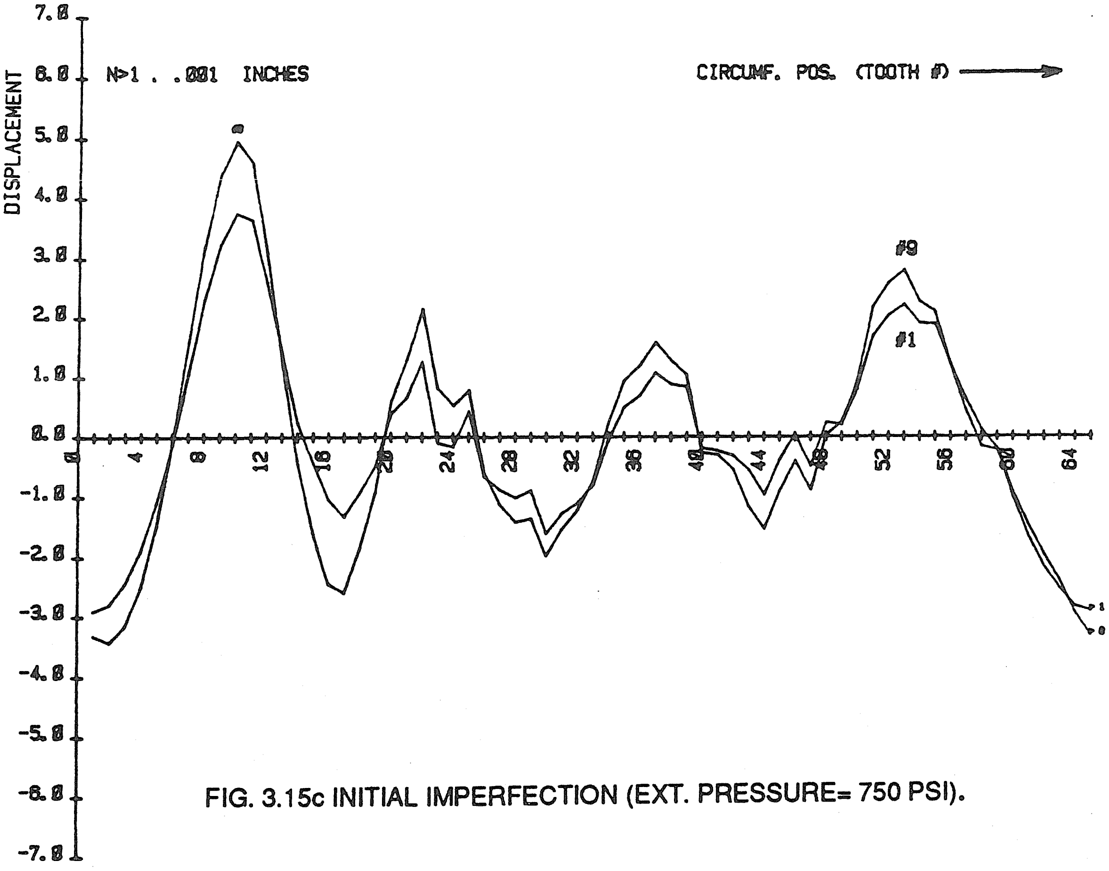

FIG. 3.15c INITIAL IMPERFECTION (EXT. PRESSURE= 750 PSI).

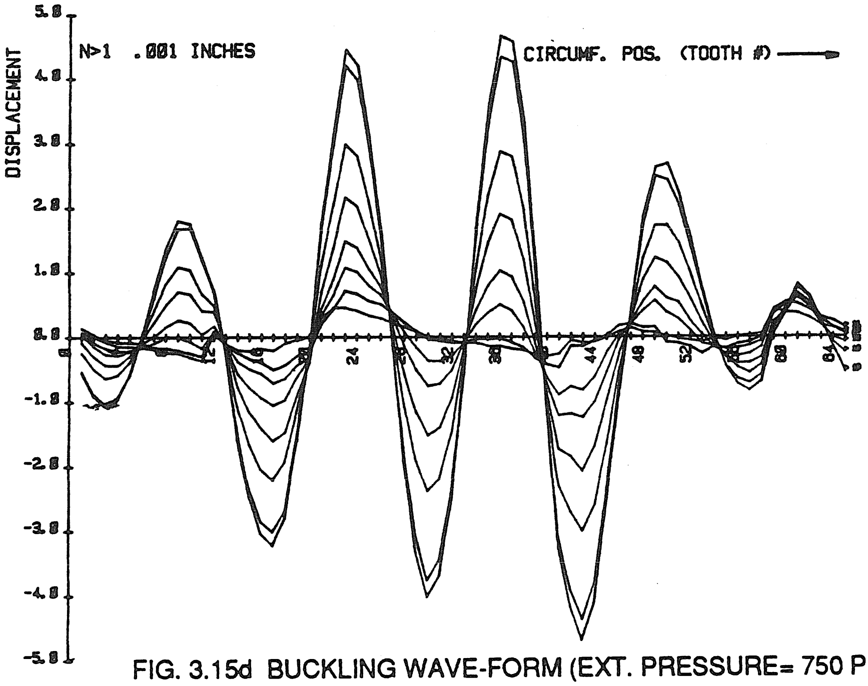

FIG. 3.15d BUCKLING WAVE-FORM (EXT. PRESSURE= 750 PSI).

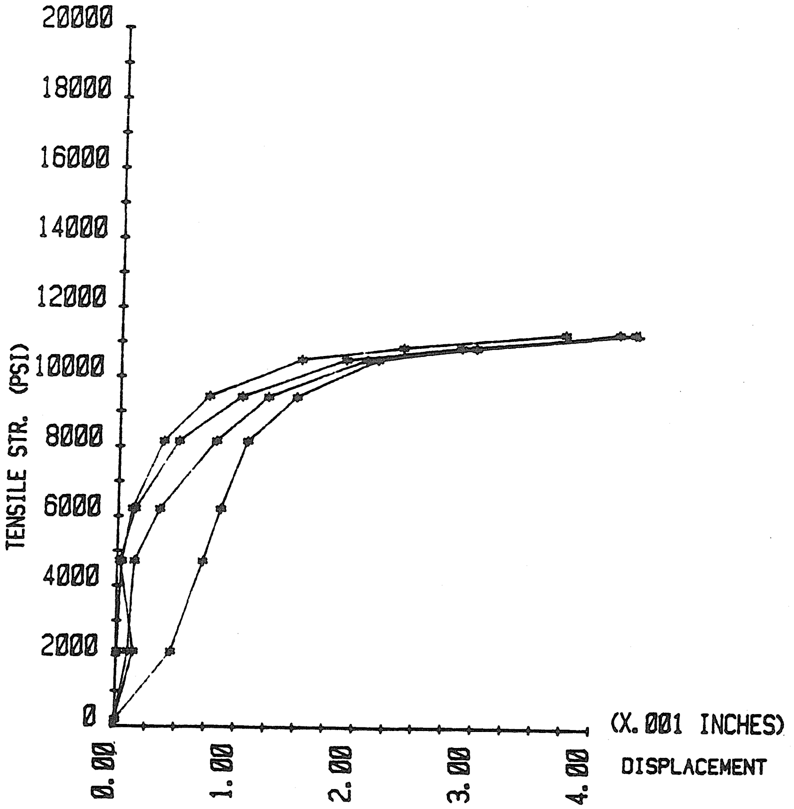

FIG. 3.15e LOAD-DISPLACEMENT (NORMALIZED) PLOT (E.P.= 750 PSI).

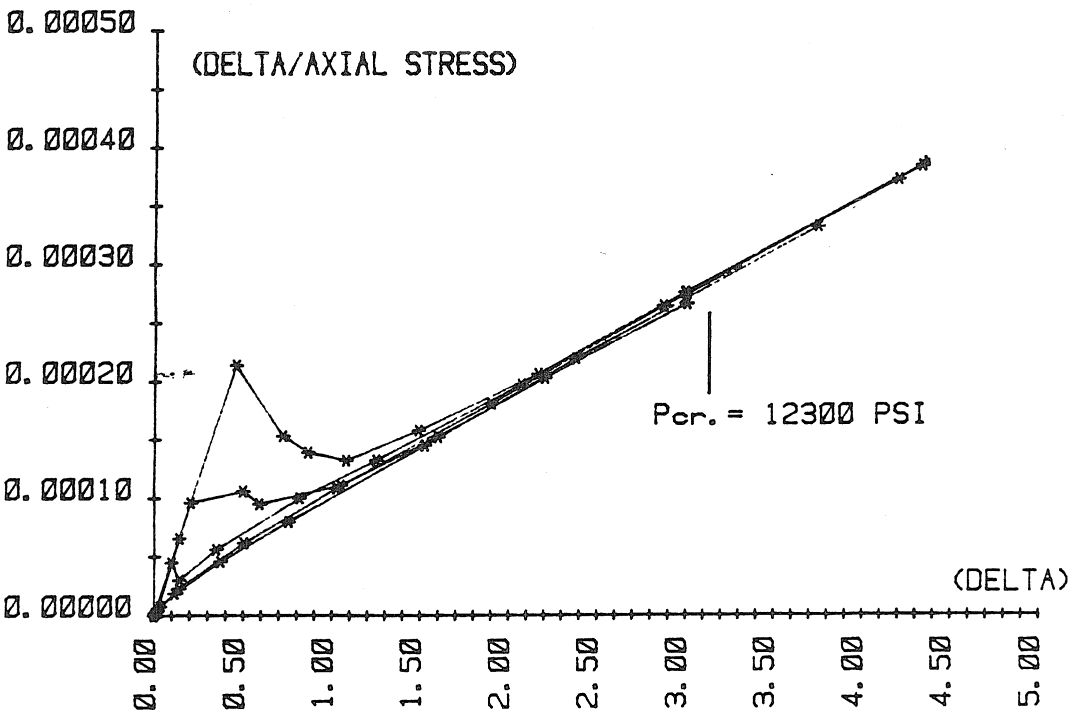

FIG. 3.15f SOUTHWELL PLOT (E.P.= 750 PSI).

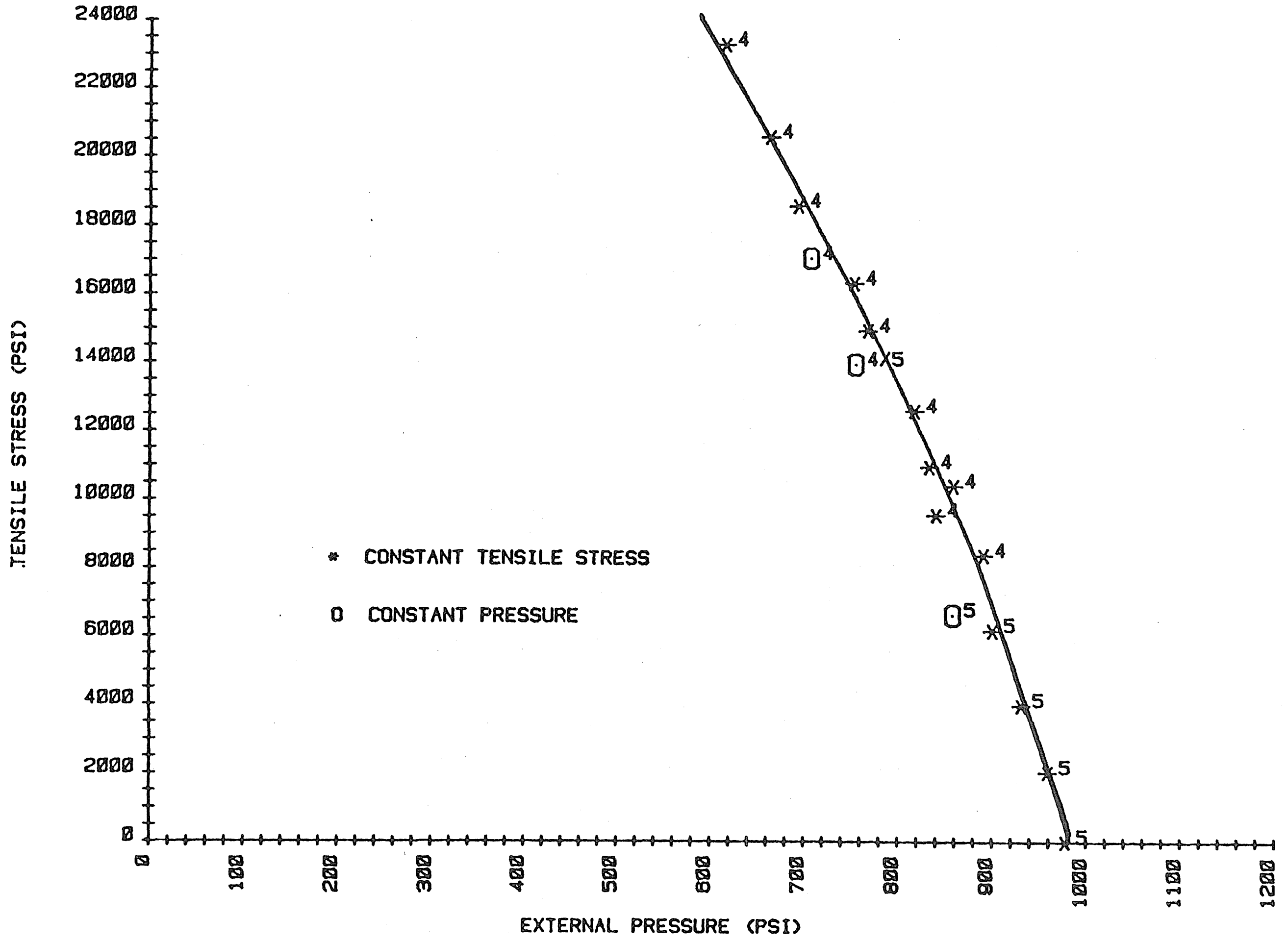

FIG. 3.16 a EXPERIMENTAL RESULTS.

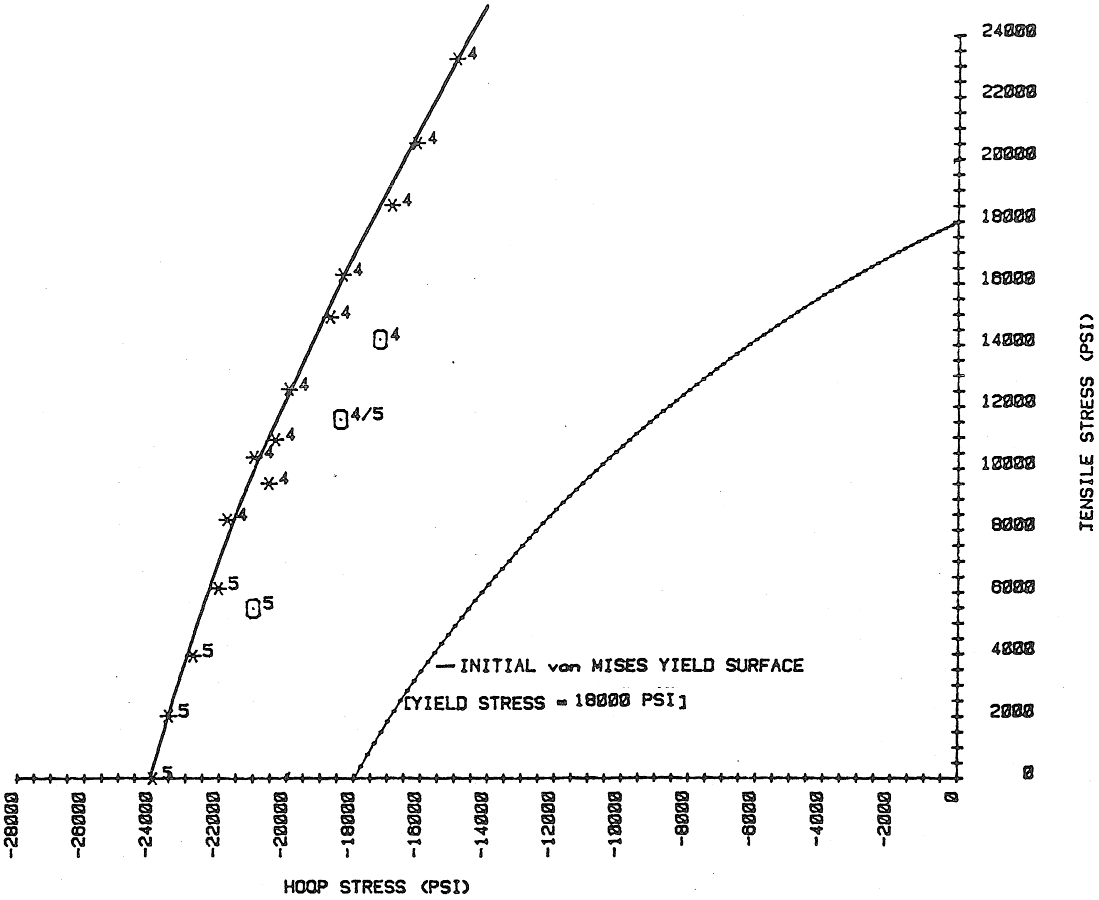

FIG. 3.16 b EXPERIMENTAL RESULTS IN STRESS-SPACE.

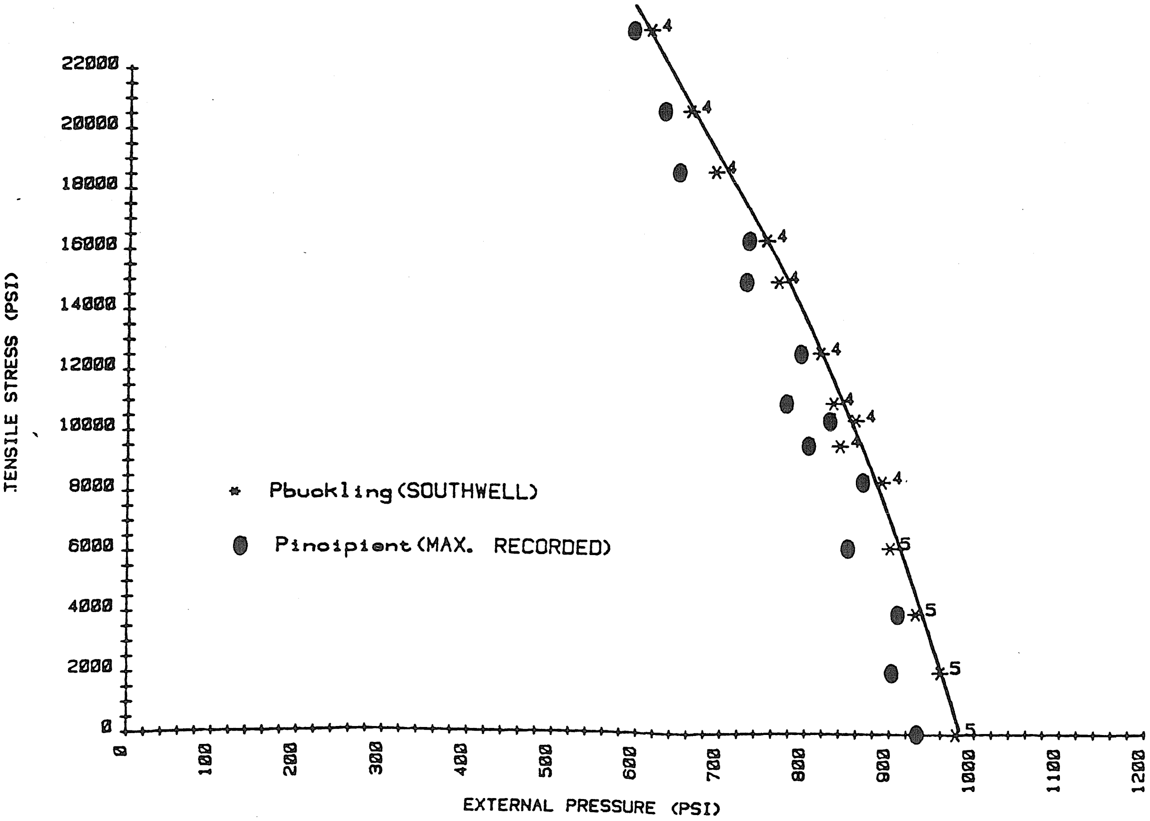

FIG. 3.16 c SOUTHWELL SMOOTHING OF EXPERIMENTAL RESULTS [SET A].

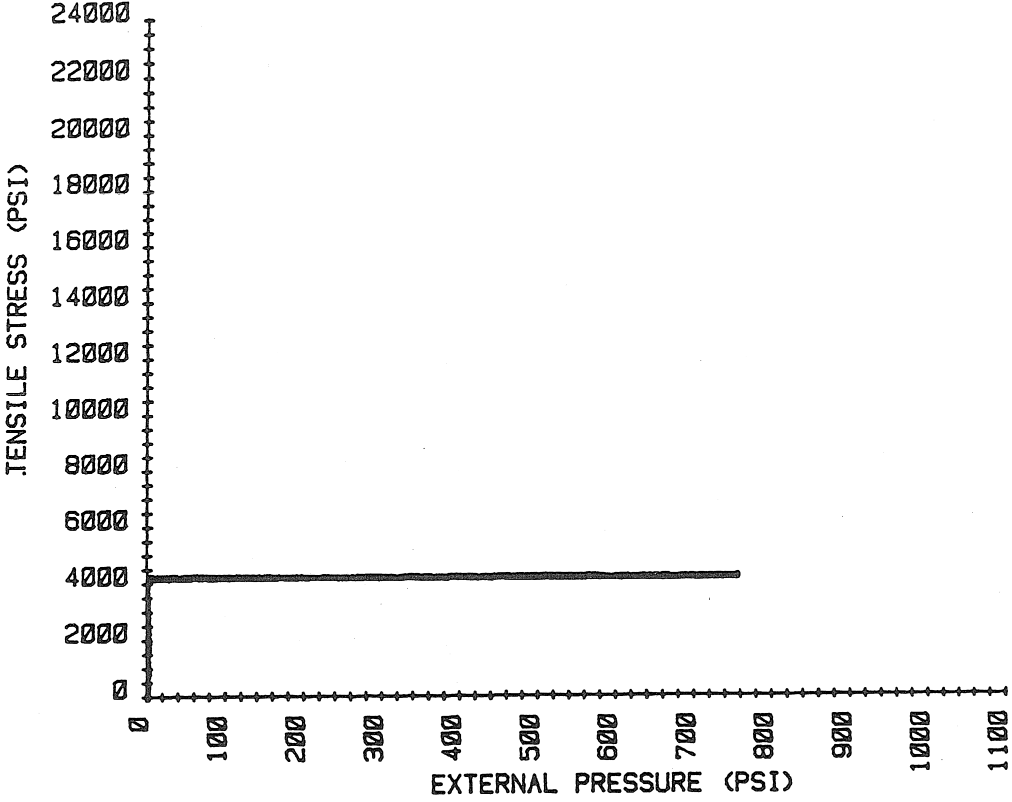

FIG. 3.17a LOAD-PATH DIAGRAM.

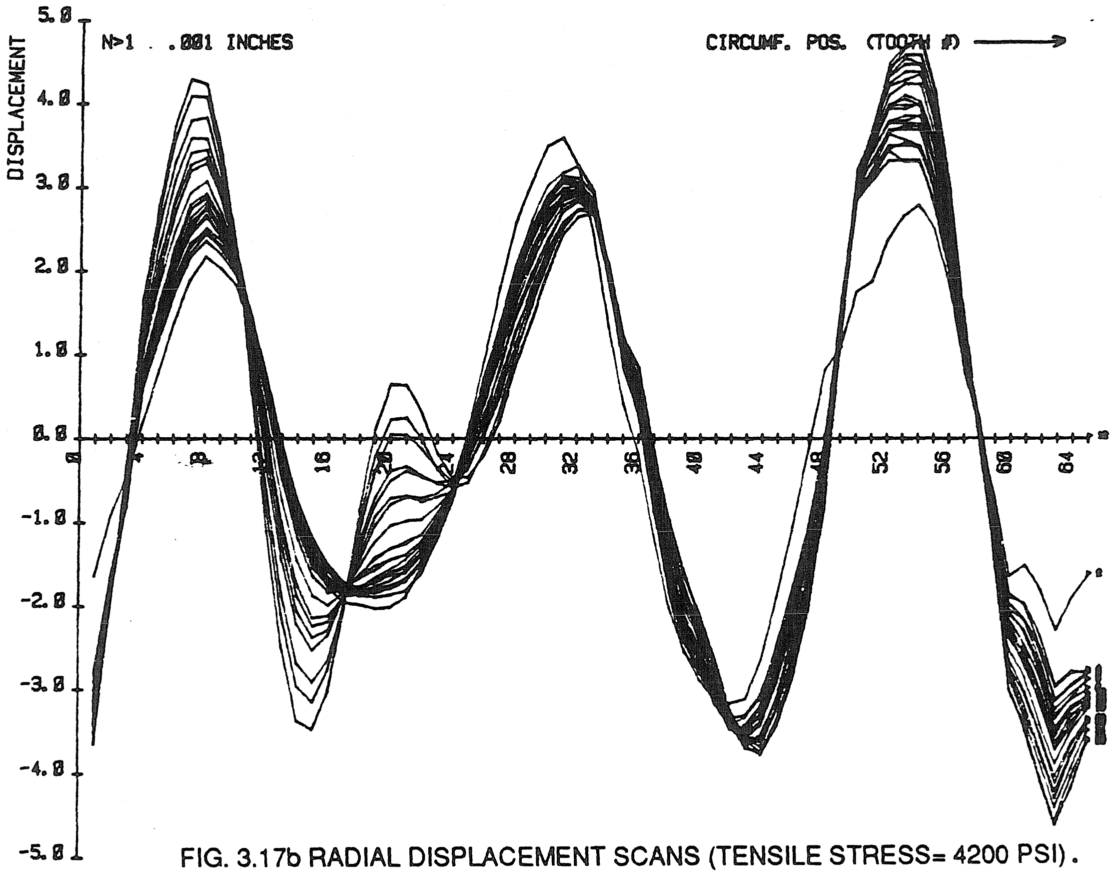

FIG. 3.17b RADIAL DISPLACEMENT SCANS (TENSILE STRESS= 4200 PSI).

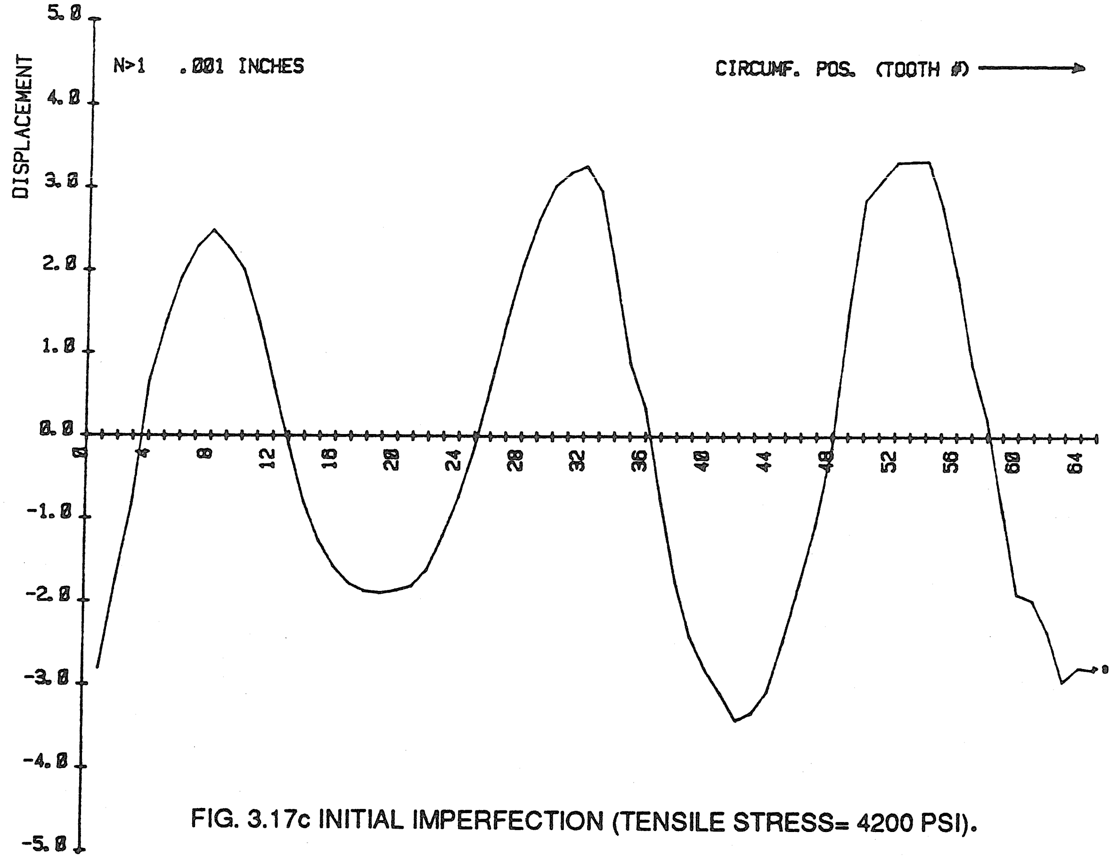

FIG. 3.17c INITIAL IMPERFECTION (TENSILE STRESS= 4200 PSI).

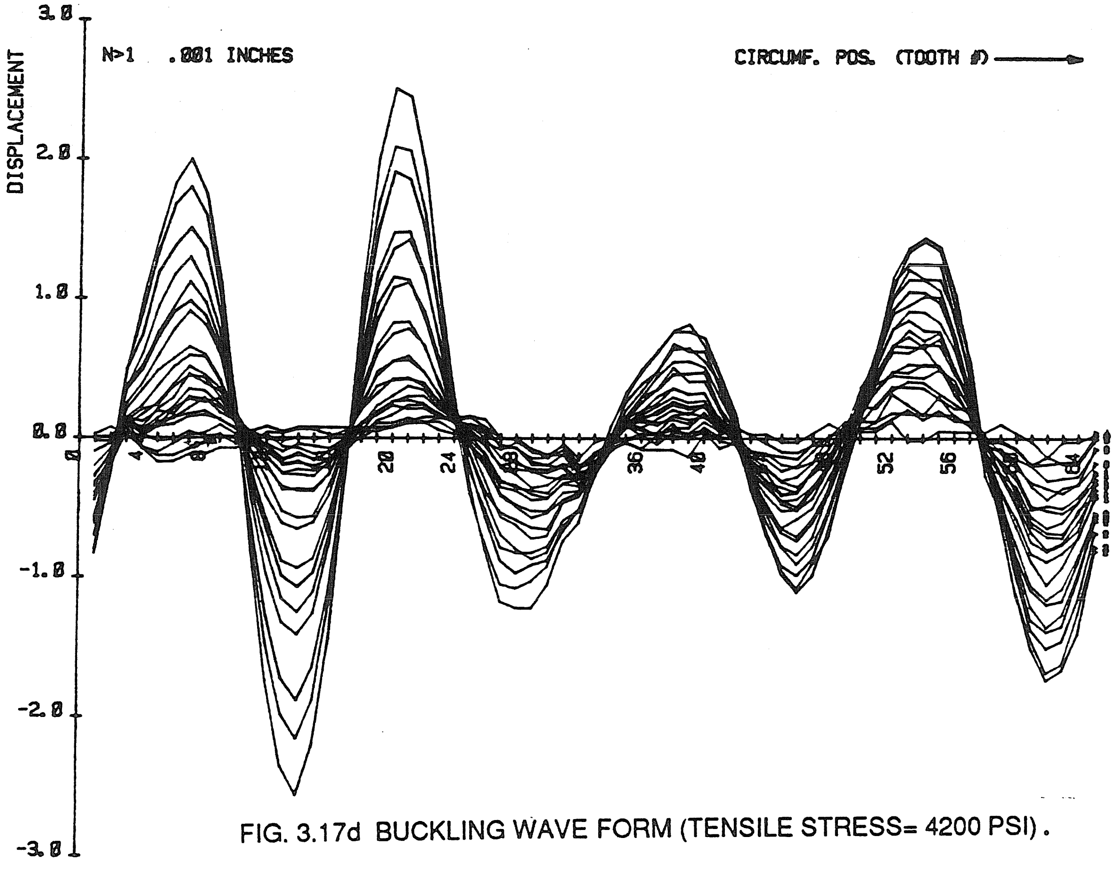

FIG. 3.17d BUCKLING WAVE FORM (TENSILE STRESS= 4200 PSI).

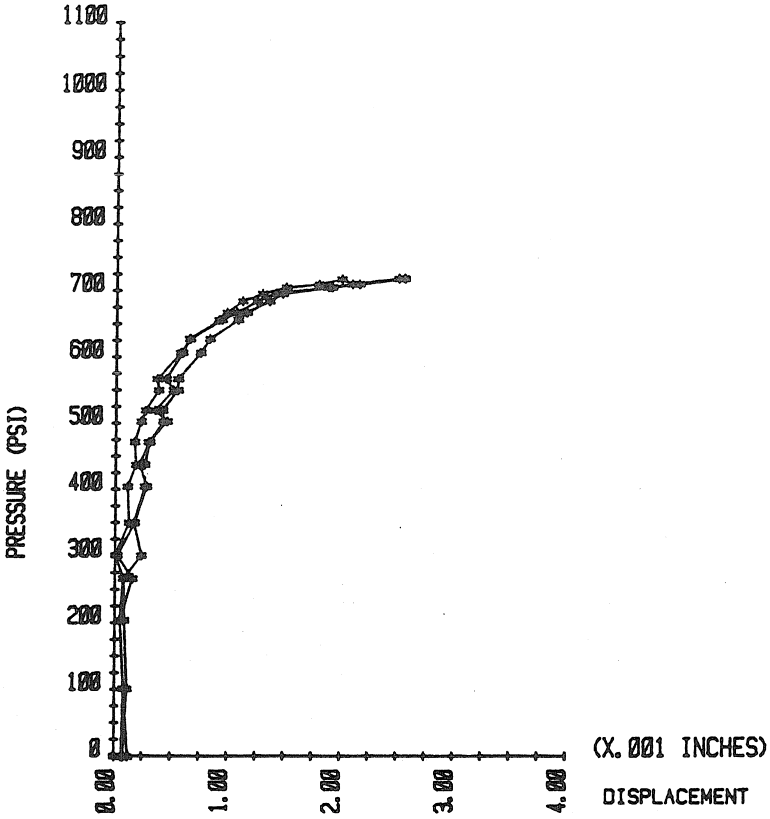

FIG. 3.17e LOAD-DISPLACEMENT (NORMALIZED) PLOT (T.S.= 4200 PSI).

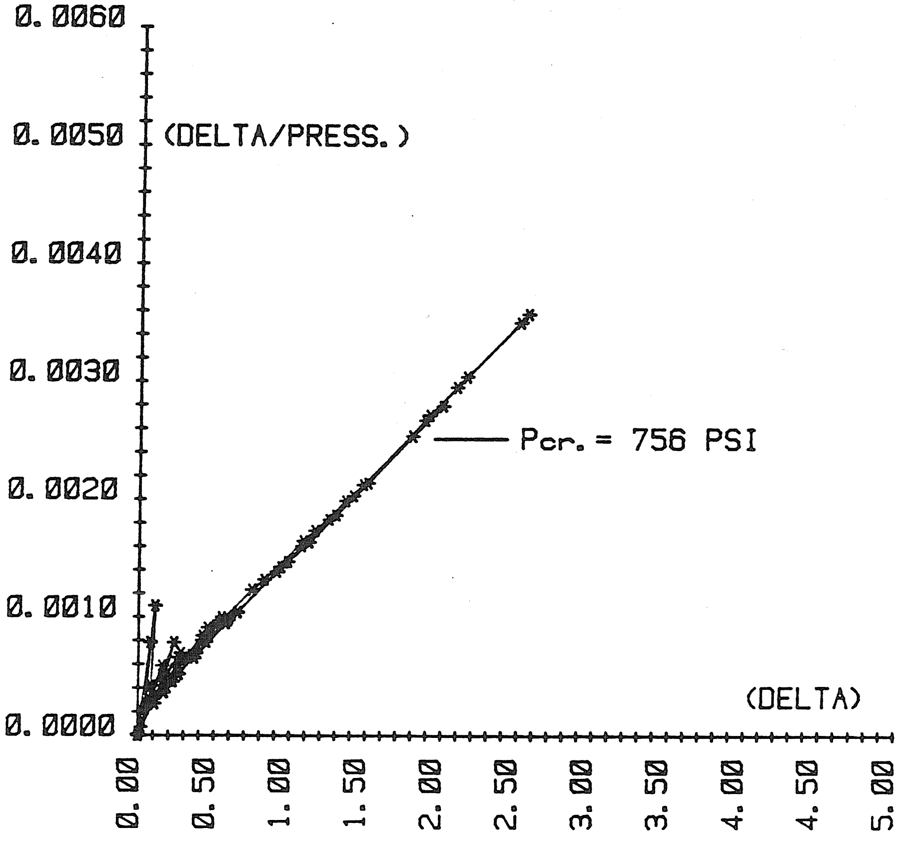

FIG. 3.17f SOUTHWELL PLOT (T.S.= 4200 PSI).

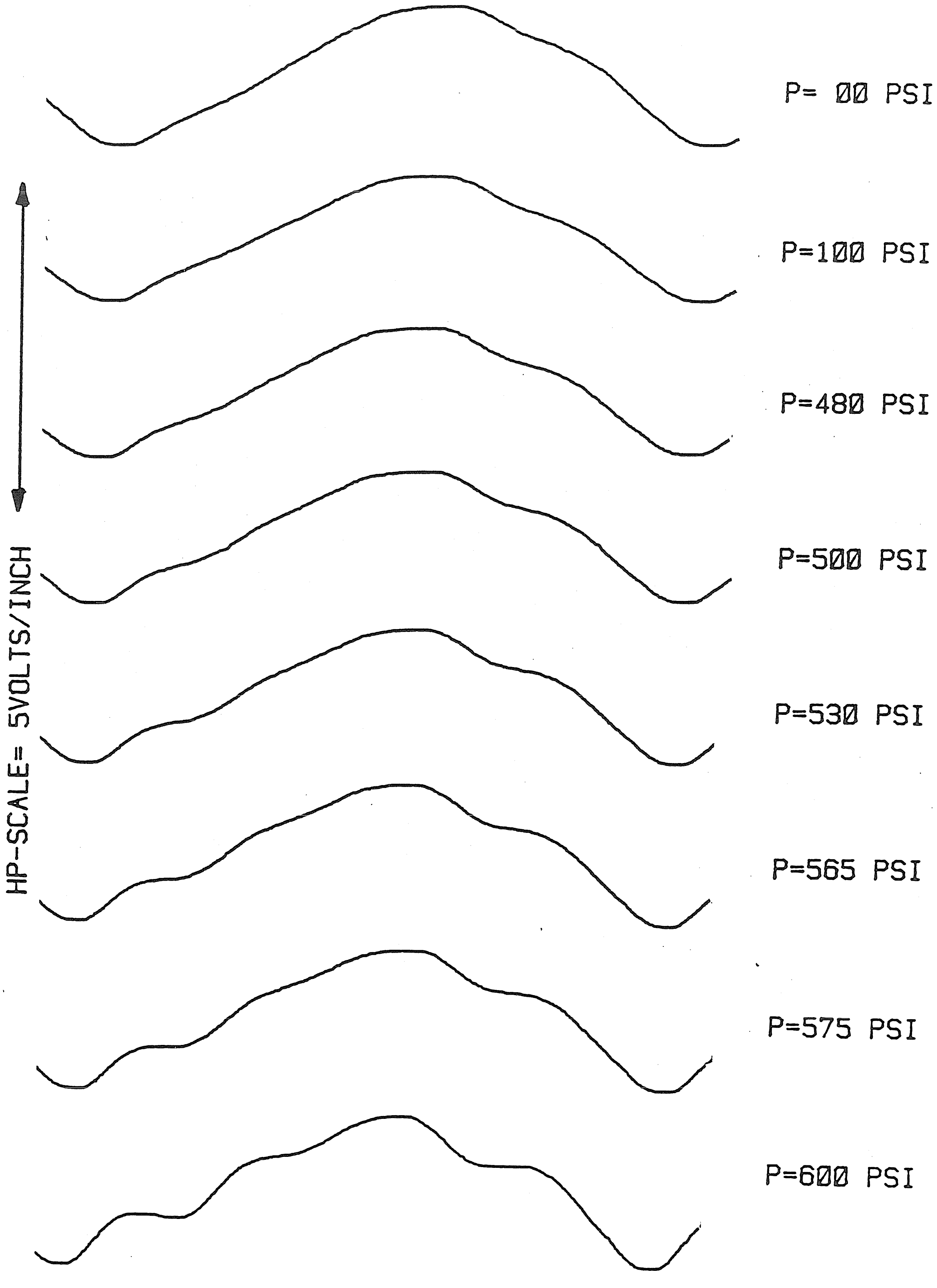

FIG. 3.18 FULL SCAN PROFILES [TENSILE STRESS= 12100 PSI].

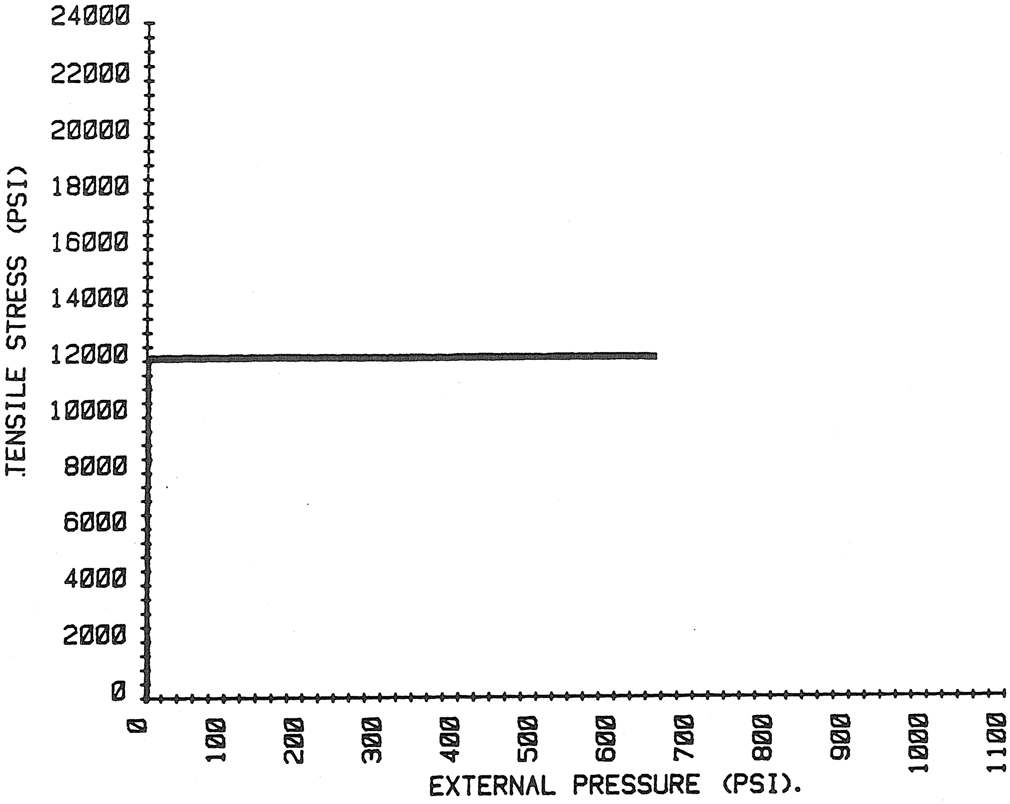

FIG. 3.19a LOAD-PATH DIAGRAM

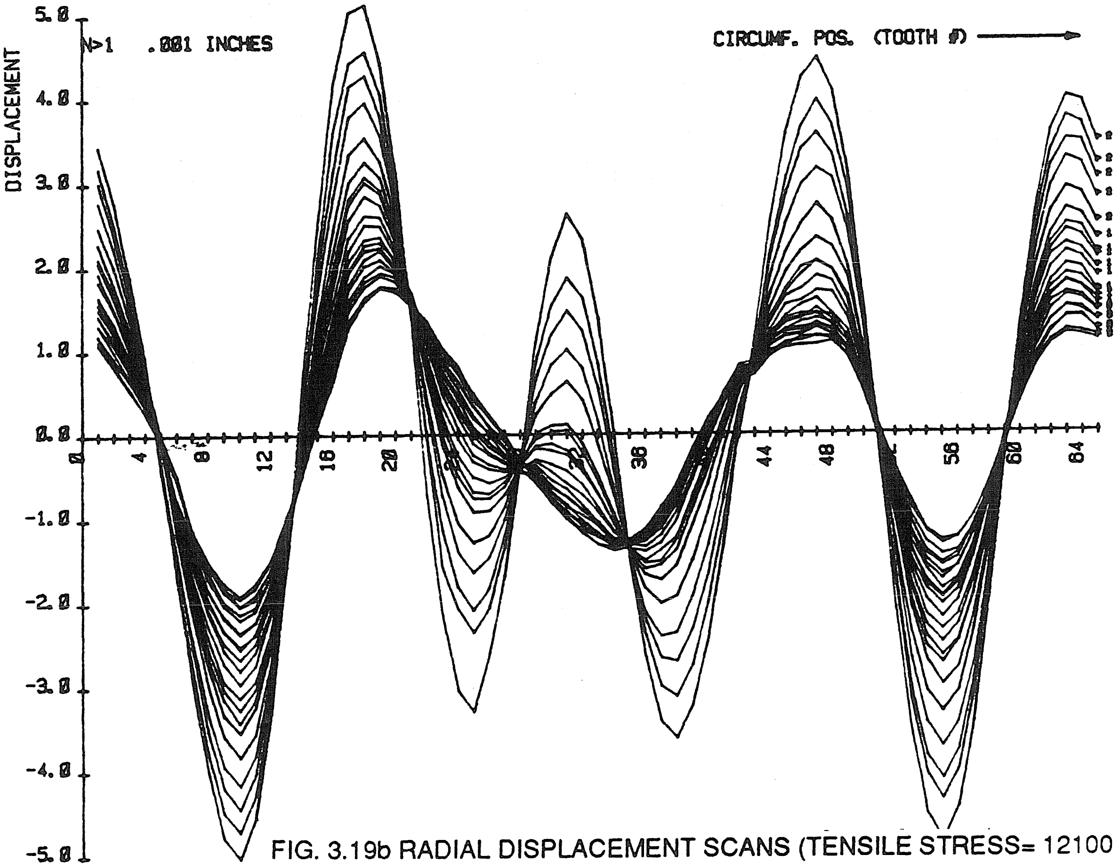

FIG. 3.19b RADIAL DISPLACEMENT SCANS (TENSILE STRESS= 12100 PSI).

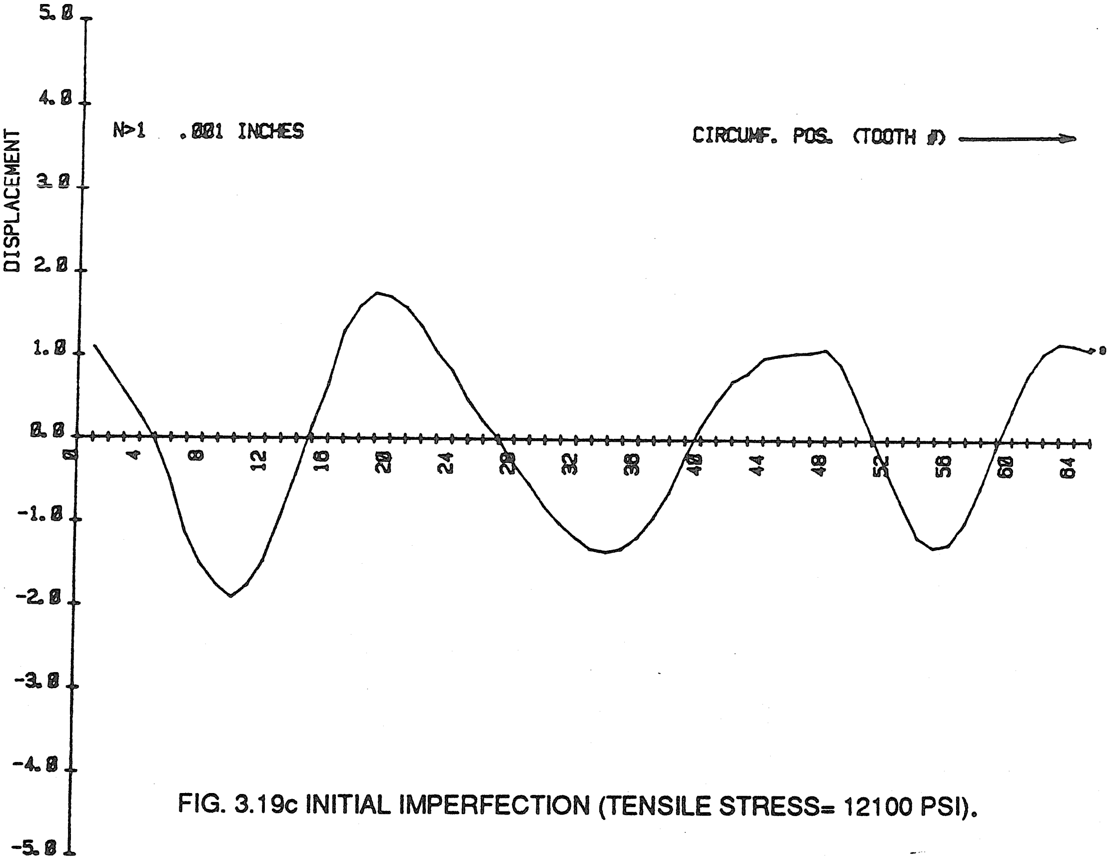

FIG. 3.19c INITIAL IMPERFECTION (TENSILE STRESS= 12100 PSI).

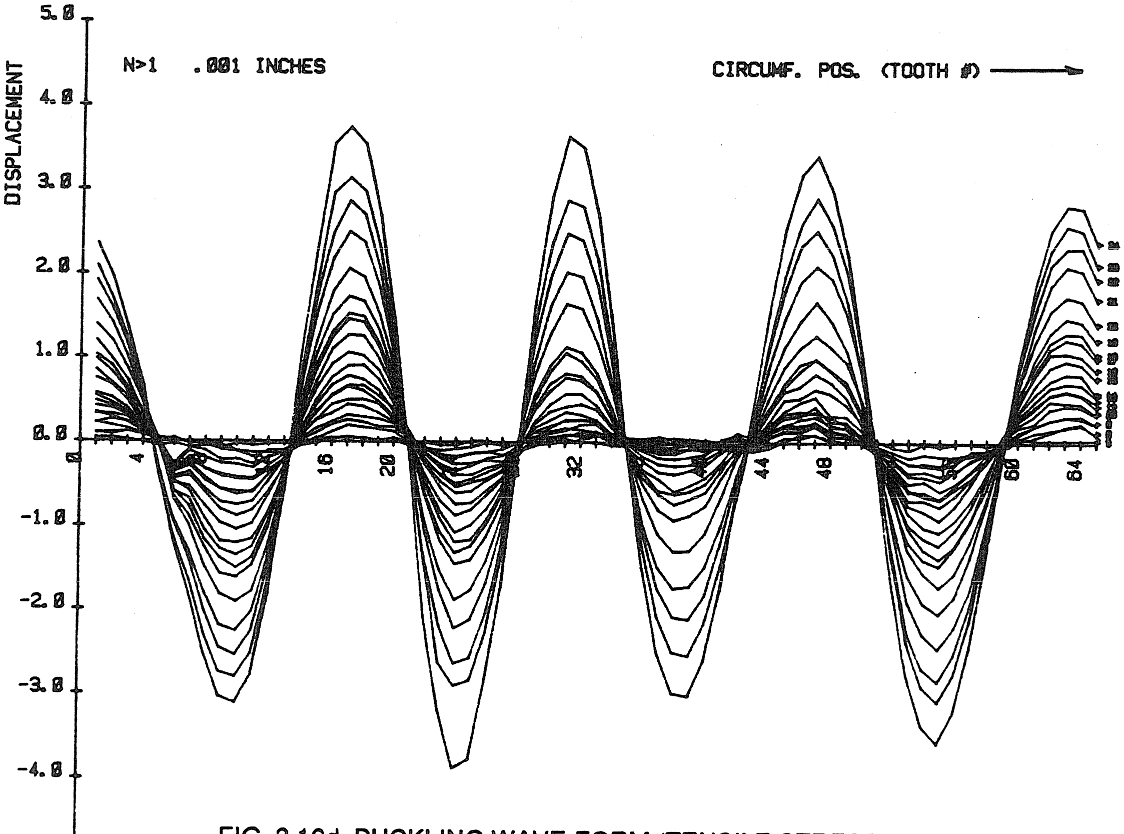

FIG. 3.19d BUCKLING WAVE-FORM (TENSILE STRESS= 12100 PSI).

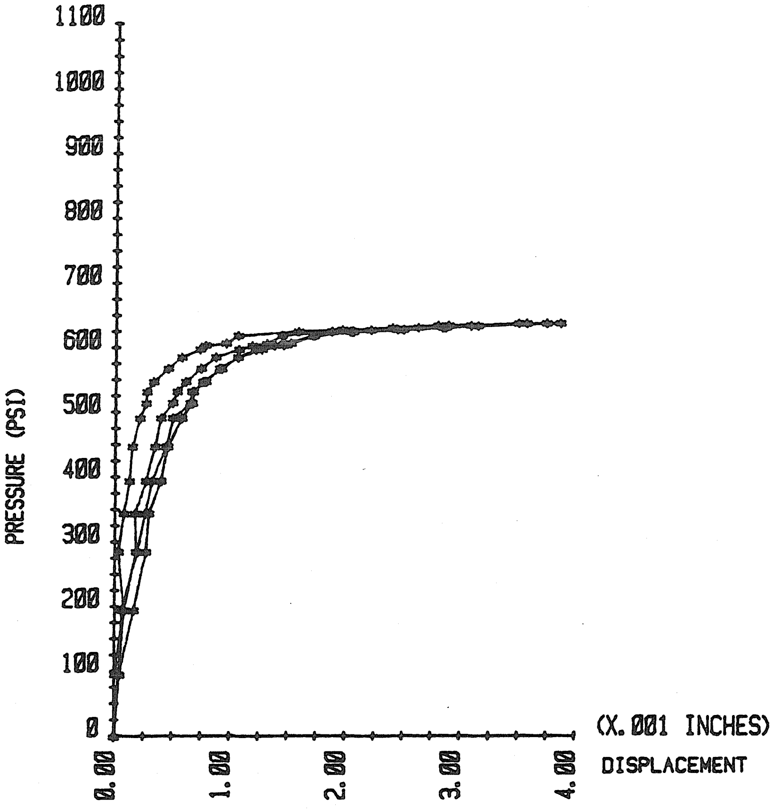

FIG. 3.19e LOAD-DISPLACEMENT (NORMALIZED) PLOT (T.S.= 12100 PSI).

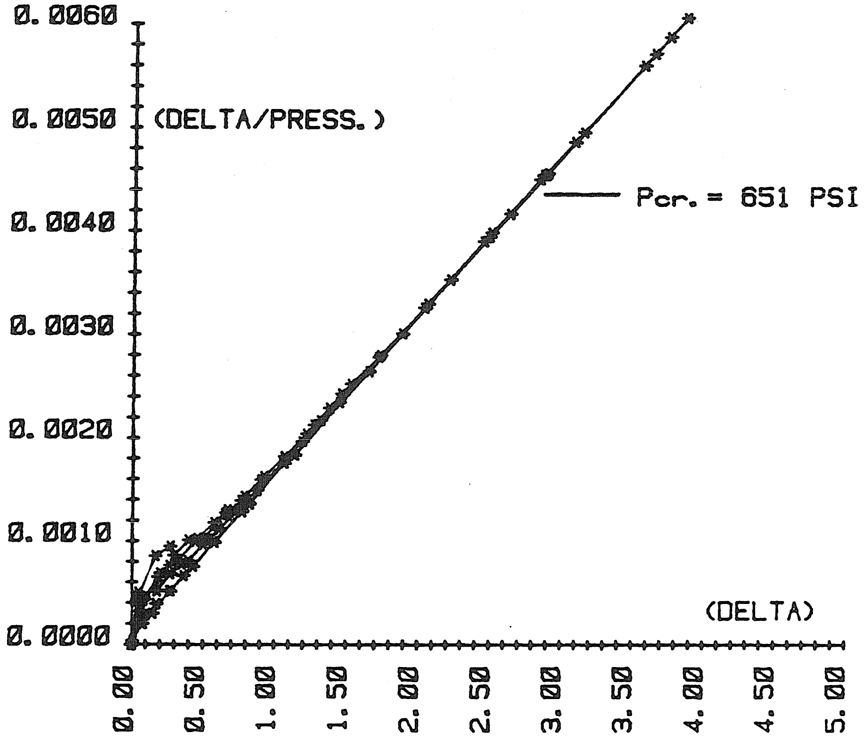

FIG. 3.19f SOUTHWELL PLOT (T.S.= 12100 PSI).

	FOURIER COEFFICIENTS (n=0 & n=1)			EXT.	TENSILE	AXIAL
SCAN#	A_0	A_1	B_1	PRESS(PSI)	STR.(PSI)	DISPLCMT.(0.001")
1	80.2	12.8	4.2	0	0	6.0
2	80.3	12.8	4.2	0	200	6.7
3	80.3	10.9	4.6	0	12100	39.7
4	80.1	10.9	4.6	94	12100	40.1
5	80.0	11.0	4.6	194	12100	40.4
6	79.8	11.0	4.6	285	12100	40.7
7	79.7	11.0	4.6	344	12100	40.9
8	79.6	11.0	4.6	394	12100	41.1
9	79.5	11.0	4.6	447	12100	41.3
10	79.4	11.1	4.5	492	12100	41.6
11	79.3	11.1	4.5	514	12100	41.7
12	79.3	11.1	4.5	532	12100	41.9
13	79.2	11.1	4.5	547	12100	42.1
14	79.0	11.1	4.5	567	12100	42.3
15	78.9	11.1	4.5	585	12100	42.6
16	78.8	11.1	4.4	597	12100	42.9
17	78.7	11.1	4.4	603	12100	43.1
18	78.6	11.1	4.4	605	12100	43.2
19	78.5	11.1	4.4	619	12100	43.4
20	78.4	11.2	4.4	626	12100	43.8
21	78.2	11.2	4.4	628	12100	43.9
22	78.1	11.2	4.4	632	12100	44.1
23	78.0	11.2	4.4	635	12100	44.3
24	77.8	11.2	4.3	638	12100	44.5

IMPERFECTION SCAN = $D(\theta)$ (0.001")

$$D(\theta) = A_0 + A_n \cos(n\theta) + B_n \sin(n\theta)$$

TABLE 3.4 SCAN DATA FOR CONSTANT TENSILE STRESS = 12100 PSI ("SET B").

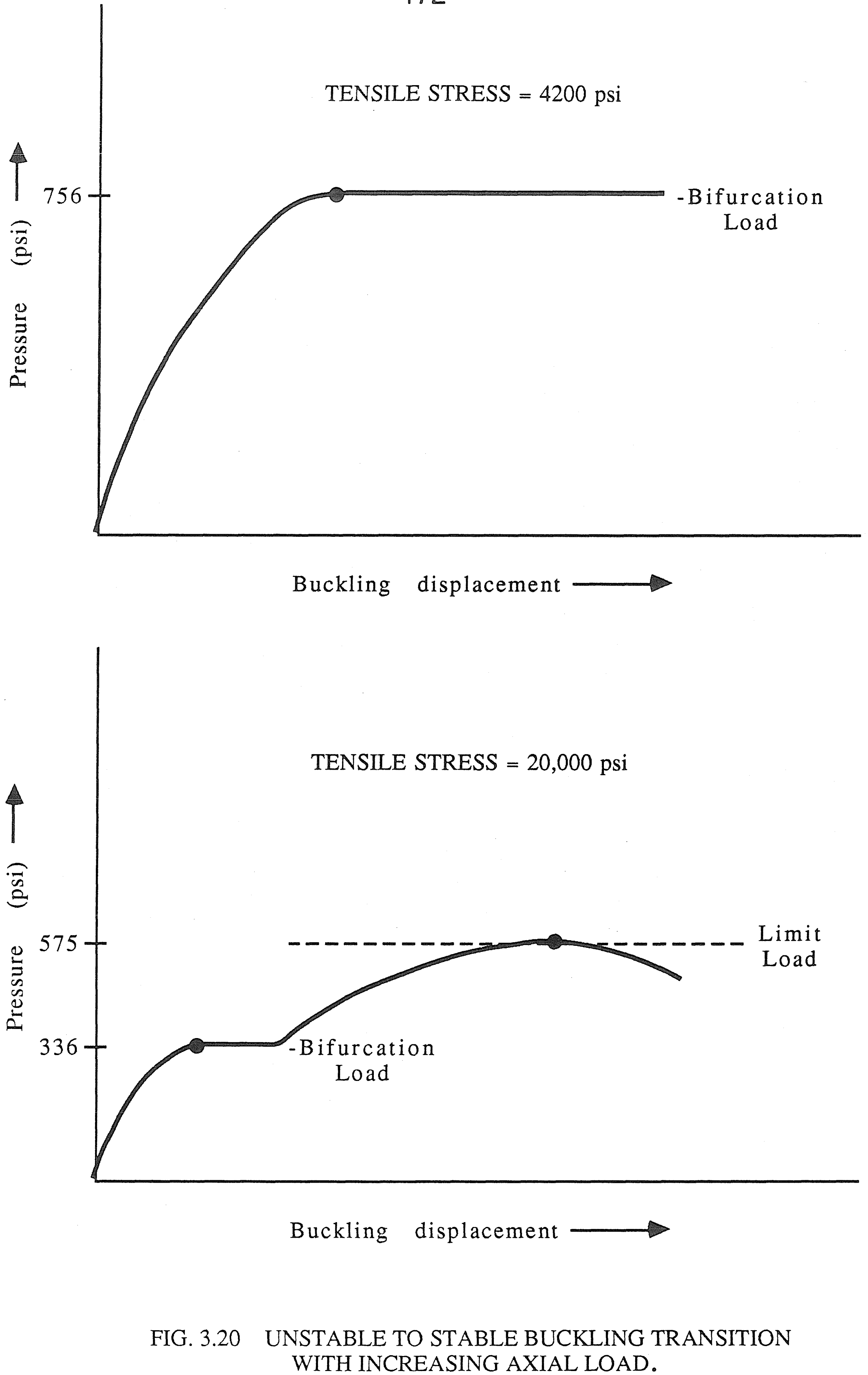

FIG. 3.20 UNSTABLE TO STABLE BUCKLING TRANSITION WITH INCREASING AXIAL LOAD.

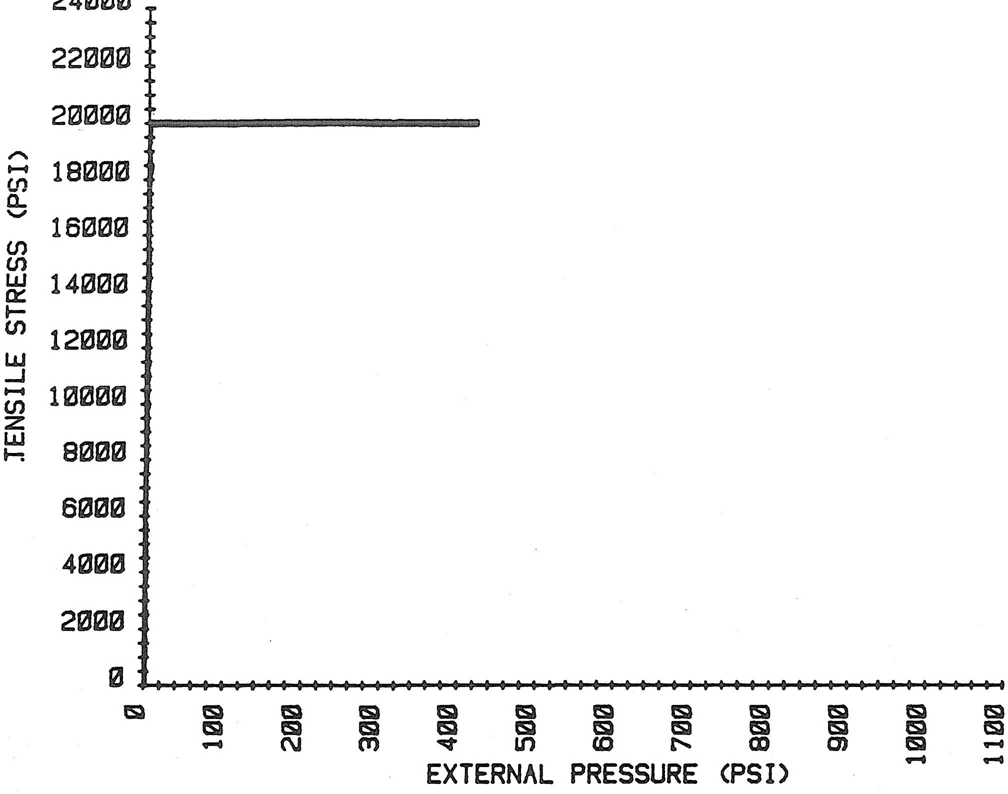

FIG. 3.21a LOAD-PATH DIAGRAM.

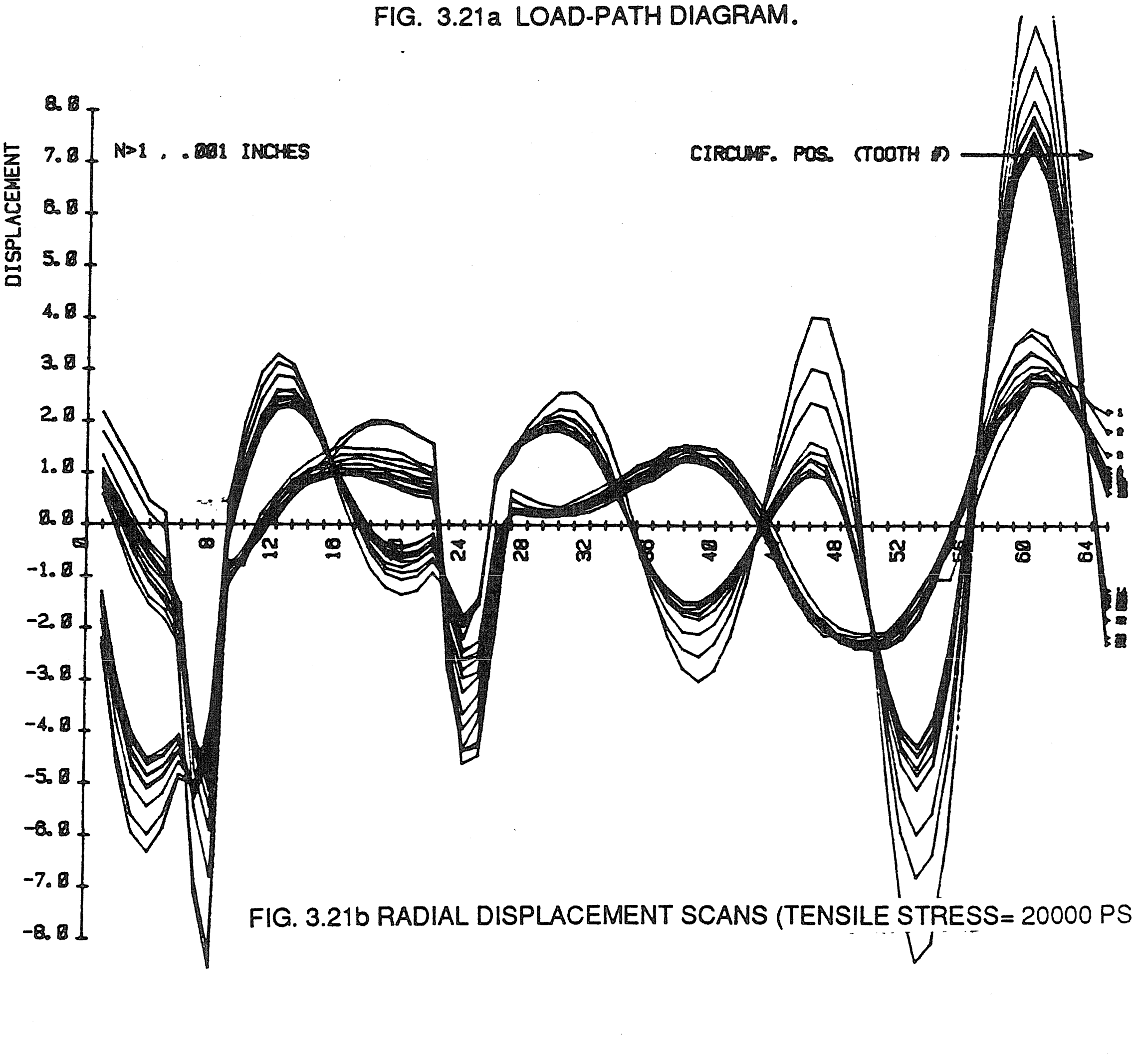

FIG. 3.21b RADIAL DISPLACEMENT SCANS (TENSILE STRESS= 20000 PSI) .

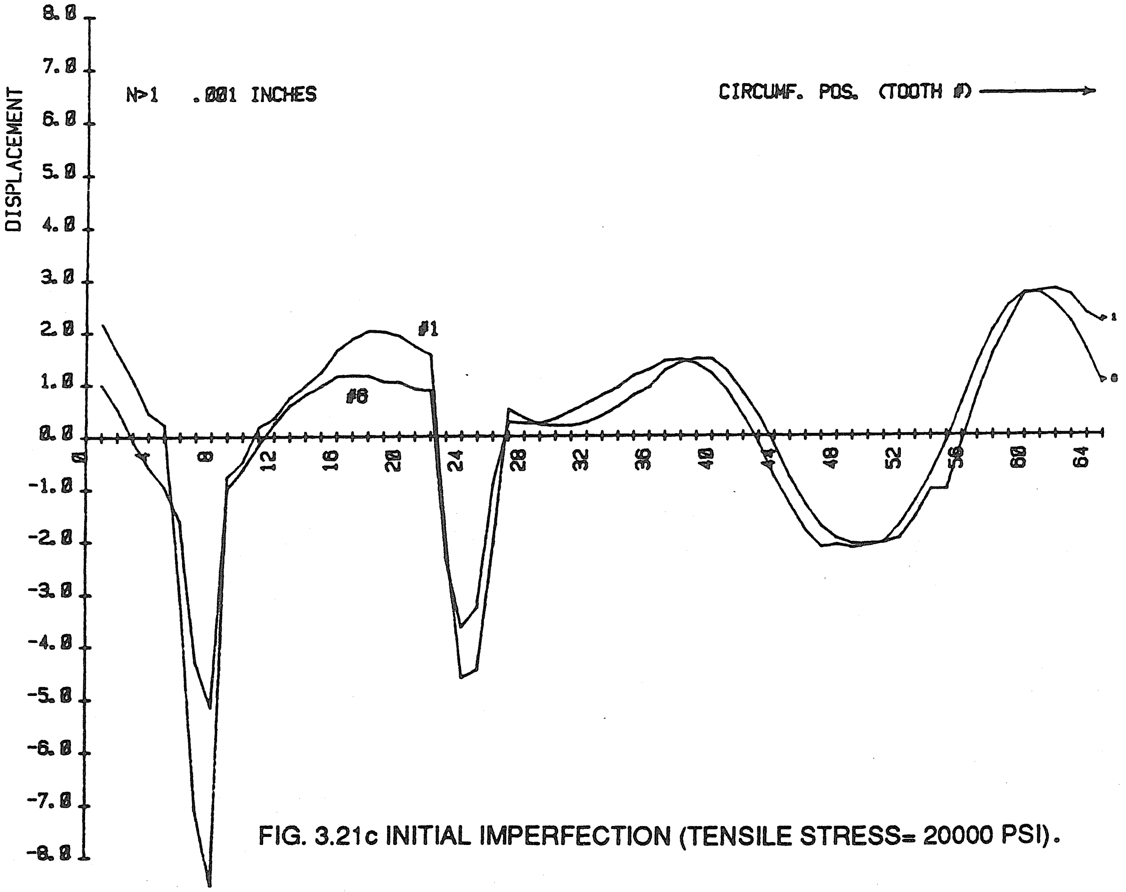

FIG. 3.21c INITIAL IMPERFECTION (TENSILE STRESS= 20000 PSI).

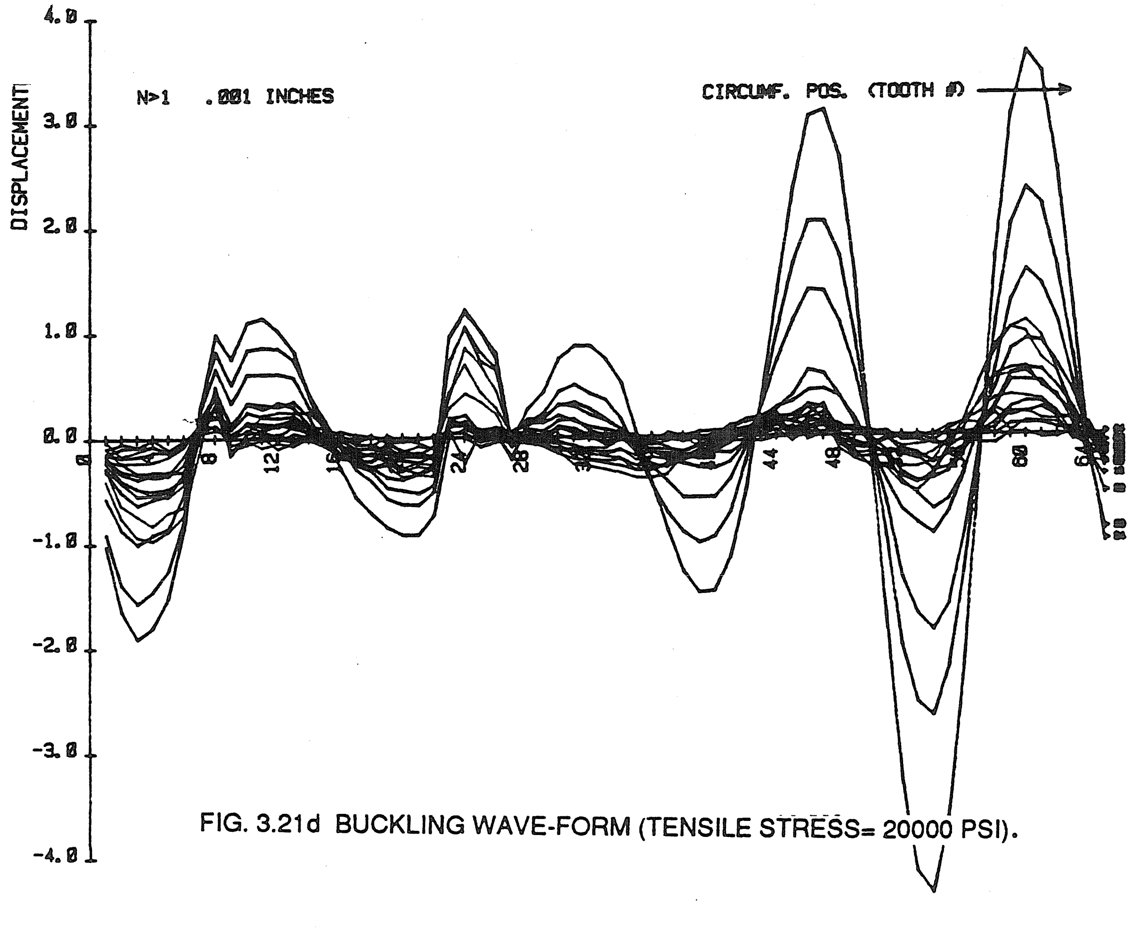

FIG. 3.21d BUCKLING WAVE-FORM (TENSILE STRESS= 20000 PSI).

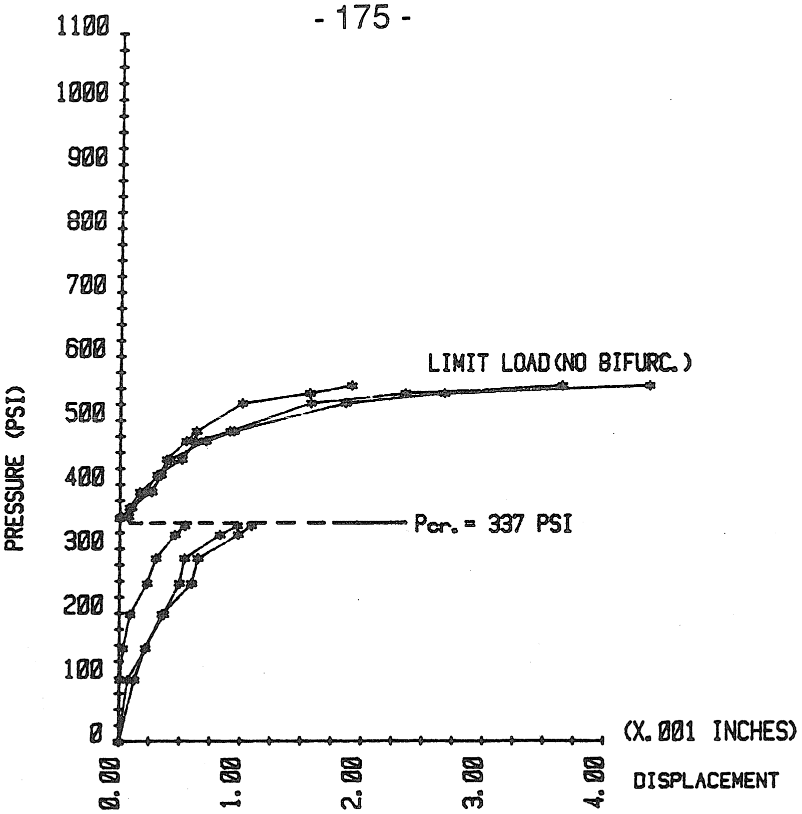

FIG. 3.21e LOAD-DISPLACEMENT (NORMALIZED) PLOT (T.S.= 20000 PSI).

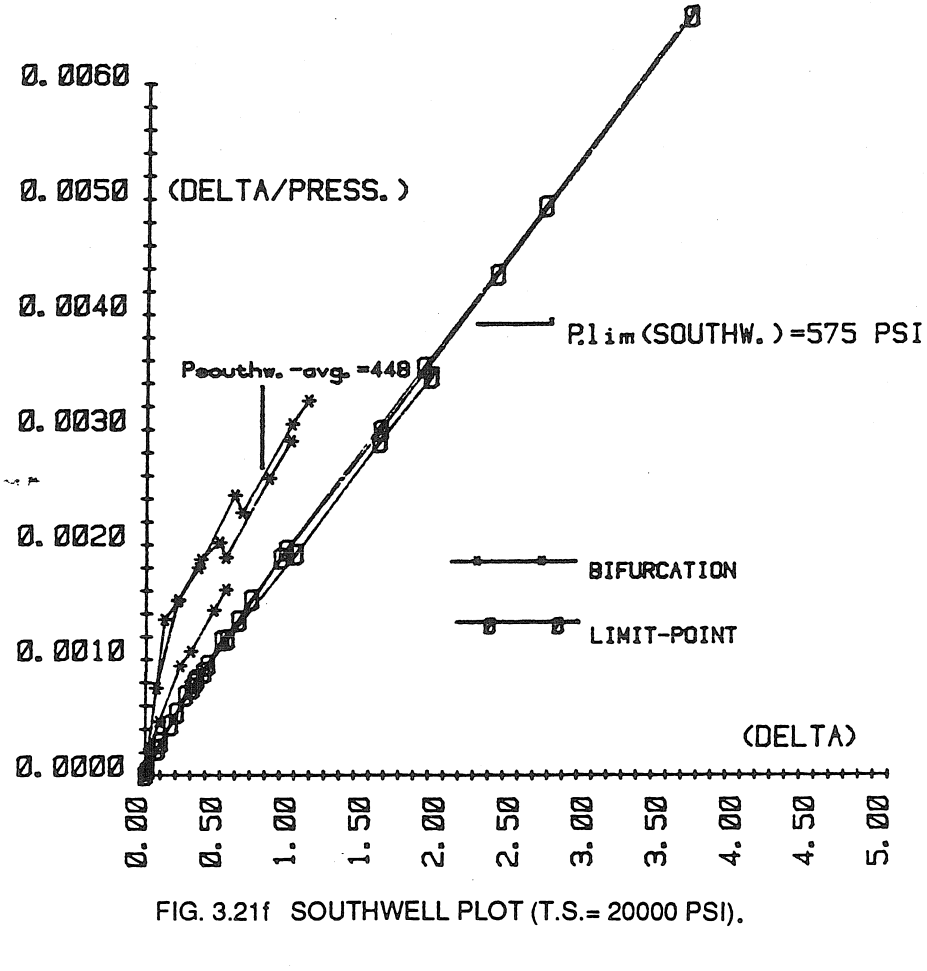

FIG. 3.21f SOUTHWELL PLOT (T.S.= 20000 PSI).

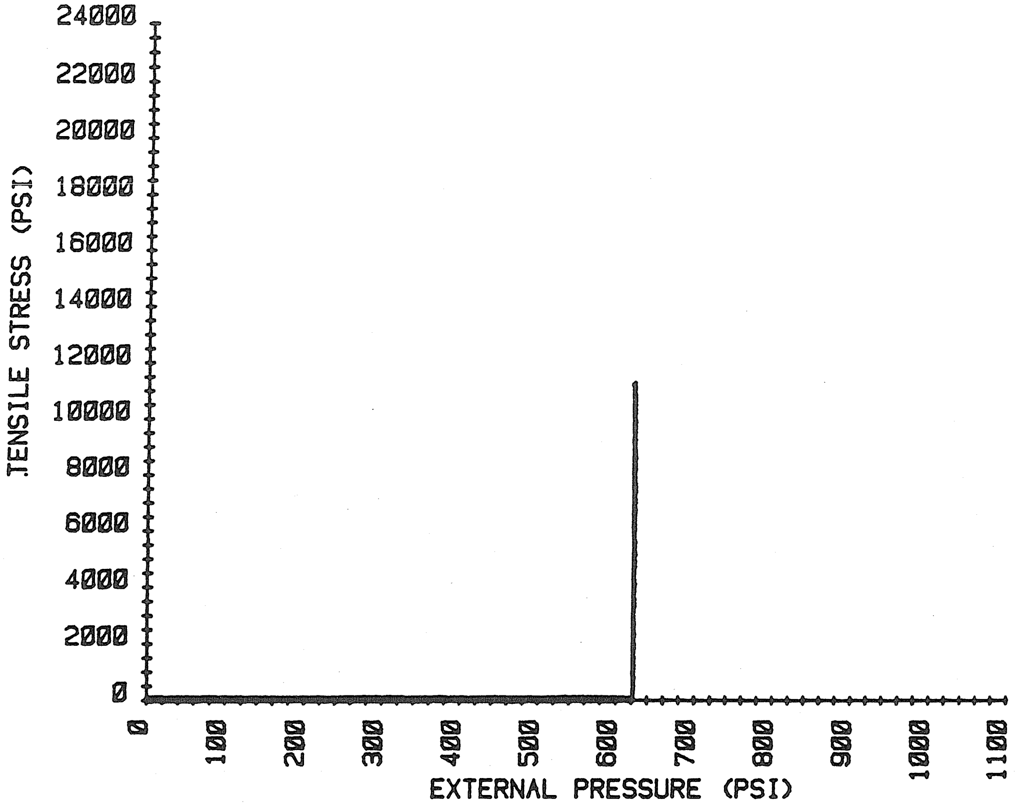

FIG. 3.22a LOAD-PATH DIAGRAM.

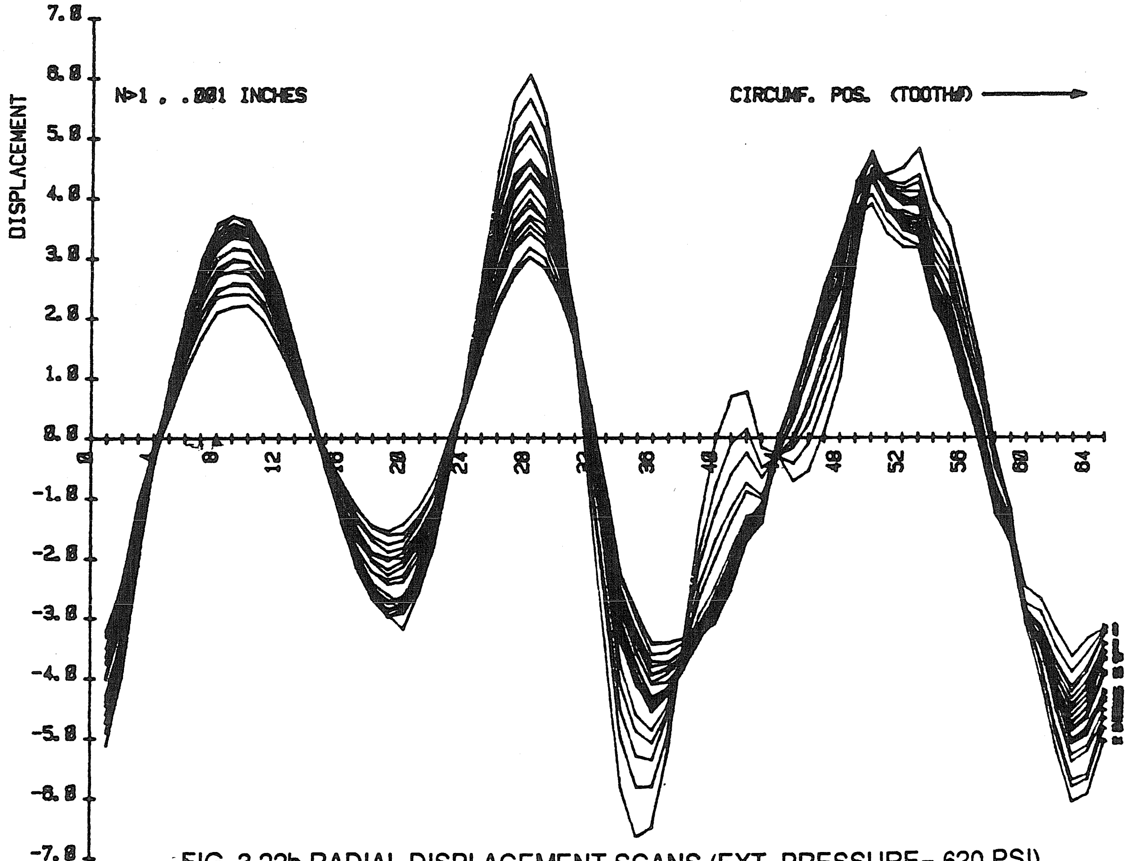

FIG. 3.22b RADIAL DISPLACEMENT SCANS (EXT. PRESSURE= 620 PSI).

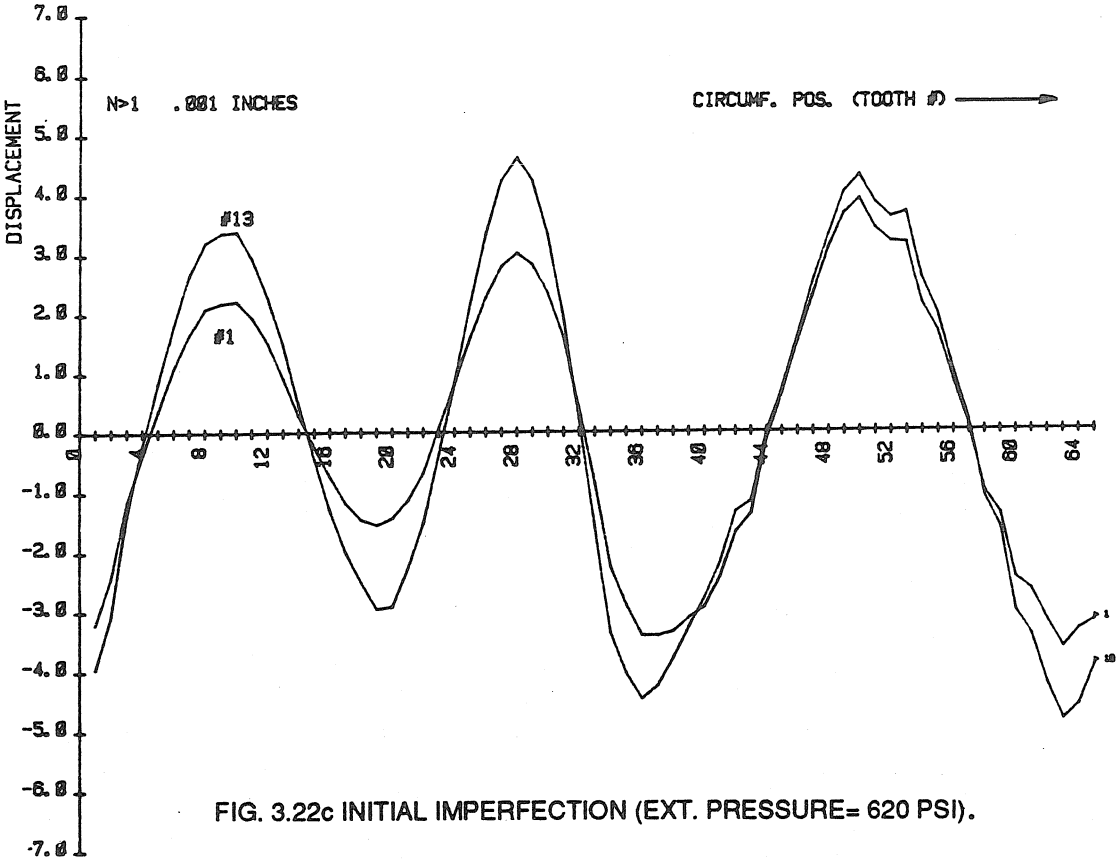

FIG. 3.22c INITIAL IMPERFECTION (EXT. PRESSURE= 620 PSI).

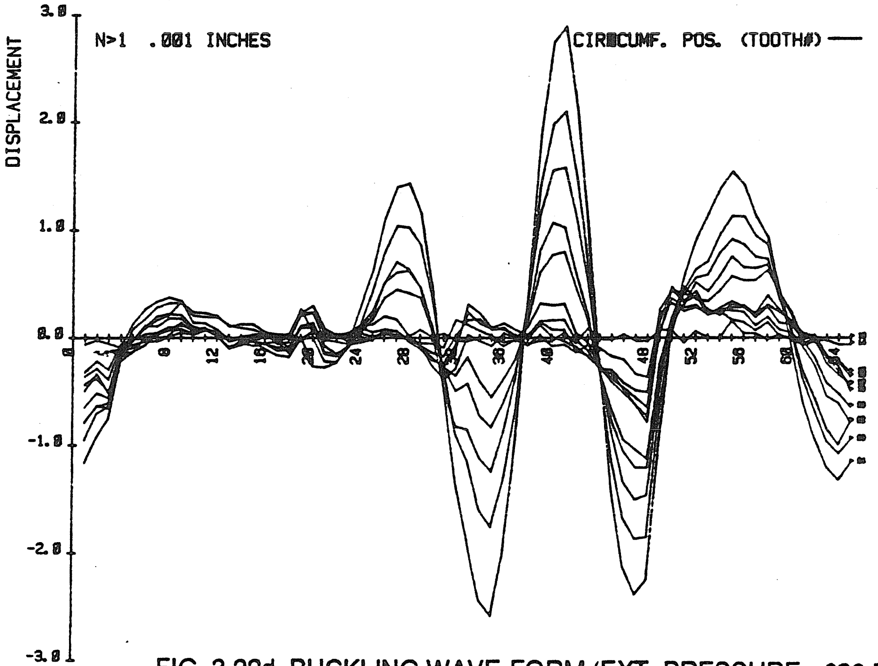

FIG. 3.22d BUCKLING WAVE-FORM (EXT. PRESSURE= 620 PSI).

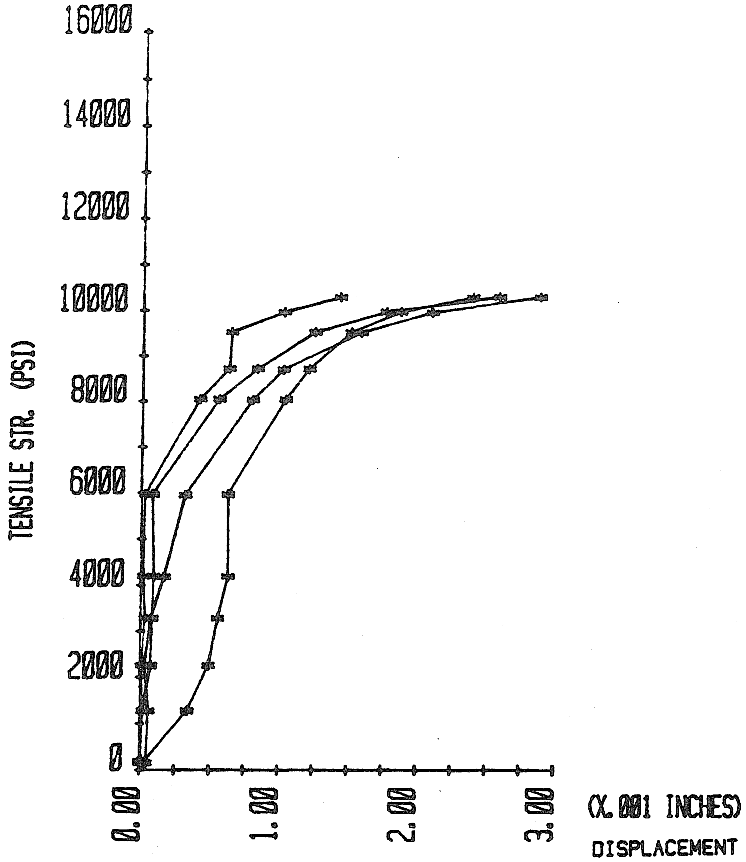

FIG. 3.22e LOAD-DISPLACEMENT (NORMALIZED) PLOT (E.P.= 620 PSI).

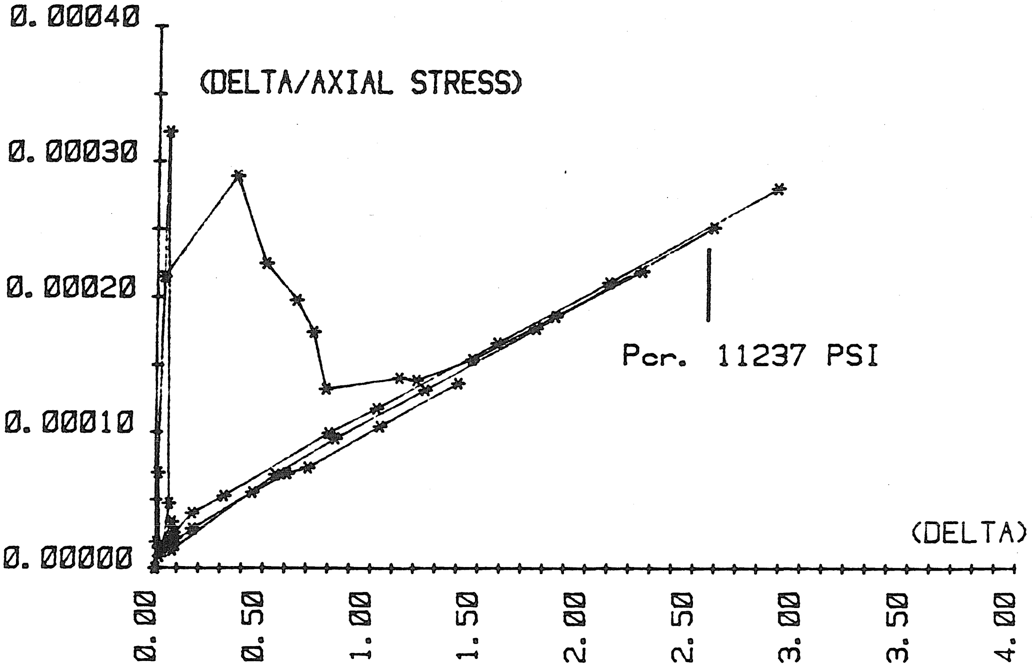

FIG. 3.22f SOUTHWELL PLOT (E.P.= 620 PSI).

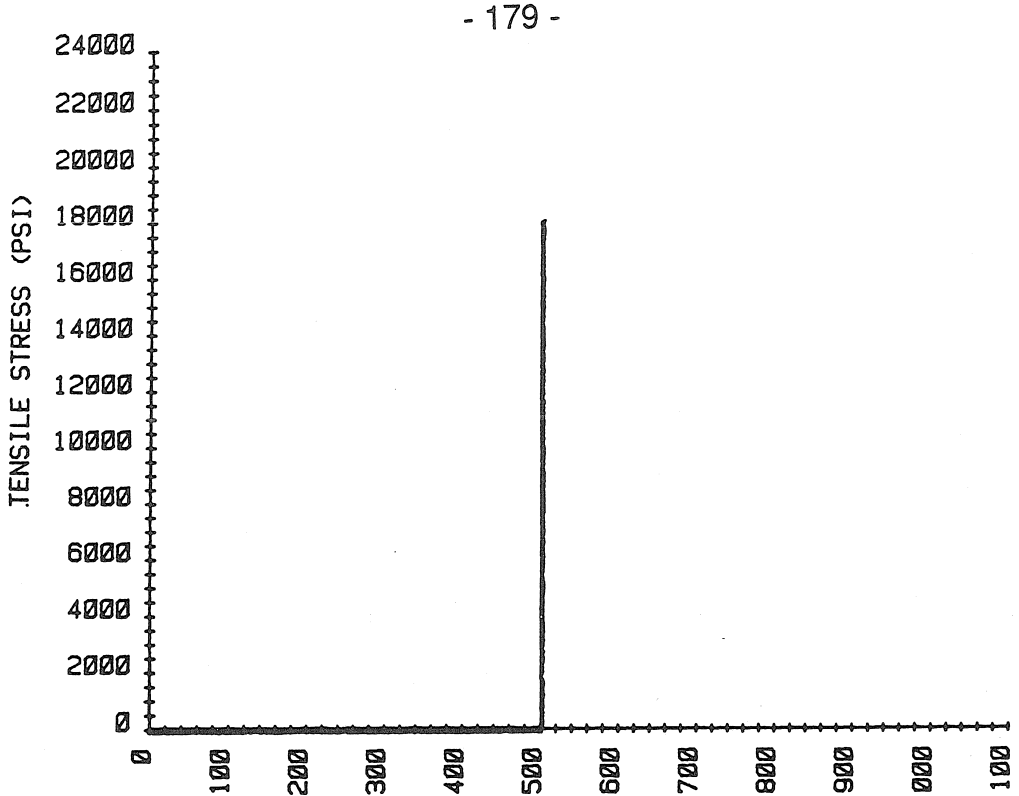

FIG. 3.23a LOAD-PATH DIAGRAM.

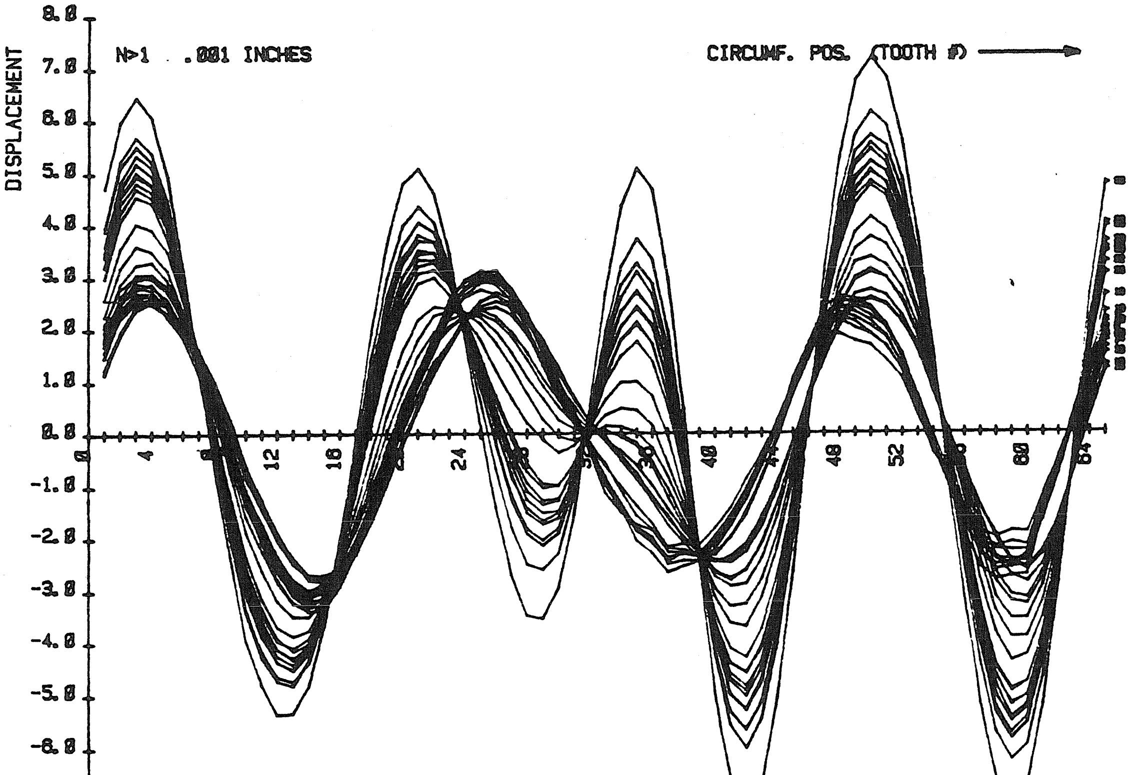

FIG. 3.23b RADIAL DISPLACEMENT SCANS (EXT. PRESSURE= 500 PSI).

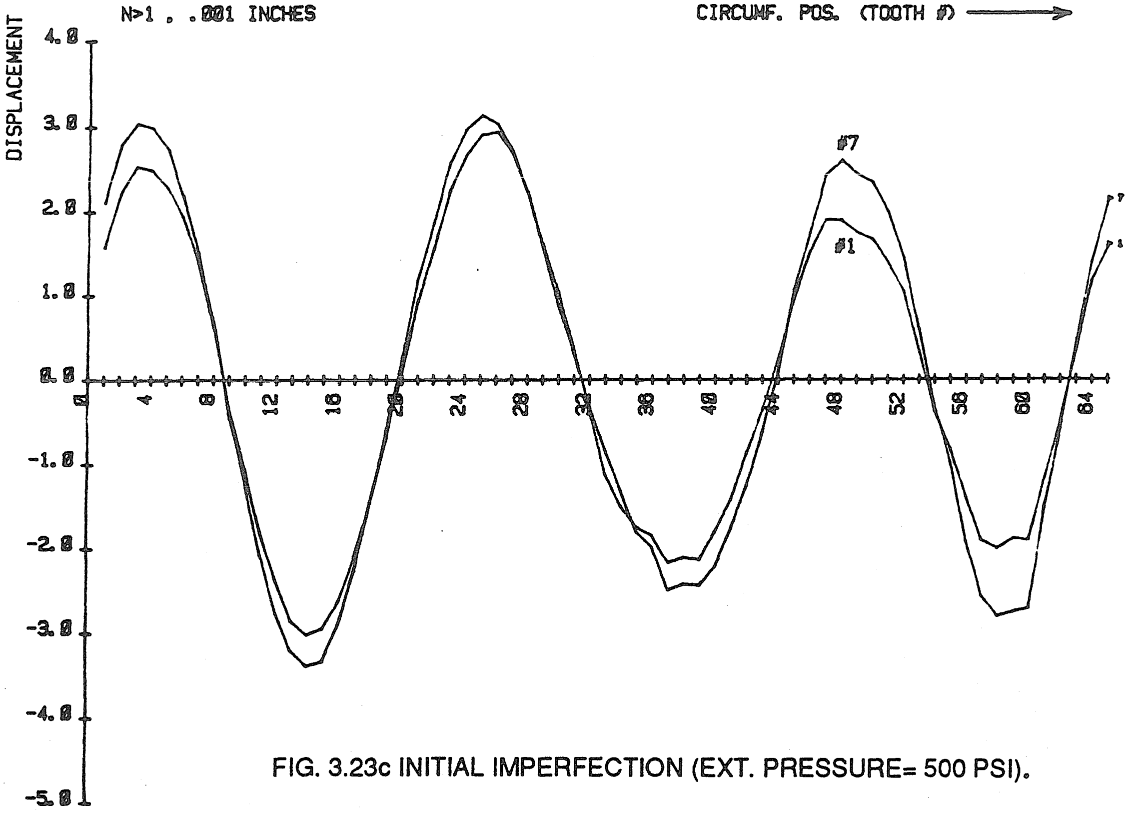

FIG. 3.23c INITIAL IMPERFECTION (EXT. PRESSURE= 500 PSI).

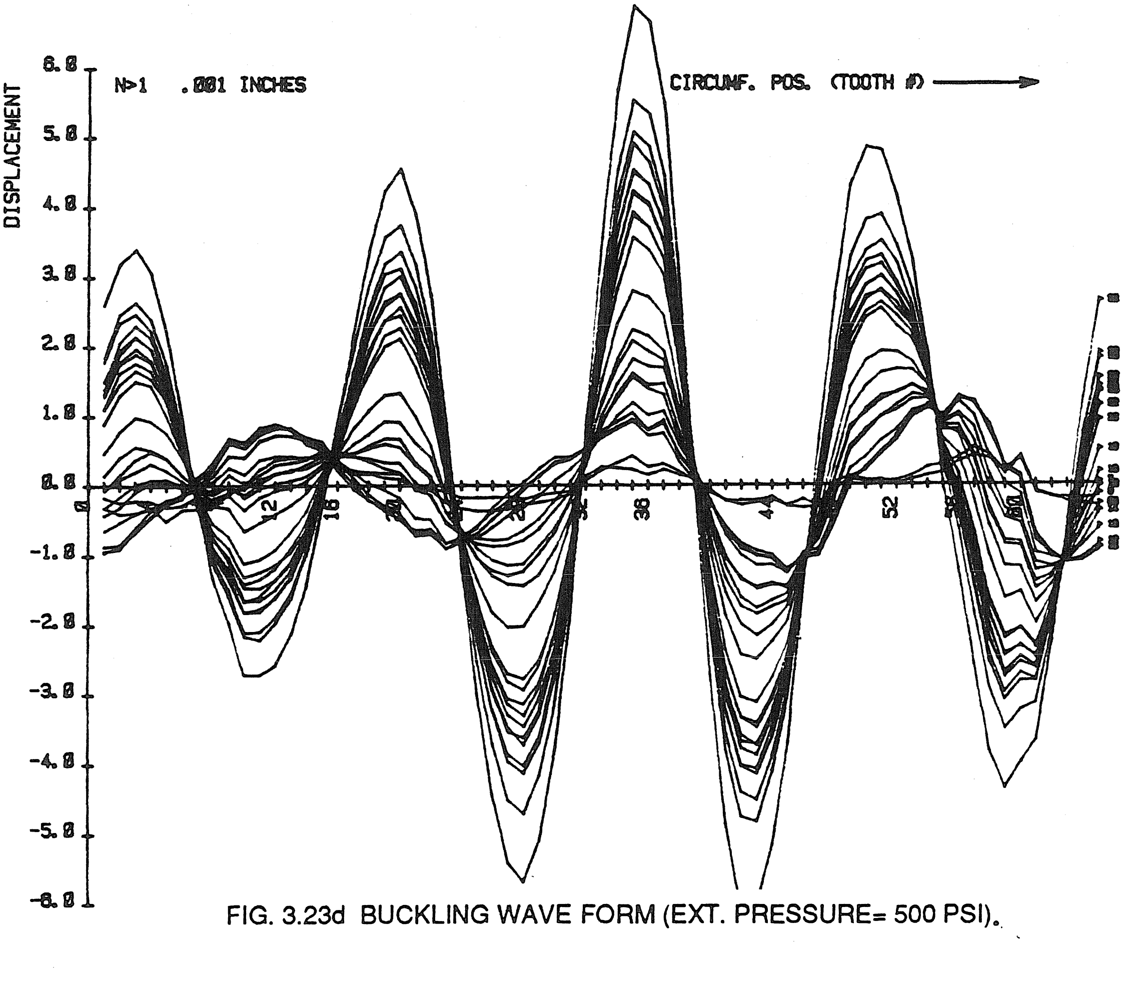

FIG. 3.23d BUCKLING WAVE FORM (EXT. PRESSURE= 500 PSI).

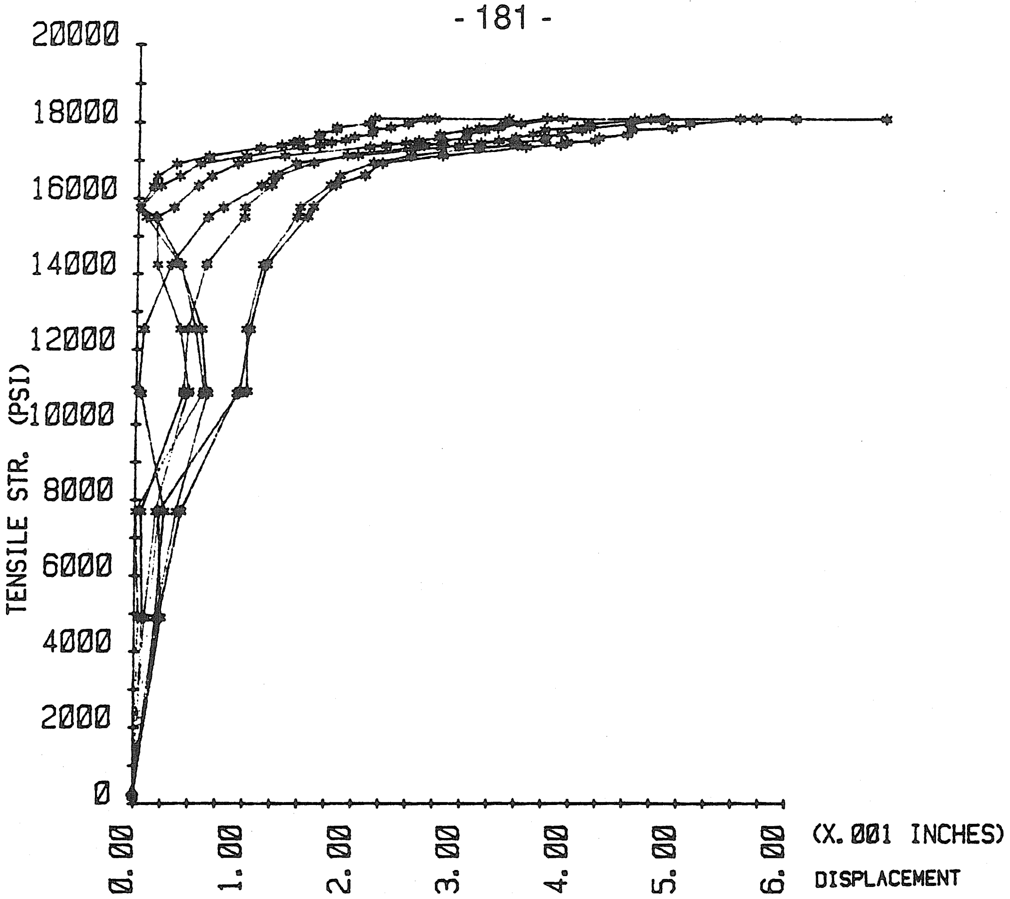

FIG. 3.23e LOAD-DISPLACEMENT (NORMALIZED) PLOT (E.P.= 500 PSI).

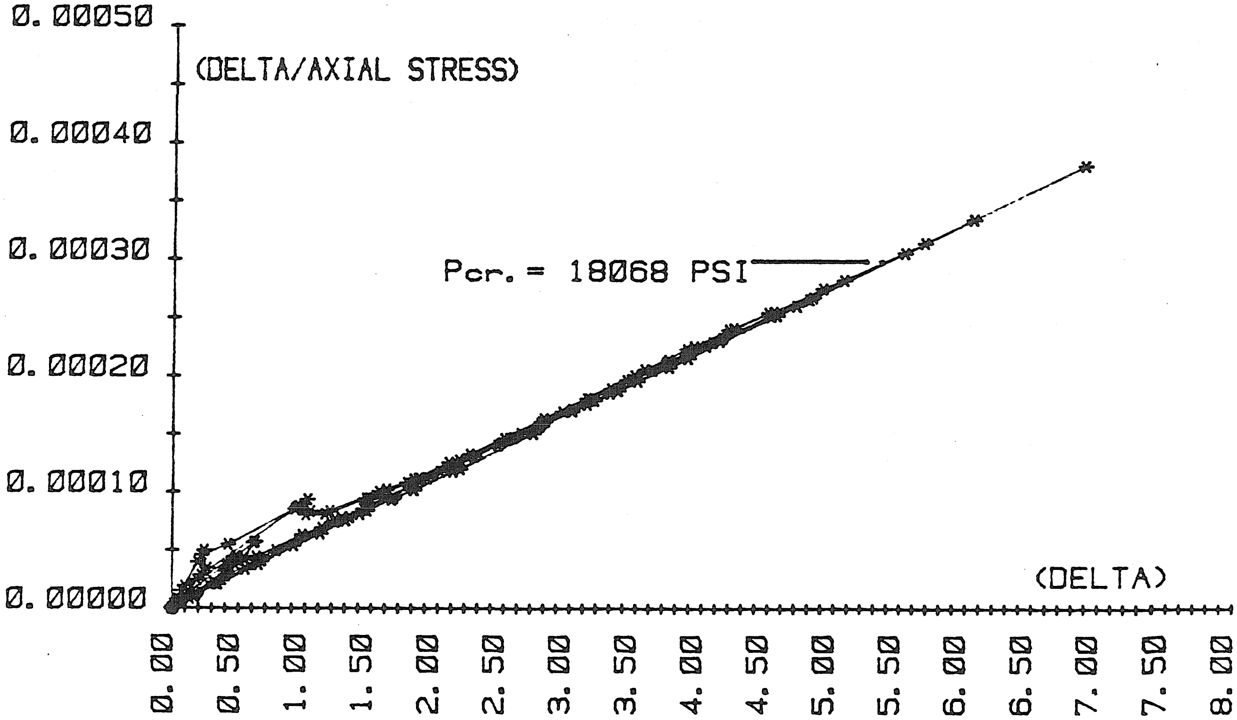

FIG. 3.23f SOUTHWELL PLOT (E.P.= 500 PSI) .

	FOURIER COEFFECIENTS (n=0 & n=1)					
SCAN#	A_0	A_1	B_1	EXT. PRESS.(PSI)	TENSILE STRESS(PSI)	AXIAL DISPLCMT(0.001")
1	104.3	13.1	-0.8	0	0	16.5
2	104.8	13.6	-1.8	0	0	16.5
3	104.7	13.6	-1.7	95	0	16.5
4	104.6	13.6	-1.7	197	0	16.8
5	104.5	13.6	-1.7	298	0	17.0
6	104.3	13.6	-1.7	393	0	17.1
7	104.2	13.6	-1.6	502	0	17.5
8	104.4	13.0	-1.4	500	4900	27.1
9	104.4	12.7	-1.4	500	7700	31.4
10	104.3	12.3	-2.5	500	10830	35.9
11	104.3	12.3	-2.5	500	10900	36.0
12	104.3	12.2	-2.5	500	12540	38.4
13	103.9	12.0	-2.4	500	14250	41.3
14	103.4	11.9	-2.3	500	15500	43.9
15	103.3	11.9	-2.2	500	15760	44.5
16	103.2	12.0	-2.2	500	16340	45.9
17	102.9	11.8	-2.2	500	16590	46.6
18	102.9	11.8	-2.1	500	16910	47.5
19	102.3	11.7	-2.1	500	17100	48.5
20	101.8	11.7	-2.0	500	17320	49.6
21	101.7	11.7	-2.0	500	17380	49.9
22	101.6	11.6	-2.0	500	17450	50.0
23	101.5	11.6	-2.0	500	17500	50.3
24	101. 4	11.6	-2.0	500	17580	50.5
25	101.4	11.6	-2.0	500	17670	50.7
26	101.3	11.6	-2.0	500	17800	51.0
27	101.2	11.6	-1.9	500	17840	51.3
28	101.1	11.5	-1.9	500	17940	51.6
29	101.0	11.5	-1.9	500	18070	52.2

IMPERFECTION SCAN = $D(\theta)$ (0.001")

$D(\theta) = A_0 + A_n \cos(n\theta) + B_n \sin(n\theta)$

TABLE 3.5 SCAN DATA FOR CONSTANT EXTERNAL PRESSURE = 500 PSI ("SET B").

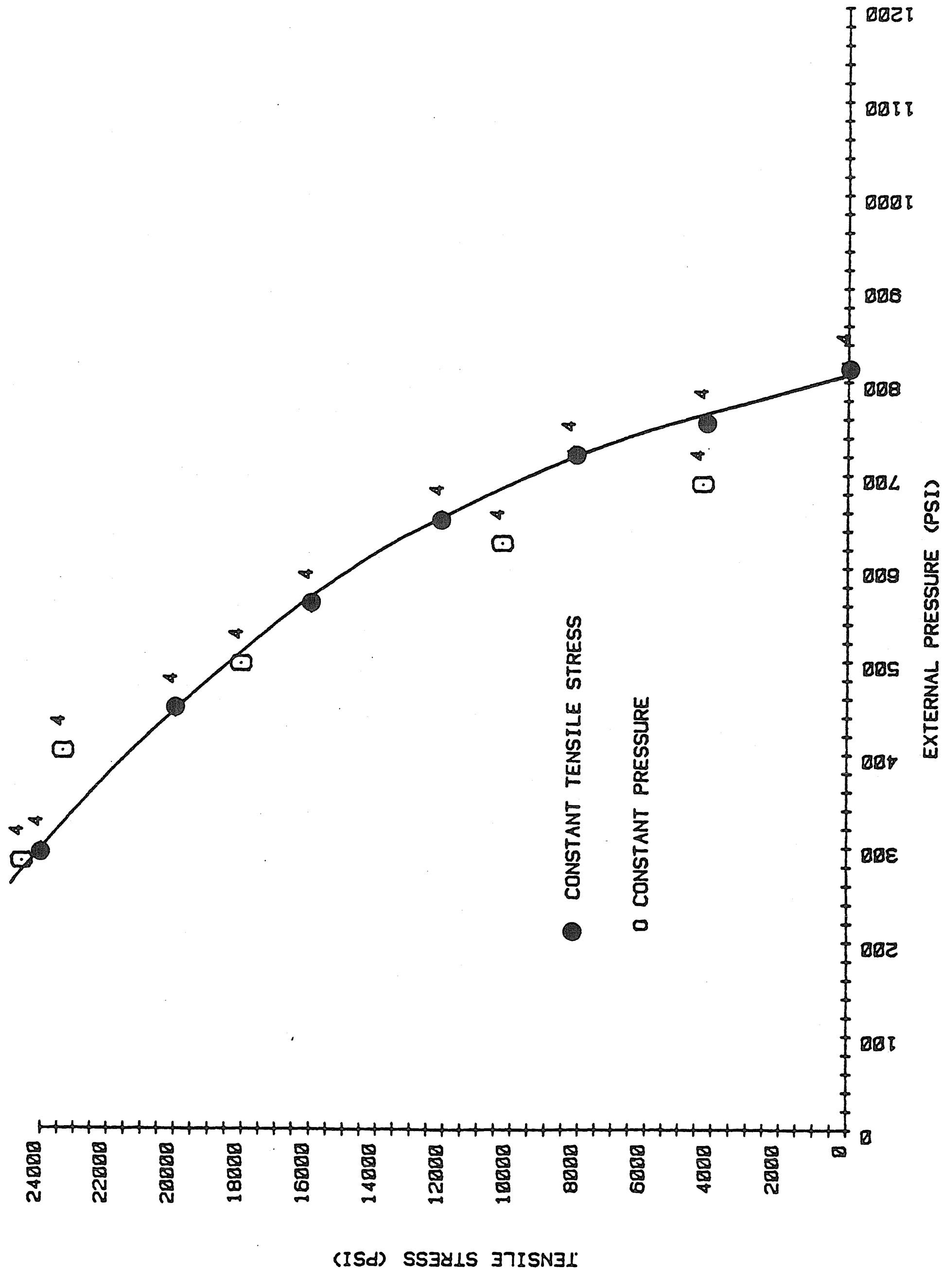

FIG. 3.24 a EXPERIMENTAL RESULTS [SET B] .

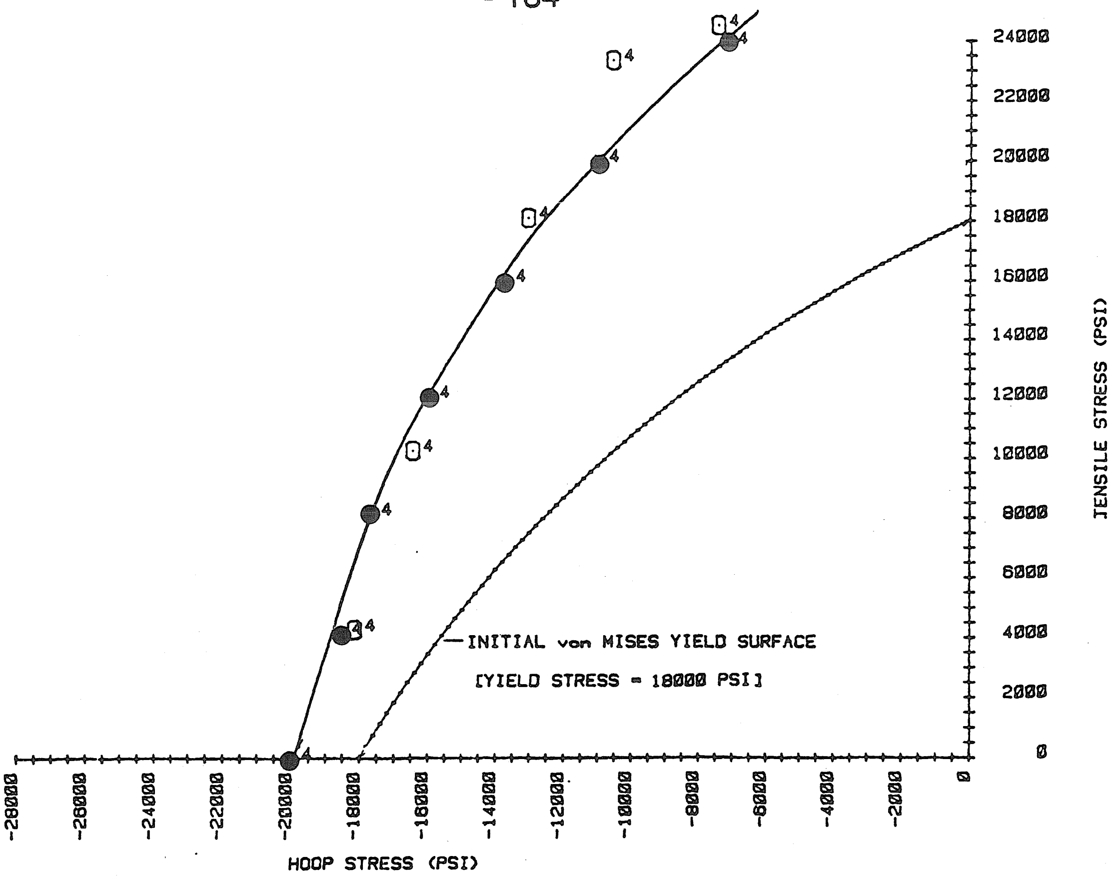

FIG. 3.24 b EXPERIMENTAL RESULTS IN STRESS-SPACE [SET B].

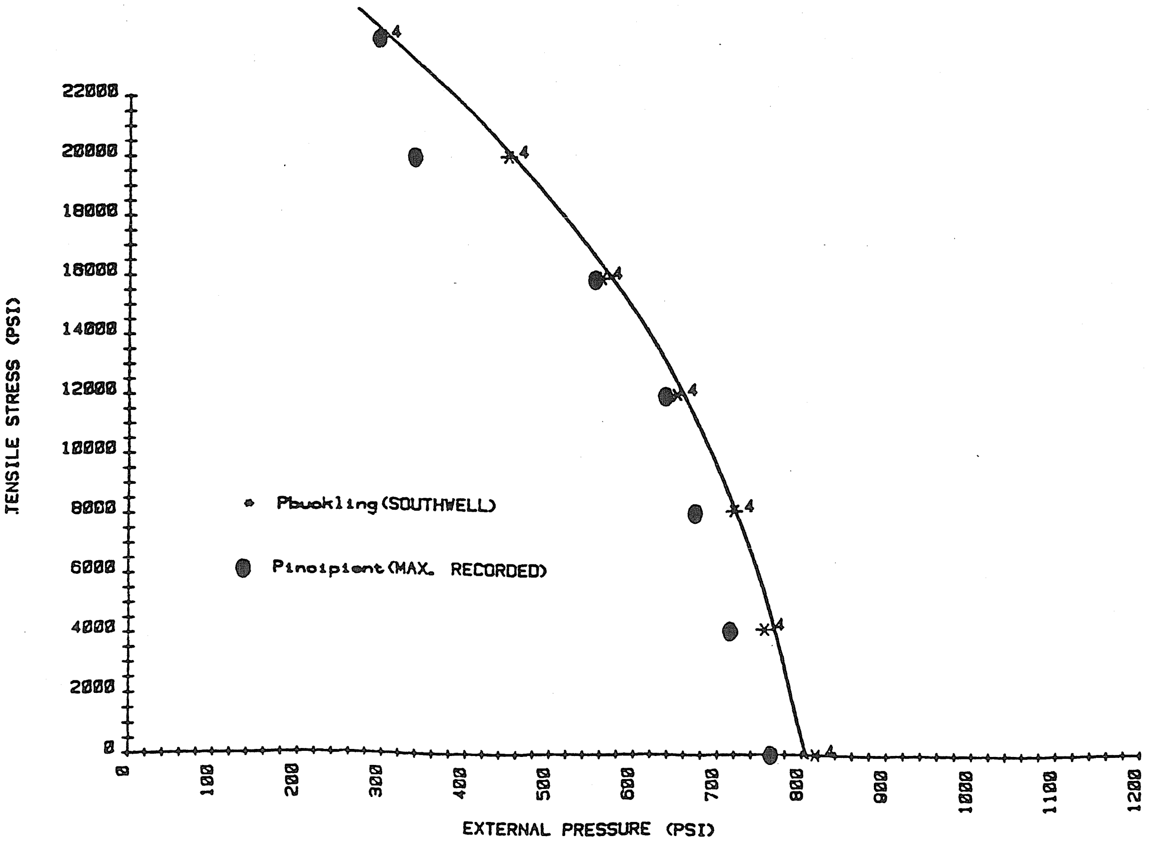

FIG. 3.24 c SOUTHWELL SMOOTHING OF EXPERIMENTAL RESULTS [SET B].

CONSTANT TENSILE STRESS (C.T.S.)

"SET A"				"SET B"			
C.T.S(PSI)	$P_{south.}$(PSI)	$P_{inc.}$(PSI)	CIRCUMF. # WAVES	C.T.S(PSI)	$P_{south.}$(PSI)	$P_{inc.}$(PSI)	CIRCUMF. # WAVES
0 (3.11)	978	932	5	0	816	763	4
2000	959	902	5				
4000	930	909	5	4000 (3.17)	756	707	4
6500	899	849	5				
8300 (3.12)	889	865	4	8180	720	673	4
9600	839	802	4				
10400	857	827	4	12100(3.19)	651	637	4
11000	831	775	4				
12600	815	792	4	16000	"560"	553	4
15000	765	727	4				
16300	750	730	4	20100(3.21)	"575"	335	4
18600	650	690	4				
20600	660	630	4	24000	"366"	295	4
23300(3.14)	612	589	4				

" " = SOUTHWELL INCORRECT AND $P_{inc.}$ USED

CONSTANT EXTERNAL PRESSURE (C.E.P.)

C.E.P. (PSI)	$T.S._{crit.}$(PSI)	# CIRCUMF. WAVES	C.E.P. (PSI)	$T.S._{crit.}$(PSI)	# CIRCUMF. WAVES
850	550	5	690	4300	4
750 (3.15)	11600	4/5	620 (3.22)	10300	4
700	14200	4	500 (3.23)	18200	4
			400	23300	4
			290	24600	4

C.T.S. = CONSTANT TENSILE STRESS
* ALL PRESSURES IN LBS/INCH^2

TABLE 3.6 EXPERIMENTAL RESULTS FROM FIGURES 3.16 AND 3.24.

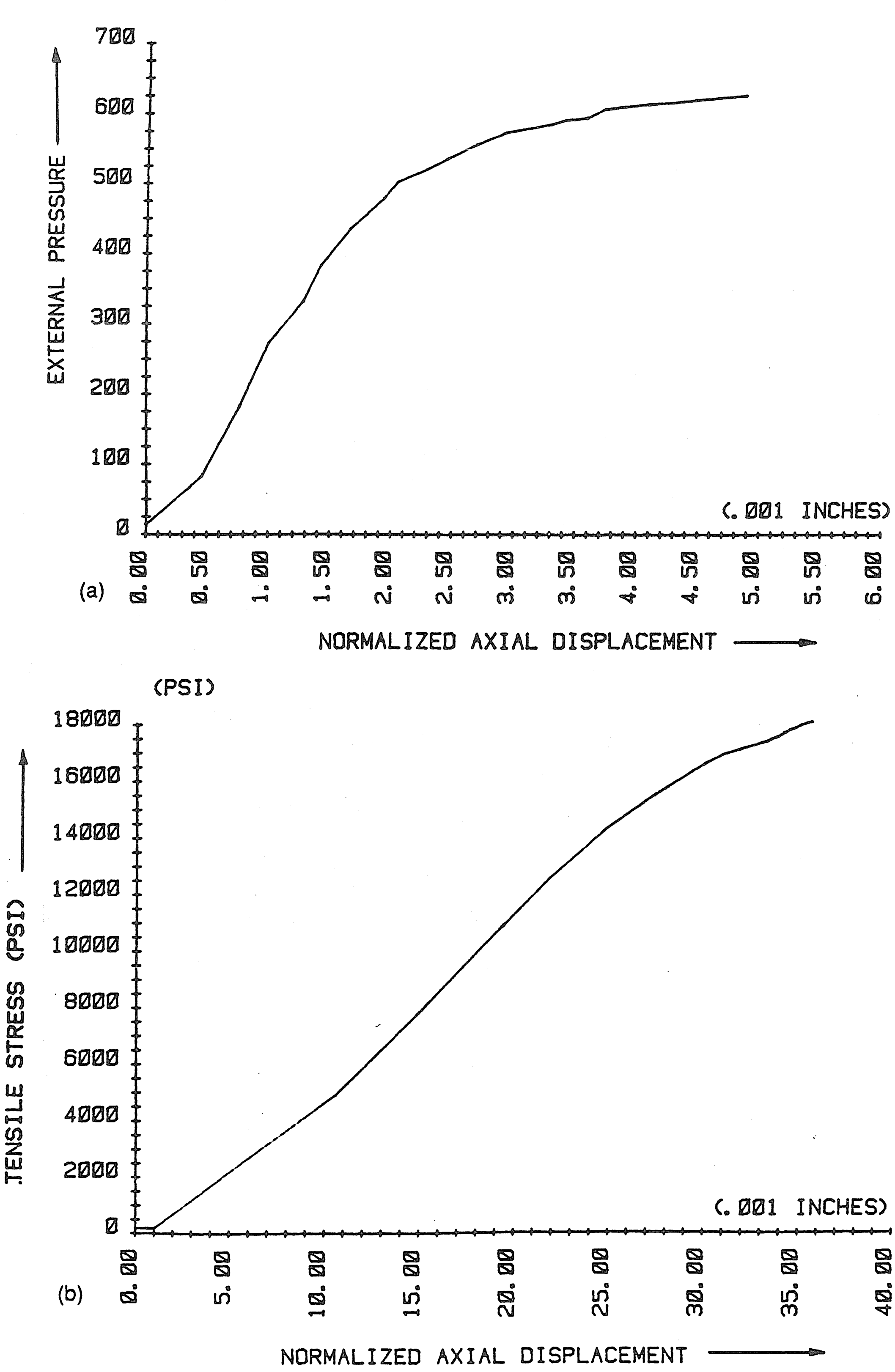

FIG. 2.25 a and b NORMALIZED AXIAL DISPLACEMENT PLOTS FOR; (a) TENSILE STRESS= 12100 PSI, (b) EXTERNAL PRESSURE= 500 PSI.

```
DUA1:[USER.JJG33563]IIII.ALL;120          20-DEC-1987 09:17          Page 1

IIIIIIIIIIIIIIIIIIIIIIIIIIIIIIIIIII
       1        $ NSEG  = number of shell segments (less than 95)
    H           $
    H           $ SEGMENT NUMBER    1    1    1    1    1    1    1    1
    H           $ NODAL POINT DISTRIBUTION FOLLOWS...
      21        $ NMESH=no. of node points (5=min.;98=max.)
       3        $ NTYPEH= control integer (1 or 2 or 3) for nodal point spacing
    H           $ REFERENCE SURFACE GEOMETRY FOLLOWS...
       1        $ NSHAPE= indicator (1,2 or 4) for geometry of meridian
 0.7360000      $ R1      = radius at beginning of segment (see p. P7)
 0.0000000E+00  $ Z1      = axial coordinate at beginning of segment
 0.7360000      $ R2      = radius at end of segment
 0.7500000      $ Z2      = axial coordinate at end of segment
    H           $ IMPERFECTION SHAPE FOLLOWS...
       0        $ IMP   = indicator for imperfection (0=none, 1=some)
    H           $ REFERENCE SURFACE LOCATION RELATIVE TO WALL
       3        $ NTYPEZ= control (1 or 3) for reference surface location
 0.1400000E-01  $ ZVAL  = distance from leftmost surf. to reference surf.
    Y           $ Do you want to print out r(s), r'(s), etc. for this segment?
    H           $ DISCRETE RING INPUT FOLLOWS...
       1        $ NRINGS= number (max=20) of discrete rings in this segment
       2        $ NTYPE = control for identification of ring location (2=z, 3=r)
 0.7500000      $ Z(I)  = axial coordinate of Ith ring, z( 1)
       0        $ NTYPER= type (0 or 1 ) of discrete ring no.( 1)
    H           $ TEMPERATURE INPUT FOLLOWS...
    Y           $ Do you want general information on loading?
       0        $ NTSTAT = number of temperature callout points along meridian
    H           $ PRESSURE INPUT FOLLOWS...
       1        $ NPSTAT = number of meridional callouts for pressure
-1.000000       $ PN = normal pressure, positive as shown on p. P41.
 0.0000000E+00  $ PT = meridional traction, positive along increasing s.
       1        $ ISTEP = control integer for time variation of pressure
    Y           $ Do you want to print out distributed loads along meridian?
    H           $ LINE LOAD INPUT FOLLOWS...
       1        $ LINTYP=control for line loads or disp.(0=none,1=some)
    Y           $ Any axial loads or imposed axial disp. in this seg.?
-1.000000       $ V(K)=axial disp. or load/length of circ. at ring no.( 1)
       2        $ ISTEP1 = pointer to time function associated with V( 1)
    N           $ Any radial loads or imposed radial disp. in this seg.?
    N           $ Any applied meridional rotat. or moments in this seg.?
    H           $ SHELL WALL CONSTRUCTION FOLLOWS...
    N           $ Do you want to include smeared stiffeners?
       1        $ LAYERS = number of layers (max. = 6)
    Y           $ Are all the layers of constant thickness?
       1        $ MATL = type of material for shell wall layer no.( 1)
 0.2800000E-01  $ T(i) = thickness of ith layer (i=1 = leftmost), T( 1)
  3760000.      $ G(i) = shear modulus of ith layer, G( 1)
  9400000.      $ EX(i)= modulus in meridional direction, EX( 1)
  9400000.      $ EY(i)= modulus in circumferential direction, EY( 1)
 0.3000000      $ UXY(i)= Poisson's ratio (EY*UXY = EX*UYX).   UXY( 1)
 0.0000000E+00  $ ALPHA1(i)=coef. thermal exp. in merid. direction, ALPHA1( 1)
 0.0000000E+00  $ ALPHA2(i)=coef. thermal exp. in circ. direction, ALPHA2( 1)
    Y           $ Do you wish to include plasticity in this segment?
    N           $ Do you wish to include creep in this segment?
    Y           $ Is this a new shell wall material?
      14        $ NPOINT = number of points in s.s.curve, layer no.( 1)
       7        $ NITEG=no. integration pts. thru thickness, layer no.( 1)
    Y           $ Do you want to use power law for stress-strain curve?
  23400.00      $ SYP = yield stress (.2%) of material in layer no.( 1)
      16.5      $ POWER=power in power law for strain as f(stress)
 0.0000000E+00  $ SIG(i)=stress coordinates of s-s curve, SIG( 1)
  17000.00      $ SIG(i)=stress coordinates of s-s curve, SIG( 2)
  20000.00      $ SIG(i)=stress coordinates of s-s curve, SIG( 3)
  21000.00      $ SIG(i)=stress coordinates of s-s curve, SIG( 4)
  22000.00      $ SIG(i)=stress coordinates of s-s curve, SIG( 5)
  23000.00      $ SIG(i)=stress coordinates of s-s curve, SIG( 6)
  23500.00      $ SIG(i)=stress coordinates of s-s curve, SIG( 7)
  24000.00      $ SIG(i)=stress coordinates of s-s curve, SIG( 8)
  24500.00      $ SIG(i)=stress coordinates of s-s curve, SIG( 9)
  25000.00      $ SIG(i)=stress coordinates of s-s curve, SIG(10)
  25500.00      $ SIG(i)=stress coordinates of s-s curve, SIG(11)
  26000.00      $ SIG(i)=stress coordinates of s-s curve, SIG(12)
  27000.00      $ SIG(i)=stress coordinates of s-s curve, SIG(13)
  27500.00      $ SIG(i)=stress coordinates of s-s curve, SIG(14)
    Y           $ Do you want to have C(i,j) printed for this segment?
    H           $ END OF DATA FOR THIS SEGMENT
```

FIG. 4.1 ELEMENT OR LOCAL INPUT FILE [BOSOR5].

```
      H          $ GLOBAL DATA BEGINS...
      H          $ LOADING TIME FUNCTIONS FOLLOW
      N          $ Do you want information on time functions for loading?
         1       $ IUTIME = control for time increment (0 or 1). IUTIME
  10.00000       $ DTIME = time increment
  1500.000       $ TMAX = maximum time to be encountered during this case
         2       $ NFTIME= number of different functions of time
         4       $ NPOINT=no. of points j for ith load factor F(i,j). i=( 1)
         4       $ NPOINT=no. of points j for ith load factor F(i,j). i=( 2)
0.0000000E+00    $ T(i,j)=jth time callout for ith time function, j =( 1)
  40.00000       $ T(i,j)
  120.0000       $ T(i,j)
  1120.000       $ T(i,j)=jth time callout for ith time function, j =( 4)
0.0000000E+00    $ F(i,j)=jth value for ith load factor. j =( 1)
  000.0000       $ F(i,j)
  200.0000       $ F(i,j)=jth value for ith load factor. j =( 3)
 1200.0000       $ F(i,j)
0.0000000E+00    $ T(i,j)=jth time callout for ith time function, j =( 1)
  40.00000       $ T(i,j)=jth time callout for ith time function, j =( 2)
  120.0000       $ T(i,j)
  1120.000       $ T(i,j)=jth time callout for ith time function, j =( 4)
  200.0000       $ F(i,j)=jth value for ith load factor. j =( 1)
  400.0000       $ F(i,j)=jth value for ith load factor. j =( 2)
  400.0000       $ F(i,j)=jth value for ith load factor. j =( 3)
  400.0000       $ F(i,j)
     H           $ CONSTRAINT CONDITIONS FOLLOW....
        1        $ How many segments are there in the structure?
     H           $
     H           $ CONSTRAINT CONDITIONS FOR SEGMENT NO.    1     1     1     1
     H           $ POLES INPUT FOLLOWS...
        0        $ Number of poles (places where r=0) in SEGMENT
     H           $ INPUT FOR CONSTRAINTS TO GROUND FOLLOWS...
        2        $ At how many stations is this segment constrained to ground?
        1        $ INODE = nodal point number of constraint to ground, INODE( 1)
        1        $ IUSTAR=axial displacement constraint (0 or 1 or 2)
        0        $ IVSTAR= circumferential displacement (0=free, 1=constrained)
        0        $ IWSTAR=radial displacement(0=free,1=constrained,2=imposed)
        1        $ ICHI=meridional rotation (0=free,1=constrained,2=imposed)
0.0000000E+00    $ D1    = radial component of offset of ground support
0.0000000E+00    $ D2    = axial component of offset of ground support
     Y           $ Is this constraint the same for both prebuckling and buckling?
       21        $ INODE = nodal point number of constraint to ground, INODE( 2)
        0        $ IUSTAR=axial displacement constraint (0 or 1 or 2)
        1        $ IVSTAR= circumferential displacement (0=free, 1=constrained)
        1        $ IWSTAR=radial displacement(0=free,1=constrained,2=imposed)
        1        $ ICHI=meridional rotation (0=free,1=constrained,2=imposed)
0.0000000E+00    $ D1    = radial component of offset of ground support
0.0000000E+00    $ D2    = axial component of offset of ground support
     N           $ Is this constraint the same for both prebuckling and buckling?
        1        $ IUSTARB= axial displacement for buckling or vibration phase
        1        $ IVSTARB= circ. displacement for buckling or vibration phase
        1        $ IWSTARB= radial displacement for buckling or vibration
        1        $ ICHIB  = meridional rotation for buckling or vibration
     H           $ JUNCTION CONDITION INPUT FOLLOWS...
     N           $ Is this segment joined to any lower-numbered segments?
     H           $ RIGID BODY CONSTRAINT INPUT FOLLOWS...
     N           $ Given existing constraints, are rigid body modes possible?

_DUA1:[USER.JJG33563]IIII.IMP;157          20-DEC-1987 09:19          Page 1

      -2         $ INDIC = analysis type indicator (0 or -2 or -3). INDIC
    N            $ Type HELP or H for more information on INDIC, N for "no more"
       0         $ IDEFORM=indicator (0 or 1) for type of plasticity theory
       0         $ ICPRE = control (0 or 1) for type of eigenvalue problem
    N            $ Do you want to reverse the rate of loading?
       0         $ KSTEP = starting time step number
      39         $ KMAX = maximum (less than 49) time step number
       9         $ MAXTRL =  maximum number of trials at each load level
       9         $ ITMAX = maximum number of Newton iterations for each trial
       1         $ ITIME = control (0 or 1) for time increments
    N            $ Do you wish to force the material to remain elastic?
       4         $ NOB   = starting number of circ. waves (buckling analysis)
       2         $ NMINB = minimum number of circ. waves  (buckling analysis)
       7         $ NMAXB = maximum number of circ. waves  (buckling analysis)
       1         $ INCRB = increment in number of circ. waves (buckling)
       0         $ TIME = starting time (need not be zero in initial run)
  40.00000       $ DTIME = new time increment
    Y            $ Do you want stations where plastic flow occurs listed?
```

FIG. 4.2 GLOBAL INPUT FILE [BOSOR5].

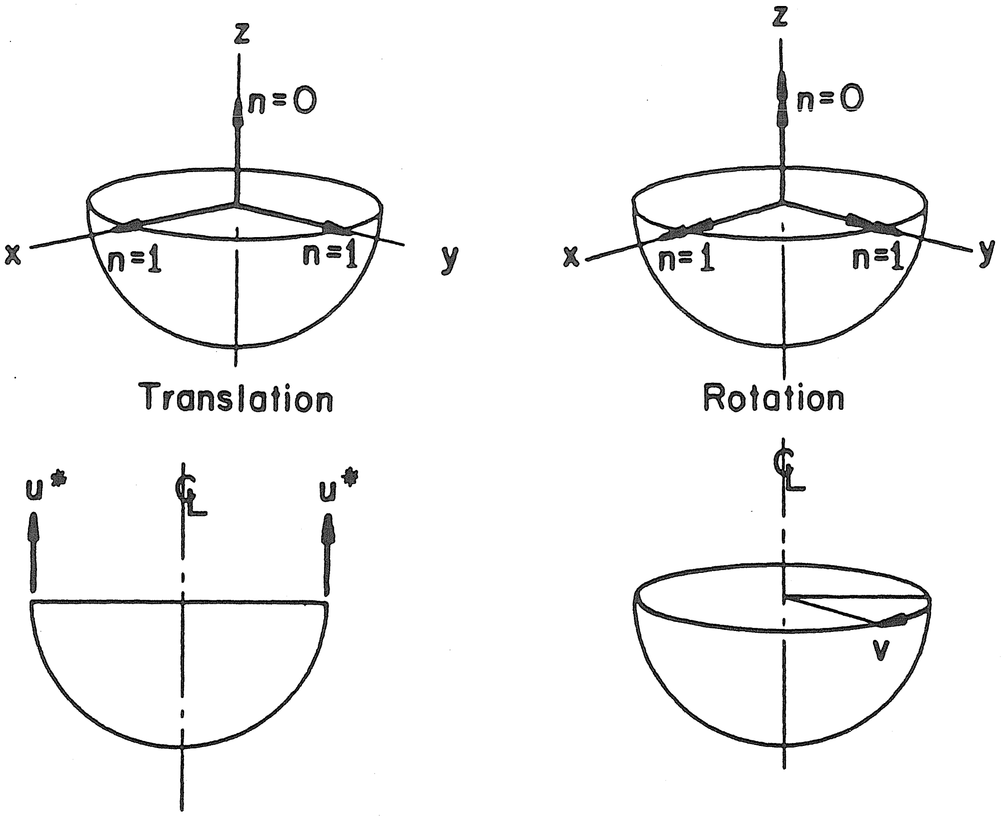

<u>The constraint u* = 0 prevents:</u>

(1) Translation along z-axis (n=0)
(2) Rotation about x-axis (n=1)
(3) Rotation about y-axis (n=2)

<u>The constraint v = 0 prevents:</u>

(1) Rotation about z-axis (n=0)
(2) Translation along x-axis (n=1)
(3) Translation along y-axis (n=2)

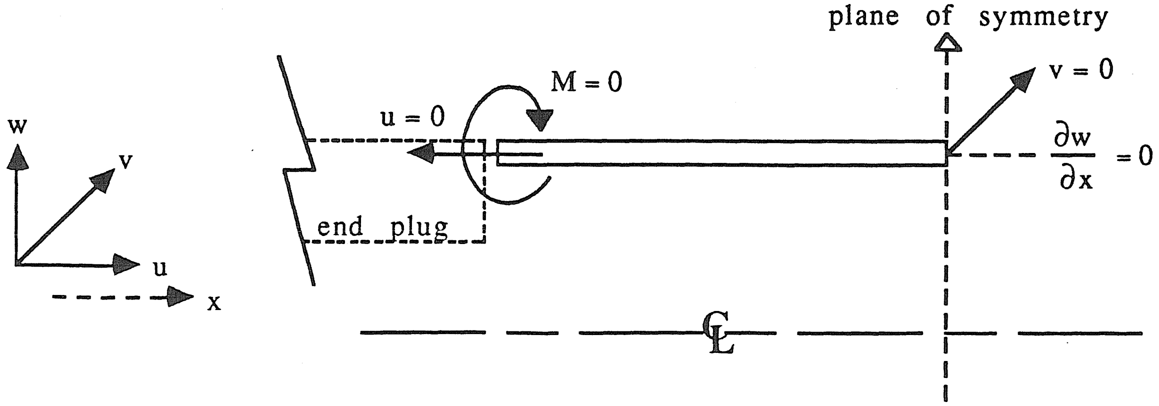

FIG. 4.3 RIGID BODY MOTIONS AND TEST SHELL END CONDITION MODELING.

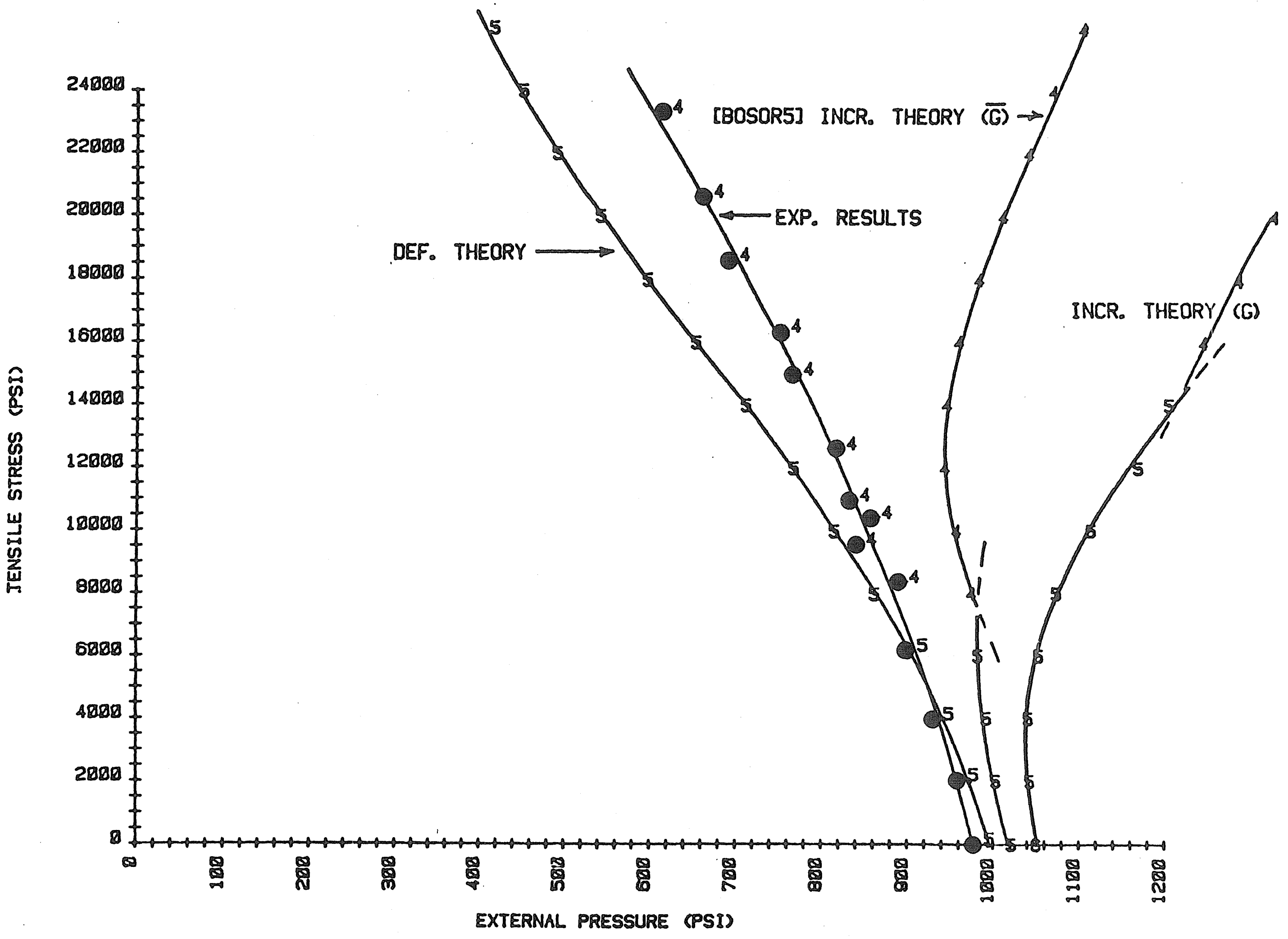

FIG. 4.4 NUMERICAL (BOSOR5) AND EXPERIMENTAL RESULTS [SET A].

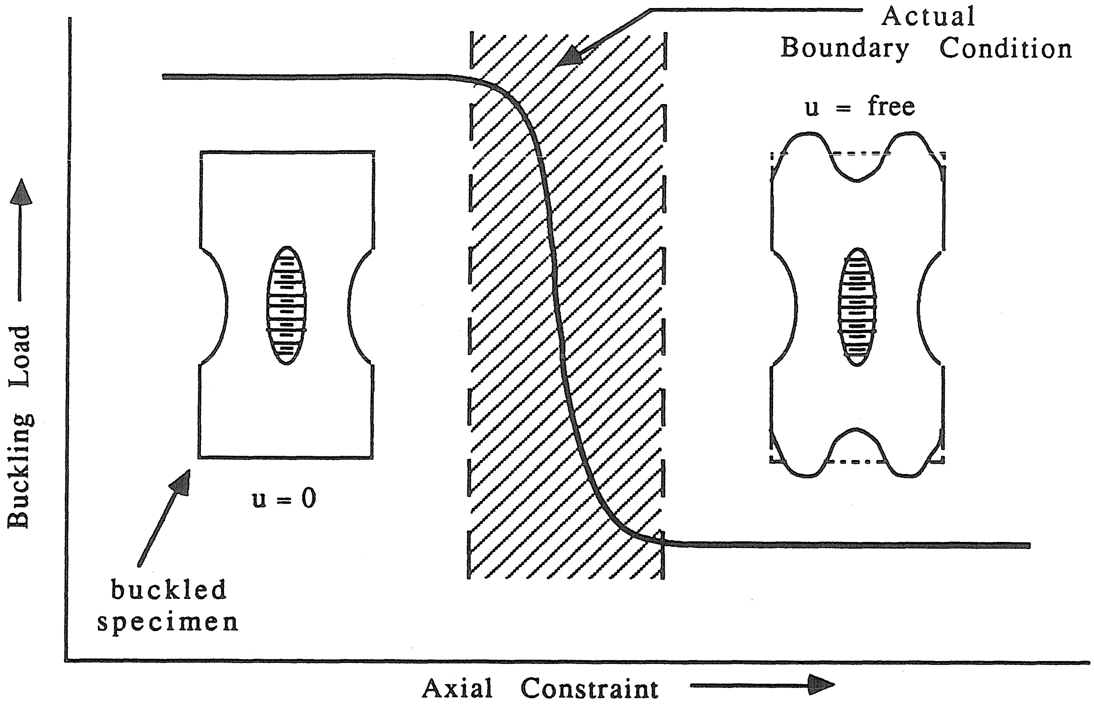

FIG. 4.5a INFLUENCE OF THE IN-PLANE END CONDITION ON THE BUCKLING LOAD.

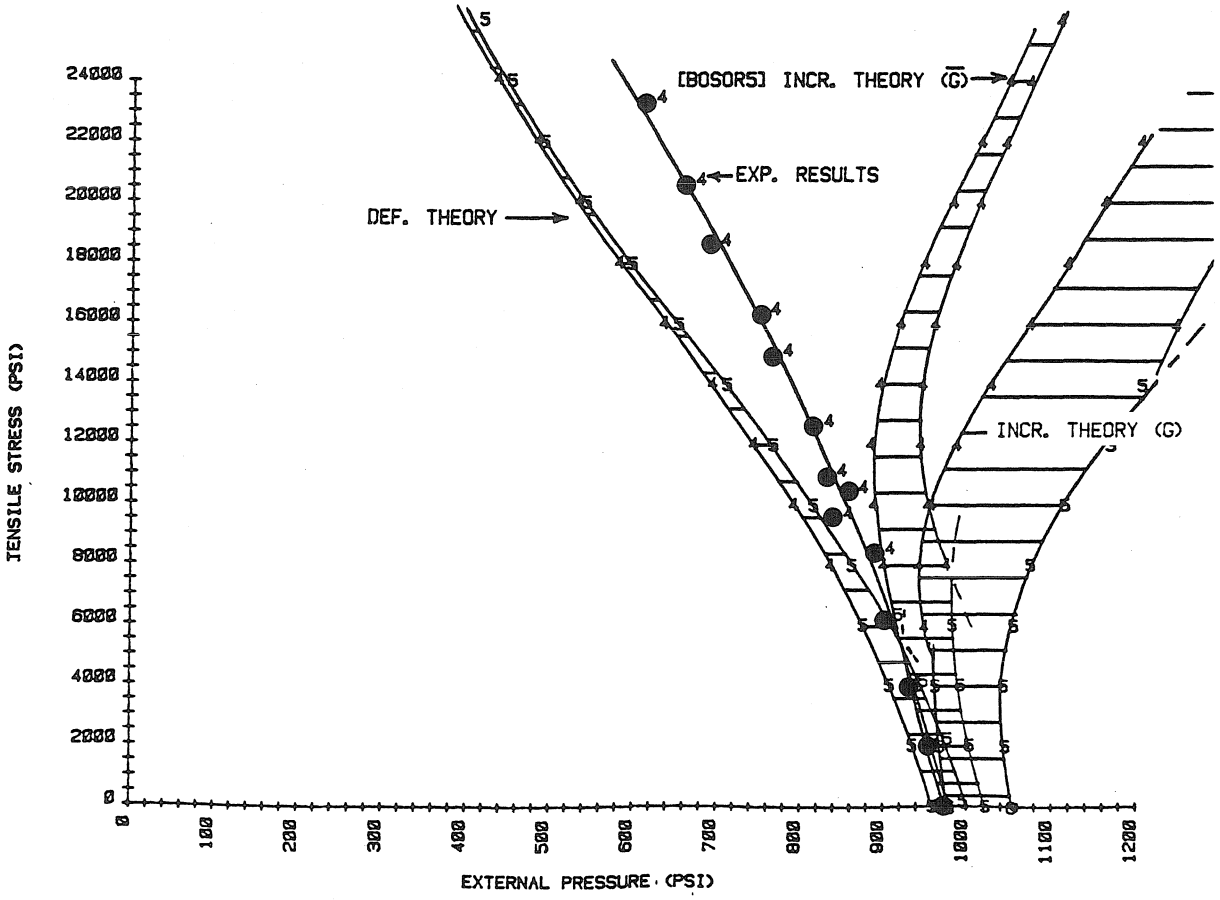

FIG. 4.5 b EFFECTS OF END IN-PLANE WARPING ON [BOSOR5] BUCKLING LOADS [SET A].

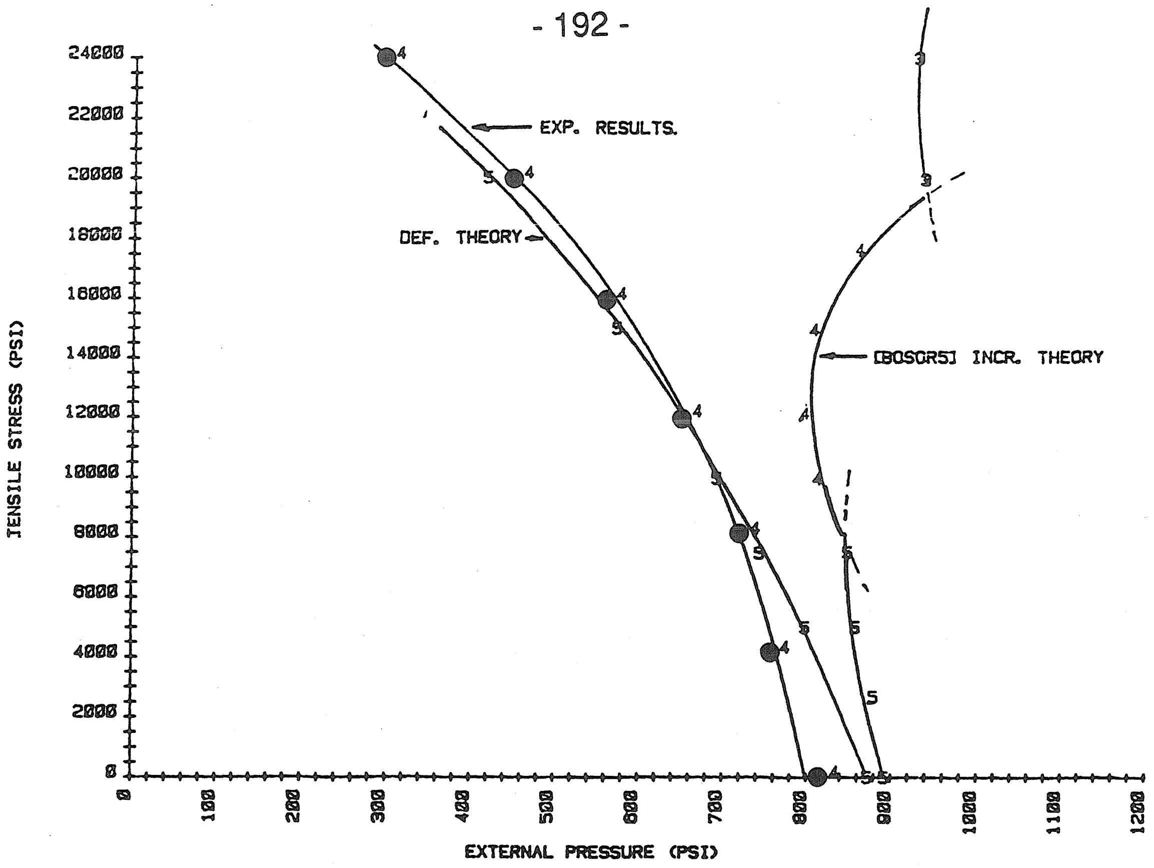

FIG. 4.6 NUMERICAL RESULTS [BOSOR5] USING AXIAL MATERIAL PROPERTIES [SET B].

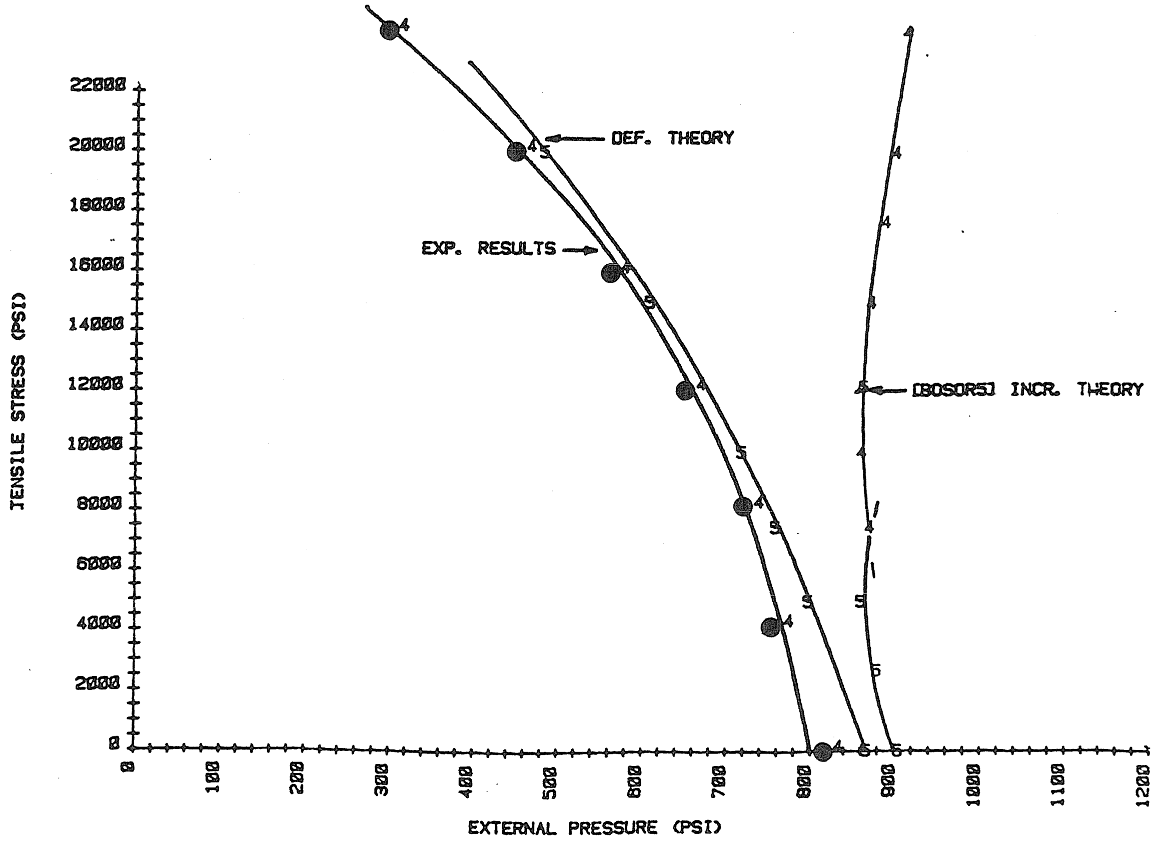

FIG. 4.7 NUMERICAL RESULTS [BOSOR5] USING CIRCUMFERENTIAL PROPERTIES.

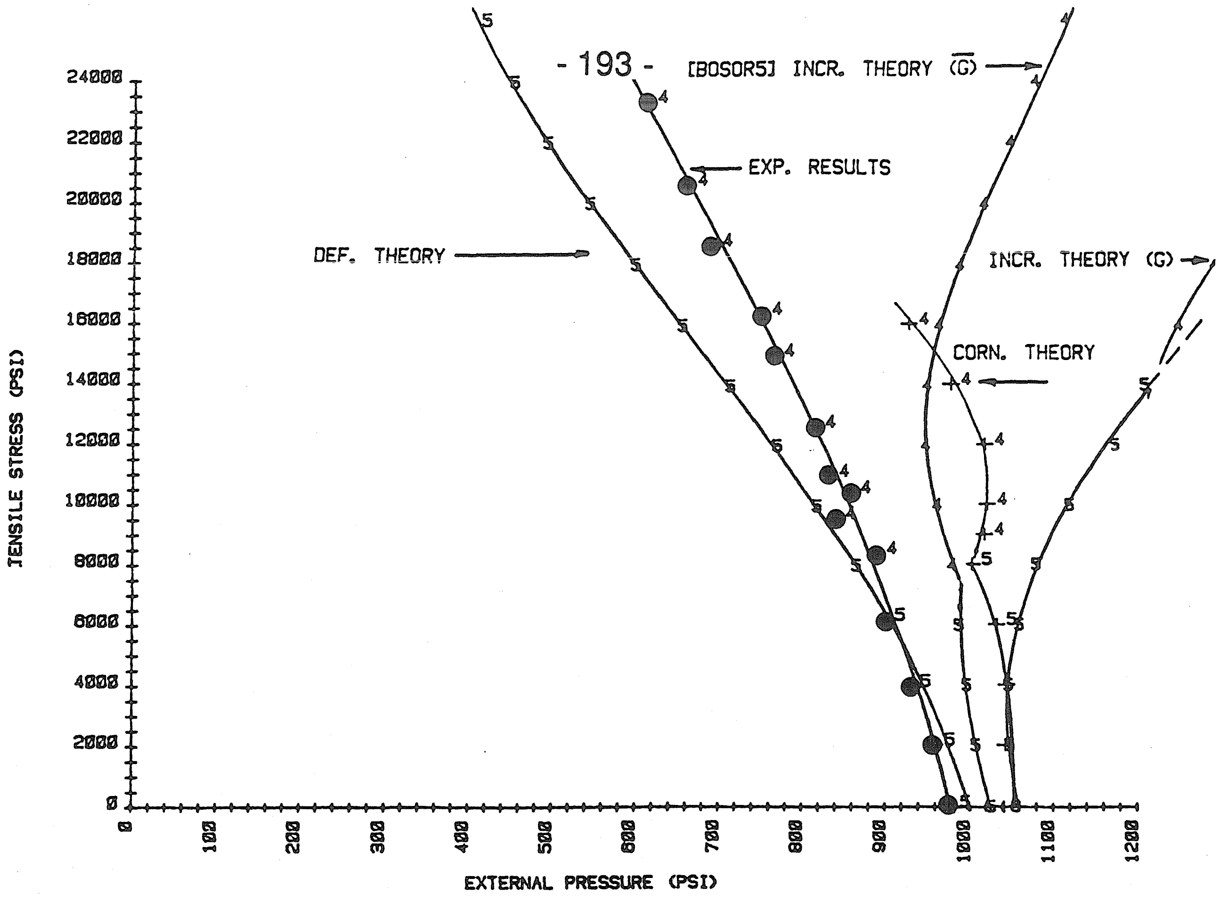

FIG. 4.8 C-H CORNER THEORY IN BOSOR5 [SET A].

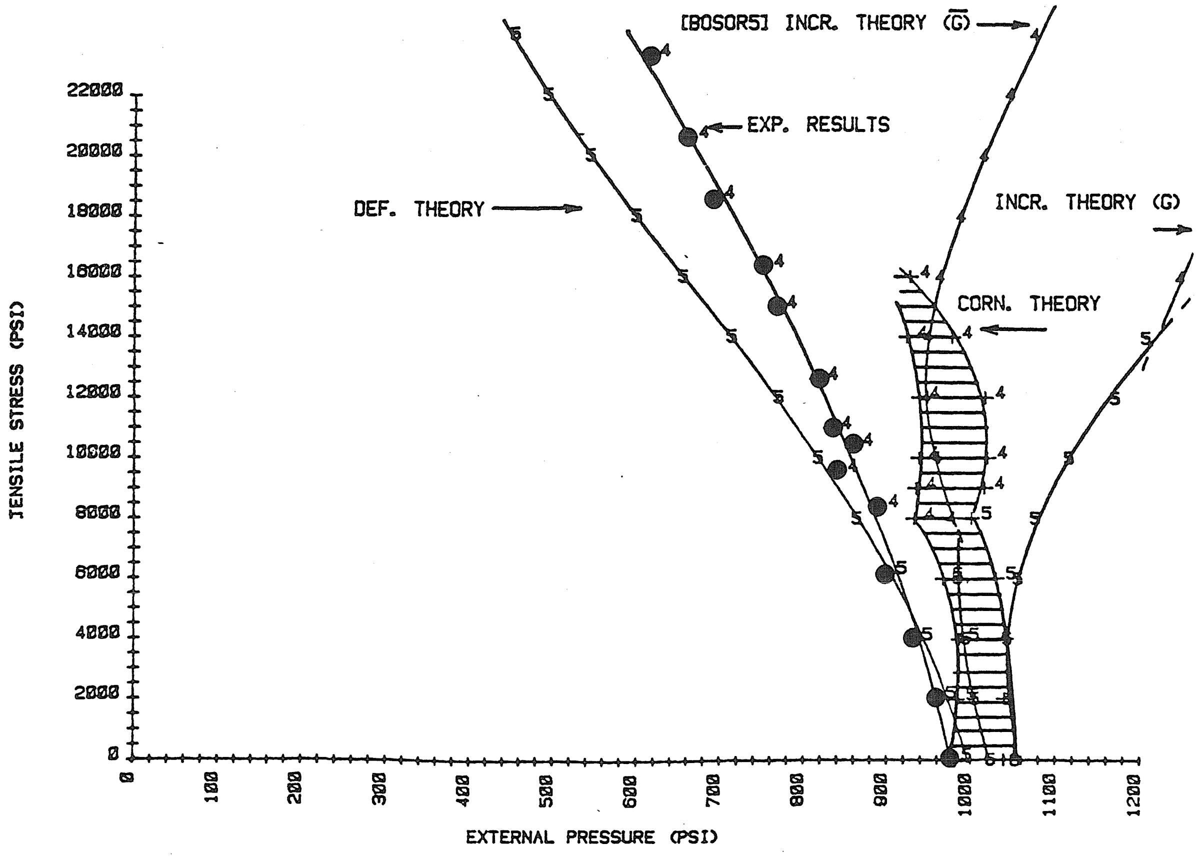

FIG. 4.9 C-H THEORY AND EFFECTS DUE TO (IN-PLANE) WARPING [SET A].

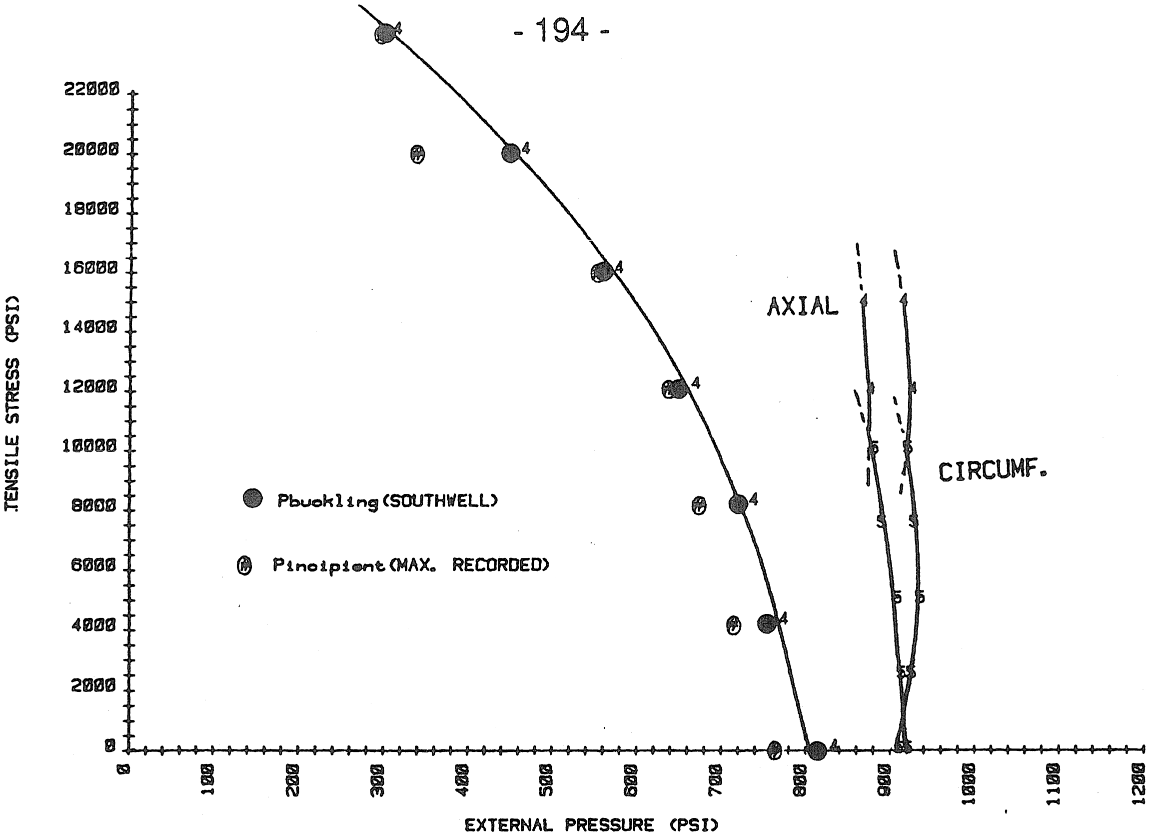

FIG. 4.10 C-H THEORY USING AXIAL AND CIRCUMF. MATERIAL PROPERTIES [SET B].

AXIAL DISPLACEMENT RESTRAINED ($u^* = 0$) DURING BUCKLING

C.T.S. (Psi)	$P_{incr.}$(Bushnell)	$P_{incr.}$(G)	$P_{def.}$	$P_{corn.}$
0	1023 (5)	1053 (6)	997 (5)	1040 (5)
2000	1004 (5)	1045 (5)	974 (5)	1041 (5)
4000	993 (5)	1043 (5)	941 (5)	1042 (5)
6000	983 (5)	1055 (5)	902 (5)	1030 (5)
8000	975 (4)	1075 (5)	862 (5)	1000 (5)
9000				1015 (4)
10000	957 (4)	1115 (5)	815 (5)	1018 (4)
12000	943 (4)	1169 (5)	767 (5)	1015 (4)
14000	945 (4)	1205 (4)	711 (5)	975 (4)
16000	959 (4)	1245 (4)	653 (5)	925 (4)
18000	983 (4)	1287 (4)	597 (5)	-
20000	1011 (4)	1329 (4)	542 (5)	-
22000	1041 (4)	1371 (4)	491 (5)	-
24000	1070 (4)		451 (5)	-
26000	1105 (4)		417 (5)	-

C.T.S. = CONSTANT TENSILE STRESS

* ALL PRESSURE IN $LBS/INCH^2$

TABLE 4.1 EXTERNAL BUCKLING PRESSURES (PSI) AND (#) CIRCUMFERENTIAL WAVES ($u^* = 0$) FROM BOSOR5 ANALYSIS ("SET A").

AXIAL DISPLACEMENT RELEASED (u^* = FREE) DURING BUCKLING

C.T.S.(PSI)	$P_{incr.(BUSHNELL)}$	$P_{incr.}(G)$	$P_{def.}$	$P_{corn.}$
0	972 (5)	981 (5)	960 (5)	980 (5)
2000	957 (5)	969 (5)	935 (5)	982 (5)
4000	941 (4)	963 (4)	907 (5)	985 (5)
6000	913 (4)	949 (4)	875 (4)	965 (5)
8000	899 (4)	941 (4)	835 (4)	930 (4)
				932 (4)
10000	887 (4)	951 (4)	791 (4)	935 (4)
12000	883 (4)	985 (4)	743 (4)	935 (4)
14000	893 (4)	1025 (4)	693 (4)	920 (4)
16000	917 (4)	1071 (4)	635 (4)	905 (4)
18000	945 (4)	1115 (4)	581 (4)	-
20000	978 (4)	1159 (4)	532 (4)	-
22000	1011 (4)	1203 (4)	483 (4)	-
24000	1044 (4)		434 (4)	-

C.T.S. = CONSTANT TENSILE STRESS

* ALL PRESSURES IN LBS/INCH^2

TABLE 4.2 EXTERNAL BUCKLING PRESSURES (PSI) AND (#) CIRCUMFERENTIAL WAVES (u^* = F.| FROM BOSOR5 ANALYSIS ("SET A").

	AXIAL MAT. PROPERTIES		CIRCUMFEMEMTIAL MAT. PROPERTIES	
C.T.S. (PSI)	$P_{incr.}$(BUSHNELL)	$P_{def.}$	$P_{incr.}$(BUSHNELL)	$P_{def.}$
0	892 (5)	872 (5)	902 (5)	867 (5)
2500	878 (5)		892 (5)	
5000	857 (5)	797 (5)	857 (5)	797 (5)
7500	847 (5)		867 (5)	
10000	812 (4)	692 (5)	857 (4)	717 (5)
12000	792 (4)		852 (4)	
15000	807 (4)	572 (5)	867 (4)	607 (5)
17500	862 (4)		872 (4)	
20000	937 (3)	417 (5)	895 (4)	482 (5)
24000	927 (3)		907 (4)	

CH-CORNER THEORY

C.T.S	$P_{corn.}$	$P_{corn.}$
0	922 (5)	907
2500	910 (5)	922 (5)
5000	897 (5)	932 (5)
7500	887 (5)	925 (5)
10000	878 (5)	920 (5)
12000	875 (4)	928 (4)
15000	875 (4)	918 (4)
17000	-	-

C.T.S = CONSTANT TENSILE STRESS
* ALL PRESSURES IN LBS/INCH^2

TABLE 4.3 EXTERNAL BUCKLING PRESSURES (PSI) AND (#) CIRCUMFERENTIAL WAVES ($u^* = 0$) FROM BOSOR5 ANALYSIS ("SET B").

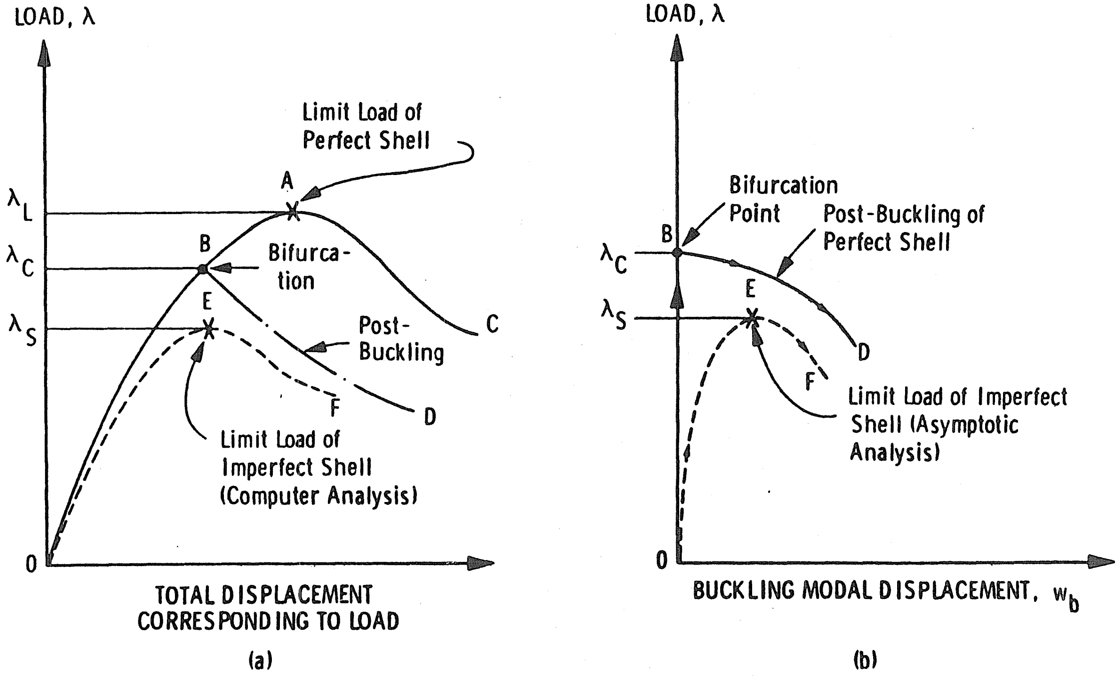

FIG. 5.1a and b LOAD-DEFLECTION CURVES SHOWING LIMIT AND BIFURCATION POINTS.
(a) GENERAL NONLINEAR ANALYSIS. (b) ASYMPTOTIC ANALYSIS.

$$\underline{\varepsilon}^{e} = L\,\underline{\sigma}$$

$$\underline{\varepsilon}^{T} = \underline{\varepsilon}^{e} + \underline{\varepsilon}^{p}$$

Deformation Theory

$$\underline{\varepsilon}^{p} = f(\underline{\sigma})$$

f = nonlinear material function

Incremental Theory
(with associative flow rule)

$$d\underline{\varepsilon}^{p} = \lambda \frac{\partial F}{\partial \underline{\sigma}}$$

$\lambda(\underline{\sigma}, d\underline{\sigma})$ = hardening parameter

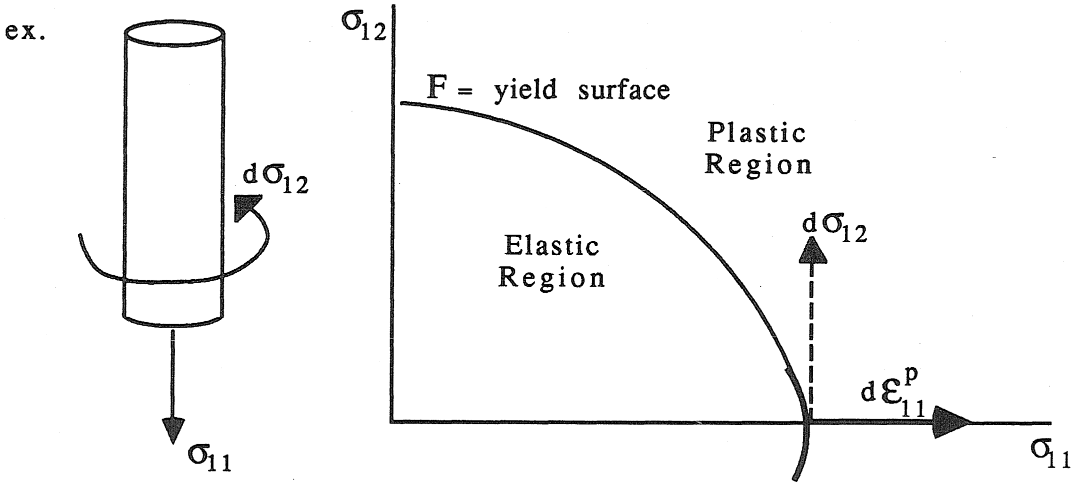

FIG. 5.2 DEFORMATION VS. INCREMENTAL THEORY.

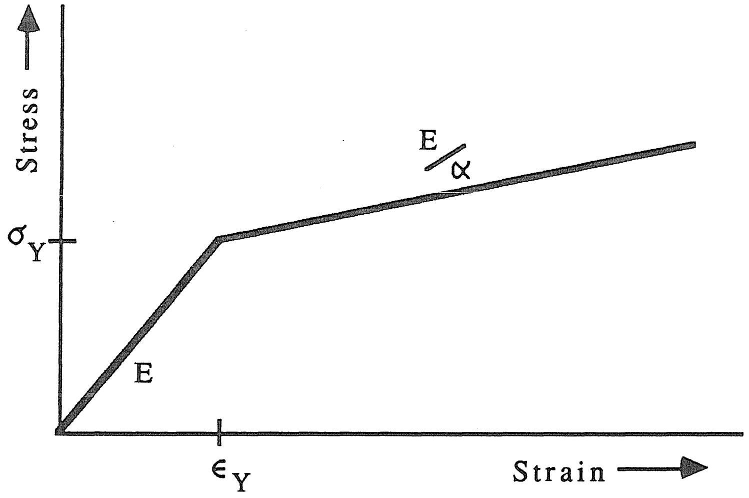

FIG. 5.3 BILINEAR STRESS-STRAIN CURVE.

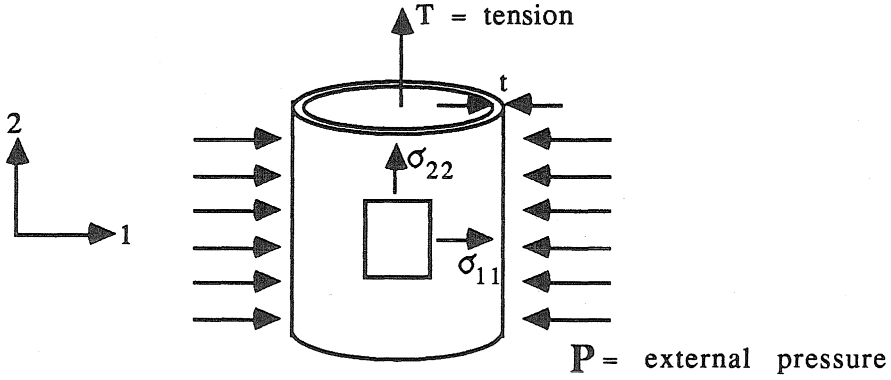

FIG. 5.4 SPECIMEN AND LOADING.

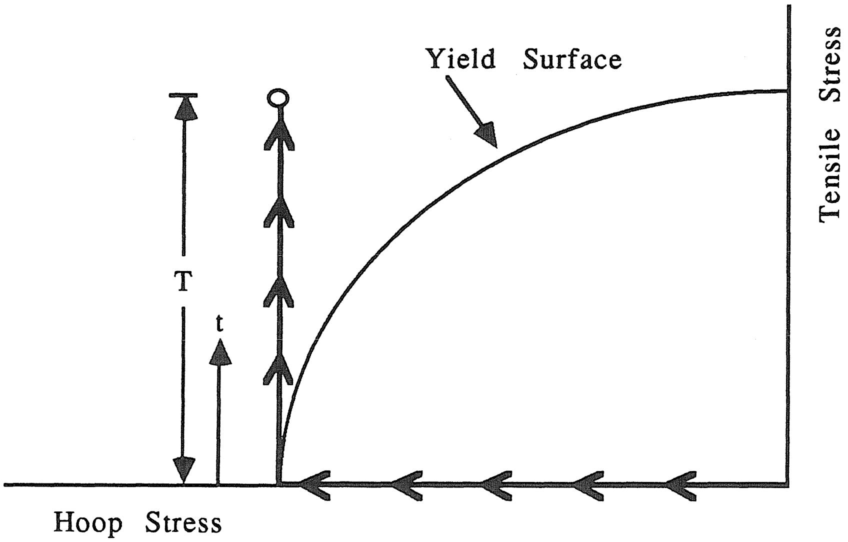

FIG. 5.5 LOAD-PATH.

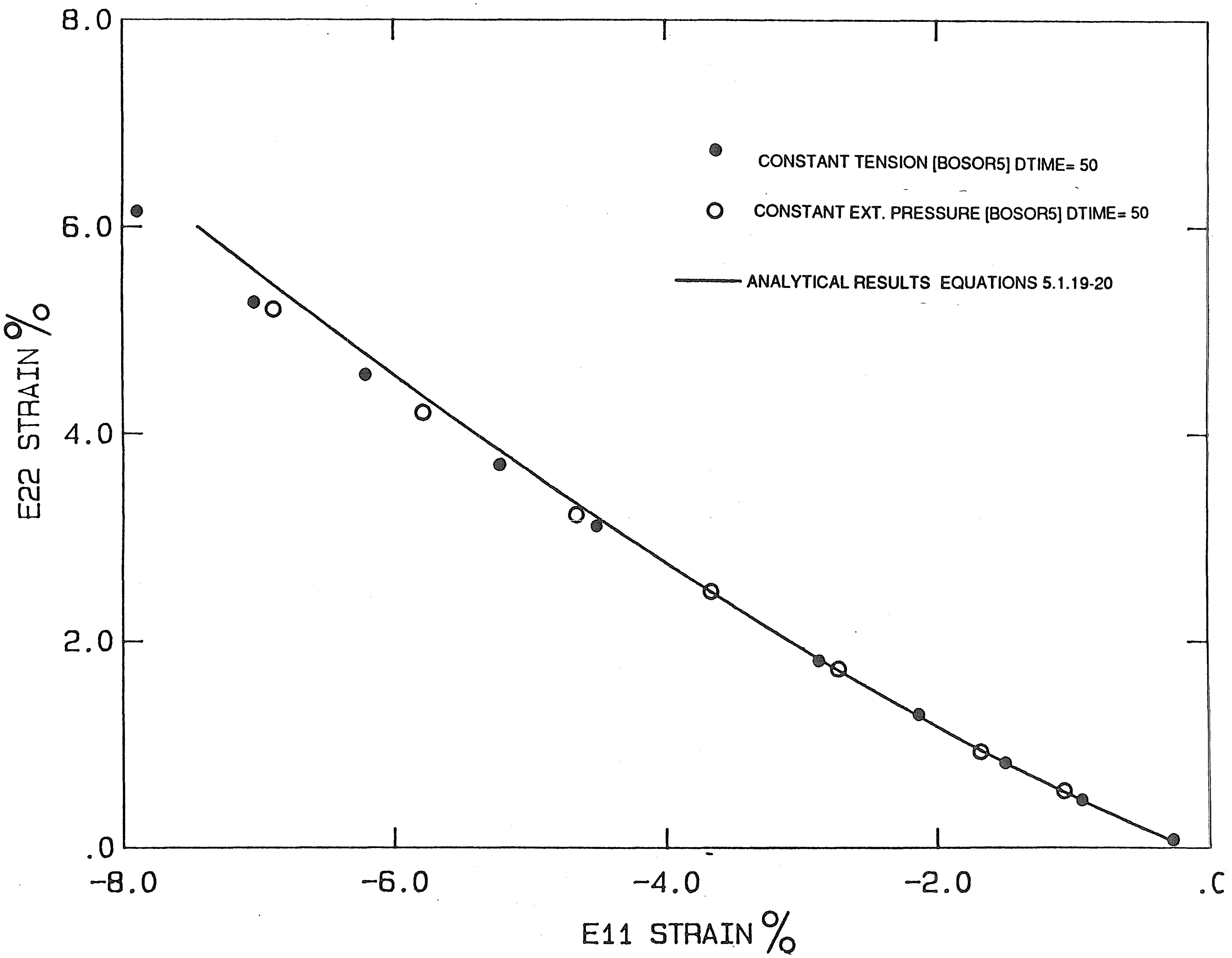

FIG. 5.6 STRAIN-PATH AND BOSOR5 RESULTS FOR LOAD-STEP CONVERGENCE TEST.

#	ε_{11} (%)	ε_{22} (%)
1	0.260	-0.065
2	0.823	-0.390
3	0.829	-0.393
4	1.462	-0.800
5	1.468	-0.803
6	2.151	-1.282
7	2.158	-1.287
8	2.165	-1.292
9	2.900	-1.849
10	2.907	-1.855
11	3.678	-2.479
12	3.686	-2.485
13	4.484	-3.171
14	4.492	-3.177
15	5.320	-3.926
16	5.327	-3.933
17	6.163	-4.725
18	6.171	-4.732
19	7.027	-5.578
20	7.035	-5.586

TABLE 5.1 ANALYTICALLY CALCULATED TOTAL STRAIN LEVELS FROM EQUATIONS 5.1.19 AND 5.1.20 AS SHOWN IN FIGURE 5.6.

DTIME = 25 [BOSOR5]

TIME	$\varepsilon_{11}(\%)$	$\varepsilon_{22}(\%)$	$\varepsilon_{11}^{P}(\%)$	$\varepsilon_{22}^{P}(\%)$	YIELD STRESS
100	-.065	.260	0	0	26000
200	-.391	.826	-.300	.560	26010
300	-.799	1.464	-.682	1.190	26020
400	-1.285	2.159	-1.141	1.879	26060
500	-1.844	2.902	-1.674	2.615	26120
600	-2.470	3.682	-2.273	3.387	26200
700	-3.156	4.491	-2.933	4.188	26310
800	-3.897	5.322	-3.646	5.011	26450
900	-4.685	6.170	-4.408	5.852	26630
1000	-5.516	7.033	-5.212	6.705	66850

Max. Error 1%

DTIME = 50 [BOSOR5]

100	-0.065	.260	0	0	26000
200	-0.392	.826	-.301	.560	26010
300	-0.801	1.464	-.683	1.190	26030
400	-1.287	2.159	-1.144	1.879	26080
500	-1.847	2.902	-1.677	2.614	26130
600	-2.473	3.681	-2.277	3.386	26210
700	-3.160	4.490	-2.937	4.187	26320
800	-3.901	5.321	-3.650	5.010	26460
950	-4688	6.169	-4.412	5.850	26680
1000	-5.519	7.032	-5.215	6.704	26900

Max. Error 2%

DTIME = 100 [BOSOR5]

100	-.065	.260	0	0	26000
200	-.396	.826	-.305	.559	26000
300	-.807	1.463	-.690	1.189	26040
400	-1.297	2.157	-1.155	1.870	26080
500	-1.858	2.899	-1.689	2.611	26160
600	-2.487	3.677	-2.290	3.382	26240
700	-3.174	4.485	-2.952	4.182	26390
800	-3.196	5.315	-3.666	5.004	26530
900	-4.703	6.163	-4.427	5.843	26790
1000	-5.533	7.025	-5.231	6.697	27000

Max. Error 2%

FOR DTIME = 200 MAX ERROR = 3 - 5% (NOT SHOWN)

TABLE 5.2 BOSOR5 NUMERICAL ANALYSIS OF PLANE-STRESS PROBLEM WITH RESULTING STRAINS.

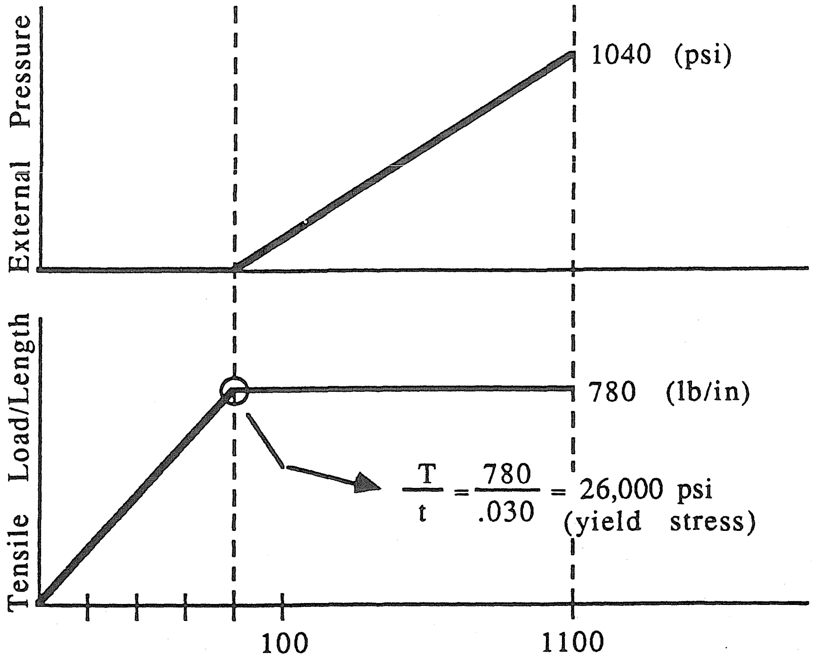

FIG. 5.7 LOAD FUNCTIONS IN BOSORS FOR CONSTANT TENSILE LOAD (SHELL THICKNESS = .030").

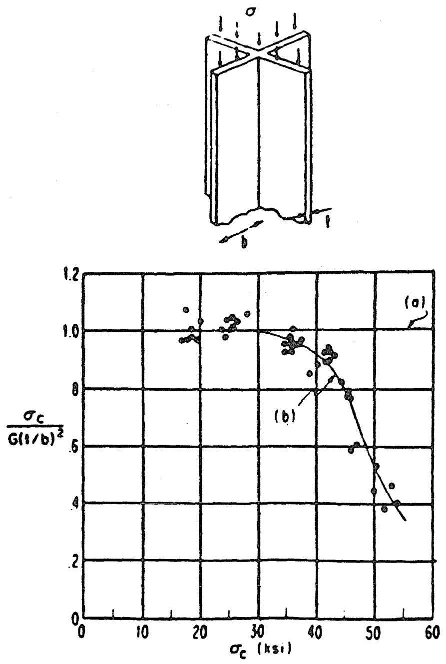

FIG. 5.8 THEORETICAL AND EXPERIMENTAL RESULTS FOR PLASTIC BUCKLING OF A CRUCIFORM COLUMN. CURVE (a) PREDICTION OF INCREMENTAL THEORY WITH A SMOOTH YIELD SURFACE; CURVE (b), PREDICTION OF ANY DEFORMATION THEORY WITH √=.5; TEST DATA FROM 2024-T4 CRUCIFORM SECTION (FROM GERARD AND BECKER [42]).

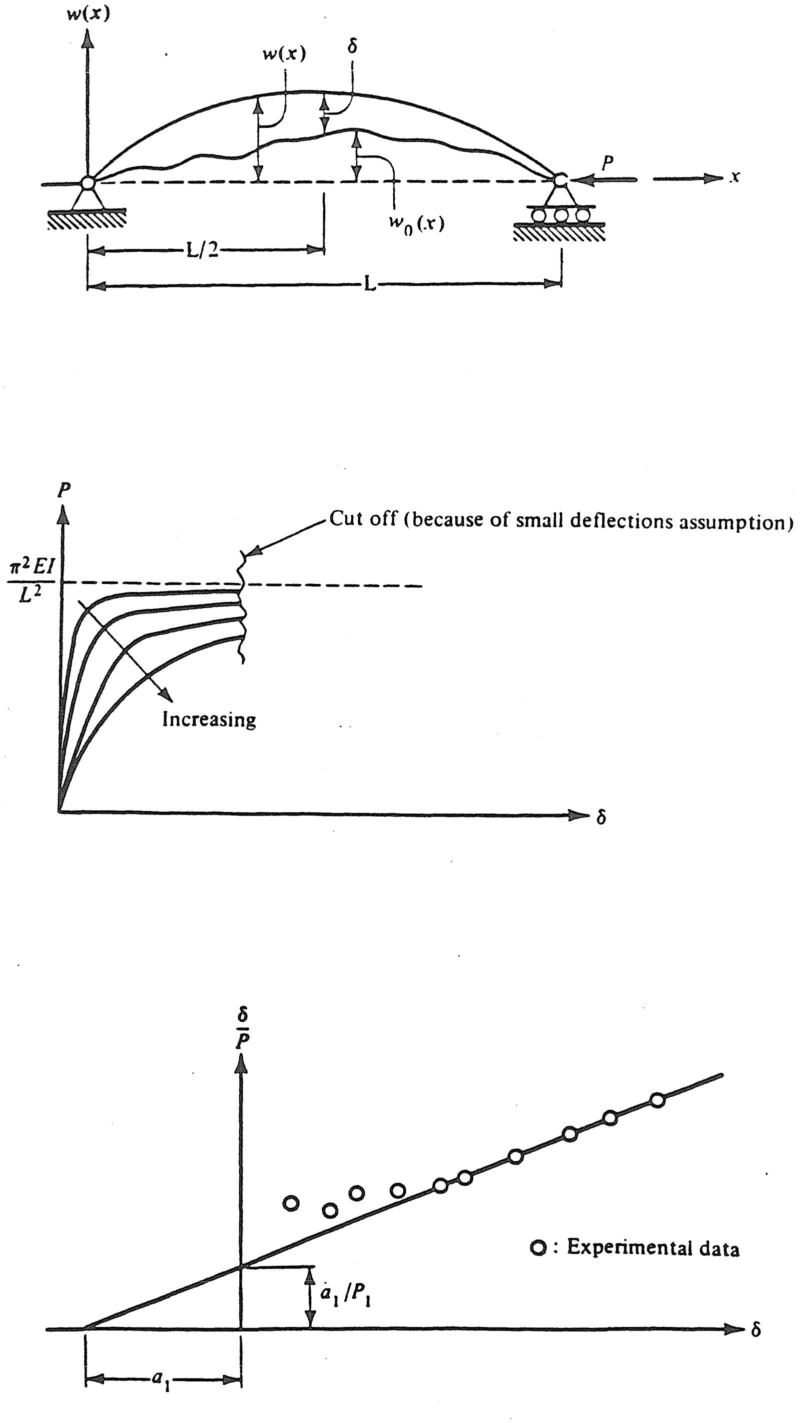

FIG. 6.1 a,b and c SOUTHWELL PLOT FOR AN IMPERFECT COLUMN.

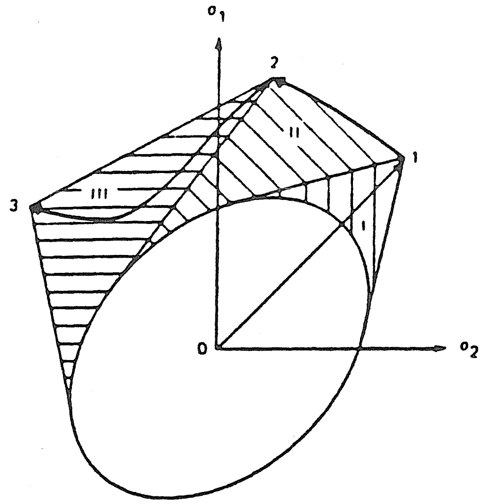

FIG. 7.1 SLIP THEORY HARDENING (FROM ARMEN).

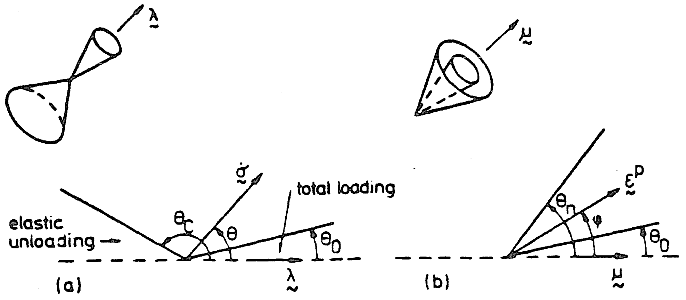

FIG. 7.2 (a) STRESS-RATE SPACE; (b) STRAIN-RATE SPACE, AS DEFINED BY CHRISTOFFERSEN AND HUTCHINSON [53].

MAIN	The main program, calls the other subroutines.	
FACTR	Decomposes a coefficient matrix into its lower triangular form.	Equation
SOLVE	Performs back substitution for solution of equation system.	Solver
LOADS	Finds loads on the shell corresponding to the next time step.	
PRE11	Sets up and solves the nonlinear (large deflection) prebuckling equations, given material properties. APREB Sets up the equations for the next Newton iteration. SOLN Factors and solves the system of linear equations derived by APREB. (loop over APREB and SOLN until Newton iterations converge.)	
PRE22	Derives strains and stress resultants, given the solution obtained by PRE11.	
PRE33	Finds updated material properties, given new values of total strains by PRE22. PLAST retrives temperature distrubition and calculates new plastic and creep strain components in shell wall and in discrete rings. . . . FLOW uses flow or deformation theory to find plastic and creep strain components for a given point along the meridian and within the thickness of the shell wall (or within discrete ring).	
ARRAYS	Derives the stability equations for given circumferential wavenumber, n, and calculates the stability determinant for a given time step. STABIL calculates the stiffness matrix and the load-geometric matrix.	
BUCKLE	Eigenvalue solver for given circumferential wavenumber, n. EBAND2 Uses inverse power iteration method to extract eigenvalues for stability problem.	

FIG 7.3 IMPORTANT SUBROUTINES OF THE BOSOR5 MAIN PROCESSOR.

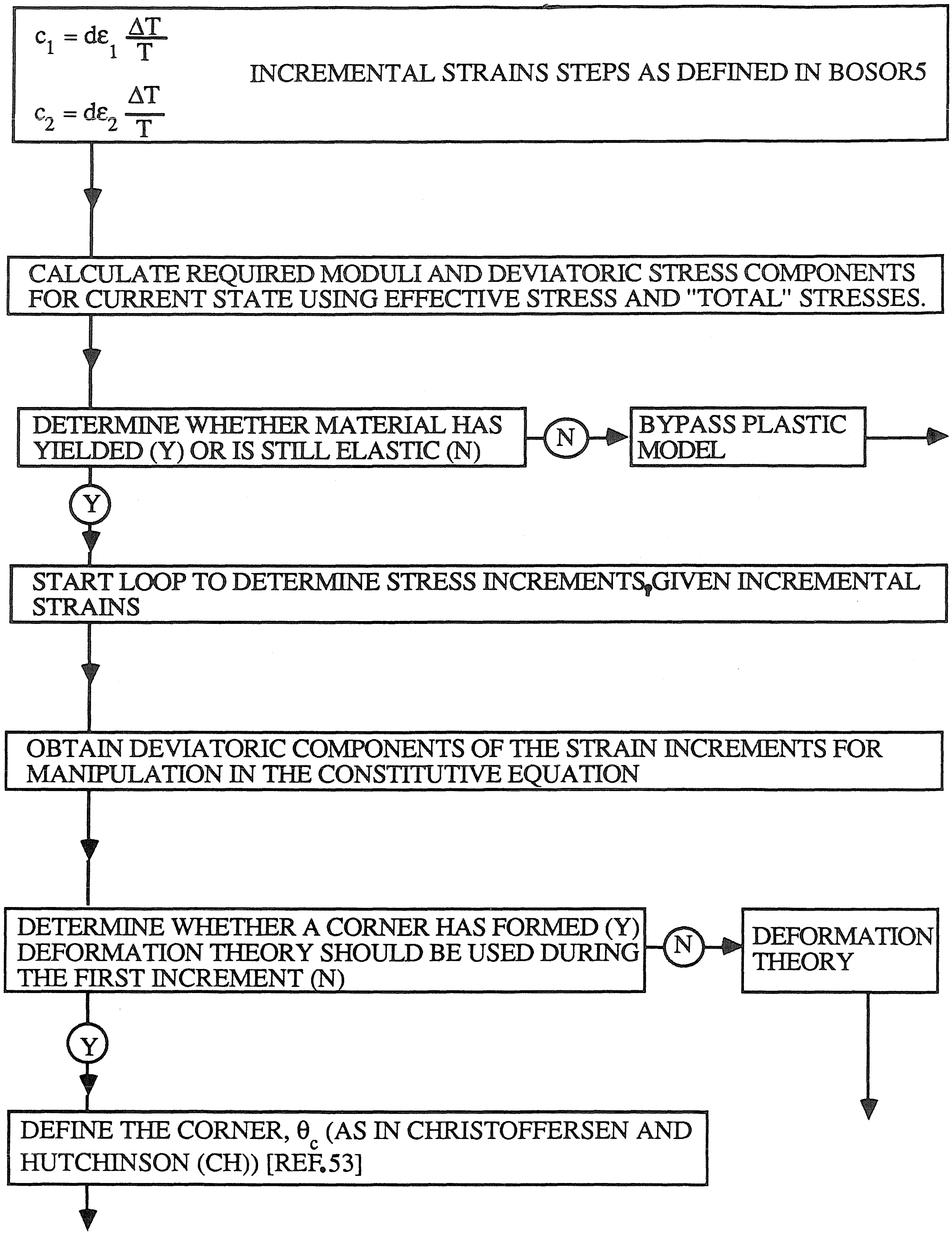

FIG 7.4a BLOCK-DIAGRAM OF J_2 CORNER THEORY IN BOSOR5.

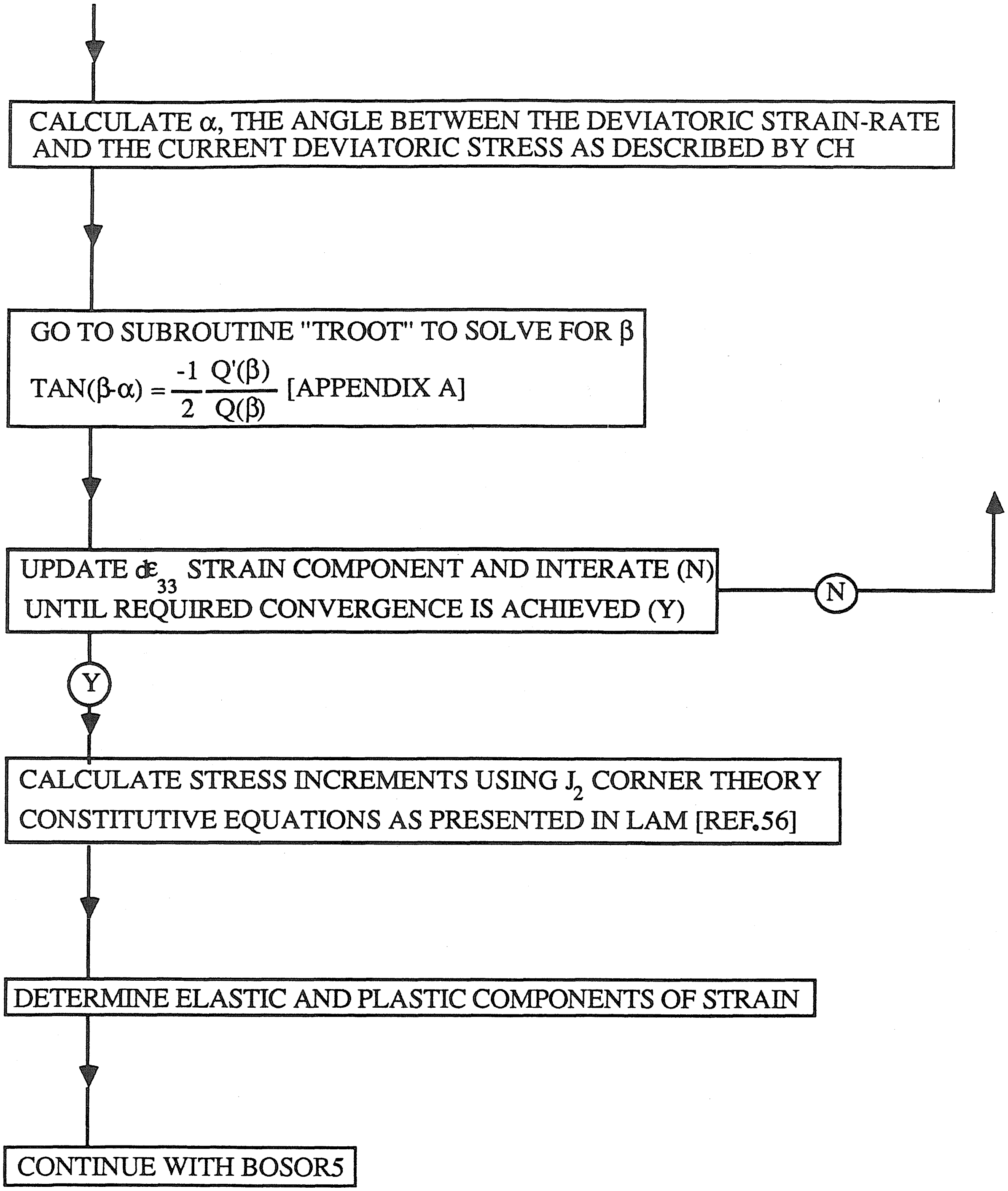

FIG 7.4b BLOCK-DIAGRAM OF J_2 CORNER THEORY IN BOSOR5 (CONTINUED).